Magnetism In Iron Based Compound

FRAWLEY, THOMAS,WILLIAM

MAGNETISM IN IRON BASED COMPOUNDS

by

Thomas Frawley

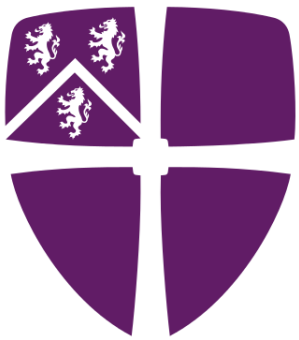

Supervisor: Professor P.D.Hatton

Submitted in conformity with the requirements
for the degree of PhD
Department of Physics
University of Durham

Declaration

The material contained within this thesis has not previously been submitted for a degree at the University of Durham or any other university. The research reported within this thesis has been conducted by the author unless indicated otherwise.

Copyright Notice

Magnetism in Iron based Compounds

Thomas Frawley

Submitted for the degree of Doctor of Philosophy
December 2015

Abstract

This thesis describes the investigation of a range of iron-based compounds which exhibit a variety of different electronic phases, from magnetoresistance to ferroelectricity. X-ray diffraction, neutron diffraction, and muon spectroscopy techniques were used to probe the magnetism to provide an explanation of the microscopic mechanism for the bulk electronic properties. X-ray diffraction is a set of techniques that probe electronic ordering in a periodic crystalline system. If the x-ray energy is tuned to an absorption edge of a magnetically active ion in the compound sensitivity to the magnetic order can be gained. These x-ray techniques were used to study magnetoresistance in $SrFeO_{3-\delta}$, revealing an interplay between the structural, charge and magnetic order as the origin. Neutron diffraction is an established set of techniques that can directly probe the magnetic order of a crystalline compound. Neutron diffraction was used in conjunction with x-rays to study the ferroelectric and Ising-like phases in the triangular lattice antiferromagnet $CuFeO_2$, revealing strong spin-lattice coupling, the coexistence of antiferromagnetic and ferromagnetic phases and the splitting of the magnetic order in the ferroelectric phase into two inequivalent orbits with a phase separation between them. Diffraction techniques require long-range order of the magnetic ground state to be of utility. Muon spectroscopy is a local probe that can study magnetism in systems where the magnetic order remains short-ranged. Muon spectroscopy was used to study the spin-freezing phenomena in FeCrAs, and revealed a two stage transition and interaction energies associated with them. Polarisation analysis was used together with resonant x-ray scattering to obtain quantitative information on the structure of the magnetic helical structure of FeAs, quantifying the degree of ellipticity to the magnetic helix, and revealing an out-of-plane oscillating canted structure to the spin helix.

Acknowledgements

The research presented in this thesis is the culmination of several years work, involving collaboration with research groups around the world. As a result there is a multitude of people who should be thanked and acknowledged, as this work would not have been possible without their support and expertise.

First of all I thank my research group at Durham University. My supervisor Professor Peter Hatton has been a constant source of advice, guidance, and support, which has allowed me to pursue the areas of research which interested me. Dr Thomas Beale, who spent countless hours and late nights teaching me to be both a better experimentalist and data analyst. There would have been a lot more failed experiments without his support. Philip Dean, my fellow PhD student, who provided endless experimental support and wisdom.

Also at Durham University, I wish to thank John Dobson, who always managed to salvage our x-ray generator from the jaws of death in the nick of time. John Summerill and Reece Stockport who always provided technical support when it was needed. Steve Lishman and the entirety of the mechanical workshop, for always managing to fit my jobs in even with a three week waiting list. Dr Tom Lancaster for providing help, support and wisdom on the muon spectroscopy work on FeCrAs. Dr Ian Terry for the use of the MPMS, Professor Damian Hampshire and Dr Mark Raine for the use of the PPMS, Dr Budhika Mendis for the use of the electron microscope.

Outside of Durham, I need to thank Professor Chao-Hung Du and his student Snow Lee; they grew a number of my crystal samples, as well as providing a strong collaboration on the study of $SrFeO_3$. Professor Khalil Al-Ziq who provided the samples of FeAs and FeCrAs.

There is a huge cadre of people that need thanking for providing the experimental facilities at ESRF, DESY, Diamond, ISIS, and the NSRRC, and if I forget anyone I am sorry.

The staff at XMaS, ESRF, including Dr Simon Brown, Paul Thompson, and Dr Laurence Bouchenoire, who go above and beyond to accommodate whatever experiment a user can think up. The former beamline ID08, ESRF and Dr Flora Yakhou who maintained the soft x-ray diffractometer. At DESY I thank Dr Martin Von Zimmermann who provided the high energy x-ray beamline at BW5, DORIS, and Dr Jörg Strempfer and Dr Sonia Francoual who provided the resonant scattering facility at P09, Petra 3. At Diamond I thank the staff of I16 and I10. From I16, Dr Steve Collins, Dr Alessandro Bombardi, and Dr Federica Fabrizi were incredibly helpful, in particular Federica who provided useful discussion about methods of modelling magnetic scattering. From I10, Dr Paul Steadman, who meticulously maintained the RASOR soft x-ray diffractometer, which has been an incredibly useful instrument throughout this thesis. From ISIS, I wish to thank everyone at the neutron instrument WISH, and the Muon instrument ARGUS. At WISH, Dr Pascal Manuel and Dr Dmitry Khalyavin who not only provided support on the experiments, but were patient teachers of neutron scattering and Rietveld refinement throughout my PhD. At ARGUS, I would like to thank Dr Francis Pratt and Dr Peter Baker, for their help with muon Spectroscopy.

Finally, Dr Ed Twiddy, and Dr Chris Sparks. Although we only crossed paths in the final months of my PhD, I would like to thank them both immeasurably as they showed me not only is there space for PhDs and academic thought outside of academia, but that it can positively thrive.

To my parents, Kathryn and Patrick, for their tireless support of my education.

Contents

List of Figures

List of Tables

Chapter 1

Introduction

The study of electronic phenomena in solids is a huge area of condensed matter research, encompassing a range of effects including superconductivity, magnetoresistance, metal-insulator transitions, and ferromagnetism. The formation of ordered phases of the structural, spin, charge and orbital degrees of freedom are often tied to the more macroscopic bulk effects. How these degrees of freedom couple to one another and to external parameters like temperature, magnetic field, electric field, and pressure is central to understanding these materials. For example the coupling between the charge, spin, orbital, and lattice degrees of freedom in the perovskite manganites systems leads to metal-insulator transition and colossal magnetoresistance-type behaviour [3]. Ordering can occur in the arrangement of the constituent atoms, the alignment of magnetic and electric moments, the valency of the atoms (charge ordering), the alignment of occupied orbitals (orbital ordering), as well as more unconventional orderings such as the axial and polar toroidal moments. The formation of an ordered phase is associated with the breaking of symmetries. Landau theory describes phases of matter which can be described by spontaneous symmetry breaking, and the associated continuous phase transition. There are a few examples of order in condensed matter which are not described by spontaneous symmetry breaking but instead are described as a topological order, such as the fractional quantum hall effect [4] and spin-liquid phases [5]. Topological ordered phases will not be expanded upon as they are outside the scope of this thesis. Understanding the symmetry of the phases is important in understanding the material properties. For example, piezoelectricity can only occur in a crystal which have no centre of inversion (non-centrosymmetric). Of the 32 crystal classes, only 21 are non-centrosymmetric, and of these only 20 permit

piezoelectricity (for cubic crystal class 432 the piezoelectric charge forms along the $\langle 110 \rangle$ axes cancelling one another out). Further to this for a material to exhibit ferroelectricity, the crystal symmetry has to belong to one of the eight polar classes out of the 21 non-centrosymmetric classes [6].

In a piezoelectric material an elastic deformation induces an electric dipole, and an electric field induces a elastic deformation. There are a class of materials where magnetic and electric order parameters are coupled. Where an electric field can induce an magnetic response and magnetic field can induce an electric response. Materials where ordered phases are coupled are known as multiferroics, and are simply defined as materials which have more than one (multi) ferroic or antiferroic order, *i.e.* ferromagnetism and ferroelectricity [7]. In particular the class of multiferroics where electric and magnetic order parameters are coupled are known as magnetoelectrics.

Understanding how order parameters couple to give rise to effects like multiferroicity and magnetoresistance, is necessary in designing smart materials for device applications. Geometrically frustrated systems, although may not be suitable for devices directly, provide the opportunity to study the effects of secondary interactions which is important for designing smart materials.

In this thesis, both x-ray diffraction, neutron diffraction techniques, and muon spectroscopy have been used. Diffraction techniques can be used to elucidate the nature of periodic structures. Neutrons and x-ray diffraction are complementary techniques, both are sensitive to the crystal and magnetic structures, but can provide different information. Neutrons interact with the nuclei and magnetic moments in the system, whereas x-rays interact with the electron density directly. Both techniques can be used to study magnetic periodic structures, but x-rays can also be used to study charge ordering, lattice distortions and orbital ordering (as well as a whole host of higher order symmetry objects including magnetic and electric quadrupoles and octopoles and polar and axial toroidal moments [8]).

When the formation of the electronic phase does not exhibit a periodic structure, as is the case with a spin glass, a different technique is needed. Muon spectroscopy interacts with a material implanting in an interstitial site and precessing in local magnetic fields. Muons are a useful probe in systems where the interactions remain short-range or the ordered phases does not have periodicity.

1.1 Order Parameters and Phase transitions

The order parameter indicates the degree of order of a system, with the order parameter taking the value of zero on the disordered side of the phase transition [9]. For example, for a ferromagnet the net magnetisation can be used as the order parameter of the transition. Above the Curie temperature where the magnetism is described by a paramagnetic phase the net magnetisation is zero. Below the Curie temperature, there is a spontaneous symmetry breaking where the magnetic moments align and a net magnetization forms [10]. Although there is some debate on whether the symmetry breaking for the ferromagnetic phase transition can be classified as "spontaneous" symmetry breaking [11]. The debate stems from the fact the ferromagnetic ground state is an eigenstate of the relevant continuous symmetry, and as a result does not fit the rigorous definition of spontaneous symmetry breaking [12]. Antiferromagnetism on the other hand does meet the criteria to be considered spontaneous symmetry breaking. The magnetisation can no longer be used for the order parameter for the antiferromagnetic case as it remains zero on both sides of the phase transition. In the case of an Ising antiferromagnet, the staggered magnetisation is used as the order parameter. In the case of an antiferromagnet the magnetisation on one sublattice is equal and opposite to the magnetisation on the other sublattice. The magnetisation on a single sublattice is used as the order parameter, as this is zero in the disordered phase and non-zero in the antiferromagnetic phase.

A transition between the ordered and disordered phases is not gradual over the whole phase, but sharp, confined to a small temperature region. The region between the ordered and disordered state is called the critical region. The phase transition at the critical region, can be described as either first-order or continuous. The order of the phase transition is given by the lowest differential of the free energy which shows a discontinuity. A first-order transition has a discontinuous jump in the first derivative of the free energy, whilst a continuous transition is continuous in the first derivative but will have a discontinuous jump in either the second, third or fourth *et cetera* derivative. First-order transitions have an associated latent heat. Quantities such as volume, magnetisation and entropy which are proportional to the first derivative, would show a discontinuity if the transition was first order, but not if the transition was continuous.

In the critical region around a phase transition, a phenomenological model of critical

exponents can be employed. By defining a dimensionless reduced temperature, t

$$t = \frac{T - T_c}{T_c} \tag{1.1}$$

where T_c is the phase transition temperature, the transition occurs at $t = 1$, and the phase transitions can be compared between systems. The magnetisation in the critical region can expressed in terms of a critical exponent, β, such that $M = (-t)^\beta$ where $t < 1$ [13]. For a continuous phase transition, the critical exponent depends on three properties only. The first is the dimensionality of the system, d, whether the interactions in the system are one-, two-, or three-dimensional. The second property is the dimensionality of the order parameter, D. For the simple cases this is the number of dimensions in which the order parameter varies. For the Ising magnet, D is one, for the XY magnet D is two and for the Heisenberg magnet D is three. The last property that effects the critical exponent is whether the forces are short-range or long-range.

1.2 Ordered Phases

In condensed matter, a system of fixed charges and permanent currents can be expanded using a multipole moment approach [8, 14, 15]. Using a multipole moment expansion approach, a condensed matter system can be broken up into four families of objects, the axial (magnetic), polar (electric), axial-toroidal, and polar-toroidal moments. The multipole expansion of the moments leads to a series of objects with monopole, dipole, quadrupole, octupole and hexadecapole *et cetera* symmetry. The nomenclature for the terms in the multipole expansion comes from the greek word for the number 2^n. The existence of a magnetic monopole is still an area of active debate and research. For the work in this thesis the magnetic monopole does not play a role. The axial-toroidal dipole can be considered as a ring of electric dipoles, all pointing around the loop in the same direction, resulting in an axial-toriodal dipole pointing through the loop in a right-handed screw direction. The polar-toroidal dipole can be considered a ring of magnetic dipoles, all pointing around the loop in the same direction, with the polar-toroidal dipole pointing through the loop in a right-handed screw direction. Since a magnetic dipole can be thought of as a current loop, the polar-toroidal is often referred to as an orbital current. Table 1.1 shows the space-inversion and time reversal properties of these multipole objects (taken from [8]). The magnetic dipole can be considered a current loop, under time-reversal the

Multipole	Time Reversal	Space Inversion	Spherical-tensor rank
Electric dipole	+	-	1
Magnetic dipole	-	+	1
Polar toroidal dipole	-	-	1
Axial toroidal dipole	+	+	1
Electric quadrupole	+	+	2
Magnetic quadrupole	-	-	2
Polar toroidal quadrupole	-	+	2
Axial toroidal quadrupole	+	-	2

Table 1.1: Symmetry of electronic multipoles. Effect of parity operations of time-reversal and space-inversion of the terms in the electronic multipole expansion, fourth column shows the spherical-tensor rank of the multipole terms.

current flows backwards changing the direction of the magnetic dipole. The ordering of these more unusual symmetry objects has been seen in nature with electric quadrupoles having been detected in $LaMnO_3$ [16], magnetic octupole ordering having been detected in NpO_2, axial-toroidal quadrupoles having been detected in V_2O_3 [17], and polar-toroidal dipoles in CuO [18].

There are four principal ferroic orderings in condensed matter, ferroelasticity, ferroelectricity, ferromagnetism and ferrotoroidicity. Ferroelasticity is the property of a material to exhibit a spontaneous strain below a transition temperature. Ferroelectricity is the property of a material to exhibit a spontaneous electric polarisation below a transition temperature, through the long-range order of electric dipoles. Ferromagnetism is the property of a material to exhibit a spontaneous magnetization below a transition temperature, through the long-range order of magnetic dipoles. Ferrotoroidicity is the more unusual property, where a material exhibits a spontaneous long-range order of magnetic toroidal moments below a transition temperature. These four phases are known as the principal ferroic orderings due to how they transform under the parity operations of space inversion and time reversal [19]. Table 1.2 has been reproduced from reference [19], it shows the four principle ferroics all behave differently under space-inversion and time-reversal.

In addition to the primary ferroic orders, ordering of other electronic degrees of freedom can exist in condensed matter systems, such as orbital ordering. The orderings rele-

Time \ Space	Invariant	Change
Invariant	Ferroelastic	Ferroelectric
Change	Ferromagnetic	Ferrotoroidic

Table 1.2: Time-reversal and space inversion symmetry of principle ferroic orders.

vant to this thesis will be touched upon in the the following subsections.

1.2.1 Charge Order

If the electron density is sufficiently localised on an atomic site, the language of electron valency can be used to described system. A charge-order transition involves an ordering in the valency of the metal ion, for example a square lattice of iron ions which could have a valency of $Fe^{3.5+}$ at high temperatures in the delocalised phase, could transition to a checker-board pattern of Fe^{3+} and Fe^{4+} ions in the localised phase, which doubles the unit cell. The charge-order transition is often accompanied by an increase in resistivity, as conduction electrons are localised onto the atomic sites, consequently charge ordering can be associated with metal-insulator transitions [20] and colossal magnetoresistance [21]. The charge-ordering opens a band gap splitting the conduction band, localising some of the conduction electrons into a filled band. The transition temperature associated with a charge-ordering phenomena is associated with the thermal energy needed to overcome the small charge-order band gap.

Charge-ordering can form a variety of structures from one dimensional charge stripes described by a single wavevector, to more complex checker-board and three-dimensional arrangements described by multiple wavevectors. Charge-order can take commensurate or incommensurate wavevectors [22]. Charge ordering also does not have to oscillate between integer values of valency. In the literature incommensurate charge-order is often referred to as a charge-density wave, although sometimes a distinction is made with charge-density waves being used to describe the phenomena associated with a charge modulations with a Fermi surface nesting wavevector which occurs with the Peierls distortion.

1.2.2 Magnetic Order

The magnetic moment in a condensed matter system is realised with the orbital and spin angular momentum associated with the electron density. The magnetic moment for the majority of cases is quite well approximated by the magnetic dipole. For some metallic systems like iron the magnetic moment is delocalised, and the ferromagnetic ground state is described by a spin polarised band structure. For transition metal oxides and rare-earth systems the magnetic moments are far more localised on to atomic sites, and the picture of a lattice of magnetic dipoles on atomic sites is a useful tool to employ. Magnetic dipoles can interact directly through their respective dipolar fields, but this is an extremely weak effect, and would not cause long-range order above 1 K. The magnetic moment is quantum mechanical in origin, and magnetic moments can interact through a quantum mechanical exchange. Through these quantum mechanical exchange interactions long-range magnetic ordering can occur at ambient temperatures. There are several exchange interactions relevant to the formation of magnetic ground states, from direct exchange between neighbouring magnetic orbitals, to indirect exchange and anisotropic interactions. When neighbouring magnetically active ions are far enough apart that there is insufficient overlap between magnetic orbitals, indirect exchange plays a crucial role in determining the ground state. Superexchange and double-exchange interactions are mediated via a shared anion, *e.g.* oxygen. In metallic materials, indirect exchange is mediated by a spin-polarised conduction band, this is known as itinerant exchange or the RKKY interaction [23–25]. The spin-orbit coupling can mediate the exchange in a similar role to the oxygen in superexchange. In this case the exchange is anisotropic, and is known as the Dzyaloshinsky-Moriya interaction [26, 27]. This anisotropic interaction can lead to a slight ferromagnetic component to antiferromagnetic ground states and favours spin canting. It is an important interaction in the field of multiferroics as it can lead to a coupling between the magnetic ground state and electric polarization of the system through the "Inverse Dzyaloshinsky-Moriya effect" [28].

In addition to the simple ferromagnetic and antiferromagnetic cases, there exists a host of more complex magnetic ground states. Magnetic structures can be classified as being collinear or non-collinear and commensurate or incommensurate. If all the magnetic moments in the structure lie in the same axis, then the structure is collinear. If different moments in the magnetic structure point along different directions then the magnetic ground

state is non-collinear. If the repeat of the magnetic structure or magnetic unit cell can be expressed as an integer multiple of the underlying crystallographic unit cell, the magnetic ground state is commensurate. If the magnetic unit cell can not be expressed as an integer multiple of the underlying unit cell the magnetic ground state is incommensurate with the lattice.

Figure 1.1 shows schematic examples of three complex magnetic structures. Figure 1.1 (a) and (b) shows two non-collinear examples of spin structures. (a) shows a helical magnetic structure, where the magnetic moments rotate in a plane perpendicular to the propagation vector. (b) shows a cycloidal magnetic structure where the magnetic moments rotate in a plane parallel to the propagation vector. Both the helical and cycloidal structure are chiral, having a choice in the sense of rotation. The structure shown in figure 1.1(c) is a spin density wave. This is a collinear structure where the magnitude of the moment varies along the propagation vector.

1.2.3 Structural Order

In addition to the charge and magnetic degrees of freedom, transitions between different structural phases in the material can also occur. In the simple case a slight rearrangement in atom position lowers the symmetry of the crystal lattice in the low temperature phase. In such cases the lower symmetry unit cell description can be used to describe both sides of the transition, with different atomic positions, whereas the high symmetry unit cell can only describe the high temperature phase.

Other types of structural transitions include Jahn Teller distortions and lattice- modulations. Jahn Teller distortions occur in materials with a degenerate ground state. The Jahn Teller distortion is a geometrical distortion which lowers the total energy of the system [29]. For example an Mn^{4-} ion in an octahedral co-ordination in high-spin configuration, has a degenerate ground state. The lower energy t_{2g} has three spin-up electrons, whereas the higher energy e_g state has one spin-up electron out a possible two and is orbitally degenerate. The system responds with a distortion of the octahedra changing the ligand bond lengths, splitting this orbital degeneracy. Cooperative Jahn Teller distortions result in a long-range ordered structure where neighbouring octahedra distort along different axes creating a tiled structure which can double the unit cell [30].

Lattice strain can drive long-range structural modulations, which have an associated wavevector which can be either commensurate or incommensurate to the lattice. These

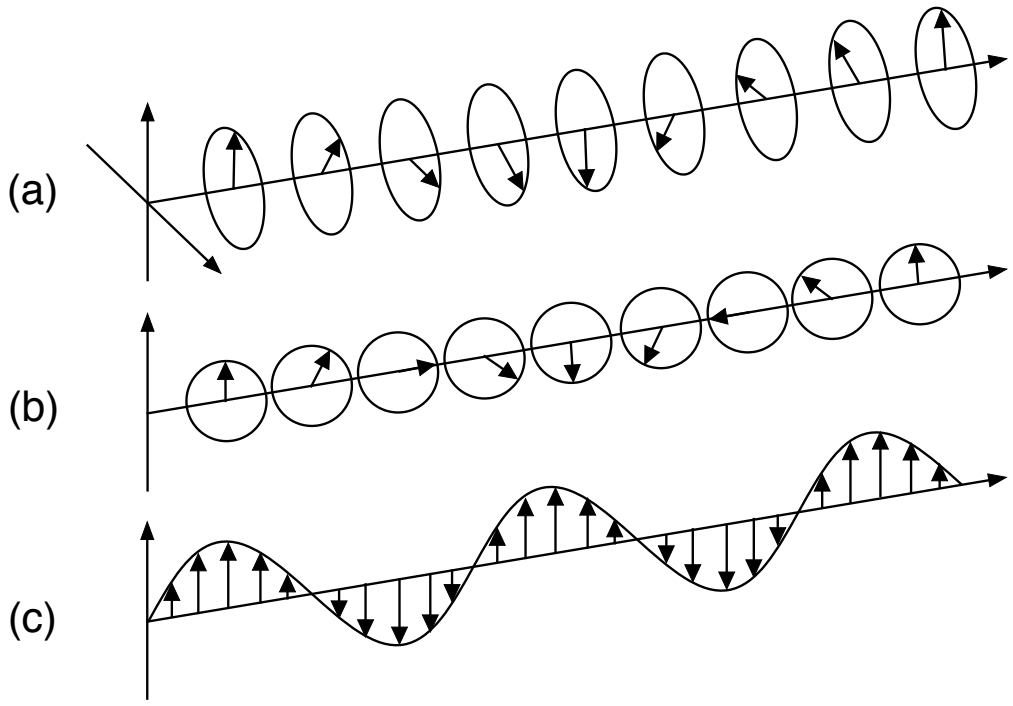

Figure 1.1: (a) Helical magnetic structure. The magnetic moments rotate in a plane perpendicular to the propagation vector. (b) Cycloidal magnetic structure. The magnetic moments rotate in a plane parallel to the propagation axis. (c) Spin density wave. The magnet moments all point along the same axis but vary in magnitude.

modulations can be a small effect, leading to a description of the crystal using the original unit cell with an additional modulation wavevector.

1.3 Magnetic Propagation Vector

The magnetic structure can be expressed using a magnetic unit cell in a similar way as the underlying atomic structure is described by a crystal unit cell. This method may suffice for ferromagnetism and simple antiferromagnets but for extended structures the magnetic unit cell could contain 1000's of atoms, and is a cumbersome description of the magnetism. A more concise description of the magnetism uses the crystal unit cell and a propagation vector which describes how magnetic moments on the i^{th} atom in adjacent unit cells relate to one another. This method expresses the magnetism in terms of Fourier

components of the periodicity of the crystallographic unit cell.

The magnetic moment on the i^{th} atom in the unit cell, $\mathbf{\Psi}_i$ is described using the basis vectors of the unit cell. If the magnetism has a propagation vector, $\boldsymbol{\tau}$ expressed in the basis of the reciprocal unit cell, the moment distribution for the i^{th} atom across the crystal can be described using:

$$\mathbf{m}_i = \sum_{\tau} \mathbf{\Psi}_i^{\tau} e^{-2\pi i \boldsymbol{\tau}\cdot\mathbf{R}} \tag{1.2}$$

where $\boldsymbol{R}$ describes the translation vectors between unit cells of the crystal. More complex magnetic ground states may require more than one propagation vector to fully describe the magnetic structure. For this reason the description of the moment distribution includes a sum over multiple propagation vectors. The operation of the symmetry of the space group of the crystal structure on the propagation vector can generate a star of inequivalent propagation vectors. This can lead to four different types of multi-$\boldsymbol{\tau}$ structures. The multi-domain structure, where the system breaks into domains where the magnetism is described by a single τ. The system has two propagation vectors $\boldsymbol{\tau}$ and $-\boldsymbol{\tau}$. A true multi-$\boldsymbol{\tau}$ structure where a single magnetic domain is described by different arms of the propagation vector star. Finally a magnetic structure by a propagation vector $\boldsymbol{\tau}$ and its harmonics.

Three different scenarios arise from equation 1.2. The simplest case where $\mathbf{\Psi}$ is real and $\boldsymbol{\tau}$ takes values such that $e^{-2\pi i \boldsymbol{\tau}\cdot\mathbf{R}}$ is also real. In this case the magnitude of the moment is constant and only the direction of the moment changes. The second case where $\mathbf{\Psi}$ is real, but $\boldsymbol{\tau}$ takes values such that $e^{-2\pi i \boldsymbol{\tau}\cdot\mathbf{R}}$ is complex. In this case, the structure is defined by both $\boldsymbol{\tau}$ and $-\boldsymbol{\tau}$ propagation vector. This results in the magnitude of the moment changing with translation through the crystal and leads to a sine modulated spin density wave. Finally, the third case where both $\mathbf{\Psi}$ is complex and $\boldsymbol{\tau}$ takes values such that $e^{-2\pi i \boldsymbol{\tau}\cdot\mathbf{R}}$ is complex. In this case a whole range of helical and cycloidal structures can be described.

The symmetry of the space group is important in determining the magnetic structure. The symmetry elements of the space group which leave the propagation vector unchanged are called the little group. Depending on the symmetry of the little, the situation can arise where equivalent sites in the crystal structure become inequivalent in the magnetic structure forming different orbits of the magnetic structure with an phase difference between them. The symmery of the little group can lead to counter intuitive situations as in the case for $LaMnO_3$. "Normally" a $\boldsymbol{\tau} = 0$ structure refers to a ferromagnetic case, as the

propagation vector is zero. For $LaMnO_3$ the symmetry of the little group requires the $\tau = 0$ structure to be antiferromagnetic between planes in the c-direction [31].

1.4 Plan of Thesis

This thesis is divided up into six chapters, an experimental techniques, four research chapters and finally a conclusions chapter. The theory of x-ray and neutron diffraction and muon spectroscopy are expanded upon in the experimental techniques chapter. The magnetism of a number of different iron-based compounds have been studied in this thesis. Iron is the oldest known magnetic material, but can show a wealth of different electronic phenomena when arranged in different compounds, including superconductivity in the iron pnictides, spin glasses, multiferroicity, magnetoresistance. In this thesis four different iron-based materials have been studied: (i) a vacancy-ordered transition metal oxide, $SrFeO_{3-\delta}$ showing large magnetoresistance: (ii) a rhombohedral triangular lattice multiferroic, $CuFeO_2$, which has an usual Ising-like ground state: (iii) a frustrated kagomé lattice system, FeCrAs, with both iron and chromium moments, and finally, (iv) an iron pnictide, FeAs which shows a helical structure. In each research chapter the above materials are introduced in further detail, an overview of the experimental detail and results, discussions and conclusions are drawn.

Chapter 2

Experimental Techniques

2.1 X-ray Scattering

X-ray scattering is a general term describing a whole host of techniques which probe a system using x-ray radiation. X-rays, defined most generally, are an electromagnetic (EM) wave of energies in the range of 100 eV to 100 keV. In condensed matter, x-rays can be further defined, as originating as an emission from a core electron transition. Two additional types of radiation that are often categorised as x-rays, are bremsstrahlung and synchrotron radiation, these both originate from a change in velocity of electrons, and are used to generate a source of x-rays for experiments.

2.1.1 X-ray formalism

An x-ray is a transverse electromagnetic wave [32], made up of oscillating electric field and magnetic field, which are orthogonal to each other and to the direction of propagation. To describe the radiation field, we need to use the electric and magnetic fields **E**, **B** described by Maxwell's equations in terms of the scalar and vector field potentials.

$$\mathbf{B} = \boldsymbol{\nabla} \times \mathbf{A} \tag{2.1}$$

$$\mathbf{E} = -\boldsymbol{\nabla}\Phi - \left(\frac{1}{c}\right)\frac{\partial \mathbf{A}}{\partial t} \tag{2.2}$$

Choosing a gauge in such a way to cause the scalar potential to vanish, and the vector potential **A** to be divergence free $\boldsymbol{\nabla} \cdot \mathbf{A} = 0$. The vector potential is expanded in terms of

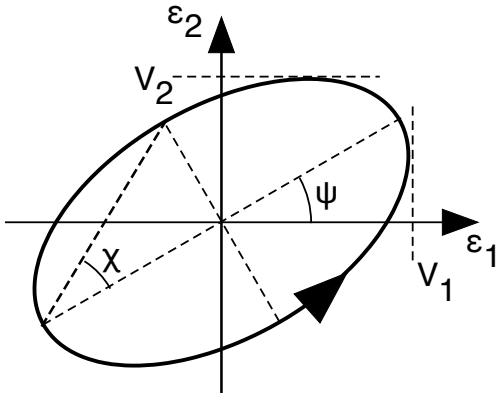

Figure 2.1: Polarisation ellipse of elliptically polarised beam. For linearly polarised x-ray beam $\chi = 0$.

plane waves, with a wavevector $\mathbf{k}$ and polarisation mode $\lambda = 1, 2$.

$$\mathbf{A}(\mathbf{r}, t) = \sum_{k,\lambda} \sqrt{\frac{hc^2}{V_0 \omega_{\mathbf{k}}}} \left[\hat{\boldsymbol{\varepsilon}}_\lambda a_{\mathbf{k},\lambda} e^{i(\mathbf{k}\cdot\mathbf{r} - \omega_{\mathbf{k}} t)} + \hat{\boldsymbol{\varepsilon}}^*_\lambda a^\dagger_{\mathbf{k},\lambda} e^{-i(\mathbf{k}\cdot\mathbf{r} - \omega_{\mathbf{k}} t)} \right] \tag{2.3}$$

The vector $\hat{\boldsymbol{\varepsilon}}_\lambda$ describes the polarisation unit vector of the associated mode λ, and a and $a^\dagger$ are the annihilation and creation vectors of a photon with quantum numbers $(\mathbf{k}, \lambda)$. V_0 is the volume of quantisation and $\omega_{\mathbf{k}}$ is the frequency of the photon with a wavevector $\mathbf{k}$. The x-ray, being a transverse wave, is polarised orthogonally to the direction of propagation, *i.e.* $\mathbf{k} \cdot \hat{\boldsymbol{\varepsilon}}_\lambda(\mathbf{k}) = 0$. The polarisation state of the x-ray can be defined by two orthogonal vectors, $\hat{\boldsymbol{\varepsilon}}_1$, and $\hat{\boldsymbol{\varepsilon}}_2$, both orthogonal to the wavevector $\mathbf{k}$. Using $\hat{\boldsymbol{\varepsilon}}_1$, and $\hat{\boldsymbol{\varepsilon}}_2$ as a basis the polarisation can be expressed as a Jones vector [33], $\mathbf{V} = \begin{pmatrix} V_1 \\ V_2 \end{pmatrix}$. The Jones vector can be complex, as is the case with circular polarisation. The polarisation vectors fall onto an ellipse, in a plane perpendicular to $\mathbf{k}$, known as the polarisation ellipse, shown in figure 2.1.

An alternate way of defining the polarisation of an EM wave is using Poincaré-Stokes parameters, P_1, P_2, and P_3. The Poincaré-Stokes parameters can be related to both the Jones vector and the polarisation ellipse. P_1 and P_2 define the degree of linear polarisation, $P_{\text{lin}} = \sqrt{P_1^2 + P_2^2}$, and have even parity, whilst P_3 the degree of circular polarisation, and has odd parity. $P_{1,2,3}$ can be related to χ and ψ of the polarisation ellipse using the

relations below.

$$P_1 = \cos 2\psi \cos 2\chi \tag{2.4}$$

$$P_2 = \sin 2\psi \cos 2\chi \tag{2.5}$$

$$P_3 = \sin 2\chi \tag{2.6}$$

The advantage of using the Poincaré-Stokes parameters over Jones vectors becomes apparent when the x-ray beam is composed of an ensemble of independent waves. Such a beam may be partially polarised. The Jones vector formalism cannot describe a partially polarised beam. In order to describe such a polarisation state, the x-ray beam can be described by a density matrix [34–38]. The density matrix is a 2×2 matrix in the basis of the polarisation vectors $\hat{\boldsymbol{\varepsilon}}_1$, and $\hat{\boldsymbol{\varepsilon}}_2$, where for each element the average taken over the ensemble of waves [33] is given by;

$$\boldsymbol{\rho} = \langle \mathbf{V}\mathbf{V}^{\dagger} \rangle = \begin{pmatrix} \langle V_1 V_1^{\dagger} \rangle & \langle V_1 V_2^{\dagger} \rangle \\ \langle V_2 V_1^{\dagger} \rangle & \langle V_2 V_2^{\dagger} \rangle \end{pmatrix} = \frac{I}{2} (\mathbb{I} + \boldsymbol{\sigma} \cdot \mathbf{P}) \tag{2.7}$$

The advantages of the Poincaré-Stokes parameters should now become apparent. The density matrix $\boldsymbol{\rho}$ is a Hermitian, and consequently can be expressed in the orthonormal basis of the identity, $\mathbb{I}$ and the Pauli spin matrices $\boldsymbol{\sigma} = (\sigma_1, \sigma_2, \sigma_3)$(where $\sigma_1 = \left(\begin{smallmatrix} 1 & 0 \\ 0 & -1 \end{smallmatrix}\right)$, $\sigma_2 = \left(\begin{smallmatrix} 0 & 1 \\ 1 & 0 \end{smallmatrix}\right)$, and $\sigma_3 = \left(\begin{smallmatrix} 0 & i \\ -i & 0 \end{smallmatrix}\right)$). By definition the Poincaré-Stokes parameters, $\mathbf{P} = (P_1, P_2, P_3)$ and intensity, I are the coefficients when the density matrix, $\boldsymbol{\rho}$ is expressed in Pauli spin matrices basis.

$$\begin{aligned} \boldsymbol{\rho} &= \frac{I}{2}\left(\begin{pmatrix} 1 & 0 \\ 0 & 1 \end{pmatrix} + P_1 \begin{pmatrix} 1 & 0 \\ 0 & -1 \end{pmatrix} + P_2 \begin{pmatrix} 0 & 1 \\ 1 & 0 \end{pmatrix} + P_3 \begin{pmatrix} 0 & i \\ -i & -0 \end{pmatrix}\right) \\ \boldsymbol{\rho} &= \frac{I}{2} \begin{pmatrix} 1 + P_1 & P_2 + iP_3 \\ P_2 - iP_3 & 1 - P_1 \end{pmatrix} \end{aligned} \tag{2.8}$$

The Poincaré-Stokes parameters, P_1, P_2, and P_3, I can thus be extracted for an x-ray beam from the density matrix, ρ using the trace function, which simply sums the diagonal

elements of a square matrix.

$$I = \mathrm{tr}(\boldsymbol{\rho}) \tag{2.9}$$

$$P_i = \frac{1}{I}\mathrm{tr}(\sigma_i \cdot \boldsymbol{\rho}) \tag{2.10}$$

2.1.2 Jones Matrices

Using the density matrix description of the polarisation state of the x-ray beam defined in section 2.1.1, the effects of a scattering process on the polarisation of the beam can be described by a Jones matrix. For a scattering process, M, which could be a diffraction from a sample, a polarisation analyser, or a phase plate, a 2×2 Jones matrix can be constructed [39–42].

$$\mathbf{M} = \begin{pmatrix} \langle \hat{\boldsymbol{\varepsilon}}_1' | M | \hat{\boldsymbol{\varepsilon}}_1 \rangle & \langle \hat{\boldsymbol{\varepsilon}}_1' | M | \hat{\boldsymbol{\varepsilon}}_2 \rangle \\ \langle \hat{\boldsymbol{\varepsilon}}_2' | M | \hat{\boldsymbol{\varepsilon}}_1 \rangle & \langle \hat{\boldsymbol{\varepsilon}}_2' | M | \hat{\boldsymbol{\varepsilon}}_2 \rangle \end{pmatrix} \tag{2.11}$$

In the nomenclature of a scattering process, distinctions are needed between the incident x-ray and the scattered x-ray. In this thesis if the notation where A represents the property A of the incident x-ray, then A' would represent the same property A of the scattered x-ray, *i.e.* $\mathbf{k}$ and $\mathbf{k}'$ represent the wavevector of the incident and scattered beam respectively.

Jones matrices transform the Jones vector of the incident beam, $\mathbf{V}$ into the corresponding Jones vector for the scattered beam,$\mathbf{V}'$, such that $\mathbf{V}' = \mathbf{M} \cdot \mathbf{V}$. The Jones matrix representation of the scattering process can be used with the density matrix formalism, $\boldsymbol{\rho}$, by simply multiplying the density matrix that represents the incident beam, $\boldsymbol{\rho}$ by the Jones matrix, $\mathbf{M}$ and the adjoint of Jones matrix $M^\dagger$.

$$\boldsymbol{\rho}' = \mathbf{M} \cdot \boldsymbol{\rho} \cdot \mathbf{M}^\dagger \tag{2.12}$$

For the case where the x-ray beam undergoes multiple scattering events, such as diffraction from a sample and subsequently an analyser crystal, the process in equation 2.12 can be applied multiple times.

$$\boldsymbol{\rho}' = \ldots \left(\mathbf{M}_2 \cdot \left(\mathbf{M}_1 \cdot \boldsymbol{\rho} \cdot \mathbf{M}_1^\dagger \right) \cdot \mathbf{M}_2^\dagger \right) \ldots = (\ldots M_2 \cdot M_1) \cdot \boldsymbol{\rho} \cdot (\ldots M_2 \cdot M_1)^\dagger \tag{2.13}$$

By being able to describe a scattering process as a Jones matrix, will enable predictions

of its polarisation dependence, using Poincaré-Stokes parameters and density matrices.

2.1.3 Interaction of X-rays with Matter

The theory of electrodynamics sets out to explain the interactions of electromagnetic waves with matter. In the context of an x-ray interacting with matter, we approximate matter to be composed of moving electrons interacting with one another and with a set of static nuclei. The Hamiltonian of the total system can be written as the Hamiltonian of the free electromagnetic wave, the Hamiltonian describing the electronic system, and interaction terms between the two. Using the description of the x-ray, using the vector potential in equation 2.3, which is linear in annihilation and creation vectors, the Hamiltonian of the radiation can be written as the quantum harmonic oscillator.

$$\mathcal{H}_{rad} = \sum_{k,\lambda} \hbar\omega_{\mathbf{k}}(a^{\dagger}(k,\lambda)a(k,\lambda) + \frac{1}{2}) \tag{2.14}$$

Using this description for the Hamiltonian of the radiation, the Hamiltonian for a system of electrons in an electromagnetic field, taking the non-relativistic limit, can be expressed in terms of the vector potential, $\mathbf{A}(\mathbf{r}_i)$ [43, 44]. The non-relativistic limit can be taken as the typical x-ray is of order 10 keV, whist the electron rest mass energy is 511 keV.

$$\begin{aligned}\mathcal{H} =& \frac{1}{2m}\sum_{i=1}^{N}(\mathbf{p}_i - \frac{e}{c}\mathbf{A}(r_i))^2 + \sum_{j>i}^{N,N} V(|\mathbf{r}_i - \mathbf{r}_j|) - \frac{e\hbar}{2mc}\sum_{i=1}^{N}\mathbf{s}_i \cdot [\boldsymbol{\nabla}\times\mathbf{A}(\mathbf{r}_i)] \\ &- \frac{e\hbar}{2m^2c^2}\sum_{i=1}^{N}\mathbf{s}_i \cdot \left[\mathbf{E}(\mathbf{r}_i)\times\left(\mathbf{p}_i - \frac{e}{c}\mathbf{A}(\mathbf{r}_i)\right)\right] + \mathcal{H}_{\text{rad}}\end{aligned} \tag{2.15}$$

Where e, and m are the electrons charge and mass, $\hbar$ is the reduced Planck's constant. The first term is the modification of the kinetic energy in the presence of a field, where $\mathbf{p}_i - \frac{e}{c}\mathbf{A}(\mathbf{r}_i)$ is the canonical momentum. The second term is the Coulomb interaction between electron. The third term is the interaction of the electrons spin $\mathbf{s}_i$ with the $\mathbf{B}$ field of the x-ray, *i.e.* $\mathbf{B} = \boldsymbol{\nabla}\times(A)$. The fourth term is the spin-orbit interaction, and arises from the interaction of the electrons spin, $\mathbf{s}_i$ with the magnetic field created by the electron moving through the $\mathbf{E}$ field from the nucleus and the x-ray. The spin-orbit term can be expanded, in the usual way using Maxwell's equation $\mathbf{E}(\mathbf{r}_i) = -\boldsymbol{\nabla}\phi - \frac{1}{c}\frac{\partial\mathbf{A}(\mathbf{r}_i)}{\partial t}$, where ϕ is

the electrostatic potential from the electrons and $\mathbf{A}$ is the vector potential of the x-ray.

$$\mathcal{H} = \ldots \frac{e\hbar}{2m^2c^2} \sum_{i=1}^{N} \mathbf{s}_i \cdot \left[-\boldsymbol{\nabla}\phi \times \mathbf{p}_i + \frac{e}{c}\boldsymbol{\nabla}\phi \times \mathbf{A}(\mathbf{r}_i) - \frac{1}{c}\frac{\partial \mathbf{A}(\mathbf{r}_i)}{\partial t} \times \mathbf{p}_i + \frac{e}{c^2}\frac{\partial \mathbf{A}(\mathbf{r}_i)}{\partial t} \times \mathbf{A}(\mathbf{r}_i) \right] \ldots \quad (2.16)$$

As shown earlier in equation 2.3, the vector potential is linear in the photon annihilation and creation operators, a and $a^\dagger$. Scattering requires both the annihilation and creation of a photon, subsequently only those terms squared in $\mathbf{A}(\mathbf{r}_i)$ under first-order perturbation theory, and linear in $\mathbf{A}(\mathbf{r}_i)$ under second-order perturbation theory cause scattering. The spin-orbit term, equation 2.16, is already of order $(v/c)^2$, allowing the second-order perturbation terms to be neglected, as these will be insignificant [45]. Only the first and fourth term will contribute to the x-ray scattering.

The terms in the Hamiltonian, $\mathcal{H}$ can be collected together and written as a sum of the Hamiltonian of the electron system, the Hamiltonian of the radiation field and the Hamiltonian of the interaction, $\mathcal{H} = \mathcal{H}_{\text{el}} + \mathcal{H}_{\text{rad}} + \mathcal{H}_{\text{int}}$.

$$\mathcal{H}_{\text{el}} = \frac{1}{2m}\sum_{i=1}^{N} \mathbf{p}_i^2 + \sum_{j>i}^{N,N} V(|\mathbf{r}_i - \mathbf{r}_j|) + \frac{e\hbar}{2m^2c^2}\sum_{i=1}^{N} \mathbf{s}_i \cdot [\boldsymbol{\nabla}\phi \times \mathbf{p}_i] \quad (2.17)$$

$$\begin{aligned} \mathcal{H}_{\text{int}} =& \frac{e^2}{2mc^2}\sum_{i=1}^{N} [\mathbf{A}(\mathbf{r}_i)]^2 - \frac{e}{2mc}\sum_{i=1}^{N} [\mathbf{p}_i \cdot \mathbf{A}(\mathbf{r}_i) + \mathbf{A}(\mathbf{r}_i) \cdot \mathbf{p}_i] \\ & - \frac{e\hbar}{2mc}\sum_{i=1}^{N} \mathbf{s}_i \cdot [\boldsymbol{\nabla} \times \mathbf{A}(\mathbf{r}_i)] - \frac{e^2\hbar}{2m^2c^4}\sum_{i=1}^{N} \mathbf{s}_i \cdot \left[\frac{\partial \mathbf{A}(\mathbf{r}_i)}{\partial t} \times \mathbf{A}(\mathbf{r}_i)\right] \quad (2.18) \\ \mathcal{H}_{\text{int}} =& \mathcal{H}_1 + \mathcal{H}_2 + \mathcal{H}_3 + \mathcal{H}_4 \end{aligned}$$

Scattering processes can be described as transitions between eigenstates of $\mathcal{H}_{\text{el}}$ and $\mathcal{H}_{\text{rad}}$, driven by a perturbation $\mathcal{H}_{\text{int}}$. Under this description $\mathbf{A}(\mathbf{r}_i)$ can be considered an operator in terms of annihilation and creation operators. There are four terms in the interaction Hamiltonian, two quadratic in $\mathbf{A}$ and two linear in $\mathbf{A}$. For the first and fourth terms, which are quadratic in $\mathbf{A}$, scattering is described by first-order perturbation theory and cause non-resonant scattering. The second and third terms, which are linear in $\mathbf{A}$,

scattering is described by second-order perturbation theory and causes resonant scattering.

2.1.4 Scattering Cross-sections

The scattering cross-section is defined as the number of transitions per unit time, into photon states with energy between $\hbar\omega'$ and $\hbar\omega' + dE$, with a wavevector $\mathbf{k}'$, into a solid angle $d\Omega$, divided by the number of incident photons per unit time and area [46]. The scattering cross-section is the modulus-squared of the scattering length, where the scattering length is the expected value of the scattering operator.

$$\frac{d^2\sigma}{dEd\Omega} = |f|^2 = \frac{W\, n(E)}{\frac{c}{V_0}} = \frac{V_0^2\omega^2}{8\pi^3\hbar c^4}W \tag{2.19}$$

Where W is the transition probability, $n(E)$ is the photon density of states in quantisation volume V_0, and is equal to $n(E) = \frac{V_0\omega^2}{8\pi^3\hbar c^3}$. The transition probability, W can be calculated using Fermi's Golden Rule of time dependent perturbation theory. For first-order perturbation the transition rate is given by

$$W = \frac{2\pi}{\hbar}\left|\langle f|\mathcal{H}_{\text{pert}}|i\rangle\right|^2\delta(E_i - E_f) \tag{2.20}$$

and for second-order perturbation the transition rate is given by

$$W = \frac{2\pi}{\hbar}\left|\sum_n \frac{\langle f|\mathcal{H}_{\text{pert}}|n\rangle\langle n|\mathcal{H}_{\text{pert}}|i\rangle}{E_i - E_n}\right|^2\delta(E_i - E_f) \tag{2.21}$$

where $\mathcal{H}_{\text{pert}}$ is the perturbation part of the Hamiltonian. The states $|f\rangle$ and $|i\rangle$ are the final and initial states of the whole system, both photon and electrons. The initial and final states can be written as $|i\rangle = |\alpha;(\mathbf{k},\lambda)\rangle$ and $|f\rangle = |\beta;(\mathbf{k}',\lambda')\rangle$, where $|\alpha\rangle$ and $|\beta\rangle$ are eigenstates of the unperturbed Hamiltonian $\mathcal{H}_{el}$ and describe the assemblage of electrons, and $|\mathbf{k},\lambda\rangle$ and $|\mathbf{k}',\lambda'\rangle$ are eigenstates of the radiation field describing photons with wavevectors $\mathbf{k}$ and $\mathbf{k}'$ and polarisation λ and λ'. The δ function ensures that energy is conserved, with $E_i = E_\alpha + \hbar\omega$ and $E_f = E_\beta + \hbar\omega'$.

2.1.5 Thomson Scattering

The first and fourth terms, $\mathcal{H}_1$, $\mathcal{H}_4$ in the interaction Hamiltonian, $\mathcal{H}_{\text{int}}$ are non-resonant scattering processes. The first term, $\mathcal{H}_1$ gives rise to elastic Thomson scattering of an

electromagnetic wave from a charged particle. The fourth term, $\mathcal{H}_4$ leads to an elastic non-resonant magnetic scattering [34, 35]. Non-resonant magnetic scattering is a powerful experimental tool, and provides a direct method of distinguishing spin and orbital magnetic moments for long-range magnetic structures [34]. However non-resonant magnetic scattering was not used in this thesis, and will not be discussed, but for further derivations see [34] and [45]. For the first term, $\mathcal{H}_1$ of the interaction Hamiltonian $\mathcal{H}_{\text{int}}$ the transition probability is given by

$$W = \frac{2\pi}{\hbar}\left|\langle\beta;(\mathbf{k}',\lambda')|\frac{e^2}{2mc^2}\sum_{i=1}^{N}\left[\mathbf{A}(\mathbf{r}_i)\right]^2|\alpha;(\mathbf{k},\lambda)\rangle\right|^2\delta(E_i-E_f) \tag{2.22}$$

$$\text{where}\quad \mathbf{A}(\mathbf{r},t) = \sum_{k,\lambda}\sqrt{\frac{hc^2}{V_0\omega_{\mathbf{k}}}}\left[\hat{\boldsymbol{\epsilon}}_\lambda a_{\mathbf{k},\lambda}e^{i(\mathbf{k}\cdot\mathbf{r}-\omega_{\mathbf{k}}t)} + \hat{\boldsymbol{\epsilon}}^*_\lambda a^\dagger_{\mathbf{k},\lambda}e^{-i(\mathbf{k}\cdot\mathbf{r}-\omega_{\mathbf{k}}t)}\right]$$

The term $\mathbf{A}(\mathbf{r}_i)$ is a sum over the all the photon modes with quantum numbers $\mathbf{k}$ and polarisation state λ. For scattering, this is a sum over the incident $|\mathbf{k},\lambda\rangle$ and final state $|\mathbf{k}',\lambda'\rangle$. This leads to four terms in the expression for $\mathbf{A}(\mathbf{r}_i)$, but as scattering requires the annihilation of the incident photon, $a_{\mathbf{k},\lambda}$ and the creation of scattered photon, $a^\dagger_{\mathbf{k}',\lambda'}$, only two terms contribute to scattering (the other terms would describe the process in reverse).

$$\mathbf{A}_{\mathbf{k},\lambda,\mathbf{k}',\lambda'}(\mathbf{r}) = \sqrt{\frac{hc^2}{V_0\omega_{\mathbf{k}}}}\hat{\boldsymbol{\epsilon}}_\lambda a_{\mathbf{k},\lambda}e^{i(\mathbf{k}\cdot\mathbf{r}-\omega_{\mathbf{k}}t)} + \sqrt{\frac{hc^2}{V_0\omega_{\mathbf{k}'}}}\hat{\boldsymbol{\epsilon}}^*_{\lambda'}a^\dagger_{\mathbf{k}',\lambda'}e^{-i(\mathbf{k}'\cdot\mathbf{r}-\omega_{\mathbf{k}'}t)} \tag{2.23}$$

We can simplify the derivation of $[\mathbf{A}(\mathbf{r})]^2$ by realising only terms with one annihilation operator, $a_{\mathbf{k},\lambda}$ and one creation vector $a^\dagger_{\mathbf{k}',\lambda'}$ will contribute to the scattering, the remaining terms will be zero. If the scattering is restricted to being completely elastic so $\omega_{\mathbf{k}} = \omega_{\mathbf{k}'}$, and using the commutation relation $a^\dagger_i a_j = a_j a^\dagger_i$, the transition rate can be simplified to

$$W = \frac{2\pi}{\hbar}\left|\left\langle\beta;(\mathbf{k}',\lambda')\left|\frac{e^2}{2mc^2}\sum_{i=1}^{N}\frac{hc^2}{V_0\omega_{\mathbf{k}}}\hat{\boldsymbol{\epsilon}}^*_{\lambda'}\cdot\hat{\boldsymbol{\epsilon}}_\lambda e^{i(\mathbf{k}-\mathbf{k}')\cdot\mathbf{r}_i}2\,a^\dagger_{\mathbf{k}',\lambda'}a_{\mathbf{k},\lambda}\right|\alpha;(\mathbf{k},\lambda)\right\rangle\right|^2\delta(E_i-E_f) \tag{2.24}$$

The operator $a^\dagger_{\mathbf{k}',\lambda'}a_{\mathbf{k},\lambda}$ acts on the photon part of the combined state and annihilates the incident photon and creates the scattered photon, and returns unity for a single photon

scattering. As the scattering is elastic, the final state of the electron system, $|\beta\rangle$ is the same as the incident state, $|\alpha\rangle$, *i.e.* for elastic scattering $|\alpha\rangle \equiv |\beta\rangle$.

$$W = \frac{2\pi}{\hbar}\frac{e^4}{4m^2c^4}\frac{4\pi^2\hbar^2c^4}{V_0^2\omega_{\mathbf{k}}^2}4\left|\hat{\boldsymbol{\varepsilon}}^*_{\lambda'}\cdot\hat{\boldsymbol{\varepsilon}}_{\lambda}\right|^2\left|\left\langle\alpha\left|\sum_{i=1}^{N}e^{i(\mathbf{k}-\mathbf{k}')\cdot\mathbf{r}_i}\right|\alpha\right\rangle\right|^2\delta(E_i-E_f) \tag{2.25}$$

Using the transition probability the scattering cross-section can be found using equation 2.2.1.

$$\frac{d^2\sigma}{dEd\Omega} = \frac{e^4}{m^2c^4}\left|\hat{\boldsymbol{\varepsilon}}^*_{\lambda'}\cdot\hat{\boldsymbol{\varepsilon}}_{\lambda}\right|^2\left|F(\mathbf{k}-\mathbf{k}')\right|^2\delta(E_i-E_f) \tag{2.26}$$

where the structure factor, $F(\mathbf{k}-\mathbf{k}')$ is defined as

$$F(\mathbf{k}-\mathbf{k}') = \left\langle\alpha\left|\sum_{i=1}^{N}e^{i(\mathbf{k}-\mathbf{k})\cdot\mathbf{r}_i}\right|\alpha\right\rangle \tag{2.27}$$

If the electronic state $|\alpha\rangle$ is described by an antisymmetric wavefunction, $\psi(\mathbf{r}_1,\mathbf{r}_2,\ldots,\mathbf{r}_N)$, the electron density, $\rho(\mathbf{r})$ can be described as the integral with respect to $d\mathbf{r}_i$ of the wavefunction squared, $|\psi|^2$

$$\rho(\mathbf{r}) = N\int d\mathbf{r}_2\int d\mathbf{r}_3\ldots\int d\mathbf{r}_N\left|\psi(\mathbf{r},\mathbf{r}_2,\mathbf{r}_2,\ldots\mathbf{r}_N)\right|^2 \tag{2.28}$$

Consequently the structure factor can be written as a function of the electron density.

$$\begin{aligned}F(\mathbf{k}-\mathbf{k}') &= \left\langle\psi(\mathbf{r}_1,\ldots,\mathbf{r}_N))\left|e^{i(\mathbf{k}-\mathbf{k})\cdot\mathbf{r}_1}\ldots+e^{i(\mathbf{k}-\mathbf{k})\cdot\mathbf{r}_N}\right|\psi(\mathbf{r}_1,\ldots,\mathbf{r}_N))\right\rangle\\ &= N\int d\mathbf{r}e^{i(\mathbf{k}-\mathbf{k}')\cdot\mathbf{r}}\int d\mathbf{r}_2\int d\mathbf{r}_3\ldots\int d\mathbf{r}_N\left|\psi(\mathbf{r},\mathbf{r}_2,\mathbf{r}_3,\ldots\mathbf{r}_N)\right|^2\\ &= \int d\mathbf{r}e^{i(\mathbf{k}-\mathbf{k}')\cdot\mathbf{r}}\rho(\mathbf{r})\end{aligned} \tag{2.29}$$

The x-ray scattering structure factor is simply the Fourier transform of the electron density of the system. Experimentally x-ray scattering is used as a tool to uncover the electron density of a system by measuring the structure factor. The scattering cross-section is related to the square of the structure factor, meaning the phase information is lost in the measurement. This is known as the phase problem [47].

2.1.6 Scattering from a Periodic Electron Density

The above derivation for Thomson scattering holds for any electron density which can be described by an antisymmetric wavefunction, whether this is a molecule or the theoreticians Jellium. All the electronic phenomena studied in this thesis occur in crystalline materials where the electron density has a periodic structure. A periodic electron density can be described using a regular lattice of points and the electron density ρ_i of the repeating motif at each lattice point. The electron density of the entire structure, $\rho(\mathbf{r})$ can be described using the family of vectors $\mathbf{R}_{u_1,u_2,u_3} = u_1\mathbf{a}_1 + u_2\mathbf{a}_2 + u_3\mathbf{a}_3$, where $\mathbf{a}_1$, $\mathbf{a}_2$, $\mathbf{a}_3$ are the lattice vectors, with $\mathbf{a}_1 \cdot \mathbf{a}_2 \times \mathbf{a}_3$ the volume of lattice cell, and u_1, u_2, u_3 are integers.

$$\rho(\mathbf{r}) = \sum_{u_1,u_2,u_3} \rho_i(\mathbf{r} - \mathbf{R}_{u_1,u_2,u_3}) \tag{2.30}$$

The structure factor then becomes

$$F(\mathbf{k} - \mathbf{k}') = \sum_{u_1,u_2,u_3} e^{i(\mathbf{k}-\mathbf{k}')\cdot\mathbf{R}_{u_1,u_2,u_3}} \int d\mathbf{r} e^{i(\mathbf{k}-\mathbf{k}')\cdot(\mathbf{r}-\mathbf{R}_{u_1,u_2,u_3})} \rho_i(\mathbf{r} - \mathbf{R}_{u_1,u_2,u_3}) \tag{2.31}$$

The integral is the Fourier transform of the electron density in a single unit cell defined by the vectors $\mathbf{a}_1$, $\mathbf{a}_2$, and $\mathbf{a}_3$. The sum over all the unit cells, on the left of the integral sign introduces interesting physics. As the term $\mathbf{R}_{u_1,u_2,u_3}$ describes points equally spaced apart, the phase factors $e^{i(\mathbf{k}-\mathbf{k}')\cdot\mathbf{R}_{u_1,u_2,u_3}}$ cancel out, and the sum, $\sum_{u_1,u_2,u_3} e^{i(\mathbf{k}-\mathbf{k}')\cdot\mathbf{R}_{u_1,u_2,u_3}}$ is only non-zero when $(\mathbf{k}-\mathbf{k}')\cdot R_{u_1,u_2,u_3} = 2\pi n$, where n is an integer. When $(\mathbf{k}-\mathbf{k}')\cdot R_{u_1,u_2,u_3} = 2\pi n$ the phase factors add in unity. The sum can be replaced by a $\delta((\mathbf{k} - \mathbf{k}') - \mathbf{G})$ function, where $\mathbf{G}$ is defined $\mathbf{G} \cdot \mathbf{R}_{u_1,u_2,u_3} = 2\pi n$. The Fourier transform of a periodic lattice in position-space is a periodic lattice in momentum-space, often called the reciprocal lattice. The momentum-space can be expressed in terms of a basis, $\mathbf{b}_1$, $\mathbf{b}_2$, and $\mathbf{b}_3$ where they relate to the lattice vectors $\mathbf{a}_1$, $\mathbf{a}_2$, $\mathbf{a}_3$.

$$\mathbf{b}_1 = 2\pi\frac{\mathbf{a}_2 \times \mathbf{a}_3}{\mathbf{a}_1 \cdot \mathbf{a}_2 \times \mathbf{c}_3}; \quad \mathbf{b}_2 = 2\pi\frac{\mathbf{a}_3 \times \mathbf{a}_1}{\mathbf{a}_2 \cdot \mathbf{a}_3 \times \mathbf{a}_1}; \quad \mathbf{b}_3 = 2\pi\frac{\mathbf{a}_1 \times \mathbf{a}_2}{\mathbf{a}_3 \cdot \mathbf{a}_1 \times \mathbf{a}_2} \tag{2.32}$$

By defining a basis for the momentum-space as above, the lattice and wavevector basis obey this relation $\mathbf{a}_i \cdot \mathbf{b}_j = 2\pi\delta_{i,j}$. If $\mathbf{G} = h\mathbf{b}_1 + k\mathbf{b}_2 + l\mathbf{b}_2$ and $\mathbf{R} = u_1\mathbf{a}_1 + u_2\mathbf{a}_2 + u_3\mathbf{a}_3$, then $\mathbf{G} \cdot \mathbf{R} = 2\pi(hu_1 + ku_2 + lu_3)$. Given that the scattering cross-section only predicts

intensity when $\mathbf{G} \cdot \mathbf{R} = 2\pi n$, where n is an integer, and u_1, u_2, u_3 are also integers, $hu_1 + ku_2 + lu_3 = n$ for any value of u_1, u_2, u_3 which limits h, k, l to integers. This can be written more concisely in the form of Laue's equation.

$$\mathbf{a}_1 \cdot (\mathbf{k} - \mathbf{k}') = 2\pi h; \quad \mathbf{a}_2 \cdot (\mathbf{k} - \mathbf{k}') = 2\pi k; \quad \mathbf{a}_3 \cdot (\mathbf{k} - \mathbf{k}') = 2\pi l \quad \{h, k, l\} \in \mathbb{Z} \tag{2.33}$$

Laue's equations state that the scattering cross-section is only non-zero when the vector for the change in wavevector of the photon, $\mathbf{k} - \mathbf{k}'$ is the same as a momentum-lattice vector, $\mathbf{G}_{\text{hkl}}$ of the reciprocal lattice of the periodic electron density. The structure factor in equation 2.31 can be simplified further by approximating the repeating electron density ρ_i as a collection of atoms each with number of electrons. The integral can be replace by a sum over every atom in the unit cell and a sum over every electron on the atom. The index m sums over the atoms and the index n over the electrons for that atom type.

$$\sum_m e^{i(\mathbf{k}-\mathbf{k}')\cdot\mathbf{r}_m} \sum_n e^{i(\mathbf{k}-\mathbf{k}')\cdot\mathbf{r}_n} \int d\mathbf{r} e^{i(\mathbf{k}-\mathbf{k}')\cdot(\mathbf{r}-\mathbf{R}_{u_1,u_2,u_3}-\mathbf{r}_m-\mathbf{r}_n)} \rho_{m,n}(\mathbf{r} - \mathbf{R}_{u_1,u_2,u_3} - \mathbf{r}_m - \mathbf{r}_n) \tag{2.34}$$

The sum of the integrals for the electrons of a specific atom are known as the atomic form-factor and is given the symbol $f(\mathbf{k} - \mathbf{k}')$ and are tabulated in [48] for most elements and valencies. The structure factor can be approximated as

$$F(\mathbf{k} - \mathbf{k}') = \frac{(2\pi)^3 N}{V} \delta((\mathbf{k} - \mathbf{k}') - \mathbf{G}) \sum_m e^{i(\mathbf{k}-\mathbf{k}')\cdot\mathbf{r}_m} f_m(\mathbf{k} - \mathbf{k}') \tag{2.35}$$

The scattering cross-section from a periodic electron potential restricts scattering to specific $\mathbf{k} - \mathbf{k}'$ wavevectors given by Laue's equations in 2.33 . This type of scattering is also know as diffraction, and the spots of scattering intensity are known as reflections, which are indexed using the integers h, k, l, also known as Miller indices.

2.1.7 Scattering Geometry

For a periodic electron density the scattering occurs at well defined wavevectors. The incident wavevector $\mathbf{k}$ and scattered wavevector $\mathbf{k}'$ define the scattering plane. $\mathbf{k} - \mathbf{k}'$ is the scattering vector, and lies in the scattering plane. The vectors $\mathbf{k} - \mathbf{k}'$ and $\mathbf{k} + \mathbf{k}'$ are orthogonal and can be used to create unit vectors for the scattering plane. Figure 2.2

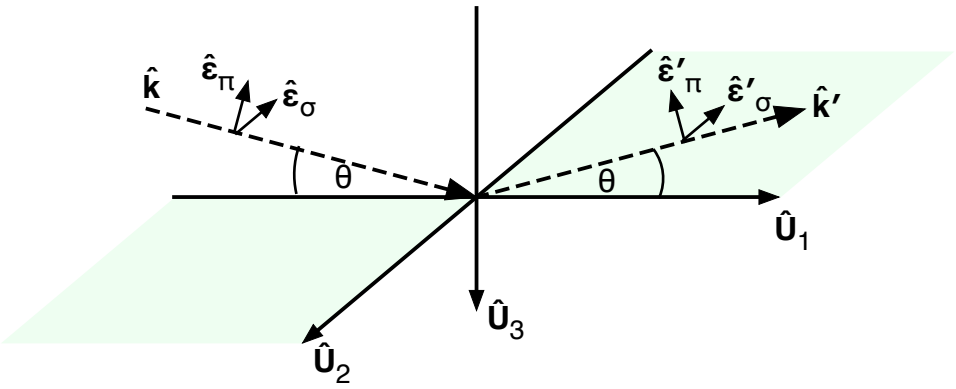

Figure 2.2: Scattering Geometry

shows the scattering geometry, $\hat{\mathbf{U}}_1 = \frac{\mathbf{k}+\mathbf{k}'}{|\mathbf{k}+\mathbf{k}'|}$, $\hat{\mathbf{U}}_3 = \frac{\mathbf{k}-\mathbf{k}'}{|\mathbf{k}-\mathbf{k}'|}$ and $\hat{\mathbf{U}}_2 = \hat{\mathbf{U}}_3 \times \hat{\mathbf{U}}_1$. Both $\mathbf{k}$, and $\mathbf{k}'$ form an angle θ with $\hat{\mathbf{U}}_1$. Starting from Laue's equation $\mathbf{k} - \mathbf{k}' = \mathbf{G}$, it is easy to solve for θ, resulting in Bragg's Law.

$$\lambda = 2\left(\frac{2\pi}{|\mathbf{G}_{h,k,l}|}\right)\sin\theta \tag{2.36}$$

Where $\frac{2\pi}{|\mathbf{G}_{h,k,l}|}$ is the d-spacing for the equivalent set of lattice plane corresponding to the reciprocal space vector h, k, l. It is convenient to define the orthogonal polarisation vectors, $\hat{\boldsymbol{\varepsilon}}_1$, $\hat{\boldsymbol{\varepsilon}}_2$, and $\hat{\boldsymbol{\varepsilon}}'_1$, $\hat{\boldsymbol{\varepsilon}}'_2$ with respect to the scattering plane, with $\lambda = 1$ out of plane and $\lambda = 2$ lying in the scattering plane. This results in $\hat{\boldsymbol{\varepsilon}}_1 = \hat{\boldsymbol{\varepsilon}}'_1 = -\hat{\mathbf{U}}_2$, and $\hat{\boldsymbol{\varepsilon}}_2 = \sin\theta\,\hat{\mathbf{U}}_1 - \cos\theta\,\hat{\mathbf{U}}_3$, $\hat{\boldsymbol{\varepsilon}}'_2 = -\sin\theta\,\hat{\mathbf{U}}_1 - \cos\theta\,\hat{\mathbf{U}}_3$. Using this basis, the nomenclature adopted in the literature [45, 49], $\lambda = 1$ channel is called σ, and $\lambda = 2$ channel is called the π.

Thomson scattering was shown to have a polarisation dependence of $\hat{\boldsymbol{\varepsilon}}' \cdot \hat{\boldsymbol{\varepsilon}}$, which can be expressed as the following Jones matrix.

$$\mathbf{M}_{\text{Thom}} = \begin{pmatrix} \hat{\boldsymbol{\varepsilon}}'_\sigma \cdot \hat{\boldsymbol{\varepsilon}}_\sigma & \hat{\boldsymbol{\varepsilon}}'_\sigma \cdot \hat{\boldsymbol{\varepsilon}}_\pi \\ \hat{\boldsymbol{\varepsilon}}'_\pi \cdot \hat{\boldsymbol{\varepsilon}}_\sigma & \hat{\boldsymbol{\varepsilon}}'_\pi \cdot \hat{\boldsymbol{\varepsilon}}_\pi \end{pmatrix} = \begin{pmatrix} 1 & 0 \\ 0 & \cos 2\theta \end{pmatrix} \tag{2.37}$$

2.1.8 Resonant X-ray Scattering

The second, $\mathcal{H}_2$ and third terms, $\mathcal{H}_3$ from the perturbation Hamiltonian are only linear in annihilation and creation operators. Consequently scattering only occurs as a second-

order perturbation effect.

$$\mathcal{H}_{\text{int}} = -\frac{e}{2mc}\sum_{i=1}^{N}\left[\mathbf{p}_i\cdot\mathbf{A}(\mathbf{r}_i)+\mathbf{A}(\mathbf{r}_i)\cdot\mathbf{p}_i\right]-\frac{e\hbar}{2mc}\sum_{i=1}^{N}\mathbf{s}_i\cdot\left[\boldsymbol{\nabla}\times\mathbf{A}(\mathbf{r}_i)\right]$$

Despite the fact that only $\mathcal{H}_3$ includes a spin term $\mathbf{s}_i$, $\mathcal{H}_3$ is an order of $\hbar$ smaller than $\mathcal{H}_2$ and can be neglected near a resonance. A scattering process requires the annihilation of the incident photon and the creation of the scattered photon. By restricting the perturbation to only those terms which include $a^{\dagger}_{\mathbf{k}',\lambda'}$ and $a_{\mathbf{k},\lambda}$, the scattering length can be written as

$$f \propto \sum_n \frac{\left\langle \alpha;(\mathbf{k}',\lambda')\left|\sum_i \hat{\boldsymbol{\varepsilon}}^{*}_{\lambda'}\cdot\mathbf{p}_i e^{-i\mathbf{k}'\cdot\mathbf{r}_i}\right|n\right\rangle\left\langle n\left|\sum_i \hat{\boldsymbol{\varepsilon}}_{\lambda}\cdot\mathbf{p}_i e^{i\mathbf{k}\cdot\mathbf{r}_i}\right|\alpha;(\mathbf{k},\lambda)\right\rangle}{E_\alpha - E_n + \hbar\omega_{\mathbf{k}} + \frac{i\Gamma_n}{2}} \tag{2.38}$$

The above elastic resonant scattering process describes the absorption of the incident photon, which excites a core electron from the ground state $|\alpha\rangle$ into an empty intermediate state, $|n\rangle$. The electron then decays from the intermediate state $|n\rangle$ back down to the ground state $|\alpha\rangle$ by the emission of a photon with wavevector $\mathbf{k}'$ and polarisation λ'. A small imaginary term has been added to the denominator of the above equation. This has been added to stop unphysical divergence of the scattering cross-section when $E_\alpha - E_n + \hbar\omega_{\mathbf{k}} = 0$ and arises because the intermediary states, $|n\rangle$ are not stationary, but have a finite lifetime [46]. Since, for a core electron $\mathbf{k}\cdot\mathbf{r} \ll 1$, it is admissible to expand the $e^{i\mathbf{k}\cdot\mathbf{r}_i}$ as a series of rapidly decreasing terms.

$$e^{i\mathbf{k}\cdot\mathbf{r}_i} \sim 1 + i\mathbf{k}\cdot\mathbf{r}_i - \frac{(\mathbf{k}\cdot\mathbf{r}_i)^2}{2}\ldots \tag{2.39}$$

The above expansion is referred to as multipole order, and the individual terms as named after the Greek number for 2^n where n is the position in the expansion starting with $n = 1$. The three terms shown above are the dipole (1), quadrupole ($i\mathbf{k}\cdot\mathbf{r}_i$) and octupole ($-\frac{(\mathbf{k}\cdot\mathbf{r}_i)^2}{2}$). By neglecting the spin-orbit contribution to the Hamiltonian of the electron system $\mathcal{H}_{\text{el}}$, the momentum operator $\mathbf{p}_i$ can be replaced by $\frac{-im}{\hbar}[\mathbf{r}_i, \mathcal{H}_{\text{el}}]$. By taking the expansion of $e^{i\mathbf{k}\cdot\mathbf{r}_i}$ to the quadrupole term, rearranging the expressions using the commutation rules to act $\mathcal{H}_{\text{el}}$ on the states $\langle n|$ and $|\alpha\rangle$, and using the vector identity $(\mathbf{A}\times\mathbf{B})\cdot(\mathbf{C}\times\mathbf{D}) \equiv$

$(\mathbf{A}\cdot\mathbf{C})(\mathbf{B}\cdot\mathbf{D})-(\mathbf{A}\cdot\mathbf{D})(\mathbf{B}\cdot\mathbf{C})$ the scattering operator can be simplified to three terms.

$$\left\langle n\left|\sum_i^N \hat{\boldsymbol{\varepsilon}}_\lambda\cdot\mathbf{p}_i e^{i\mathbf{k}\cdot\mathbf{r}_i}\right|\alpha\right\rangle = \frac{-im}{\hbar}\left\langle n\left|\sum_i^N \hat{\boldsymbol{\varepsilon}}_\lambda\cdot[\mathbf{r}_i,\mathcal{H}_{\mathrm{el}}](1+i\mathbf{k}\cdot\mathbf{r}_i\ldots)\right|\alpha\right\rangle$$

$$\begin{aligned}\left\langle n\left|\sum_i^N \hat{\boldsymbol{\varepsilon}}_\lambda\cdot\mathbf{p}_i e^{i\mathbf{k}\cdot\mathbf{r}_i}\right|\alpha\right\rangle = {}& \frac{im}{\hbar}[E_n-E_\alpha]\left\langle n\left|\sum_i^N \hat{\boldsymbol{\varepsilon}}_\lambda\cdot\mathbf{r}_i\right|\alpha\right\rangle \\ & -\frac{m}{2\hbar}[E_n-E_\alpha]\left\langle n\left|\sum_i^N(\hat{\boldsymbol{\varepsilon}}_\lambda\cdot\mathbf{r}_i)(\mathbf{k}_i\cdot\mathbf{r}_i)\right|\alpha\right\rangle \\ & +\frac{i}{2}\mathbf{k}\times\hat{\boldsymbol{\varepsilon}}_\lambda\left\langle n\left|\sum_i^N(\mathbf{r}_i\times\mathbf{p}_i)\right|\alpha\right\rangle \end{aligned} \tag{2.40}$$

The first term is the electric dipole operator, $E1$, and the scattering is induced by a photon with total angular momentum of +1. The selection rules for an electric dipole transition require $\Delta l = \pm 1$. For an excitation at the K absorption edge, a $1s$ core electron will be excited into the next empty p band above the Fermi energy, *i.e.* for iron, the $4p$ band. For an excitation at the L_{III} edge, a $2p$ core electron would be excited into the next empty s or d band, *i.e.* for iron, the $3d$ band. The second term is the electric quadrupole operator, $E2$, and the scattering is induced by a photon with a total angular momentum of +2. The selection rules for an electric quadrupole transition require $\Delta l = 0, \pm 2$. For an excitation at the K edge, a $1s$ electron would be excited into an empty s or d band. For a L_{III} edge transition, a $2p$ core electron would be excited into an empty p or f band. The third term in equation 2.40 is the orbital angular momentum operator or magnetic dipole operator, *M1*. The resonant transitions being studied in this thesis all involve a transition of a core electron to an empty valence state above the Fermi energy. As the angular momentum operator *M1* only acts on the angular part of the wavefunction, and the core and valence states have orthogonal radial parts, the magnetic-dipole matrix elements vanish for the x-ray energy range.

The resonant scattering at the x-ray energies the scattering operator can be written as a sum of $E1$ and $E2$ terms as the $M1$ term can be neglected. The scattering length from equation 2.38 which has both an excitation and decay transition, can be written as a sum of dipole and quadrupole terms, $E1E1 + E1E2 + E2E1 + E2E2\ldots$ In order

for the cross terms to exist, the state $|n\rangle$ has to be a mix of even- and odd-parity states, which requires inversion symmetry to be broken, the resonating atom must sit on a non-centrosymmetric site [50]. It should be noted at this point that if more terms were included from the expansion of $e^{i\mathbf{k}\cdot\mathbf{r}_i}$, then electric octupole, $E3$, electric hexadecapole, $E4$ and magnetic quadrupole operators would drop out. For this thesis, only $E1E1$ and $E2E2$ type transitions were observed so derivations of higher-order terms will not be shown.

If the electrons system vectors $\mathbf{r}_i$, $\mathbf{p}_i$ and polarisation vectors $\boldsymbol{\varepsilon}$ are expressed in terms of spherical components, $\mathbf{R}_m$, and spherical harmonics $\mathbf{Y}_{l,m}$ the polarisation factor can be separated from the sum over $|n\rangle$. Hannon *et al.* show the derivation for the $E1E1$ and $E2E2$ scattering terms in [51]. The $E1E1$ term can be written as three terms with different polarisation factors.

$$f_{E1E1} \propto -\frac{3}{4\pi|\mathbf{k}-\mathbf{k}'|}\left[\left(\hat{\boldsymbol{\varepsilon}}^*_{\lambda'}\cdot\hat{\boldsymbol{\varepsilon}}_{\lambda}\right)\left[F^e_{1,1}+F^e_{1,-1}\right]-\sum_i\frac{i}{2}\left(\hat{\boldsymbol{\varepsilon}}^*_{\lambda'}\times\hat{\boldsymbol{\varepsilon}}_{\lambda}\right)\cdot\hat{\mathbf{z}}_i\left[F^e_{1,1}-F^e_{1,-1}\right]\right.$$
$$\left.+\sum_i\left(\hat{\boldsymbol{\varepsilon}}^*_{\lambda'}\cdot\hat{\mathbf{z}}_i\right)\left(\hat{\boldsymbol{\varepsilon}}_{\lambda}\cdot\hat{\mathbf{z}}_i\right)\left[2F^e_{1,0}-F^e_{1,1}-F^e_{1,-1}\right]\right] \qquad (2.41)$$

where the unit vector $\hat{\mathbf{z}}_i$ is the axis of quantization of angular momentum for the i^{th} ion, for a magnetic ion this can be interpreted as the magnetic moment direction. $F^e_{1,m}$ are resonant structure strengths and are dependent on the material and the wavelength of the x-ray. The superscript e and subscript 1 represents the electric dipole nature of transition. They are defined as

$$F^e_{1,m} = m_e\sum_n\frac{[E_n-E_\alpha]^3}{\hbar^3\omega_{\mathbf{k}}}\frac{\left|\left\langle n\left|R_m\right|\alpha\right\rangle\right|^2}{E_\alpha-E_n+\hbar\omega_{\mathbf{k}}+i\frac{\Gamma_n}{2}} \qquad (2.42)$$

The first term in the scattering length does not depend on the magnetic moment and is proportional to $F^e_{1,1}+F^e_{1,-1}$ and is always present. The second term provides sensitivity to the magnetism as it is proportional to the difference of $F^e_{1,1}$ and $F^e_{1,-1}$, which only arises in the presence of a magnetic preference for one sense of rotation around the quantization axis [46, 51]. The third term is non-vanishing for any anisotropic system which includes magnetism but could also occur due to crystal anisotropy [46, 51]. Both the magnetic terms include a sensitivity to moment direction in the polarisation factors. The Jones

matrices for the $E1E1$ scattering can be constructed using the scattering geometry, $\hat{\mathbf{U}}_1$, $\hat{\mathbf{U}}_2$ and $\hat{\mathbf{U}}_3$ shown in figure 2.2. The Jones matrices are shown in Hill *et al.* [49], but are straight-forward to calculate from equation 2.41.

$$\begin{aligned} f_{E1E1} =& F^{(0)} \begin{pmatrix} 1 & 0 \\ 0 & \cos 2\theta \end{pmatrix} \\ & - iF^{(1)} \begin{pmatrix} 0 & z_1 \cos\theta + z_3 \sin\theta \\ z_3 \sin\theta - z_1 \cos\theta & -z_2 \sin 2\theta \end{pmatrix} \\ & + F^{(2)} \begin{pmatrix} z_2^2 & -z_2(z_1 \sin\theta - z_3 cos\theta) \\ z_2(z_1 \sin\theta + z_3 cos\theta) & -\cos^2\theta(z_1^2 \tan^2\theta + z_3^2) \end{pmatrix} \end{aligned} \tag{2.43}$$

The constants F^n are simply shorthand for the coefficients in front of the three terms in equation 2.41, z_1, z_2 and z_3 are the components of the anisotropy axis $\hat{\mathbf{z}}_i$ projected onto the basis of $\hat{\mathbf{U}}_1$, $\hat{\mathbf{U}}_2$ and $\hat{\mathbf{U}}_3$. The principle result to draw is the cross polarisation channel, $\sigma - \pi'$ and $\pi - \sigma'$ are non-zero for magnetic scattering. In addition for the purely magnetic term, the $\sigma - \sigma$ channel is zero, meaning a tell-tale sign for magnetic scattering is if incident light is σ polarised, then scattered light is entirely π polarised.

Similar arguments can be made for $E2E2$ scattering, which generates thirteen separate terms. Of these thirteen terms, one is independent on $\hat{\mathbf{z}}_i$, two are linear in $\hat{\mathbf{z}}_i$, five have quadratic dependence in $\hat{\mathbf{z}}_i$, three cubic and one quartic. The Jones matrices for all thirteen terms are shown in [49], the linear terms which are sensitive to the magnetism are reproduced below.

$$f_{E2E2} = i\left[(\mathbf{k}' \cdot \mathbf{k})\left(\hat{\boldsymbol{\varepsilon}}^*_{\lambda'} \times \hat{\boldsymbol{\varepsilon}}_\lambda\right) \cdot \hat{\mathbf{z}}_i + \left(\hat{\boldsymbol{\varepsilon}}^*_{\lambda'} \cdot \hat{\boldsymbol{\varepsilon}}_\lambda\right)(\mathbf{k}' \times \mathbf{k}) \cdot \hat{\mathbf{z}}_i\right]\left[F^e_{2,2} - F^e_{2,-2}\right] \tag{2.44}$$

where $F^e_{2,2}$ and $F^e_{2,-2}$ are resonant structure strengths for the electric quadrupole transition.

$$F^e_{2,m} = \frac{m_e}{\hbar^3 c^2} \sum_n \left[E_n - E_\alpha\right]^3 \omega_{\mathbf{k}} \frac{\left|\left\langle n \left| \sqrt{\frac{4\pi}{5}} R^2 Y^2_m(\theta,\phi) \right| \alpha \right\rangle\right|^2}{E_\alpha - E_n + \hbar\omega_{\mathbf{k}} + i\frac{\Gamma_n}{2}} \tag{2.45}$$

$$f_{E2E2} = i\cos 2\theta\left[F^e_{2,2} - F^e_{2,-2}\right] \begin{pmatrix} z_2 \tan 2\theta & -z_1 \cos\theta - z_3 \sin\theta \\ z_1 \cos\theta - z_3 \sin\theta & 2z_2 sin2\theta \end{pmatrix} \tag{2.46}$$

For a periodic system the Thomson scattering was shown to be restricted to specific values of $\mathbf{k}$ where the $\mathbf{k} - \mathbf{k}' = G_{\mathrm{hkl}}$. By describing the magnetism in the system in terms of Fourier components of the crystallographic unit cell, $e^{i\boldsymbol{\tau}\cdot\mathbf{r}_i}$ where $\boldsymbol{\tau}$ is the magnetic wavevector, the sum over all the lattice points becomes $\sum_{u_1,u_2,u_3} e^{i(\mathbf{k}-\mathbf{k}'\pm n\boldsymbol{\tau})\cdot\mathbf{R}}$ where n is an integer and relates to the order of $\hat{\mathbf{z}}$ in the scattering operator. The resonant scattering condition can be expressed as $(\mathbf{k}-\mathbf{k}')\pm n\boldsymbol{\tau} = G_{\mathrm{hkl}}$, causing scattering to occur at positions $\mathbf{k} - \mathbf{k}' = h\mathbf{b}_1 + k\mathbf{b}_2 + l\mathbf{b}_3 \pm n\boldsymbol{\tau}$.

2.1.9 X-ray Polarisation Analysis

The magnetic scattering for both $E1E1$ and $E2E2$ transitions have characteristic polarisation dependences. The polarisation of the scattered beam is also dependent on the moment direction $\hat{\mathbf{z}}_i$. This magnetic moment can be complex as in the case of a non-collinear ordering. In order to investigate the origin of the scattering, the polarisation dependence can be measured. In order to measure the polarisation state of the scattered beam, Thomson scattering can be used. Thomson scattering is non-resonant, intense and has a simple polarisation dependence that only depends on the scattering angle θ. By selecting an analyser crystal which has a Bragg peak which scatters at $\theta = 45^\circ$ at the energy of interest, the polarisation dependence of the analyser simply becomes

$$\mathbf{M}_{\mathrm{Thom}} = \begin{pmatrix} 1 & 0 \\ 0 & \cos 2\theta_p \end{pmatrix} = \begin{pmatrix} 1 & 0 \\ 0 & 0 \end{pmatrix} \tag{2.47}$$

If π polarised light is incident on the analyser there is no scattering. By combining this analyser crystal with a rotation, η_p around $\mathbf{k}'$ from the sample, as shown in figure 2.3, the polarisation state can be found, as the intensity of the scattering is maximised when the angle η_p aligns with the polarisation of the beam. This rotation is known as both an η_p scan and a Stokes scan in the literature.

The change of coordinate system associated with rotating the analyser crystal by an angle, η_p around the incoming x-ray beam, can be expressed as a 2×2 rotation matrix.

$$\mathbf{R}_\eta = \begin{pmatrix} \cos\eta_p & \sin\eta_p \\ -\sin\eta_p & \cos\eta_p \end{pmatrix} \tag{2.48}$$

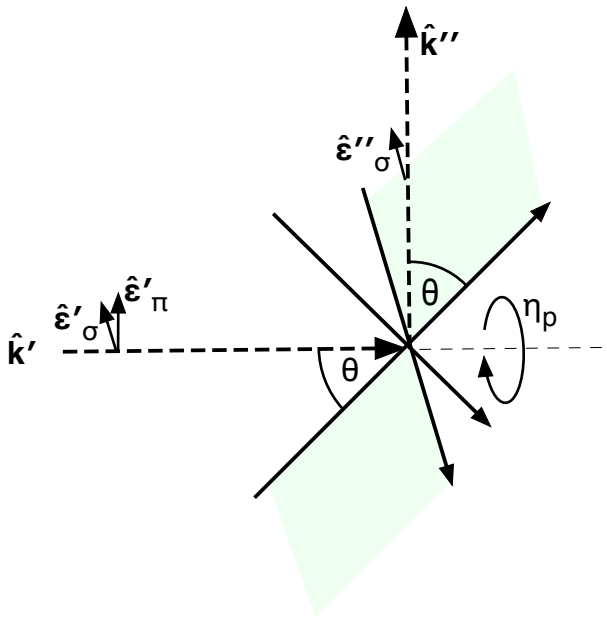

Figure 2.3: Polarisation Analyser geometry

The basis of the density matrix of the x-ray beam being examined, $\boldsymbol{\rho}'$ is transformed by multiplying by $\mathbf{R}_\eta$ and its inverse $\mathbf{R}_\eta^{-1}$.

$$\boldsymbol{\rho}' = \mathbf{R}_\eta \boldsymbol{\rho}' \mathbf{R}_\eta^{-1} \tag{2.49}$$

The intensity from the polarisation analyser can calculated using Jones Calculus rules from section 2.1.2.

$$I'' = \frac{I_0'}{2} tr\left(\mathbf{M}_{\text{Thom}} \cdot \mathbf{R}_\eta \cdot \boldsymbol{\rho}' \cdot \mathbf{R}_\eta^{-1} \cdot \mathbf{M}_{\text{Thom}}^\dagger\right) \tag{2.50}$$

As the analyser may not be perfect for the exact energy of interest (scattering may be offset from $\theta_p = 45^\circ$), the intensity is calculated including the θ_p term.

$$I'' = \frac{I_0}{2}\left(1 + \frac{2\cos^2 2\theta_p}{1 - \cos^2 2\theta_p} + P_1' \cos 2\eta + P_2' \sin 2\eta\right) \tag{2.51}$$

This equation is known as the Stokes equation, and links the rotation angle of the polarisation analyser to the Poincaré-Stokes parameters of the beam being examined. When

the analyser matches the incident energy perfectly, such that the scattering occurs at $\theta_p = 45^\circ$, the intensity of a Stokes scan described in equation 2.51 simplifies to $I'' = \frac{I_0}{2}(1 + P_1' \cos 2\eta + P_2' \sin 2\eta)$. The Stokes equation reveals that only P_1 and P_2 parameters can be extracted, and that it is not possible to distinguish between circular polarisation and a partly unpolarised beam. When the analyser scatters at $\theta_p = 45^\circ$ a diffraction measurement carried out at $\eta_p = 0$ is said to be looking in the σ' polarisation channel, when $\eta_p = 90$ is said to be in the π' polarisation channel. When θ_p is away from 45° this is no longer true, as spillover intensity remains from the $\frac{2\cos^2 2\theta_p}{1-\cos^2 2\theta_p}$ term.

The polarisation analyser provides a way to experimentally investigate the origin of the resonant scattering. There are two main types of experiments which use the polarisation analyser. The first involves looking in a specific polarisation channel, *i.e.* $\sigma - \pi'$, and rotating the sample around the scattering vector. This is known as an azimuthal scan, and is often given the notation ψ. By rotating the sample around $\hat{\mathbf{U}}_3$, the condition for scattering remains unchanged, (*i.e.* $\mathbf{G}_{\mathrm{hkl}}$ is still surface normal) but the scattering plane bisects the sample along a different crystallographic axis. This makes use of the fact that for magnetic resonant scattering the different polarisation channels are dependent on different components of $\hat{\mathbf{z}}$. In the experimental basis, $\hat{\mathbf{U}}_1$, $\hat{\mathbf{U}}_2$, $\hat{\mathbf{U}}_3$, the components of the moment z_1 and z_2 can be replaced $z_1' = z_1 \cos(\psi - \phi) - z_2 \sin(\psi - \phi)$ and $z_1' = z_1 \cos(\psi - \phi) - z_2 \sin(\psi - \phi)$. The zero position($\phi$) of the azimuth is arbitrary and is defined on a per experiment basis. By rotating the azimuth, the intensity of the scattered beam changes depending on proportion of moment in and out of the scattering plane, and along the scattering vector. If the moments in the sample all point along the scattering vector then no azimuthal dependence is expected. Since $I \propto |f|^2$, for scattering linear in $\hat{\mathbf{z}}$, the azimuthal dependence will be a function of $\sin^2\psi$, $\cos^2\psi$, $\sin\psi$, $\cos\psi$ and a constant, depending on the scattering operator and magnetic moment structure.

The other experiment that can be performed is a Full Linear Polarisation Analysis (FLPA). This involves a rotation of the incident polarisation, which is also given the symbol ψ, from the definition of the polarisation ellipse, in section 2.1.1. The polarisation of an x-ray generated by a synchrotron, can be controlled using either the undulator directly in the case of soft x-ray energies, or with the use of a phase plate setup for hard x-ray energies. Once calibrated both these setups allow the production of a polarised x-ray either circularly polarised or linearly polarised at any angle with respect to the experimental

geometry.

At each incident linear polarisation angle, a Stokes rotation of the analyser is performed to extract the Poincaré-Stoke Parameters of the scattered beam. The Stokes rotation involves collecting a reciprocal space scan or θ_p scan for each η_p position, and then fitting the resulting integrated intensity using the Stokes equation in 2.51 to extract P_1' and P_2'. An FLPA measurement shows how P_1' and P_2' varies for the incident polarisation. A FLPA is more complicated to model than an azimuth, as it involves using Jones matrix calculus for each incident polarisation.

FLPA and Azimuthal measurements can be used together to solve the magnetic structure of a material. FLPA has the advantage, that once the scattering condition is found, the sample remains fixed as the measurement is performed by undulator and polarisation analyser. Azimuthal measurements require the sample to be rotated which experimentally is more difficult due to constraints from the cryostat, and can also be effected by anisotropic absorption due to sample shape.

2.2 Neutron Scattering

Neutrons scattering is an established probe for looking at atomic scale in condensed matter systems. The neutron is a charge neutral particle, and can penetrate deeply into matter, giving information about the bulk properties. A neutron with a wavevector $\mathbf{k}$, has an energy given from its de Broglie wavelength as

$$E = \frac{\hbar^2 \mathbf{k}^2}{2m} = \left(2.08 \text{ meV}\text{Å}^2\right) \mathbf{k}^2 \tag{2.52}$$

where m is the mass of neutron [52]. Cold neutrons with a wavevector of a few Å^{-1} have an energy of a few meV. Alternatively the wavelength can be expressed in terms of energy, $\lambda = 9.04 E^{-\frac{1}{2}}\text{Å}$, where E is measured in meV. A neutron of 25 meV has a wavelength, $\lambda = 1.81\text{Å}$. In condensed matter systems the energy associated with lattice vibrations and spin excitations is of the order of meV, making neutrons an ideal probe to use. The wavelength is also similar to the atomic spacing in condensed matter systems. Neutrons also have a magnetic moment of $-1.91\mu_N$, where μ_N is the nuclear magneton. This makes neutrons a ideal probe to investigate magnetic materials [53].

2.2.1 Neutron Interaction with Matter

Due to the neutrons charge neutrality they do not interact with the charge of the electron density. Instead neutrons interact with the atomic nuclei through the strong nuclear force. Using a similar approach to x-rays a Hamiltonian can be written describing the neutron's interaction with a sample.

$$\mathcal{H} = \mathcal{H}_0 + \frac{\mathbf{p}^2}{2m} + V(\mathbf{r}) \tag{2.53}$$

$\mathcal{H}_0$ is the Hamiltonian describing the unperturbed sample, $\frac{\mathbf{p}^2}{2m}$ is the kinetic energy of the neutron and $V(\mathbf{r})$ is the interaction energy between the neutron and sample. The interaction term can be split up into two terms, $V(\mathbf{r}) = V_{\text{nuclear}}(\mathbf{r}) + V_{\text{magnetic}}(\mathbf{r})$. The nuclear term is between the neutron and the atomic nuclei in the system, whilst the magnetic term is between the neutron and the magnetic moment from the unpaired electrons in the system. The scattering cross-section given in equation for x-rays, is correct for neutrons, with the density of states for the neutrons in a solid angle $d\Omega$ being

$$n(E) = \frac{V_0}{8\pi^3}\frac{mk_f}{\hbar^2}d\Omega \tag{2.54}$$

Combining the density of states with the incident flux, $I_0 = {}^{v}/_{V_0} = \frac{\hbar\mathbf{k}_i}{V_0 m}$ and Fermi golden rule, the scattering cross-section can be written as

$$\frac{d^2\sigma}{dEd\Omega} = \left(\frac{V_0 m}{2\pi\hbar^2}\right)^2 \frac{k_f}{k_i}\left|\left\langle(\mathbf{k}',\sigma')\,;\Psi_\beta\left|V(\mathbf{r})\right|(\mathbf{k},\sigma)\,;\Psi_\alpha\right\rangle\right|^2 \delta(E_i - E_f) \tag{2.55}$$

where the incident neutron is described by wavevector $\mathbf{k}$ and spin σ and the scattered neutron by $\mathbf{k}'$ and σ' [54]. The eigenstates of the unperturbed sample, $\mathcal{H}_0$ are given by $|\Psi\rangle$, and the initial and final energies, E_i and E_f are given as $E_\alpha + \frac{\mathbf{p}^2}{2m}$ and $E_\beta + \frac{\mathbf{p}'^2}{2m}$ respectively. Assuming the neutron beam can be described by plane waves, then the states of the incident and scattered neutrons can be written as the wavefunctions

$$\Phi_k = \frac{1}{\sqrt{V_0}}e^{i\mathbf{k}\cdot\mathbf{r}}$$

and

$$\Phi_{k'} = \frac{1}{\sqrt{V_0}} e^{i\mathbf{k}'\cdot\mathbf{r}}$$

The initial state $|\Psi_\alpha\rangle$ of the sample is unknown and in general there will be a range of accessible initial states. The same can be said for the final states, $|\Psi_\beta\rangle$. Without some form of discrimination all the final states will be observed. The scattering cross-section can be written as a sum over all the accessible initial states weighted by a probability factor p_α and all the final states.

$$\frac{d^2\sigma}{dEd\Omega} = \left(\frac{V_0 m}{2\pi\hbar^2}\right)^2 \frac{k'}{k} \sum_\alpha \sum_\beta p_\alpha \left|\left\langle (\mathbf{k}', \sigma') ; \Psi_\beta \left| V(\mathbf{r}) \right| (\mathbf{k}, \sigma) ; \Psi_\alpha \right\rangle\right|^2 \delta(E_i - E_f) \qquad (2.56)$$

Further discussion will be limited to elastic scattering of an unpolarised neutron beam from both the nuclear and magnetic interactions. Assuming elastic scattering, the state of the sample remains unchanged so $|\Psi_\beta\rangle = |\Psi_\alpha\rangle$, and $\left|\mathbf{k}'\right| = |\mathbf{k}|$.

2.2.2 Nuclear Scattering

Unlike the case for an x-ray scattering from an electron, which could be described through quantum electrodynamics, there is no complete theory of nucleon-nucleon scattering [52, 55]. From experiments, the interaction between neutron and a nucleus is known to be short range, $\sim 10^{-14}$ m. The wavelength of a low energy neutron is much larger than the range of the interaction resulting in isotropic scattering. This isotropic scattering can be described by a single parameter, b called the scattering length. The scattering length b is different for each atom type and isotope, and is assumed to be independent of energy for the range of interest in condensed matter. The interaction energy between the neutron and the nucleus can be approximated by the Fermi pseudo-potential, which gives isotropic scattering as a δ function [54].

$$V_{\text{nuclear}}(\mathbf{r}) = \frac{2\pi\hbar^2}{m} \sum_i b_i \delta(\mathbf{r} - \mathbf{R}_i) \qquad (2.57)$$

The sum in the above term is over all nuclei in the system, where $\mathbf{R}_i$ is the position of the i^{th} nucleus. The scattering cross-section for an unpolarised neutron beam becomes

$$\begin{aligned}\frac{d^2\sigma}{dEd\Omega} &= \left|\left\langle (\mathbf{k}', \sigma') ; \Psi_\beta \left| \sum_i b_i \delta(\mathbf{r} - \mathbf{R}_i) \right| (\mathbf{k}, \sigma) ; \Psi_\alpha \right\rangle\right|^2 \delta(E_i - E_f) \\ &= \left| \sum_i b_i \int d^3\mathbf{r}\, e^{-i\mathbf{k}'\cdot\mathbf{R}_i} \delta(\mathbf{r} - \mathbf{R}_i)\, e^{i\mathbf{k}\cdot\mathbf{R}_i} \right|^2 \delta(E_i - E_f) \\ &= \left| \sum_i b_i e^{i(\mathbf{k}-\mathbf{k}')\cdot\mathbf{R}_i} \right|^2 \delta(E_i - E_f) \end{aligned} \tag{2.58}$$

If the nuclei are arranged in a periodic structure as in the case for a crystal system, the same reasoning can be used as in the case for x-rays, section 2.1.6. This results in scattering only occurring when $\mathbf{k} - \mathbf{k}'$ is equal to a reciprocal lattice point, $\mathbf{G}_{\text{hkl}}$ of the sample. The scattering cross-section for an unpolarised neutron beam scattering from a periodic lattice of nuclei is written as

$$\frac{d^2\sigma}{dEd\Omega} = \frac{8\pi^3 N}{V} \delta((\mathbf{k} - \mathbf{k}') - G_{\text{hkl}}) \left| \sum_i b_i e^{i(\mathbf{k}-\mathbf{k}')\cdot\mathbf{R}_i} \right|^2 \delta(E_i - E_f) \tag{2.59}$$

Where N is the number of unit cells exposed to the neutron beam and V is the volume of a single unit cell. The index i now ranges over the nuclei in a single unit cell, rather than the entire crystal. The above cross-section assumes the lattice is fixed and neglects the nuclei's thermal motion. Isotopes of the same atomic type can have markedly different scattering lengths. The isotopes are not distributed in a crystal with any periodicity, and lead to incoherent scattering effects not accounted for by the above model.

2.2.3 Magnetic Scattering

As stated earlier, the neutron has a magnetic moment, which allows it to interact with any unpaired electrons in the system. The interaction potential of a neutron in a magnetic field is described by $-\boldsymbol{\mu}_n \cdot \mathbf{H}$, where $\boldsymbol{\mu}_n$ is the magnetic moment operator for a neutron. The operator $\boldsymbol{\mu}$ can be expressed as $\gamma\mu_N\hat{\boldsymbol{\sigma}}$ where gyromagnetic ratio, γ is -1.91, μ_N is the nuclear magneton, and $\hat{\boldsymbol{\sigma}}$ is the Pauli matrix with $\hat{\sigma}/2$ being the neutron spin operator. For magnetic neutron scattering from a condensed matter system the magnetic field is due to

the electron density. The magnetic field due to a single electron is given in Landau and Lifshitz [56], as

$$\mathbf{H} = \boldsymbol{\nabla} \times \left(\frac{\boldsymbol{\mu}_e \times (\mathbf{r} - \mathbf{r}_i)}{\left|\mathbf{r} - \mathbf{r}_i\right|^3} \right) + \frac{-e}{c} \frac{\mathbf{v}_e \times (\mathbf{r} - \mathbf{r}_i)}{\left|\mathbf{r} - \mathbf{r}_i\right|^3} \tag{2.60}$$

The vector $\mathbf{r}_i$ is the position of the electron, $\mathbf{r}$ is the position at which the field is measured and $\mathbf{v}$ the velocity of the electron. $\boldsymbol{\mu}_e$ is the magnetic moment operator of the electron, and can be written as $\boldsymbol{\mu}_e = -2\mu_B \hat{\mathbf{s}}$, where μ_B is the Bohr Magneton and $\hat{\mathbf{s}}$ the electron spin operator. The first term arises from the spin moment of the electron, whilst the second term to the H-field arises from the orbital moment. As shown in [57], the interaction potential between a neutron and an system of electrons becomes

$$\begin{aligned} V_{\text{magnetic}} =& -\gamma \mu_N \hat{\boldsymbol{\sigma}} \cdot \mathbf{H} \\ =& 2\gamma \mu_N \mu_B \sum_i \hat{\boldsymbol{\sigma}} \cdot \boldsymbol{\nabla} \times \left(\frac{\hat{\mathbf{s}}_i \times (\mathbf{r} - \mathbf{r}_i)}{\left|\mathbf{r} - \mathbf{r}_i\right|^3} \right) \\ & - \frac{\gamma \mu_N e}{2 m_e c} \sum_i \left(\mathbf{p}_i \cdot \frac{\hat{\boldsymbol{\sigma}} \times (\mathbf{r} - \mathbf{r}_i)}{\left|\mathbf{r} - \mathbf{r}_i\right|^3} + \frac{\hat{\boldsymbol{\sigma}} \times (\mathbf{r} - \mathbf{r}_i)}{\left|\mathbf{r} - \mathbf{r}_i\right|^3} \cdot \mathbf{p}_i \right) \\ =& V_{\text{spin}}(\mathbf{r}) + V_{\text{orbit}}(\mathbf{r}) \end{aligned}$$

The operators $\hat{\mathbf{s}}_i$ and $\mathbf{p}_i$ are the spin and linear momentum operators which act on the i^{th} electron. The orbital term has been split to take into account the operator nature of $\mathbf{p}_i$. In c.g.s. units the definition of a Bohr magneton is $\mu_B = \frac{e\hbar}{2m_e c}$, and nuclear magneton is $\mu_N = \frac{e\hbar}{2m_p c}$, these can be used to take a common factor of $2\mu_N\mu_B$ out of the interaction potential.

$$\begin{aligned} \frac{d^2\sigma}{dE d\Omega} =& \left(\frac{V_0 m}{2\pi\hbar^2} \right)^2 (2\gamma\mu_N\mu_B)^2 \sum_\alpha p_\alpha \left| \left\langle (\mathbf{k}', \sigma') ; \Psi_\alpha \right| \sum_i \hat{\boldsymbol{\sigma}} \cdot \boldsymbol{\nabla} \times \left(\frac{\hat{\mathbf{s}}_i \times (\mathbf{r} - \mathbf{r}_i)}{\left|\mathbf{r} - \mathbf{r}_i\right|^3} \right) \right. \\ & \left. - \frac{1}{2\hbar} \sum_i \left(\mathbf{p}_i \cdot \frac{\hat{\boldsymbol{\sigma}} \times (\mathbf{r} - \mathbf{r}_i)}{\left|\mathbf{r} - \mathbf{r}_i\right|^3} + \frac{\hat{\boldsymbol{\sigma}} \times (\mathbf{r} - \mathbf{r}_i)}{\left|\mathbf{r} - \mathbf{r}_i\right|^3} \cdot \mathbf{p}_i \right) \right| (\mathbf{k}, \sigma) ; \Psi_\alpha \Big\rangle \Big|^2 \delta(E_i - E_f) \end{aligned} \tag{2.61}$$

The cross-section can simplified by integrating the interaction potential over the neutron coordinates $\mathbf{k}$ and $\mathbf{k}'$. The notation $\boldsymbol{\kappa} = \mathbf{k} - \mathbf{k}'$ and $\hat{\boldsymbol{\kappa}} = \frac{\mathbf{k}-\mathbf{k}'}{|\mathbf{k}-\mathbf{k}'|}$ is used to simplify the

expression.

$$\begin{aligned}\frac{d^2\sigma}{dEd\Omega} &= \left(\frac{m}{2\pi\hbar^2}\right)^2 (2\gamma\mu_N\mu_B)^2 (4\pi)^2 \sum_\alpha p_\alpha \left|\left\langle \sigma';\Psi_\alpha \left| \hat{\boldsymbol{\sigma}} \cdot \left[\sum_i e^{i\boldsymbol{\kappa}\cdot\mathbf{r}_i} \hat{\boldsymbol{\kappa}} \times (\hat{\mathbf{s}}_i \times \hat{\boldsymbol{\kappa}}) \right.\right.\right. \\ &\quad \left.\left.\left. -\frac{i}{\hbar|\boldsymbol{\kappa}|} \sum_i e^{i\boldsymbol{\kappa}\cdot\mathbf{r}_i} \hat{\boldsymbol{\kappa}} \times \mathbf{p}_i \right] \right| \sigma;\Psi_\alpha \right\rangle \right|^2 \delta(E_i - E_f) \\ &= \left(\frac{\gamma e^2}{m_e c^2}\right)^2 \sum_\alpha p_\alpha \left|\left\langle \sigma';\Psi_\alpha \left| \hat{\boldsymbol{\sigma}} \cdot \mathbf{M}_\perp(\boldsymbol{\kappa}) \right| \sigma;\Psi_\alpha \right\rangle\right|^2 \delta(E_i - E_f) \end{aligned} \tag{2.62}$$

The operator $\mathbf{M}_\perp$ is the magnetic interaction vector and can be written in terms of the magnetic structure factor, $\mathbf{M}(\boldsymbol{\kappa})$, as $\mathbf{M}_\perp(\boldsymbol{\kappa}) = \hat{\boldsymbol{\kappa}} \times \mathbf{M}(\boldsymbol{\kappa}) \times \hat{\boldsymbol{\kappa}}$. The magnetic structure factor is the Fourier transform of the total magnetisation distribution. This can be written as a summation of magnetic moments, $\boldsymbol{\mu}_i$ over all the magnetically active ions [57].

$$\mathbf{M}(\mathbf{k} - \mathbf{k}') = \sum_i f_i^{\text{mag}}(\mathbf{k} - \mathbf{k}') \boldsymbol{\mu}_i e^{i(\mathbf{k}-\mathbf{k}')\cdot\mathbf{r}_i} \tag{2.63}$$

$f_i^{\text{mag}}(\mathbf{k} - \mathbf{k}')$ is the magnetic form-factor and is the Fourier transform of the magnetisation distribution of the i^{th} ion. This form-factor is dependent on the value of $\mathbf{k} - \mathbf{k}'$, and in this respect it is more similar to the charge scattering of x-rays, than the nuclear scattering of neutrons, where the form-factor b_i was constant with $\mathbf{k} - \mathbf{k}'$. For the work in this thesis, unpolarised neutrons were used, this removes any sensitivity to the $\hat{\boldsymbol{\sigma}} \cdot \mathbf{M}_\perp(\mathbf{k} - \mathbf{k}')$ term. The advantage of using unpolarised neutrons is intensity. Neutrons, unlike synchrotron radiation, are produced unpolarised, and spin filters are required to produce a beam of polarised neutrons, by filtering out any neutrons with the non-desired polarisation. This dramatically reduces the beam intensity.

2.2.4 Time-of-Flight

The neutron work presented in this thesis was collected from the ISIS neutron spallation source, in the UK. Neutron spallation works by bombarding a heavy metal target with protons, releasing two or three smaller nuclei and several neutrons. The ISIS source uses a 70 MeV linear accelerator to speed up H^- ions to an 800 MeV synchrotron ring. The synchrotron magnetic field is designed so positive ions bend into the ring direction. The H^- ions enter the ring they are passed through a gold stripper foil which removes two

electrons to give a bare proton. The synchrotron accelerates the protons to a velocity of $0.84c$. This process continues until 2.8×10^{13} protons accumulate in the ring. The proton beam has a charge of 4.5 μC, and is split into two pulses each of 100 ns. The whole process happens 50 times a second, resulting in a mean current of 200 μA. There are two target stations at ISIS, the WISH instrument used in this thesis, is situated on target station two, which receives one in four pulses, resulting in a mean current of 42 μA. The target is composed of tungsten clad in tantalum, and a decoupled solid methane moderator. The decoupled moderator provides the WISH instrument with a energetically broad pulse, with little to no tail and a width of 30-50 μs.

X-ray diffraction experiments are performed with a monochromatic x-ray beam. Diffraction from a particular G_{hkl} reciprocal lattice point occurs at a specific point. Neutrons from spallation sources are non monochromatic and are produced with a range of energies. Unlike the case with electromagnetic radiation, a neutron's velocity is related to its energy through the kinetic energy relation $E_K = \frac{1}{2} m_n v^2$. Neutrons of different energies travel at different speeds, combined with the pulsed nature of the spallation source, means that in addition to the scattered position, the time-of-flight since the pulse origin can be measured. For example, the WISH instrument has two-dimensional detectors covering a scattering angle from 10-170° and an out of plane angle of ±12.8° [58]. For every scattering event, the time-of-flight, tof is recorded, resulting in each pixel having a time-of-flight *vs* intensity spectrum. In this manner two scattering conditions which are on top of each other, *i.e.* the $[1, 1, 0]$ at E and $[2, 2, 0]$ at $4E$ which have the same scattering angle θ, are separable in time-of-flight. Using the distance from source to detector, the time-of-flight can be converted to crystallographic d-spacing. The relationship between time-of-flight and d-spacing, d is given by the following quadratic relationship.

$$tof = \text{DIFC}\, d + \text{DIFA}\, d^2 + \text{ZERO} \tag{2.64}$$

The first term, DIFC which is the linear d coefficient, is the theoretical time-of-flight of a

measured Bragg reflection. This arises from de Broglie relation and Bragg's Law.

$$\begin{aligned} \lambda = \frac{h}{m_n v} = \frac{h}{m_n L} tof &= 2d_{\text{hkl}} \sin\theta \\ tof &= \frac{2m_n}{h} L d_{\text{hkl}} \sin\theta \\ &= 505.56 L d_{\text{hkl}} \sin\theta \end{aligned} \tag{2.65}$$

The simplification of the above equation holds when d_{hkl} is measured in Å, the flight path L measured in m, and time-of-flight in ms.

The DIFA value is the coefficient of the quadratic d-spacing term, d^2. This term arises from wavelength dependent absorption cross-section. Short wavelengths experience less absorption than longer wavelength. The average penetration into the sample is wavelength dependent, and therefore the total flight path L is wavelength dependent. DIFA is a small correction term, that empirically has been shown to have a d^2 relationship.

The ZERO term corresponds to small differences between various timing signals and the synchrotron, as well as response times for detectors. The ZERO term is instrument specific.

During a neutron time-of-flight experiment, the scattering angle and time-of-flight are recorded. The analysis is more complicated than in the monochromatic diffraction case, but a d-spacing spectra can be extracted from the time-of-flight. Using the scattering angle and d-spacing the diffraction pattern can be indexed using the reciprocal space hkl notation. The WISH instrument, although built as a time-of-flight powder diffraction instrument, has the capabilities for single crystal diffraction, using a transmission Laue geometry, with the advantage that families of peaks can be separated in the d-spacing spectra.

2.3 Muon Spin Relaxation

Muon spin relaxation experiments, μSR use a beam of spin polarised muons to probe the local magnetism in the target sample.

2.3.1 The muon particle

The muon is a lepton with a mass of 206 m_e (approximately 1/9 the mass of a proton), carries a charge of $\pm e$, and has a lifetime of 2.2 μS. In order to use muons as a successful

magnetic probe, the incident muons need to be spin polarised.

It is important to note, unlike the x-ray and neutron techniques used in this thesis, muon spectroscopy is not a scattering technique. Muons implant in materials, where they remain for the rest of their lifetime before decaying in to a positron or electron depending on charge of muon. Positive muons, for this purpose can be thought of as lightweight protons, and sit in positions well away from the nucleus, in regions of high electron density, before decaying into a positron. Negative muons are attracted to the nucleus and tend to displace an electron from the atom and drop down to the $1s$ state, where it either decays into an electron or undergoes μ^- capture with a proton in the nucleus and forms a neutron and a neutrino. For condensed matter systems, positive muons provide a far more interesting probe, as they are far more sensitive to the electron cloud. The ARGUS instrument operates using positive muons.

Muon facilities, such as ISIS, produce muons by passing an energetic proton beam, from a proton synchrotron through a thin graphite target. Collisions between the protons (800 MeV) in the beam and protons and neutrons in the graphite, lead to the production of pions, $\pi^{\pm}$.

$$p + p \rightarrow p + n + \pi^+$$
$$p + n \rightarrow n + n + \pi^-$$

The pions have a relatively short lifetime of 0.026 μs and subsequently decay into muons.

$$\pi^+ \rightarrow \mu^+ + \nu_\mu$$
$$\pi^- \rightarrow \mu^- + \bar{\nu}_\mu$$

The pion has a spin quantum number of zero, $S = 0$, and neutrinos possess negative helicity meaning there spin is antiparallel to their momentum. Under conservation of linear and angular momentum, in the pion rest frame the muon is forced to have negative helicity. The muons are produced in pulses of nearly 100% spin polarised meaning their spin is antiparallel to their momentum.

2.3.2 Muon interaction with matter

The muons enter the sample and undergo a number of stopping processes, including ionisation of atoms, scattering with electrons, electron capture/loss reactions. Damage to the sample by the muon beam, occurs near the sample surface, early in the muon's trajectory. All later stopping mechanisms, mainly electron capture/loss cause no permanent damage. The site where the muon finally implants (zero E_k), will be away from any possible damage caused to the sample. The various stopping processes the muon undergoes tend to leave the spin polarisation unchanged. When the muon comes to rest in the sample it will have a well defined spin direction. The muon spin will interact with the local magnetic field through a process known as Larmor precession. The moment from the muon experiences a torque when subject to an external magnetic field, this torque is given by the cross product of the magnetic moment and the B-field and is equal to the rate of change of angular momentum.

$$\frac{\mathrm{d}\boldsymbol{\mu}}{\mathrm{d}t} = \boldsymbol{\mu} \times \mathbf{B}$$

The muons spin precesses with a frequency $\omega = \frac{ge}{2m_\mu}B = 2\pi \times 135.5B$, where 135.5 MHz T^{-1} is the gyromagnetic ratio for the muon, m_μ is the mass of the muon and the g-factor $g \approx 2$.

The dominant decay channel for a muon is into a positron, electron neutrino and muon anti-neutrino.

$$\mu^+ \rightarrow e^+ + \nu_e + \bar{\nu}_\mu$$

In this decay process the positron is emitted preferentially along the direction of the muons spin, due to the parity violating weak interaction, and the conservation of linear and angular momentum. This allows us to read out the polarisation state of the muon. The angular distribution of positron emission is a function of the positrons energy ξ. The maximum energy the positron can have is 52.83 MeV, we can parametrise the decay probability using the substitution $x = {}^{\xi}/_{\xi_{max}}$. The decay probability W of the positron emission can be written a combination of the normalised energy spectrum, $E(x)$ and an

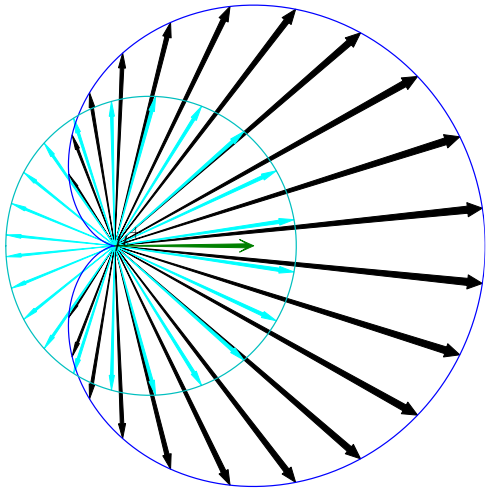

Figure 2.4: Angular distribution of the emitted positron from the decay of a μ^+, with respect to the direction of the μ^+ spin (green). The distribution is energy dependent, the figure shows the case $\xi = 0.7\xi_{max}$ (light blue) and $\xi = \xi_{max}$ (black).

asymmetry factor, $a(x)$.

$$\begin{aligned} dW(x,\theta) &= E(x)[1 + a(x)\cos\theta]dx d(\cos\theta) \\ E(x) &= 2x^2(3 - 2x) \\ a(x) &= \pm\frac{2x-1}{3-2x}, \end{aligned}$$

The asymmetric angular distribution of the emitted positron is shown in figure 2.4, for two particular positron energies $0.7\xi_{max}$ (light blue) and ξ_{max} (black).

2.3.3 Muon Spectrometer

The ARGUS instrument, (Advanced Riken General-Purpose mUsr Spectrometer) is based at the RIKEN-RAL Muon Facility at the neutron spallation source ISIS. The basic design of the ARGUS spectrometer, shown in figure 2.5, consists of two circular banks of detectors either side of the sample. Each detector bank known as forward and back, consists of 96 detector elements. The spin polarised muon beam is sent in pulses, enters the spectrometer, through the centre of the back detector bank, and implants in the sample. The positive muons implants inside the crystal in areas of high electron density, where they are

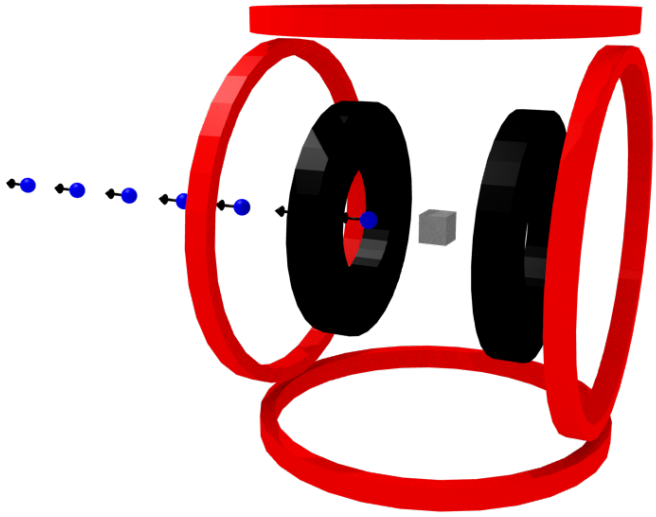

Figure 2.5: Schematic of the experimental set-up in the ARGUS spectrometer at the ISIS facility (RAL, UK). The muon beam travels in from the left hand side, spin polarised with their magnetic moment (black arrows) antiparallel to their momentum, and implant in the sample shown in grey. Two sets of detectors, forwards and back are shown in black. A magnetic field can be applied longitudinally or transverse, shown by the red rings.

subject to local magnetic fields, until they decay into positrons. The muon subsequently decays into a positron,which is emitted from the sample, and detected by either the forward or back detector bank. For each positron detection event, the detector bank (F/B) and the time since the muon pulse is created is recorded. If the muon decays immediately after implanting in the sample, it will still have its spin pointed backwards and the subsequent positron will be emitted in the direction of the back detector. If the muon decays after time, t where it has be able to precess half a revolution, the subsequent positron will be emitted in the direction of the forward detector. The time evolution of the number of events detected by the forward and back detectors are described by functions $N_F(t)$ and $N_B(t)$. The sum of these two functions is an exponential decay, as expected for a radioactive decay process. The time evolution of the spin polarisation can be seen by taking the normalised difference.

$$A(t) = \frac{N_B(t) - N_F(t)}{N_B(t) + N_F(t)} \tag{2.66}$$

Argus comes equipped with two sets of magnetic field coils, shown in red in figure 2.5. These allow a magnetic field to be applied both longitudinally and transverse across the sample.

Chapter 3

Magnetic and Charge order in oxygen deficient Transition metal oxide, Strontium Ferrate

3.1 Introduction to $SrFeO_{3-\delta}$

3.1.1 Transition Metal Oxides

Transition metal oxides (TMO) are a class of material which contain a transition metal and oxygen. Transition metals are defined as an element whose atom has an incomplete *d* sub-shell or which can give rise to cations with an incomplete *d* sub-shell [59]. The valency of these *d* orbitals allow transition metals to bond ionically, covalently and metallically across the period. Unlike other oxide classes, TMOs show a range of physical phenomena such as high temperature superconductivity in the cuprates, *e.g.* $YB_2Cu_3O_7$, $BiSrCaCu_2O_x$ [60–62], colossal magnetoresistance in the layered manganates, *e.g.* $La_{2-2x}Sr_{1+2x}Mn_2O_7$ [63], metal-insulator transitions, *e.g.* VO_2 [64] and multiferroicity, *e.g.* $BiFeO_3$,$TbMnO_3$ [65, 66] [67].

For a free ion of a transition metal the *d* orbitals are degenerate, and the electronic configuration is determined by Hund's Rules. In a transition metal oxide, the transition metal is now surrounded by oxygen. The oxygen acts as a distribution of negative charge, and as a consequence of the repulsion between electrons, the energy of the *d* orbitals increases. If this distribution of negative charge around the transition metal ion was spherically symmetric we would expect it to affect all of the *d* orbitals equally. In a crystal system the oxygen cations occupy particular sites in the unit cell. The co-ordination of the oxygen around the transition metal can vary greatly depending on the crystal structure of

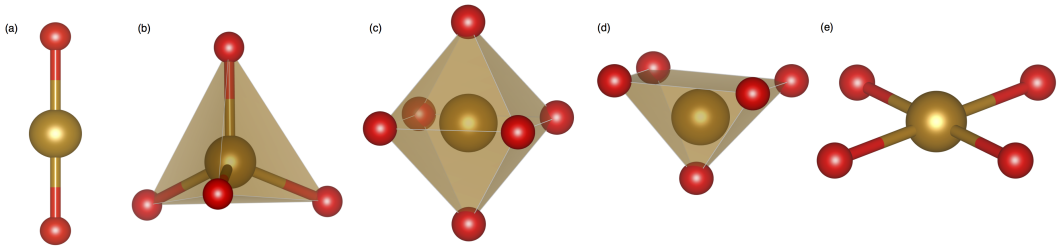

Figure 3.1: Different oxygen geometries seen amongst the transition metal oxides. The transition metal is brown and the oxygen is red. (a) Linear, (b) 'Tetrahedral, (c) Octahedral, (d) Squared-based Pyramid, (e) Square-Planar geometries.

the material. A variety of co-ordinations, shown in Figure 3.1, have been observed across the spectrum of TMOs - from linear chains, where the transition metal has two oxygen ligands; tetrahedral where four oxygen ligands surround the transition metal, maximising space; octahedral with 6 oxygen ligands; squared-based pyramidal with 5 oxygen ligands; and square-planar, where four oxygen ligands surround the transition metal ion confined to a plane.

This distribution of charge around the transition metal can vary greatly from spherical for different coordinations, affecting each of the *d*-orbitals differently. Crystal field theory uses a quantum mechanical description of the transition metal ion in the crystal electric field potential given by oxygen-cation coordination to predict the energy level splitting of the degenerate *d* sub-shell [68,69]. For the linear crystal field, an oxygen anion sits above and below the transition metal ion. The d_{z^2} orbital is located in the highest region of negative charge, and its energy level increases the most from the isolated ion case, followed by the d_{xz} and d_{yz} orbitals, lastly the d_{xy} and $d_{x^2-y^2}$ are furthest away from the oxygen anion and experience the least negative charge, having the lowest energy level. Figure 3.2 show the splitting of the degenerate *d* orbitals energy level for linear, tetrahedral, octahedral, squared-based pyramid and square planar.

As the *d* orbitals are no longer degenerate, Hund's rules are no longer sufficient to find the electron configuration, and some attention must be paid to the size of the orbital splitting. If the orbital splitting is large compared to the energy cost of pairing electrons, then the lower energy orbitals will doubly occupy before electrons fill the higher energy orbitals. If the orbital splitting is small compared to the pairing energy, then the orbitals

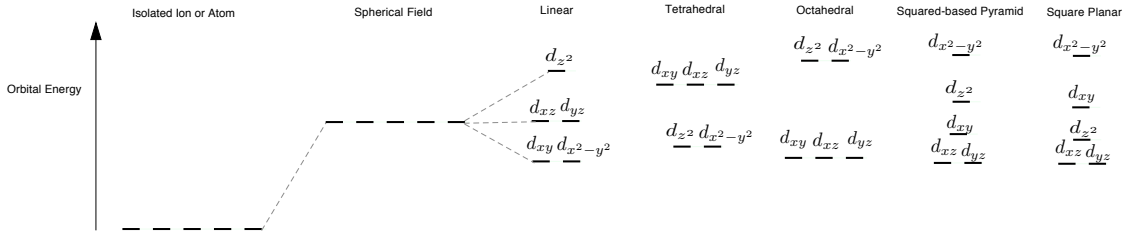

Figure 3.2: Different orbital energy level splittings for the different oxygen ligand geometries predicted by crystal field theory. (a) Linear, (b)Tetrahedral, (c) Octahedral, (d) Squared-based Pyramid, (e) Square-Planar

will all singly occupy first. The crystal field splitting and valency of the transition metal ion affect the physical properties of the system and are responsible for the wide range of behaviours observed in TMO's.

3.1.2 $SrFeO_3$

As mentioned earlier in this chapter, colossal magnetoresistance has been found in the transition metal oxides, in the manganite family [70, 71]. Magnetoresistance is the property of a material to change its resistance in the presence of an external magnetic field. The term colossal refers to the size of the magnetoresistance effect, iron and nickel experience a change in resistance of the order of 1% , whereas manganites experience changes in resistance on the scale of several orders of magnitude- with the La-Ca-Mn-O system showing a change in resistance of 10^8 % [71] . The parent of the La-Ca-Mn-O family is the cubic perovskite material $LaMnO_3$. The perovskite structure has a cubic lattice of lathanum atoms at the corner [0,0,0] position, with a body-centred manganese atom octahedrally coordinated with face-centred oxygen atoms.

$SrFeO_3$ provides an interesting comparison to $LaMnO_3$ as it also crystallises in the $Pm\bar{3}m$ cubic perovskite structure, with lattice parameter a = 3.851(1) Å [72] . Mössbauer results show the iron ion exhibits Fe^{4+} electronic configuration [73], giving it the same valency of 4 electrons in the d-orbitals as Mn^{3+}.

The octahedral crystal field splitting, breaks the d-orbitals into two degenerate subshells. The d_{z^2} and $d_{x^2-y^2}$ form the higher energy e_g orbital, and the d_{xy}, d_{xz} and d_{yz} form the lower energy t_{2g} orbital. This gives two possible electron spin configurations, a low spin state $[Ar].t_{2g}\uparrow\uparrow\uparrow\downarrow$ or a high spin state $[Ar].t_{2g}\uparrow\uparrow\uparrow.e_g\uparrow$. The magnetic structure

of $SrFeO_3$ was determined by neutron diffraction to form a helical phase at $T_N = 134$ K, with a wavevector $k = (0.13, 0.13, 0.13)$ [74]. Neutron diffraction determined the expected ground state magnetic moment of the Fe to reach the high spin value. X-ray photoemission spectroscopy (XPS) combined with cluster-model configuration-interaction calculations performed by Bocquet *et al.*, have shown the high-spin configuration, $t_{2g}^3 e_g^1$ ground state to be stable [75]. With the high spin state, a cooperative Jahn-Teller effect is expected, as is the case in $LaMnO_3$ [76]. The high spin state, $t_{2g}^3 e_g^1$ is doubly degenerate, as there is a choice of d_{z^2} and $d_{x^2-y^2}$ orbitals. The Jahn-Teller effect is a distortion of the oxygen octahedra causing the degenerate e_g state to split, lowering the overall energy of the electron configuration. No evidence has been found for the existence of the cooperative Jahn-Teller effect, either static or dynamic in $SrFeO_3$ [73, 77]. Bocquet *et al.* [75] have used a $p - d$ charge-transfer cluster-model calculation to interpret the Fe $2p$ core level spectra. They found a large amount of charge is transferred along the Fe-O bond from the oxygen $2p$ band to the iron d orbitals. This results in a ground state dominated by the d_5L configuration rather than the d_4, explaining the lack of Jahn-Teller distortions present.

3.1.3 $SrFeO_{3-\delta}$ series

One method to investigate the effects of valency and crystal field splitting in these materials, is to reduce the oxygen content, introducing oxygen vacancies. In the case of $SrFeO_{3-\delta}$, these oxygen vacancies order, creating a family of materials with the formula $Sr_nFe_nO_{3n-1}$, with n = 1, 2, 4, 8, ∞, equivalently $SrFeO_{3-\frac{1}{n}}$. The phase diagram for $SrFeO_{3-\delta}$ is known to contain the 5 vacancy ordered structures separated by miscibility gaps [72]. The $n = \infty$ case returns our cubic perovskite.

When reducing the oxygen content, the $n = 8$ structure $Sr_8Fe_8O_{23}$ (alternatively written as $SrFeO_{2.875}$) forms. $Sr_8Fe_8O_{23}$ has a tetragonal structure $2\sqrt{2}a_c \times 2\sqrt{2}a_c \times 2a_c$ where a_c is the cubic perovskite lattice parameter, with space group $I4/mmm$ and lattice parameters a = 10.929(1) Å and c = 7.698(1) Å shown in figure 3.3(b) [72]. This unit cell contains 16 iron ions, 12 of which remain octahedrally coordinated, the other 4 lose an oxygen forming square-based pyramids.

Upon reducing the oxygen content further, the $n = 4$ phase forms. $Sr_4Fe_4O_{11}$, ($SrFeO_{2.75}$) adopts an orthorhombic C-centred unit cell $2\sqrt{2}a_c \times 2a_c \times \sqrt{2}a_c$ with space group $Cmmm$ and lattice parameters a = 10.974(1) Å, b = 7.702(1) Å, c = 5.473(1) Å [72]. The unit cell, shown in figure 3.3(c), contains 8 Fe ions, 4 octahedral and four square-based pyramids.

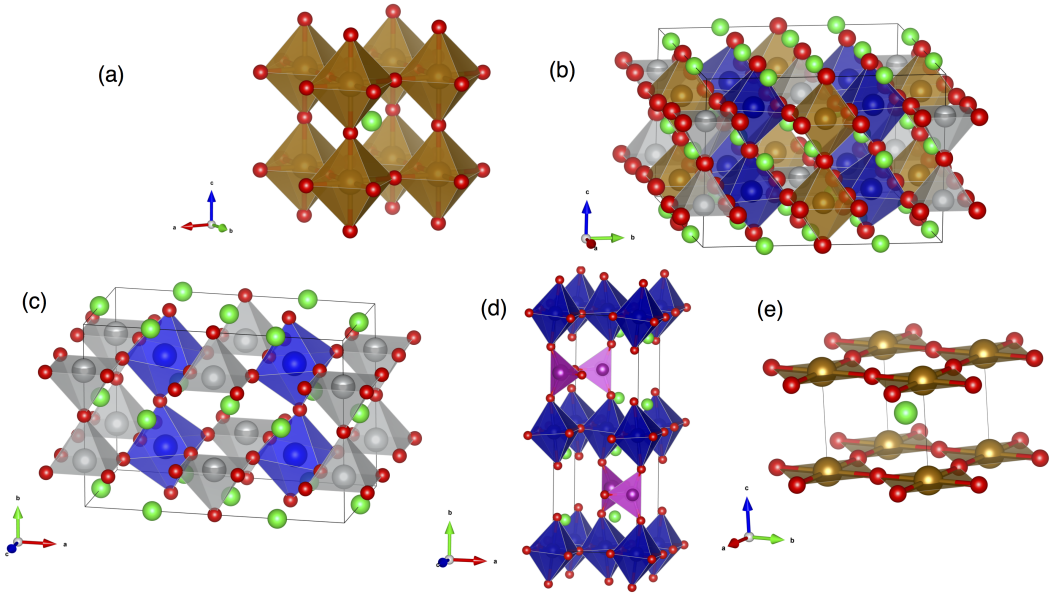

Figure 3.3: Crystal structures of members of the family $Sr_nFe_nO_{3n-1}$(a)$n = \infty$, (b)$n = 8$, (c)$n = 4$, (d)$n = 2$, (e)$n = 14$. Strontium atoms are shown in green. oxygen are shown in red, and iron is shown in brown, silver, blue and purple, to illustrate different oxygen coordinations.

The $n = 2$ compound $Sr_2Fe_2O_5(SrFeO_{2.5})$ forms the brownmillerite orthorhombic structure, $\sqrt{2}a_c \times 4a_c \times \sqrt{2}a_c$ figure 3.3(d) [78]. This consists of alternating layers of octahedra and tetrahedra. Finally in the $n = 1$ compound, $SrFeO_2$, adopts a tetragonal structure with space group $P4/mmm$ and lattice parameters $a = 3.99107(3)$ Å and $c = 3.47481(5)$ Å [79, 80]. $SrFeO_2$ contains planes of square planar FeO_4 shown in figure 3.3(e), and can be related to the cubic perovskite phase 3.3(a) with two oxygen vacancies, reducing the octahedra into square planar geometry.

$Sr_8Fe_8O_{23}$ has three inequivalent iron sites. In the unit cell, four iron ions (Fe_1) sit at the 4*e* Wyckoff site, surrounded by five oxygen in a square-based pyramid geometry. Of the remains 12 octahedra, eight (Fe_2) are tilted sitting at the 8*f* Wyckoff site, forming zig-zag lines of tilted octahedra in the *c*-direction. The remaining 4 octahedra (Fe_3) at the 4*d* Wyckoff site are nearly regular, with four Fe-O bonds 1.912 Å and two 1.925 Å, compared to the $SrFeO_3$ compound with six Fe-O bonds all 1.926 Å. Mössbauer spectra measured by Adler *et al.* [81] at room temperature show two iron valence states Fe^{4+} in the high spin configuration and $Fe^{3.5+}$ of a 1:1 ratio. Bond strength sums calculated for

all three iron sites show the tilted octahedra have a lower valency, with Fe^{4+} assigned to the Fe_1, square-based pyramids and Fe_3 regular octahedra, and $Fe^{3.5+}$ to the Fe_2 tilted octahedra site. Mössbauer measurements taken by Takano *et al.* [82] show that the $Fe^{3.5+}$ state is due to fast electron transfer between Fe^{3+} and one-third of the Fe^{4+} ions relative to 10^{-8} s characteristic Mössbauer time frame. At 4 K the Mössbauer results show two iron valencies of Fe^{3+} and Fe^{4+} in a ratio of 1:3. [72, 81, 82]. This has been interpreted [82] as the formation of charge order of Fe^{3+} and Fe^{4+} on the Fe_2 sites, or at least a slowing of the charge transfer process to a rate on a timescale larger than 10^{-8} s, the characteristic timescale of the Mössbauer process.

Due to the miscibility gaps in the phase diagram, of $SrFeO_{3-\delta}$, there has been difficulty in achieving single-phase samples in the literature. Bulk measurement techniques, such as magnetic susceptibility, resistivity, and Mössbauser spectroscopy, are insensitive to contributions from different phases, and average over the whole sample. Susceptibility and resistivity measurements reported in reference [1], show markedly different behaviour for different oxygen content, see figure 3.4. Of their three samples, $SrFeO_3$ was reported to consist entirely of the cubic perovskite phase; $SrFeO_{2.85}$ is a mix of 80% tetragonal $n = 8$, and 20% cubic perovskite; and $SrFeO_{2.81}$ is 70% tetragonal $n = 8$ and 30% orthorhombic $n = 4$. The cubic phase is metallic, and its resistivity increases with temperature. The two oxygen-deficient samples show a metal insulator transition at low temperatures, interpreted to be characteristic of the tetragonal phase.

Magnetic structure determination by Reehius *et al.* [83] used neutron diffraction on three multi-phase samples, with oxygen deficiencies identified as $\delta = 0.03$, 0.13,0.23. The $\delta = 0.13$ which is closed to the stoichiometric n=8 (δ=0.125) oxygen content was identified as a mixture tetragonal $n = 8$ and cubic $n = \infty$ of proportions 74(2):26(2). Across the $SrFeO_{3-\delta}$ phase diagram between $\delta = 0 - 0.23$ they identified seven distinct magnetic phases. Of these seven magnetic phases, four were assigned to host lattices. The helical phase belongs to the cubic $\delta = 0$ phase with a wavevector $k = (0.13, 0.13, 0.13)$ and transition temperature of $T_N = 134$ K [1]. A second helical phase with wavevector $k = (0.2, 0.2, 0.2)$ and transition temperature $T_N = 75$ K was assigned to the $\delta = 0.125$ tetragonal phase. A spin density wave with wavevector expressed in the cubic basis as $k = (0.17, 0.17, 0.17)$ and transition temperature $T_N = 75$ K was also assigned to the $\delta = 0.125$ tetragonal phase. An antiferromagnetic phase was assigned to the orthorhombic $\delta = 0.25$ phase, with a transition temperature of $T_N = 232$ K, and a periodicity commensurate with

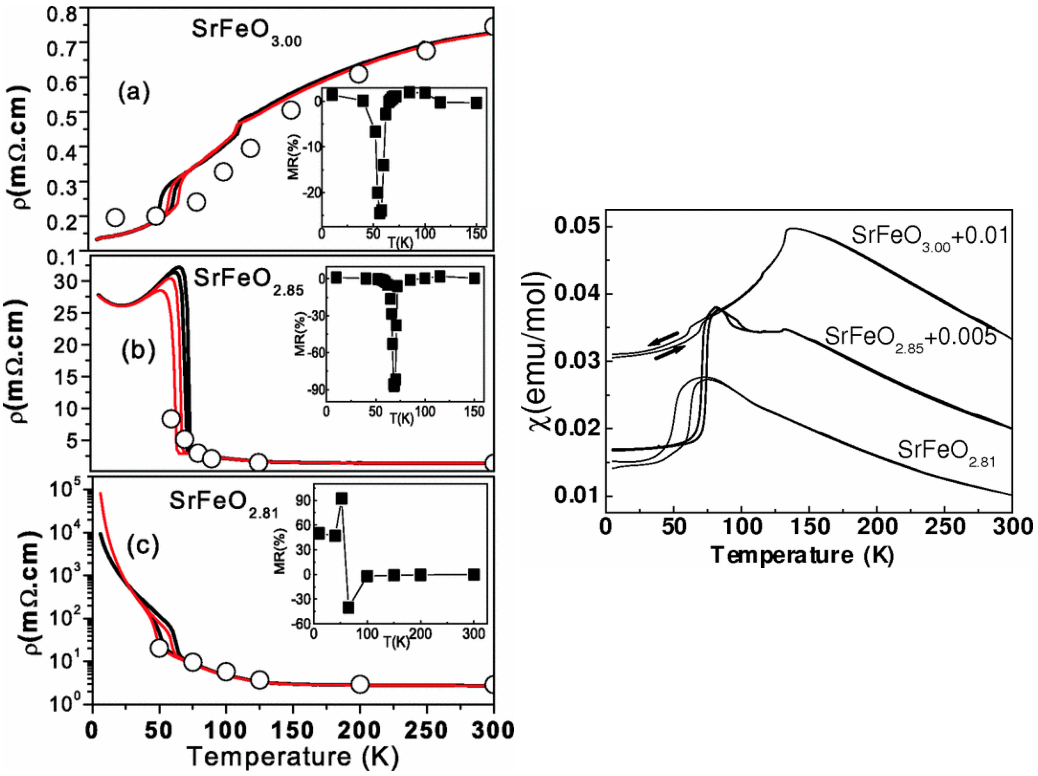

Figure 3.4: (a)-(c) Resistivity measurements on heating and cooling for zero field (black) and 9 T field (red) for three samples of different oxygen deficiencies (a) $\delta = 0$, (b) $\delta = 0.15$ and (c) $\delta = 0.19$. (Inset (a)-(c)) Magnetoresistance (MR) plots for the three samples. In this case, MR is defined as $\frac{\rho(H=9\ T)-\rho(H\ =\ 0)}{\rho(H\ =\ 0)}$. (d) Magnetic susceptibility, measure on field cooling and warming with a field of B = 1 T. The three samples have been shifted by 0, 0.005 and 0.01 emu/mol for clarity. Reprinted from reference [1].

the orthorhombic unit cell.

The last three phases were found to have magnetic wavevectors expressed in the cubic lattice as $(0.3, 0.3, 0.75)$, $(0.79, 0.79, 0)$ and tetragonal lattice $(0, 0, 1/2)$, but were not able to be associated with a particular crystallographic phase with transition temperatures 65(4) K, 110(4) K and 60(5) K respectively.

3.2 Experiment

A single crystal of $SrFeO_{3-\delta}$ was grown by the floating zone method [84] by our collaborators S. H. Lee, C. H. Du at Tamkang University, Taiwan. The crystal structure was confirmed by powder diffraction. A portion of the single crystal, was cut and finely ground.

The powder diffraction study was performed on beam line BL01C2 at the NSRRC synchrotron in Taiwan, using 17 keV incident x-rays. The results confirmed that the tetragonal ($I4/mmm$) was the majority phase with lattice parameters $a = b = 10.3931$ Å and $c = 7.7$ Å, shown in 3.3(b). The reciprocal lattice vectors will be given in the tetragonal basis unless stated otherwise.

A magnetic transport study was under taken at Tamkang university. Resistivity and susceptibility measurements were performed on this sample using a Quantum Design Physical Properties Measurement System PPMS. The sample's alignment was found using an in-house x-ray diffractometer. The sample was cut into a thin slab, and 200 nm thick gold contacts were deposited using high energy sputtering. Magnetic susceptibility was measured both field cooled (FC) and zero-field cooled (ZFC) from 300 K to 10 K. The resistivity was measured at a rate of 2 K a minute, on both cooling and warming, in zero field and a 9 T magnetic field.

A second piece of the sample was aligned for synchrotron experiments using their in-house x-ray diffractometer and a surface prepared with a [001] direction normal. The sample had dimensions $2\times3\times1$ mm^3. High energy x-ray diffraction experiments were performed at hard x-ray beamlines BL07 and BL12B2 at the NSRRC, Taiwan and SPRING-8, Japan. The incident x-ray energy was tuned to 10 keV by a pair of Si(111) single crystals and the scattered beam was analysed by LiF(400) analyser crystal.

A resonant x-ray diffraction experiment was performed on soft x-ray beamline EPU 05B3 at the NSRRC. By tuning the incident energy to the iron $L_{II/III}$ and oxygen K absorption edges, the resonance exchange scattering process provides sensitivity to the magnetic structure, allowing magnetic diffraction peaks to be measured. EPU 05B3 has a in-vacuum two circle diffractometer in a horizontal scattering setup. The diffractometer operates at a vacuum of 6.6×10^{-8} mbar. A Janis ST-400 UHV cryostat was used with a liquid helium generator, allowing a stable base temperature of 20 K for the experiment. The detector arm has both a photodiode detector and a channeltron charge detector. The channeltron is used in conjuncture with a thin film of CsI. The CsI absorbs the scattered photons and emits a large amount of secondary photons that the channeltron subsequently detects, allowing weak signals to be measured. The EPU 05B3 provides control over both the energy and polarisation state of the incident beam. Fluorescence spectra were measured using the photodiode to locate the iron $L_{II/III}$ and oxygen K absorption edges. The polarisation state of the incident beam set up to be parallel (π-polarised), perpendicular

(σ-polarised), circular left and right with respect to the scattering plane. The sample was mounted with the [0, 0, 1] surface normal, and the a-axis perpendicular to the scattering plane. The channeltron was used to measure the magnetic diffraction peaks.

3.3 Results

All experiments were carried out on two samples taken from the same growth boule. The transport measurements were carried out on one sample, and all the x-ray experiments were carried out on the other sample. Powder diffraction measurements carried out on a peice taken from the boule reveal the sample to be made up of a majority phase of the $n = 8$, tetragonal $Sr_8Fe_8O_{23}$, with lattice parameters $a = b = 10.3931$ Å and $c = 7.7$ Å. The powder diffraction showed $Sr_8Fe_8O_{23}$ to be the majority phase with a 5% unidentified phase, resulting in $\delta = 0.125 \pm 0.007$.

3.3.1 Transport measurements

The resistivity was measured along the [1,1,0] and [0,0,1] directions on both cooling and warming, in zero field and an applied field of 9 T, resulting in 8 measurements in total. Figure 3.5 shows the temperature dependence of the resistivity. The sample shows semiconductor behaviour, with resistivity increasing at lower temperatures, changing by four orders of magnitude between 10 K and 300 K. Qualitatively the resistivity shows similiar behaviour to a mixed phase sample reported by Lebon *et al.* [1] to have a $\delta = 0.19$, reproduced in figure 3.4. This disparity between the oxygen deficiency shows the need for single phase samples to get useful information from bulk transport measurement. The resistivity along the [110] direction is consistently higher over the entire measured temperature range. A transition in the resistivity can be seen around 115-120 K, below which the resistivity increases rapidly with decreasing temperature. This transition is more pronouced in the [110] than the [001] direction. There is a further transition in the resitivity around 60 K. This transition is more apparent in the [001] direction. The transition around 60 K shows thermal hysteresis, with measurements on warming having higher resistance. The thermal hysteresis has a width of 11 K.

The effect of an applied magnetic field is shown in figure 3.5 (bottom). The applied field has no effect on the resistivity until below the transition at 120 K. The effect of the applied field is easier to see in figure 3.6 which shows the magnetoresistance. Magnetoresistance has been defined as resistance in the applied field minus resistance in zero field,

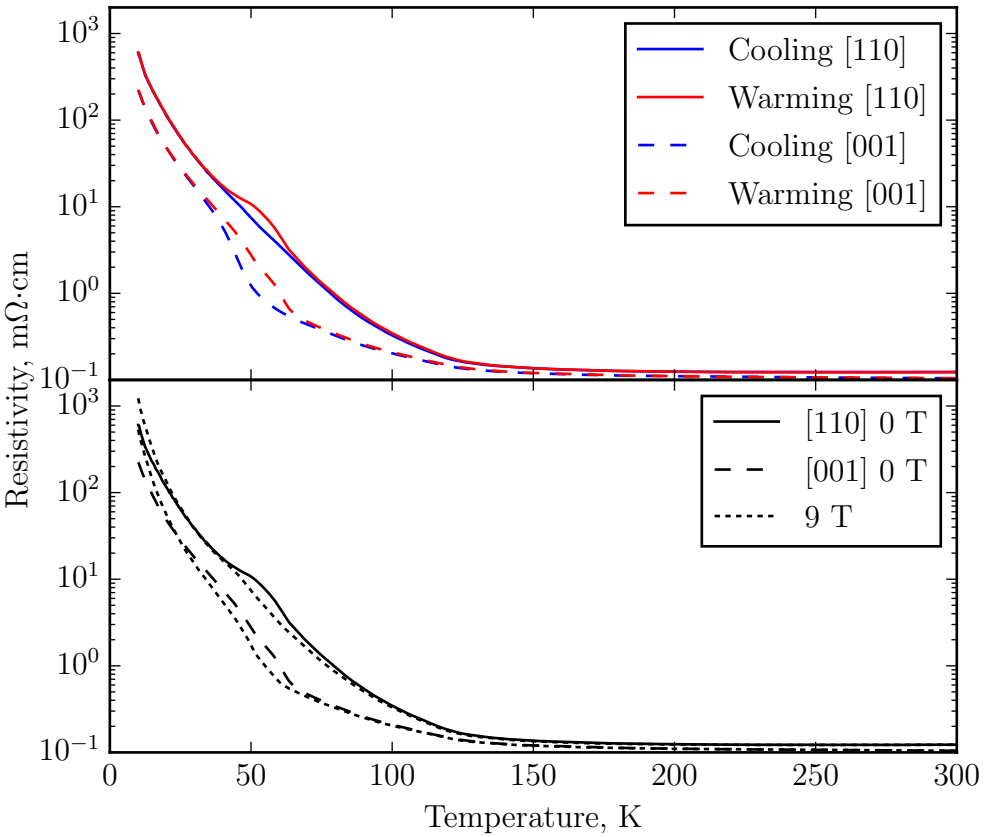

Figure 3.5: The resistivity was measured along the *c*-axis and the *ab*-plane for both warming and cooling and in zero-field and an applied field of 9 T.

all divided by the resistance in zero field.

$$MR = \frac{\rho_H(T) - \rho_0(T)}{\rho_0(T)} \tag{3.1}$$

By defining the magnetoresistance using the above formula, the negative magnetoresistance is limited to -100%, whilst positive magnetoresistance is uncapped. The system shows magnetoresistance behaviour along both the [110] and [001] axis. At the base temperature of 10 K the system exhibits positive magnetoresistance along both crystallographic directions, of around 140%. Upon warming the magnetoresistance drops and becomes negative around 45%. Further warming the magnetoresistance returns to zero. The exact transition temperatures depends on the measurement direction, and whether the

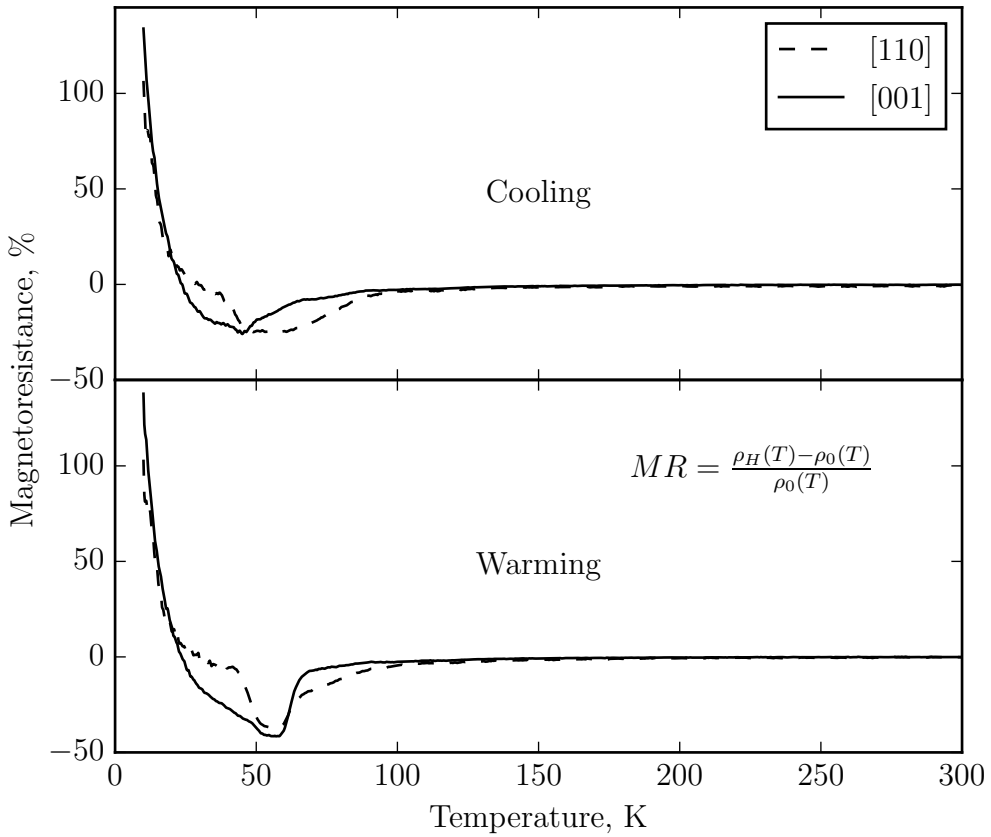

Figure 3.6: Magnetoresistance, defined by equation $MR = \frac{\rho_H(T)-\rho_0(T)}{\rho_0(T)}$. Magnetoresistance measured along the *c*-axis and *ab* plane on cooling (top) and warming (bottom).

measurement was performed upon warming or cooling.

The negative magnetoresistance effect appears along the [110] direction at the first transition in the resistivity, around 120 K, whilst the magnetoresistance along the [001] direction does not appear until the second transition at 60 K.

3.3.2 Magnetic Susceptibility measurements

Magnetic susceptibility, figure 3.7, shows an antiferromagnetic transition around 75 K. Above this transition the system exhibits paramagnetic-like behaviour with an increasing magnetic susceptiblity upon cooling. The behaviour is not true paramagnetism, as the magnetic susceptibility of paramagnetism as described by the Curie Weiss law is expected to be linear when the inverse susceptibility is plotted. The red trend line in figure 3.7

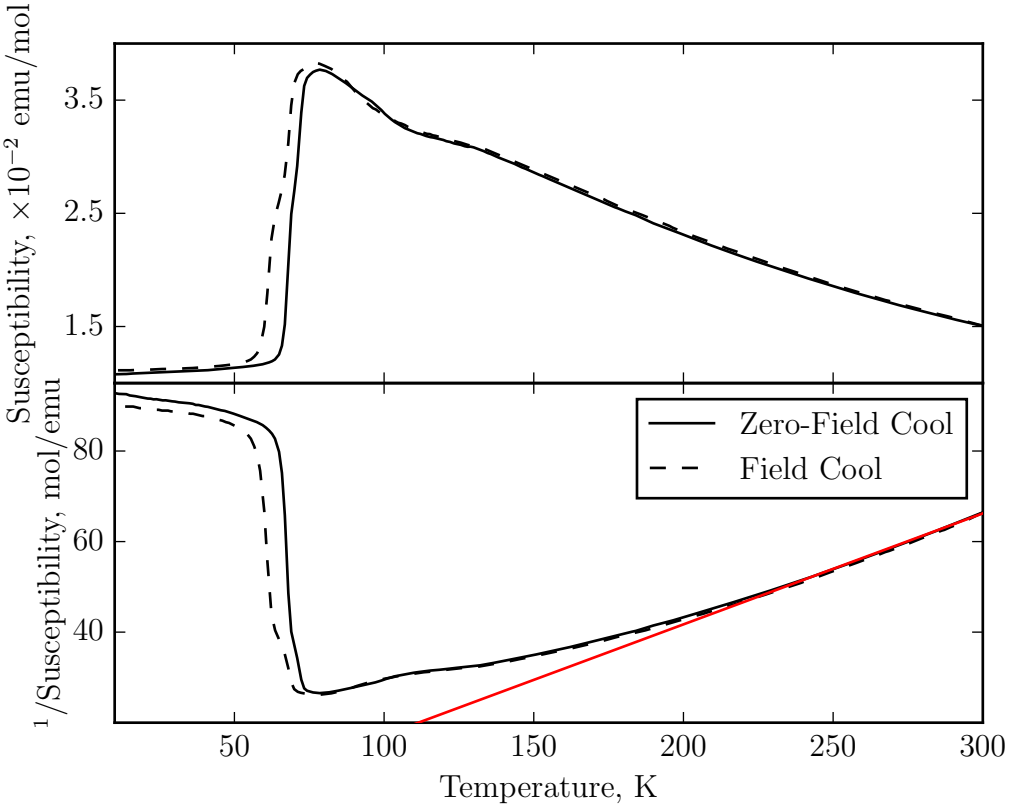

Figure 3.7: (top) Magnetic susceptibility measured on field-cooling and zero field-cooling.(bottom) The reciprocal of susceptibility. Paramagnetic behaviour is indicated by a straight line. The red line indicated a linear trend, indicating where the susceptibility departs from the Curie Weiss behaviour.

shows that the inverse susceptibility departs from a linear relationship with temperature below 240 K.

3.3.3 High Energy X-ray Diffraction

X-ray diffraction experiment was carried out at 10 keV, with the sample mounted with the c-axis along the scattering vector. A LiF analyser crystal was used to increase the resolution of the instrument. The (0,0,4) Bragg peak was found and high resolution $\theta - 2\theta$ scan were measured as a function of temperature. The $\theta - 2\theta$ peaks were analysed using a Lorentzian-Squared function, and the centre and width extracted. Figure 3.8 shows the results from the temperature dependence of the (0,0,4) Bragg peak. The centre position

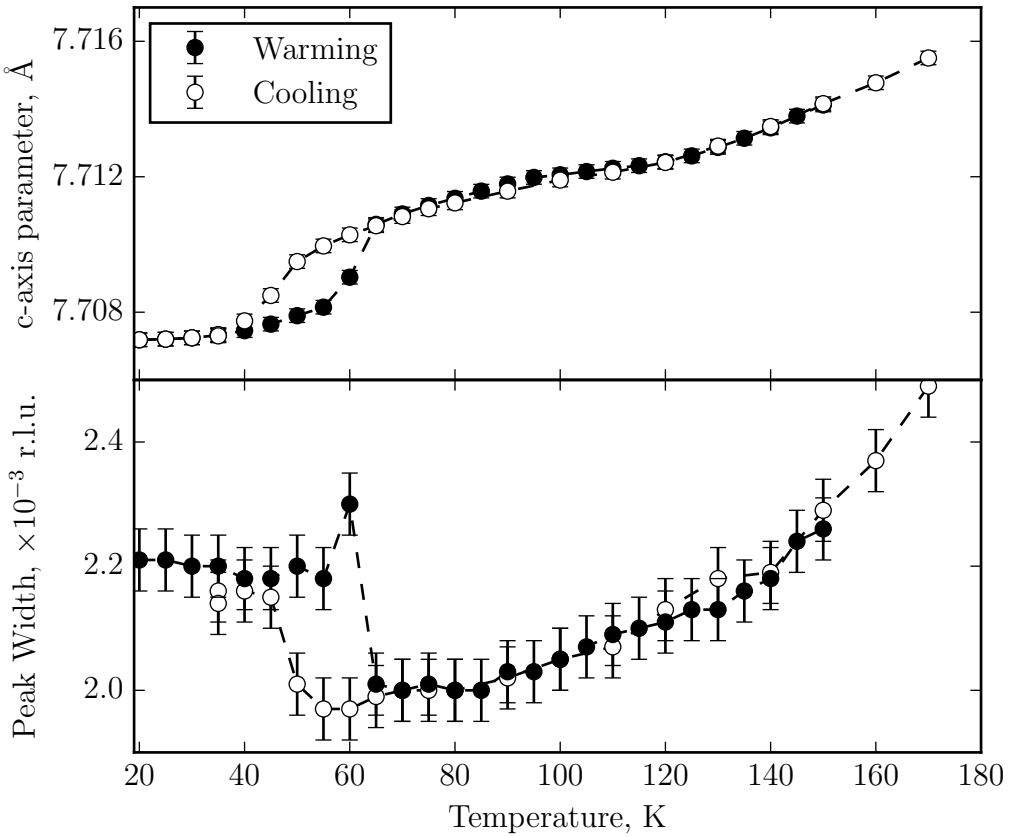

Figure 3.8: Temperature dependence of $(0, 0, 4)$ Bragg peak. (Top) Change in c lattice parameter on warming (closed circles) and cooling (open circles). (Bottom) Temperature dependence of width of $(0, 0, 4)$ Bragg peak on warming and cooling.

of the $\theta - 2\theta$ peak can be used to calculate the c-lattice parameter, and is shown in the top of figure 3.8. The width is shown the bottom of figure 3.8.

The c-axis parameter decreases from 7.7155 Å to 7.7070 Å upon cooling from 300 K to 20 K. A transition is observed around 50 - 65 K, with thermal hysteresis on warming and cooling. The width of the (0,0,4) Bragg peak decreases on cooling until the transition at 50 - 65 K, where the width increases to 2.2×10^{-3} r.l.u., On further cooling the width remains constant. The thermal hysteresis of this structural transition is also visible in the width.

A set of weak satellite reflections were also identified around Bragg peaks in the [0,0,L] direction. These satellite were found at positions (0,0,1.37), (0,0,2.63), (0,0,3.37),

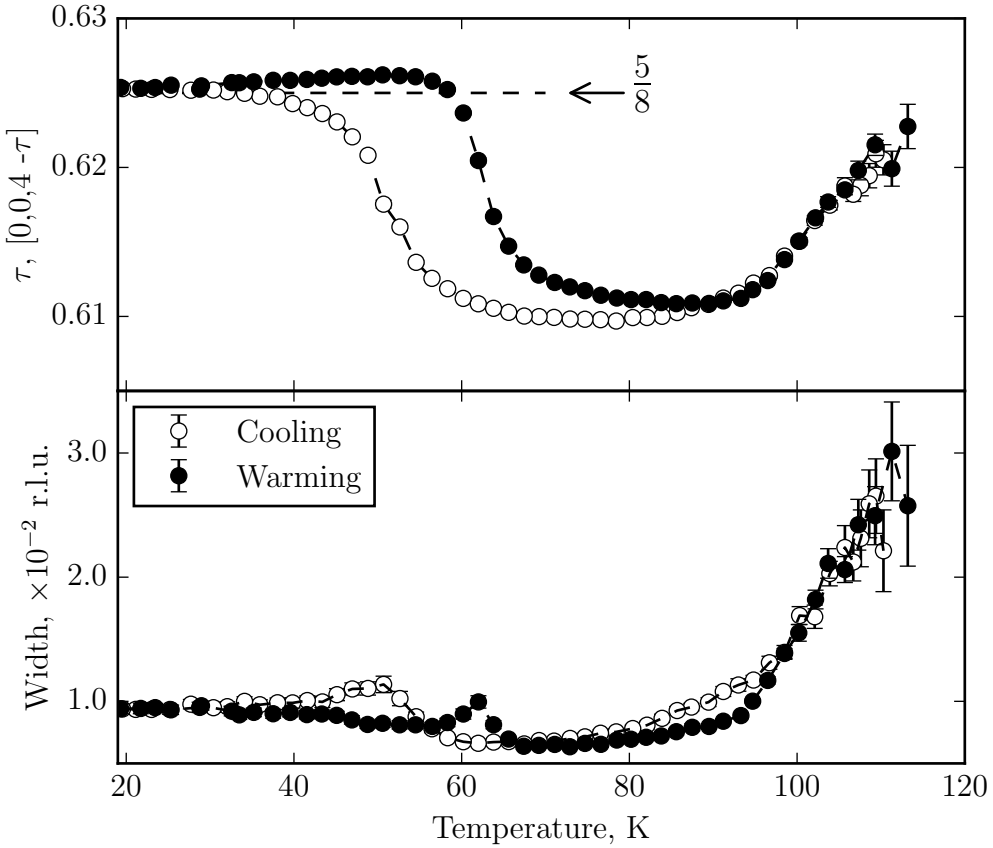

Figure 3.9: Temperature dependence of the $(0, 0, 4-\tau)$ structural satellite peak, on warming (closed circle) and cooling (open circle). (Top) Wavevector, τ of the $(0, 0, 4-\tau)$ satellite reflection. (Bottom) Width of the $(0, 0, 4-\tau)$ satellite reflection.

(0,0,4.63), (0,0,5.37), (0,0,6.63) *et cetera*. Due to the crystal symmetry of the structure only even Bragg peaks are expected along the $[0, 0, L]$ direction. The satellite peaks have been indexed as $(0, 0, L \pm \tau)$ where L is even and $\tau \sim 0.625$ at 20 K. The reciprocal space positions have been corrected for the change in c lattice parameter measured in figure 3.8.

High resolution $\theta - 2\theta$ scans were measured across the $(0, 0, 4-\tau)$ satellite reflection on both warming and cooling. The diffraction peaks were analysed with a Lorentzian peakshape, and the centre position and width extracted. Figure 3.9 shows the variation of wavevector and width of the satellite peak. The satellite peaks disappear at 115 K.

When the satellite reflections first appear at 115 K the wavevector takes an incommensurate value which varies with temperature. Upon cooling the wavevector linearly

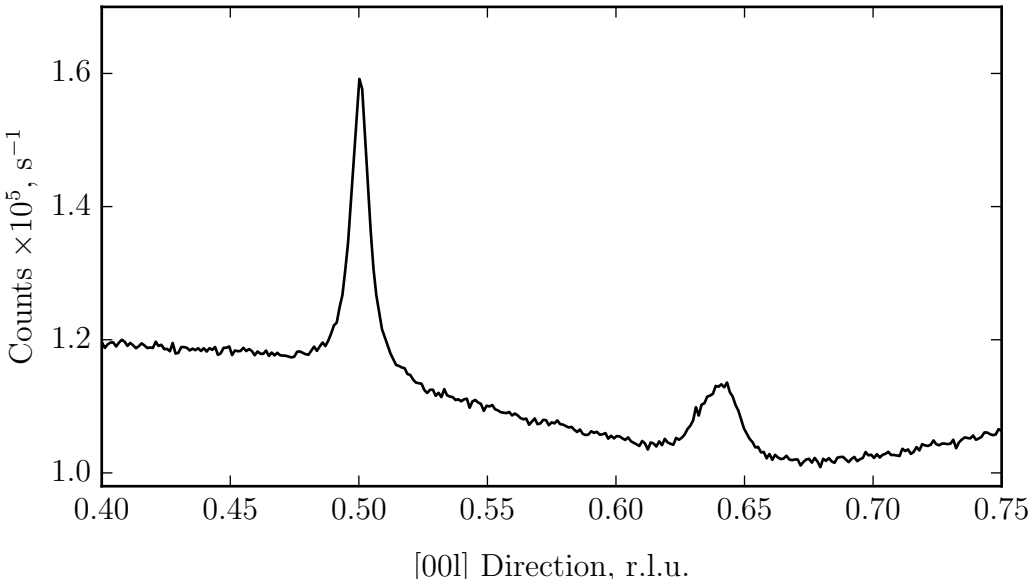

Figure 3.10: Reciprocal space scan along the [00L] direction at the Fe L_{III} with π incident polarised light.

decreases. The wavevector transitions from an incommensurate value to a higher commensurate value of $^5/_8$ around 60 K. This transition to a commensurate value shows thermal hysteresis, with a lower transition temperature on cooling than warming. The satellite peak has a width of 3×10^{-2} r.l.u. when it appears at 115 K, and quickly decreases to 1×10^{-2} r.l.u. The transition from incommensurate to commensurate wavevector is observed in the width, with a small increase in width. The 11 K hysteresis is apparent in the width, with the transitions occurring at 51 K and 62 K, on cooling and warming respectively.

3.3.4 Soft Resonant X-ray Diffraction

In order to further study the satellite reflections a resonant scattering experiment was carried out at the soft Fe $L_{\mathrm{II/III}}$ edges. The sample orientation was kept along the $[0, 0, L]$ direction. The EPU beamline 05B3 has control of the incident polarisation, but does not have the capabilities for post-scatter polarisation analysis.

The incident x-ray was tuned to the Fe L_{III} absorption edge. Figure 3.10 shows a scan along the $[0, 0, L]$ direction, performed at 20 K, with π incident light. Two peaks are present, one at (0,0,0.5) and another at (0,0,0.63) corresponding to the τ satellite peaks

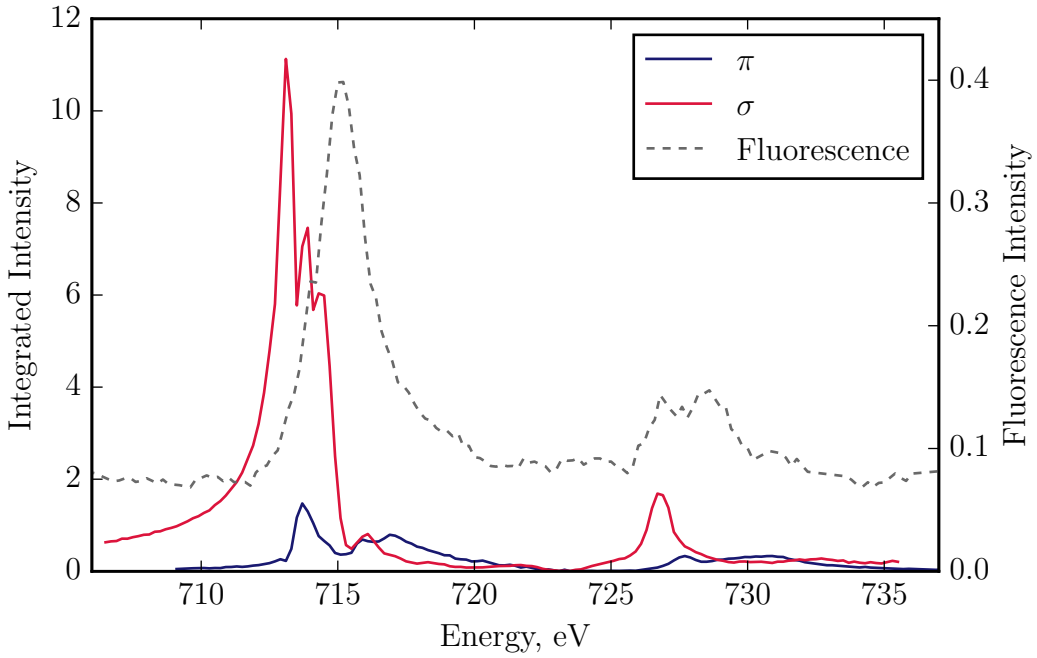

Figure 3.11: Resonance of the $(0,0,\tau)$ peak at Fe $L_{II/III}$. σ incidence light, shown in red, π incidence shown in blue.

measured non-resonantly.

Energy resonances were measured across the both peaks by measuring high resolution $\theta-2\theta$ scans as a function of incident energy. The resonances were measured with incident polarised light in the σ-, π-, circularly left-, and right- polarisation channels. Figures 3.11 and 3.12 show the resonances for the $(0,0,\tau)$ and $(0,0,0.5)$ peaks respectively. For both cases the circularly left and right channels did not show any differences, and have not been shown on the figures. For the $(0,0,\tau)$ reflection the diffraction in the σ-channel is seven times as intense as that in the π-channel. The σ- and π- channels show different resonant structures. This is suggestive of different origins to the scattering in the different channels. The resonance of the $(0,0,0.5)$, figure 3.12, shows the same structure in both channels. The π-channel is also four times more intense than the σ-channel.

The sample was warmed up and the $(0,0,\tau)$ disappeared at 115 K, confirming it to be the same origin as the non-resonant satellite peaks. A more detailed temperature dependence was carried out on the $(0,0,0.5)$ resonant peak. High resolution reciprocal

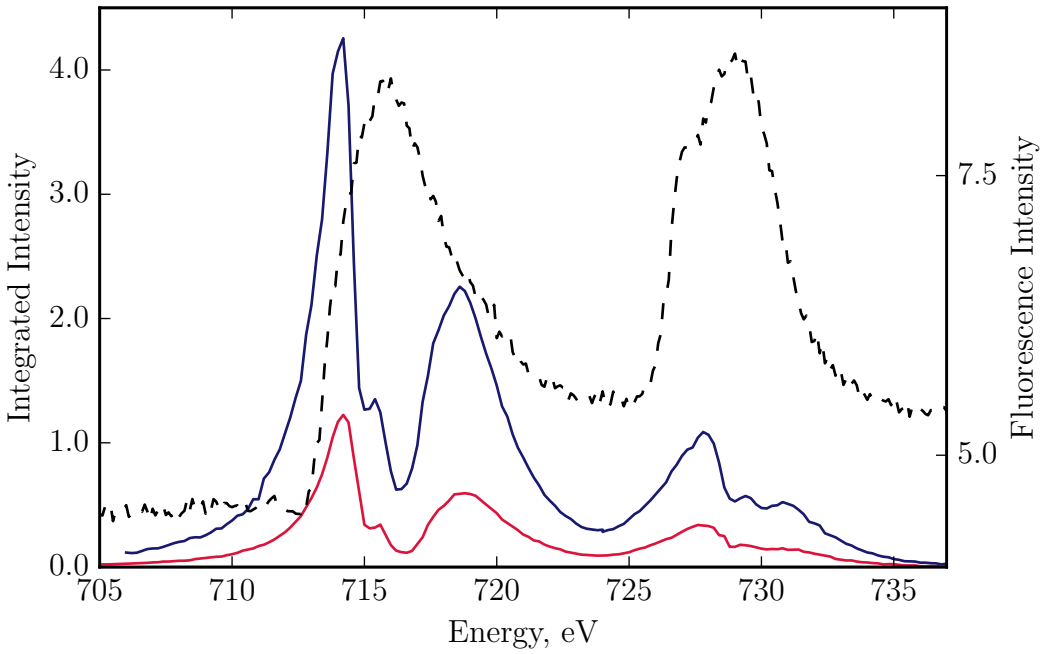

Figure 3.12: Resonance of the $(0, 0, 0.5)$ peak at Fe $L_{\text{II/III}}$. σ incidence light, shown in red, π incidence shown in blue, fluorescence shown by dashed line.

space scans were carried out in the $[0, 0, L]$ direction, and analysed with a Lorentzian-Squared peak profile. Figure 3.13 shows the temperature dependence of the $(0, 0, 0.5)$ reflection. Measuring on warming the reflection disappears around 72 K. Fitting the integrated-intensity of the peak with a critical scattering function, shown in figure 3.13 (top), refined the transiton temperature to $T_N = 71.8 \pm 0.01$, with a $\beta = 0.41 \pm 0.06$. The width, figure 3.13 (bottom), stays constant with temperature around 0.5×10^{-2} r.l.u. until the sample is warmed to a temperature around 55 - 60 K, when the widths begins to increase until the peak disappears.

In order to examine the critical behaviour around the transition, the reduced temperature was plotted against the normalised intensity and shown on a log-log plot, figure 3.14. A straight line is expected with a gradient of 2β and an intercept of zero. The fit of a straight line to the log plot results in a $\beta = 0.410 \pm 0.003$. The fit was performed using seven data points within 6 K of the transition, and the critical linear behaviour continues to 40 K.

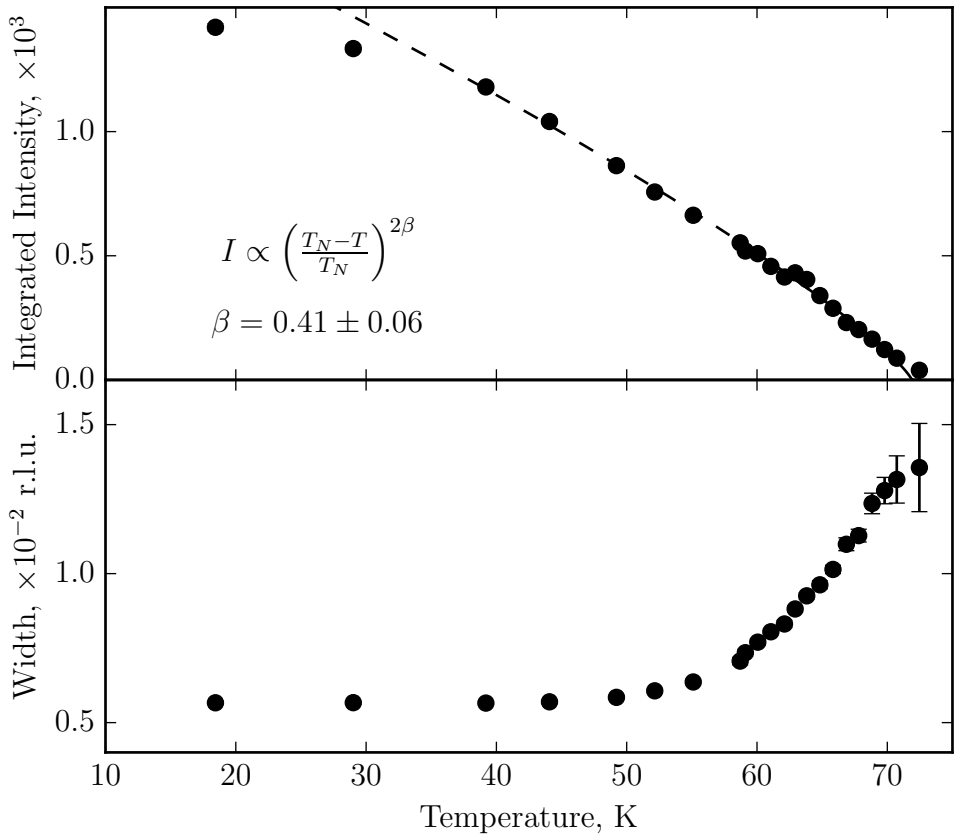

Figure 3.13: Temperature dependence of the $(0, 0, 0.5)$ at the Fe L_{III} edge in the π incidence polarisation channel. Reciprocal space scan analysed with a Lorentzian-squared peakshape (top) Integrated intensity (bottom) width. A critical scattering function has been fitted to the intensity. The fit results in a transition temperature of 71.8 K and $\beta = 0.41 \pm 0.06$.

The $(0, 0, 0.5)$ reflection was found to resonate at the oxygen K edge. Figure 3.15 shows the results of high-resolution $\theta - 2\theta$ as a funtion of energy across the oxygen K absorption edge. The resonance shows two separate features, one below the edge and one above the edge. The oxygen resonance was found only in the π-incident channel, and not the σ channel.

Temperature dependence of the $(0, 0, 0.5)$ reflection at the oxygen K edge was measured at 529.3 eV, with π-incident light. Due to higher harmonic energies present at the oxygen edge, contributions from the $(0, 0, 2)$ Bragg peak appear at the same position as

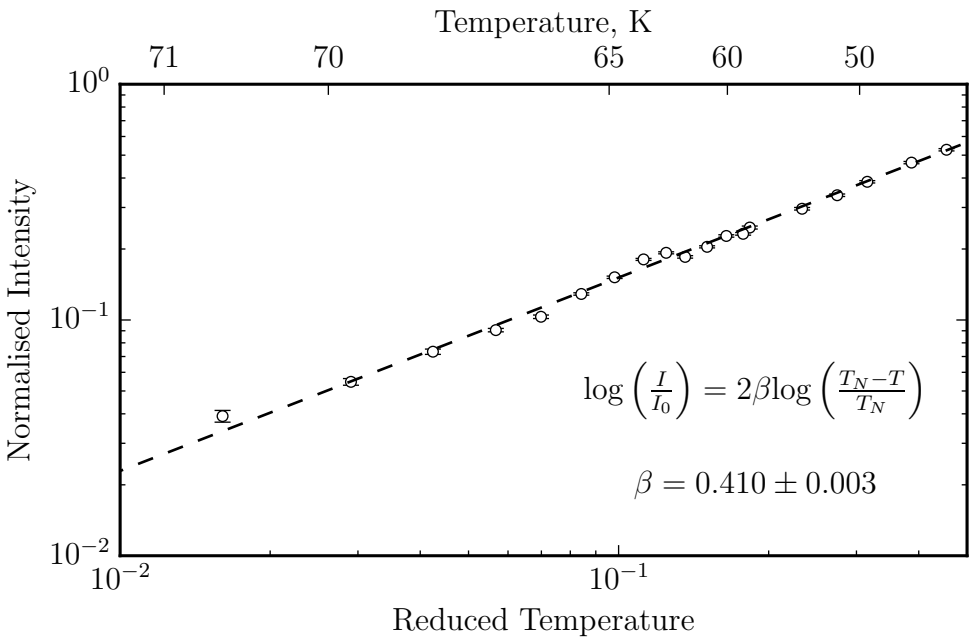

Figure 3.14: Temperature dependence of the intensity of the $(0, 0, 0.5)$ at Fe L_{III} edge. A log-log plot has been used to highlight the critical scattering. A straight line with an intercept of zero, results in $\beta = 0.410 \pm 0.003$.

the $(0, 0, 0.5)$ on resonance. The diffraction signal did not disappear at the transition temperature, but the resonant contribution disappeared. The width of the diffraction peak from the Bragg reflection is an order of magnitude narrower than the satellite peak. It is possible to extract the resonance satellite peak by fitting the contribution from a non-resonant Bragg peak and resonant satellite peak, using two Lorentzian-squared functions with different widths.

Figure 3.16 shows the temperature dependence of the intensity (top) and width (bottom) at the oxygen K edge. The width shows similar behaviour to the Fe L_{III} resonance, with the reflection having the same width. Fitting a critical scattering function results in $\beta = 0.47 \pm 0.01$, which is within error of the value at the Fe L_{III} edge. The transition temperature was found to be around 68 K, which is 4 K below the transition at the Fe L_{III}edge.

The critical scattering behaviour at the oxygen K edge is more clearly seen in the log-log plot in figure 3.17. The errors are larger at the oxygen edge as the resonance

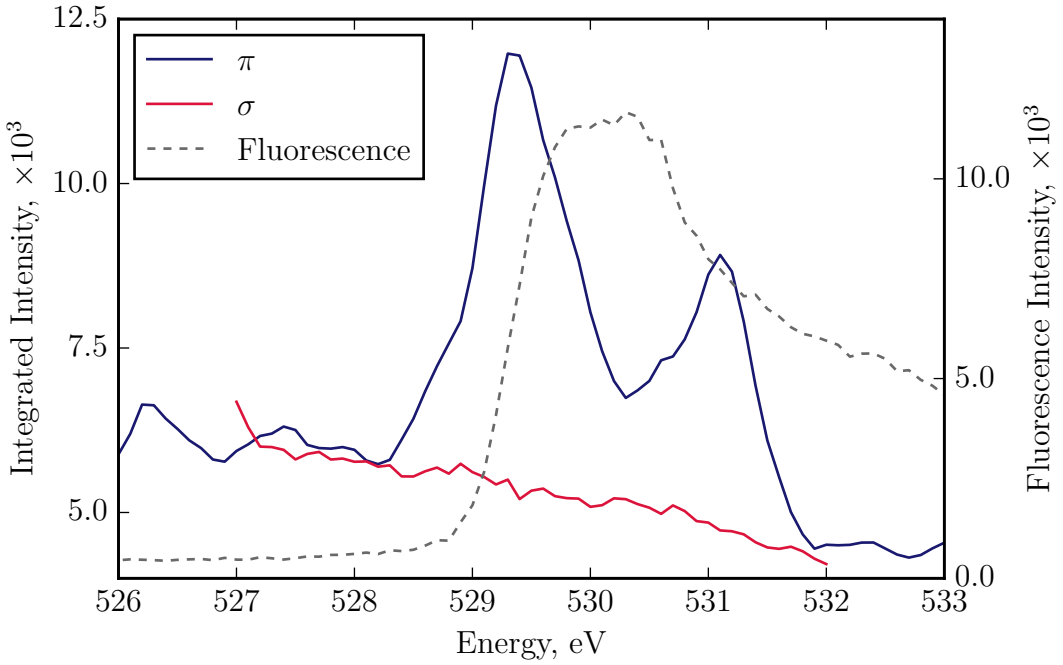

Figure 3.15: Resonance of the $(0, 0, 0.5)$ peak at the Oxygen K-edge. σ incidence light, shown in red, π incidence shown in blue, fluorescence shown by dashed line.

enhancement is very weak compared to the Fe L_{III} edge. The linear fit results in $\beta = 0.45 \pm 0.01$.

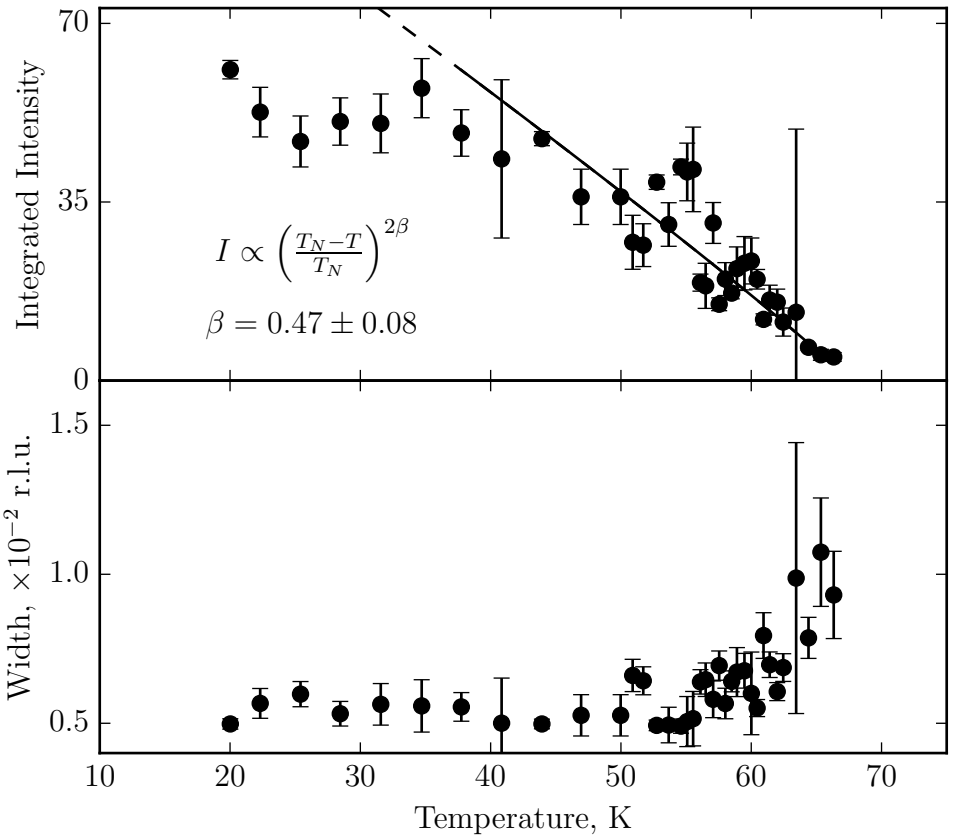

Figure 3.16: Temperature dependence of $(0, 0, 0.5)$ at the Oxygen K-edge in the π-incident polarisation channel. Reciprocal space scan analysed with a Lorentzian-squared peakshape (top) Integrated intensity (bottom) Width. A critical scattering function has been fitted to the intensity. The fit results in a transition temperature of 68.8 K and $\beta = 0.47 \pm 0.08$.

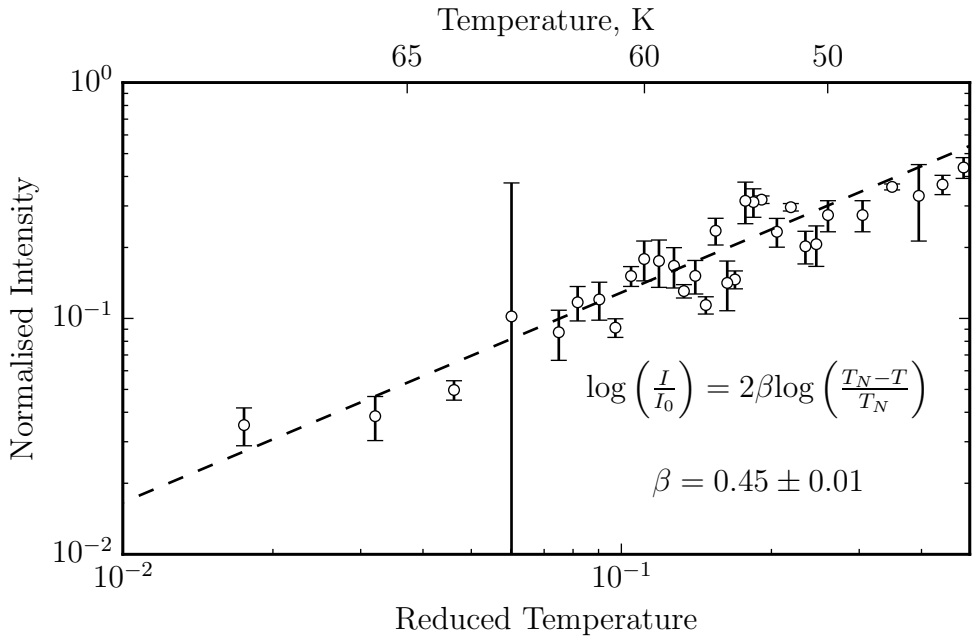

Figure 3.17: Temperature dependence of the intensity of the $(0, 0, 0.5)$ at the oxygen K-edge. A log-log plot has been used to highlight the critical scattering. A straight line with an intercept of zero, results in $\beta = 0.45 \pm 0.01$.

3.4 Discussion

Powder diffraction results show the sample used in this study to be 95% of $Sr_8Fe_8O_{23}$. The resistivity and x-ray diffraction results will be assumed to be a property of the $Sr_8Fe_8O_{23}$ system. As stated earlier this structure has three inequivalent iron sites, labelled earlier as Fe_1, Fe_2 and Fe_3. The sample shows typical semiconductor behaviour with resistivity decreasing on increasing temperature. The feature in the resistivity around 120 K below which the resistivity rises rapidly, is coincident with the appearance of the satellite peaks at positions $(0,0,\tau)$ away from Bragg peaks. The measurement of the (0,0,4) Bragg peak reveal a structural transition around 65 K. This structural transition is linked to the transition in the resistivity at the same temperature. Both the resistivity and the (0,0,4) Bragg peak show thermal hysteresis, suggesting the structural transition is not the driving order parameter, but have a common origin. Mössbauer spectroscopy has shown the Fe_2 tilted octahedra site undergoes a charge ordering transition from a valency of $Fe^{3.5+}$ to Fe^{4+} and Fe^{3+} [72,81,82]. Neutron diffraction experiments carried out by Reehuis *et al.* has associated this charge ordering with a structural transition at 75 K [83]. Due to an increase in the width of peaks above 130° the neutron powder diffraction study determined the symmetry lowered from the tetragonal *I4/mmm* to a monoclinic *I2/m* space group. The lowering of the space group splits Fe_2 into two inequivalent sites, which has been interpreted as the Fe_2 site charge ordering. Neutron diffraction is insensitive to the ion valency, and is not usually used to measure charge ordering, but differing Fe-O bond lengths were used to imply charge ordering. The transition in the *c*-axis parameter occurs 10 K below that measured by Reehuis *et al.*. Qualitatively, apart from the lower transition temperature, the change in lattice parameter agrees with that reported by Reehuis *et al.*. The appearance of structural satellites at 115 K as well as structural transition at 65 K implies a more complex charge ordering than a single structural transition.

The structural reflection has an incommensurate wavevector, which shows a lock-in transition to a high-order commensurate wavevector of $(0,0,5/8)$. This lock-in transition occurs concomitantly with the transition in *c*-axis lattice parameter and resistivity, at 65 K. The incommensurate to commensurate transition also shows the 11 K wide thermal hysteresis, suggesting this transition is not the driving order parameter. The x-ray experiment carried out at the Fe L_{III} absorption edge identified a resonant reflection with the same wavevector as the structural satellites. This resonance reveals the charge-order on the Fe_2

site has the same wavevector as the structural distortion. The polarisation analysis shows two different features in the resonance. The feature below the edge is predominantly in the σ channel, only 1% in the π-channel, and a larger feature at higher energy in both the π- and σ-channel. The reflection is at a scattering angle close to a detector angle, 2θ of 90°. Scattering from the charge-order is suppressed in π channel by a $\cos 2\theta$ dependence, and is expected to be less than 1%, which agrees with the lower energy peak. Without post-scatter polarisation analysis, it is not possible to confirm the other resonance, but due to the presence of the structural distortion having the same wavevector it is likely the anisotropic tensor of scattering is the origin.

The temperature dependence of the scattering was measured on warming, and shows the same behaviour as the structural satellite. The matching wavevectors of the charge-order and structural distortion indicates the structural distortion is brought about by the charge ordering. The formation of the charge-ordering is a localisation of charge carriers on the Fe_2 site. Localising charge carriers causes an increase in resistivity, similar to a metal-insulator transition. The formation of charge ordering, and consequent structural distortion with an incommensurate wavevector undermines a simple tetragonal to monoclinic distortion. A full structural determination is required accounting for the incommensurate satellite reflections. Charge ordering on a magnetically active site changes the magnitude of the magnetic moment, and is reflected in the paramagnetic region of the magnetic susceptibility data, by the change in gradient in figure 3.7 which accompanies the formation of charge order at 115 K.

It is clear from figure 3.9 that the charge order has three distinct phases. Upon first appearing the incommensurate wavevector decreases linearly with lowering temperature, in accordance with the behaviour of weakly localised charges [85]. In this region the width of the reflection is decreasing with cooling, as the charge ordering becomes more correlated. The temperature dependent incommensurate wavevector is a feature of the charge order being weakly correlated, and weakly localised upon its initial formation. When the charge order becomes more correlated and the peak width stabilises at 1×10^{-2} r.l.u., the incommensurate wavevector stabilises at (0,0,0.610). The charge-order stays at this wavevector until the lock-in transition occurs between 53 - 64 K. Figure 3.9 shows the lock-in transition is a sharp second order transition, as the reflection has been measured at incommensurate values between 0.610 and $^5/_8$, but also shows thermal hysteresis showing the charge-order is not driving the order parameter. The lock-in transition of the

charge-order to the commensurate wavevector is accompanied by the phase becoming less correlated.

For the cubic perovskite parent compound $SrFeO_3$, neutron [74] and x-ray photoemission spectroscopy (XPS) [75] have shown the magnetic moment takes the high spin configuration $t_{2g}^3 e_g^1$. As a consequence, a cooperative Jahn-Teller effect is expected to occur, but has not been observed. Modelling of the $2p$ core spectra has shown a large amount of charge transfer along the Fe-O bond from the oxygen $2p$ band to the iron 3d orbital [75]. The ground state of $SrFeO_3$ is dominated by a d_5L configuration, explaining the lack of Jahn-Teller distortion. In $Sr_8Fe_8O_{23}$, the charge ordering is known to occur on the Fe_2 site. The Fe_2 sites form a zig-zag chain along the c direction, where adjacent atoms share an oxygen. In the ab plane the Fe_2 atoms do not share oxygens with one another, but with Fe_1 and Fe_3 sites. Of the six oxygen around the Fe_2 atom the Fe-O bond along the c direction, shared between adajacent Fe_2's is the shortest [83]. Charge ordering is likely to occur via a charge transfer hybridisation along this Fe-O bond. The high-order commensurate wavevector of $(0, 0, 5/8)$ precludes a simple model of an arrangement Fe^{3+} and Fe^{4+}. The magnitude of the charge-order cannot be extracted from the x-ray diffraction, but Mössbauer studies [1, 81] show the valency of the Fe_2 site changes from $Fe^{3.5+}$ to Fe^{3+} and Fe^{4+} at 4 K.

The Mössbauer process has a characteristic time-scale of 10^{-8} s. The observed valency of $Fe^{3.5+}$ at room temperature, has been suggested as due to fast electron transfer between Fe^{3+} and Fe^{4+} relative to 10^{-8} s [82]. The appearance of Fe^{3+} and Fe^{4+} at 4 K is a slowing down of the electron transfer. If the charge-order is due to a cooperative charge transfer phenomena, it is expected to be through the Fe-O bond. A large amount of hybridisation is expected between the Fe $3d$ and O $2p$ bands.

The negative magnetoresistance, figure 3.6, along the [0,0,1] direction occurs at the incommensurate-commensurate charge order transition, whilst the magnetoresistance along the [1,1,0] direction appears with the formation of the charge-order at 115 K. This is similar to the magnetoresistant manganite, $La_{0.5}Ca_{0.5}MnO_6$, where a commensurate-incommensurate charge-order transition has been reported [86, 87]. In this case a first-order ferromagnetic to antiferromagnetic transition was reported to relate to an incommensurate to commensurate charge-order transition.

The appearance of the $(0, 0, 1/2)$ resonant peak at 80 K, co-incident with the antiferromagnetic transition in the magnetic susceptibility, suggests a magnetic origin. The

incident π-channel is four times larger than the σ-channel. For charge scattering the π channel is expected to be eight times weaker than the σ channel, so charge scattering can be ruled out. Distinguishing between magnetism, orbital ordering and ATS is difficult without the capability of post-scatter polarisation analysis. The framework for resonant magnetic scattering allows for the π-channel to be more intense than the σ-channel, as shown in equation 2.43, as the π-channel is sensitive to the entire moment, whilst the σ-channel is sensitive to the moment confined in the scattering plane. The coincident transition temperatures of the magnetic susceptibility and the $(0, 0, 1/2)$ satellite with the polarisation analysis is highly indicative of a magnetic origin of the $(0, 0, 1/2)$ reflection. A paramagnetic to antiferromagnetic transition, with the antiferromagnetic ground state having a supercell of $1 \times 1 \times 2$ of the crystallographic unit cell would give rise to the magnetic reflection at $(0, 0, 1/2)$. Assuming a electric dipole transition process for the magnetic resonance, the intensities for the π- and σ-incident channels for the experimental set-up can be expressed as the following.

$$\begin{aligned} I_\sigma &= z_b^* z_b \cos^2\theta + z_c^* z_c \sin^2\theta - \frac{1}{2}(z_b^* z_c + z_b z_c^*)\sin 2\theta \\ I_\pi &= z_b^* z_b \cos^2\theta + z_c^* z_c \sin^2\theta + \frac{1}{2}(z_b^* z_c + z_b z_c^*)\sin 2\theta + \quad z_a z_a^* \sin^2 2\theta \\ I_\pi &= I_\sigma + (z_b^* z_c + z_b z_c^*)\sin 2\theta + z_a z_a^* \sin^2 2\theta \end{aligned} \tag{3.2}$$

Where θ is the scattering angle and z_a,z_b, and z_c are components of the moment along the a, b, and c crystal lattice axes. Simple collinear structures along the a, b, or c direction can be can be ruled out, as these would give equal intensities in the σ- and π- channels or zero intensity in the σ channel. Neutron powder diffraction study reported by Reehuis *et al.* [83] identified seven magnetic structures in mixed phase samples of $SrFeO_{3-\delta}$. One magnetic structure had a wavevector of $(0, 0, 1/2)$ in the tetragonal basis, although they were unable to assign the magnetic structure to a specific host lattice. They were able to resolve the spin structure as a canted antiferromagnetic in the a-c plane, with a canting angle of 54° with respect to the c-axis. Due to the tetragonal unit cell, there is no difference between the a-c and b-c plane. The canted antiferromagnet can be described by a magnetisation vector $z = (i, 0, -0.24)$ or $z = (0, i, 0.24)$ for the other tetragonal domain. Due to the wavevector being along the c-axis both tetragonal domains contribute to the same reflections. The ratio of I_π/I_σ is expected to be between 1 and 8 depending on the

magnetic domains exposed to the x-ray beam. It is not possible to confirm or rule out the magnetic structure proposed by Reehuis *et al.*, without post-scatter polarisation analysis and azimuthal measurements.

The temperature dependence of width of the $(0, 0, 1/2)$ reflection, shows the transition to be second-order, starting as short-range spin correlations at 72 K and develops long-range order only at 60 K. X-ray diffraction is sensitive to long-range order, a local probe, such as muon spin relaxation, is necessary to study the short-range spin correlations.

The temperature dependence of the integrated intensity of $(0, 0, 1/2)$ reflection was fitted with a critical scattering function, which refined the transition temperature to 71.8 K and resulted in a $\beta = 0.410 \pm 0.003$. This value of β is larger than expected for Ising, $X-Y$ and Heisenberg which predict values of 0.326, 0.345, and 0.367 respectively.

The $(0, 0, 1/2)$ has multiple features in the resonance, figure 3.12. The σ- and π-channels show the same resonant structure implying a common origin to the scattering. $Sr_8Fe_8O_{23}$ has three different iron sub-lattices, with different valencies and crystal field geometries leading to different orbital splittings and a multiplet ground state, giving rise to the multiple peaks in the resonance observed [88]. An x-ray resonance experiment on cubic $SrFeO_3$ would provide a useful qualitative comparison

On warming, the structural transition and incommensurate-commensurate charge order transition occur coincident with the antiferromagnetic ground state becoming long-range ordered. The second-order nature of the magnetic transition indicates that the magnetic order is the driving force behind both the incommensurate to commensurate charge-order transition and structural transition. The appearance of the short-range spin correlations around 72 K stabilises the incommensurate charge-order wavevector with respect to temperature. The onset of long-range order around 60 K causes the incommensurate charge-order to rapidly lock into a commensurate value.

The $(0, 0, 0.5)$ magnetic reflection also shows a resonance at the oxygen K absorption edge. This reveals a hybridised band structure between the Fe *3d* and the O *2p* states. The resonance at the O K edge at the same wavevector as the magnetic ordering on the Fe atoms, shows the presence of an orbital magnetic moment on the oxygen, indicating the presence of spin polarised oxygen. This confirms the magnetism is at least in part mediated by an indirect exchange mechanism via the oxygen atoms. To get quantitative information from a resonance spectra *ab-initio* calculations are required. Calculation packages, such as FDMNES [89] are capable of predicting resonance structures, but cal-

culations for $Sr_8Fe_8O_{23}$ would not converge. The oxygen resonance has two features, one at the K edge at 529.3 eV and one above the edge at 531.1 eV The difficulty in modelling resonant scattering energy dependences, obviates any quantitative information from being extracted. Discussion on the origin of the two features will necessarily be conjecture. The polarisation analysis of the oxygen resonance is different to that of the Fe L_{III} edge, showing no signal in the σ-incidence channel whatsoever. This suggests that the moment on the oxygen may not have the same canted spin structure as the iron moments. From equation 3.2, an oxygen moment along the b direction would only give intensity in the π-channel.

The presence of three separate Fe sites, and charge-ordering on Fe_2, complicates the magnetism in the system. The charge-ordering suggests both superexchange and double-exchange interaction play a role in the long-range magnetic order. The Fe_1 squared based pyramid and Fe_3 octahedra, both have a valency of Fe^{4+}, do not share a common oxygen, but both share oxygens with the charge-ordered Fe_2 tilted octahedra. Along the c-axis each type of iron site shares an oxygen with itself, *i.e.* Fe_1-O-Fe_1, Fe_2-O-Fe_2 and Fe_3-O-Fe_3. In $Sr_8Fe_8O_{23}$, the super-exchange mechanism drives antiferro-ordering between ions of the same valency, the Fe^{4+} ions. The double-exchange mechanism drives ferromagnetic ordering between ions of different valency, Fe^{4+} of $Fe_{1,3}$ and the charge-ordered Fe_2 site. These two different exchange mechanisms could be the origin of the two resonant features at the oxygen K edge, although without quantitative modelling this is just speculation. The presence of both double-exchange and super-exchange, would create coupling between the charge and magnetic degrees of freedom, as both charge-ordering and magnetic-ordering are mediated by the oxygen anions.

Observations of resonances at the oxygen K edge at magnetic wavevectors, is not new and has been reported in a number of transition metal oxides [90, 91]. In the materials $Ba_3NbFe_2Si_2O_{14}$ and $TbMn_2O_5$ resonances at the oxygen K edge have been measured at the magnetic wavevectors [90, 91]. In both cases a single peak was measured with FWHM of 0.7 eV wide for $TbMn_2O_5$ and 1.3 eV for $Ba_3NbFe_2Si_2O_{14}$, in comparison to the double peak feature observed in $Sr_8Fe_8O_{23}$ with a FWHM of 0.75 eV and 1.0 eV. For the material $TbMn_2O_5$, modelling using FDMNES package [89] was able to replicate the single feature. $TbMn_2O_5$ is composed of two manganese sites, an Mn^{3+} in a squared based pyramid co-ordination and Mn^{4+} in octahedral co-ordination. Their study found that the oxygen resonance could only be reproduced in the model with a moment on the

Mn^{3+}, if the moment on the Mn^{3+} was set to zero, then the predicted oxygen resonance vanished. They concluded the oxygen spin polarisation arose purely from a hybridisation with the Mn^{3+}. $Sr_8Fe_8O_{23}$ has three different iron sites, and the double feature could be indicative of hybridisation with two different Fe ions.

The temperature dependence of the oxygen resonance is shown in figures 3.16 and 3.17. A fit of the critical scattering found a slightly lower transition temperature for the oxygen resonance, of 68 K. Unfortunately, this could simple be a consequence of localised beam heating due to a difference in absorption at the iron and oxygen edges. Fitting a critical scattering function to the integrated intensity, resulted in a $\beta = 0.45 \pm 0.02$. This value is higher than that found for the iron resonance, but is within twice the error.

The charge ordering is responsible for the unusual transport behaviour seen in the resistivity. Although the charge-ordering exists at temperatures above the long-range magnetic order, the formation of the magnetic long-range order drives a incommensurate-commensurate transition in the charge-order. In this way, the magnetism indirectly affects the resistivity. The magnetic susceptibility measurement shows the application of an applied field suppresses the antiferromagnetic transition to a lower temperature. This is expected to lower the transition temperature of the incommensurate-commensurate charge order transition. It is presumed the commensurate and incommensurate charge order phases have a different effect on the resistivity of the system. The negative magnetoresistance can be explained by a suppression of the incommensurate-commensurate charge-order transition, causing the system to be in the lower resistance state until lower temperatures. The magnetic field also has the effect of causing the resistivity to increase more rapidly once in the commensurate phase, causing the eventual positive magnetoresistance seen at low temperatures. In order to confirm the role of the charge-order in the magnetoresistance a repeat of the high-energy x-ray experiment in an applied magnetic field would give direct confirmation of the effect of magnetic field on the charge order transitions. A resonant experiment at the Fe *K* edge to study the charge order satellites, would also help elucidate the nature of the charge density wave. The magnetoresistance shows the same resistance as a mixed phase sample ($\delta \sim 0.17$) measured by Srinath *et al.* [92]. They concluded the negative magnetoresistance is due to double-exchange processes and the positive magnetoresistance at low temperatures, is due to the opening up of the band gap due to antiferromagnetic interactions. The observation of the $(0, 0, 1/2)$ reflections at the Fe $_{II/III}$ confirms the antiferromagnetic ground state. The resonance at

the oxygen *K* edge verifies the role of indirect exchange mechanism via a spin-polarised oxygen.

3.5 Conclusion

In conclusion, by combining bulk transport studies and x-ray scattering techniques on a single phase sample of $SrFeO_{2.875}$, this study has shown direct evidence that the giant magnetoresistance is a consequence of the coupling between the charge- and spin- order parameters and the lattice distortion. An antiferromagnetic ground state was identified, which doubles the unit cell in the *c*-axis. The additional resonance at the oxygen *K* edge reveals a hybridised band structure between the Fe *3d* and O *2p*, as well as the presence of an orbital moment on the oxygen.

This study reports the first observation of the charge-order with a wavevector of $(0, 0, {}^{5}/_{8})$, as well as the accompanying lattice distortion with the same wavevector. The charge-ordering undergoes an incommensurate to commensurate transition, which coincides with the negative magnetoresistance. The formation of the long-range magnetic order drives this incommensurate charge order transition to a high-order commensurate ground state. This coupling of the magnetic order to the charge and lattice distortion leads to the unusual magnetoresistance effects observed.

Chapter 4

Muon Spin Relaxation study of FeCrAs

4.1 Introduction

In this chapter, the magnetism of a single crystal FeCrAs has been studied using a combination of transport and heat capacity measurements, magnetic susceptibility and muon spin relaxation. The iron pnictide family of materials has become an interesting area of study, since the discovery in 2008 of high temperature superconductivity in the layered systems LaFeAs($O_{1-x}F_x$) [93], (Ba,K)Fe_2As_2 [94], LiFeAs [95] and $FeSe_{1-\delta}$ [96]. Iron is a well-known ferromagnetic material, and it is the co-existence of magnetism and high temperature superconductivity, that makes the iron pnictide family unusual [97]. Superconductivity and magnetism are often thoughts of as incompatible phenomena. In conventional s-wave superconductors, magnetic moments break up the spin singlet Cooper pairs, destroying the superconductivity [98]. The two phenomena had only been found to overlap in materials where the superconductor's dimensions have been reduced, either in layered interface films, $LaAlO_3/SrTiO_3$ [99], or materials where the magnetic moments are strongly localised to a crystallographic site isolated from the conduction path, RNi_2B_2C [100],UGe_2 [101],URhGe [102], and $ZrZn_2$ [103]. The iron pnictides, $(Ba_{1-x}K_x)Fe_2As_2$, LaFeAs($O_{1-x}F_x$) and Ca($Fe_{1-x}Co_x$)AsF all show a similar antiferromagnetic ordering in their phase diagrams, which overlap with the superconducting region. Muon spin relaxation (μsr) techniques have shown that these materials phase separate in to superconducting and magnetic phases. [104–107]

FeCrAs, although not a superconductor, is an interesting member of the iron pnictide family for it unusual transport, magnetic and thermodynamic properties showing both

non-Fermi and Fermi liquid behaviour, and can be considered a "non metallic metal". The resistivity of this material shows non-metallic behaviour with an increase in resistivity when the material is cooled, whilst the heat capacity shows classic Fermi liquid behaviour at low temperatures obeying a linear $C/T \propto T^2$ relationship [108]. FeCrAs differs from the superconducting members of the iron pnictide family, with its hexagonal three-dimensional structure. The superconductors tend to form tetragonal two-dimensional structures with insulating layers. FeCrAs has a magnetic spin density transition, similar to the superconductors. All evidence points to the magnetism being on the chromium sites instead of the iron sites as is the case with the superconductors. In the high temperature regime, FeCrAs behaves similarly to the parent compounds of the superconductors. At low temperatures, the behaviour is qualitatively different from any previous observations of non-metallic non-Fermi-liquid behaviour [108].

4.1.1 Crystal Structure of FeCrAs

FeCrAs belongs to a family of materials known as ternary transition metal monopnictides, with the chemical formula $MM'Z$, where M and M' are $3d$ or $4d$ transition metal elements and Z is a pnictogen, (N, P, As, Sb, Bi). These compounds adopt three types of crystal structure, a tetragonal Co_2P structure, hexagonal Fe_2P and the orthorhombic Cu_2Sb structure. All three structures have a common subunit which contains two kinds of metal sites, a tetrahedrally coordinated site with four Z atoms and a square-based pyramidal site co-ordinated with five Z atoms. The most electropositive transition metal generally occupies the pyramidal site.

FeCrAs adopts the Fe_2P (also known as ZrNiAl-type in some references) hexagonal structure with space group $P\bar{6}2m$, and lattice parameters a = 6.0675 Å and c = 3.657 Å. Chromium occupies the $3g$ Wyckoff site with five neighbouring arsenic atoms in a squared-based pyramidal co-ordination, whilst iron sits at the $3f$ Wyckoff site in the centre of an arsenic tetrahedron. In the more general family of RMX materials (R = Rare-Earth-like/alkali-earth, M = transition metal, p-electron element), thirty percent adopt this crystal structure [109]. The $3g$ and $3f$ sites have three equivalent positions in the unit cell each at $(x_1, 0, 1/2)$, $(0, x_1, 1/2)$, $(-x_1, -x_1, 1/2)$ and $(x_2, 0, 0)$, $(0, x_2, 0)$, $(-x_2, -x_2, 0)$, forming separate layers of the two metal atoms half a unit cell apart in the c-direction. For a given layer of $3g$ or $3f$ sites for the space group $P\bar{6}2m$, if x_i is between a third and two-thirds, $1/3 < x_i < 2/3$, the metal atoms form a distorted kagomé lattice, with the case of $x_i = 1/2$

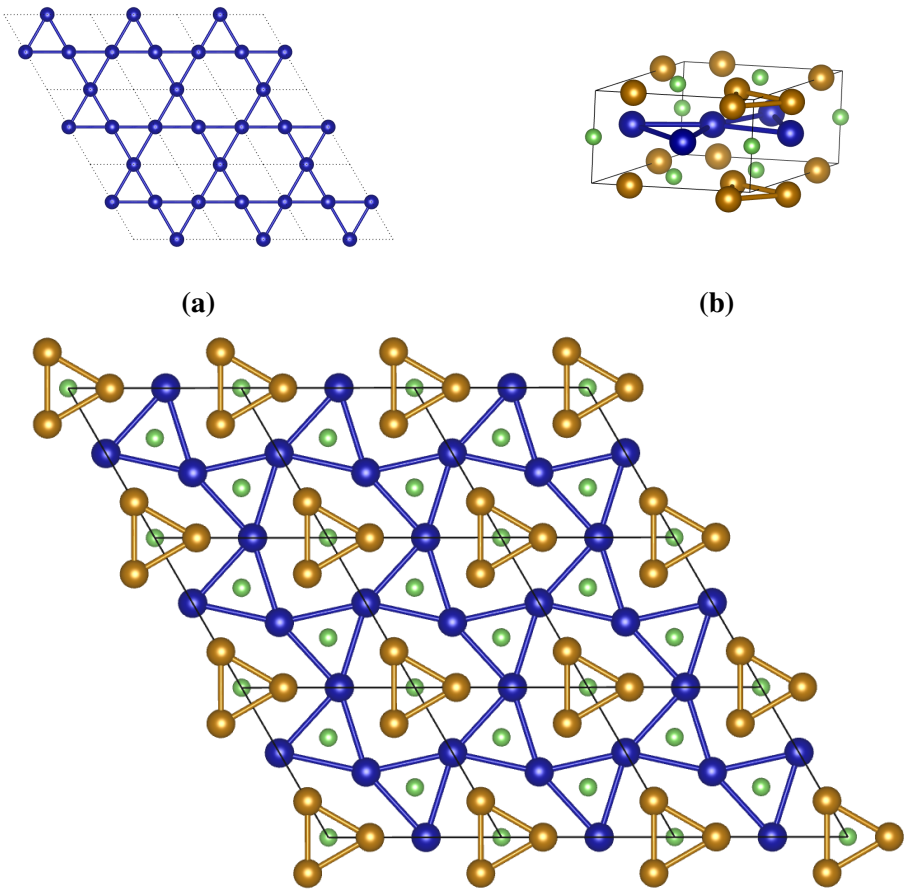

Figure 4.1: (a) The undistorted kagomé lattice. The hexagonal unit cell contains three equivalent metal sites, at ($\frac{1}{2}$, 0), (0,$\frac{1}{2}$) and ($\frac{1}{2}$, $\frac{1}{2}$). (b) The primitive hexagonal unit cell of FeCrAs, chromium atoms are shown in blue, iron atoms in yellow and arsenic in green. The *c*-axis is shown vertically up the page. (c) Supercell corresponding to (3 × 3 ×1) of the hexagonal primitive cell, shown down the *c* axis direction. The distorted kagomé lattice is shown in blues and Fe trimers are in yellow.

being the undistorted kagomé lattice. For only nearest-neighbour (*n.n.*) interactions the distorted and undistorted kagomé lattice are topologically equivalent [110]. Figure 4.1a shows the undistorted kagomé lattice structure. By placing three atoms in a two dimensional hexagonal unit cell at ($\frac{1}{2}$, 0), (0,$\frac{1}{2}$) and ($\frac{1}{2}$, $\frac{1}{2}$) positions, a tiling effect arises where every atom is a vertex of two regular hexagons and two regular equilateral triangles. If x_i is less than a third or greater than two-thirds, $0 < x_i < 1/3$ or $2/3 < x_i < 1$, the metal atoms

form isolated equilateral triangles. The case where $x_i = 1/3$ describes a a triangular lattice.

The chromium sites, ($x_i = 0.564$), form a distorted kagomé lattice and the iron sites ($x_i = 0.240$) form a triangular lattice of trimers. The distorted kagomé lattice of chromium atoms differs from an undistorted kagomé lattice by a displacement of the chromium atoms to the sites ($\frac{1}{2}$+d, 0), (0,$\frac{1}{2}$+d) and ($\frac{1}{2}$-d, $\frac{1}{2}$-d), where $d = 0.064$ or 0.388 Å.

4.1.2 Geometric Frustration

A magnetic system can be considered to be comprised of N magnetic moments fixed to a lattice. Depending on whether we consider the magnetic moments as having a discrete or continuous distribution (Ising or X-Y,Heisenberg), there is either a finite or infinite number of microstates. The ground state of the system is the microstate with the lowest energy where the interactions between all the magnetic moments are satisfied. Geometric frustration arises in particular lattices where no single unique lowest energy state exists, rather a variety of similar low energy states exist [111]. The effect of the lattice can be seen in the simplest case, the Ising model where magnetic dipole moments can be in one of two discrete states, +1 and -1. In the Ising case for N moments, there are 2^N microstates, although some of theses microstates could be symmetrically equivalent due to the underlying symmetry of the host lattice. If only nearest-neighbour interactions are considered, for the case of an antiferromagnetic exchange, antiparallel adjacent spins are energetically favourable. We can simplify the Hamiltonian for the exchange interaction.

$$\mathcal{H} = \sum_{\alpha}^{N} \sum_{\beta}^{N} J_{\alpha,\beta} S_\alpha \cdot S_\beta = J \sum_{\alpha}^{N} \sum_{\beta}^{n.n} S_\alpha S_\beta \tag{4.1}$$

For a square lattice, figure 4.2a, it is possible to satisfy the exchange interaction for all the sites. For a square lattice system with $N = 4$ sites, there are 16 different configurations of Ising spins of which four are symmetrically unequivelent. Of these four configurations, the one shown in figure 4.2a has the lowest energy, as all neighbouring spins are antiparallel, making this the ground state. For a triangular lattice, figure 4.2b, it is not possible to satisfy the antiferromagnetic exchange interaction. In the triangular lattice example shown in figure 4.2b, there are $N = 3$ sites, leading to eight possible microstates. Of these eight microstates, six have the same energy, with only the two microstates with moments either all up or all down having higher energy. In the example shown in 4.2b, once the first two spins have been placed antiparallel, the third spin cannot be placed as to min-

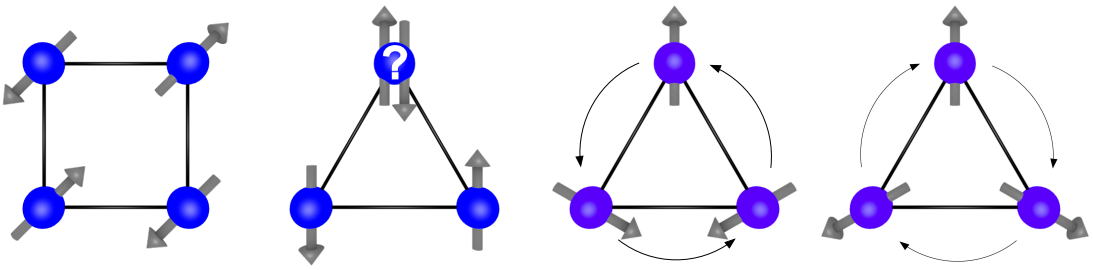

Figure 4.2: (a) Ground state configuration of antiferromagnetic Ising spins on a square lattice. (b) Frustrated configuration of antiferromagnetic Ising spins on a triangular lattice. The third spin can take either +1 or -1 and be equally frustrated. (c) & (d) Two possible ground state configurations for X-Y spins on the triangular lattice, (c) has negative chirality and (d) has positive chirality.

imise the interaction with both the first two spins at the same time, this leads to a six-fold degenerate ground state, causing frustration in the Ising nearest-neighbour case.

For the X-Y model, the magnetic moments have a continuous distribution, with the direction of all the moments confined to a plane. As the distribution of directions of the magnetic moments is continuous rather than discrete, there are an infinite number of microstates. Figure 4.2c and 4.2d, show two possible ground states for the X-Y model, here the spins are rotated by 120° to each other, resulting in a zero net moment. There is a choice of direction of the rotation, negative, figure 4.2c , or positive chirality, figure 4.2d.

4.1.3 Magnetism in FeCrAs

In magnetic materials that adopt the Fe_2P crystal structure, the magnetic ion sits on the distorted kagomé lattice [112, 113]. The distorted and undistorted kagomé lattice have the same four nearest neighbours. Each site on the kagomé lattice is a vertex of two triangles, figure 4.1. Similar to the Ising case for the triangular lattice, there is no unique ground state for the spin configuration, and frustration arises. More generally, the Mermin-Wagner theorem states that for a one- or two-dimensional isotropic spin-S Heisenberg system, at non-zero temperatures, long-range order is not expected for either ferromagnetic or antiferromagnetic exchange [114]. In a purely two-dimensional kagomé lattice we do not expect long-range order to develop at non-zero temperatures. When considering a classic Heisenberg model, two degenerate ground states exist at absolute zero, with

a $\mathbf{q} = 0$ and a $\mathbf{q} = \sqrt{3} \times \sqrt{3}$ structure [115–119]. For the $\mathbf{q} = 0$ state, the magnetic cell and the crystal cell overlap, figure 4.3a. For the $\mathbf{q} = \sqrt{3} \times \sqrt{3}$ the magnetic cell and crystal unit cell do not overlap, and a 3×3 supercell is needed to encompass the magnetic repeat. Figure 4.3b, shows the crystal unit cell, highlighted by the thin dashed lines, the $\sqrt{3} \times \sqrt{3}$ cell in thick solid line and the larger 3×3 magnetic cell in thick dashed line. The $\mathbf{q} = \sqrt{3} \times \sqrt{3}$ state can be described by a $(1/3, 1/3, 0)$ wavevector in the basis of the crystal unit cell. Monte-Carlo simulations have shown that the kagomé lattice displays an order-by-disorder transition, which breaks the degeneracy to pick a ground state $\mathbf{q} = \sqrt{3} \times \sqrt{3}$ structure as $T \rightarrow 0$, causing an entropically-driven local spin-nematic order at low temperatures, with a diverging correlation length as $T \rightarrow 0$ [115]. The order-by-disorder is brought about by the effects of thermal fluctuations around the ground states lifting the degeneracy [120].

Bulk magnetisation measurements, reported by Wu *et al.* [108] show a feature in the susceptibility at 125 K, with the susceptibility along the *a*- and *c*-axis splitting below this point. The susceptibility was shown not to exhibit Curie-Weiss behaviour up to 300 K. The effects of field cooling on the magnetisation measurements, only caused a splitting in the susceptibility at low temperatures of 7 K and 11 K for the *c*- and *a*-directions, respectively. Neutron powder diffraction was carried out by Swainson *et al.* [121]. Upon cooling to 2.8 K six magnetic satellite peaks were found at (⅓,⅓,0) positions. The intensity of the magnetic peaks could be modelled by non-collinear moments on the Cr sites only, as Mössbauer measurements report no moment on the iron site, to an error of 0.1 μB [122]. The non-collinear spin structure is shown in figure 4.3c, the alternative $\sqrt{3} \times \sqrt{3}$ cell holds for this structure. The moments on the Fe sites were zero within the error of the measurement. The chromium sites were found to vary in magnitude taking values of one-, two- and four-times 0.685(1) μB, with an average moment of 1.22 μB per chromium site, with a net moment of zero. The lack of moment on the iron site is in agreement with electronic structure calculations performed by Ishida *et al.* [123], which showed that for a range of CrMZ compounds (M = Fe, Co, Ni, Z = P, As) the magnetic moments lie only on the Cr site and that the *M* site although magnetic in its elemental form, has no magnetic moment. The electronic structure calculation for FeCrAs predicts a ferromagnetic phase, rather than the observed non-collinear antiferromagnetism.

Although experimentally FeCrAs was found to have a similar $\sqrt{3} \times \sqrt{3}$ type ordering with a wavevector of $(1/3, 1/3, 0)$, the transition temperature of 125 K is too high for the

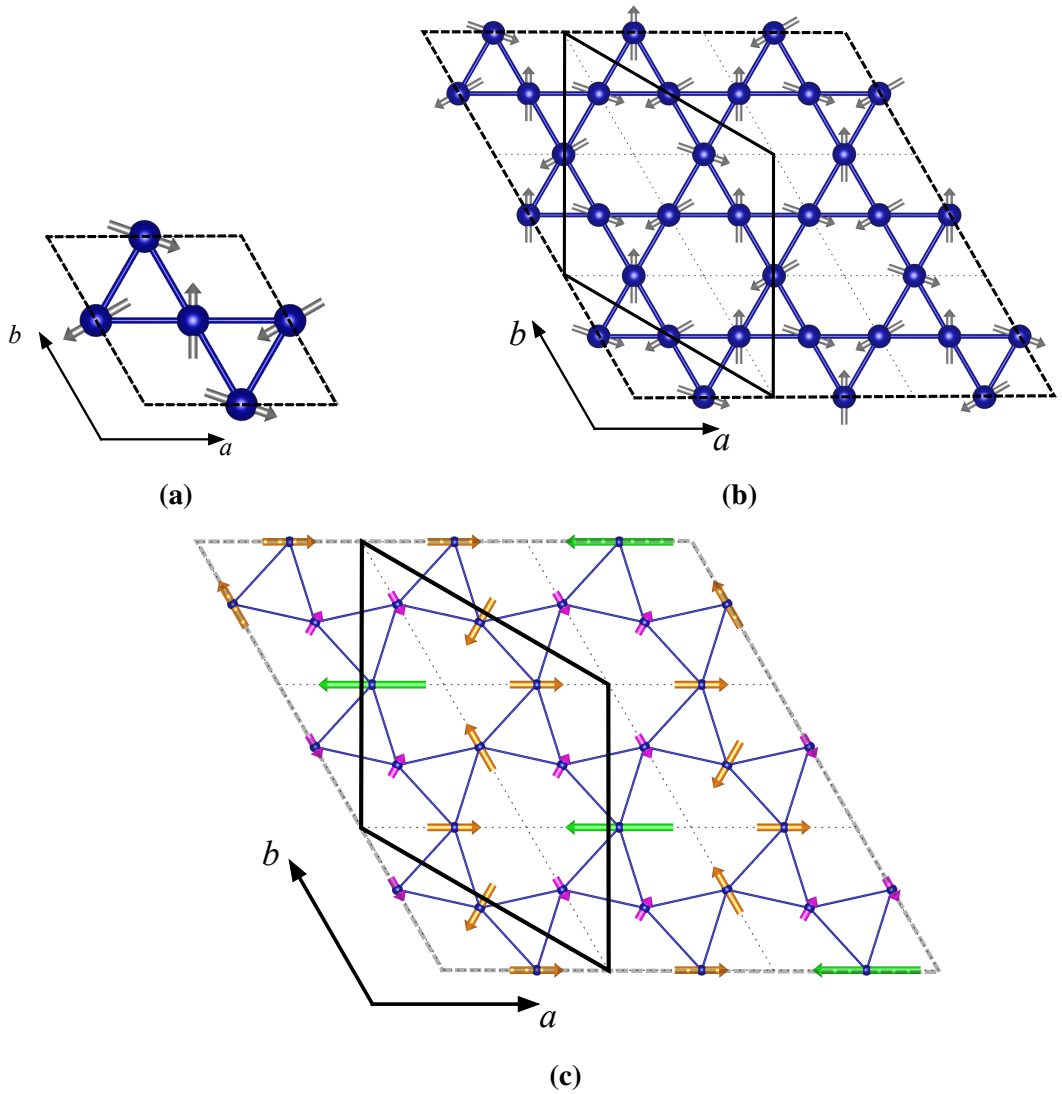

Figure 4.3: (a) The **q** = 0 magnetic structure. (b) The **q** = $\sqrt{3} \times \sqrt{3}$ magnetic structure. (c) The magnetic structure of FeCrAs, measured by the neutron powder diffraction [121], green moment is 4×0.685 μB, orange moment is 2×0.685 μB and pink moment is 1×0.685 μB. For (b) & (c) the crystal unit cell is shown by the thin dashed line, the $\sqrt{3} \times \sqrt{3}$ magnetic cell by the thicked solid line, and the larger 3×3 magnetic cell by the thick dashed line.

order-by-disorder transition to be the origin. When coupling between layers, in a stacked kagomé lattice is taken into account for the Heisenberg case, the system is found to remain short-range-ordered independent of the strength of the coupling between the planes [124,

125]. Dipolar interactions between chromium planes would allow a finite temperature magnetic ordering, although this has been estimated to occur at a temperature of the order of 1.27×10^{-4} K [110].

On the kagomé lattice, there is no inversion symmetry between two neighbouring sites. As a consequence of this the Dzyaloshinsky-Moriya (DM) interaction is non-zero. This is an anisotropic exchange between the excited state of one ion and the ground state of the other ion [126]. Although the Mermin-Wagner theory states a isotropic 2-D system should not order at non-zero temperatures [114], the DM interaction is anisotropic. Theoretical studies have shown the DM interaction can lead to non-zero ordering temperatures [127] in 2-D systems. For the undistorted kagomé lattice the addition of the DM interaction into a Monte-Carlo simulation, drives the system to ordered states [128]. For the distorted case with nearest-neighbour, next-nearest-neighbour and DM interactions being taken into account, theoretical studies [129] for the X-Y model find a number of magnetic structures, depending on the relative strengths of the various exchange interactions, including a structure with a wavevector of ($^1/_3$, $^1/_3$, 0).

A theoretical study carried out by Redpath *et al.* [110] looked at the coupling between the chromium and the iron atoms. In their study, the three nearest iron atoms which form a trimer, shown in yellow in figure 4.1c, are treated as a single magnetic site. These iron molecules form a triangular lattice, between layers of chromium in a distorted kagomé lattice. The trimer approximation holds with the assumption that the energy scales for interactions between trimers are small relative to that within the trimers [130]. Using Monte-Carlo simulations, their model [110] for FeCrAs magnetically orders at a finite temperature in a coplanar $\sqrt{3} \times \sqrt{3}$ magnetic order, predicting susceptibility qualitatively similar to that measured by Wu *et al.* [108].

4.2 Experimental

4.2.1 Crystal Growth

The samples of FeCrAs used in this study were grown by Dr K. A. Al-ziq, from the King Fahd University of Petroleum and Minerals, Saudi Arabia. The samples were grown by the self-flux method. Stoichiometric quantities of iron, chromium and arsenic were sealed under partial arsenic pressure in a quartz tube. The furnace temperature was raised by 100° an hour to a temperature of 1100° C. The furnace was kept at this temperature

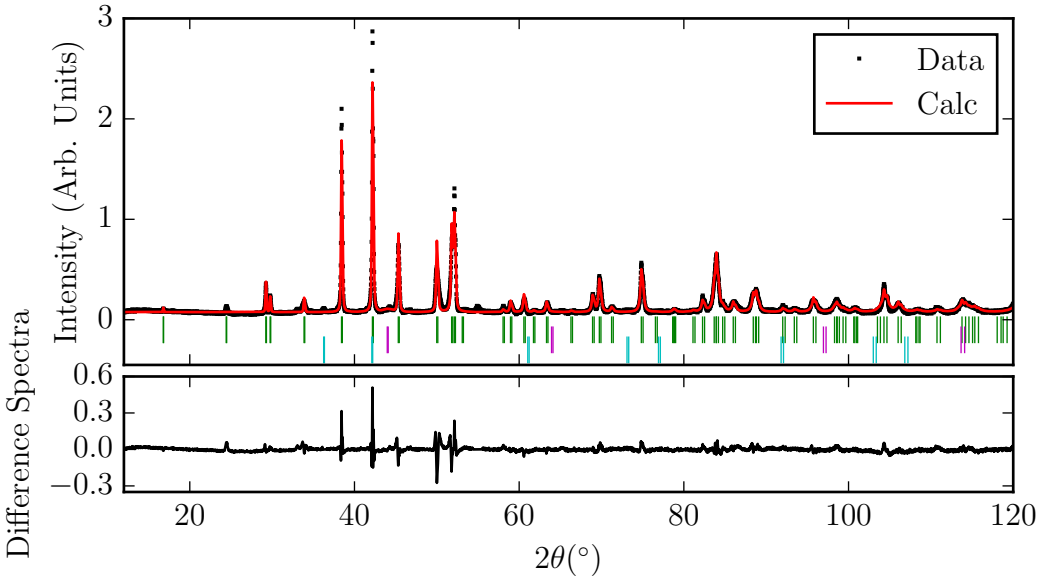

Figure 4.4: (Top) X-ray powder diffraction measurement performed on a sample of FeCrAs. The intensity measured on the detector is $2{\times}10^4$ bigger than that shown on y-axis. The observed data is shown in black squares. A refinement was made using the Fullprof software suite, and the profile is shown by the red line. The 2θ positions of the allowed bragg peaks for FeCrAs are shown with green ticks. The cyan and magenta ticks indicate positions of Bragg reflections from minority FeO and Cr phases. (Bottom) Difference spectra between the observed and calculated diffraction patterns.

for 2 hours, before being allowed to slowly cool at a rate of 2-5° an hour until it reached 700° C, when the furnace was switched off. This cooling rate allowed for the formation of crystals. The growth yields, were approximately 2.3 g of powder and small single crystals. The single crystal aligned for measurements had a mass of 1.94 mg. An attempt was made to grow the crystals using the vapour transport method using iodine gas, as was the case for FeAs [131]. This method had the side effect of partially decomposing the sample. The single crystal was aligned using the in-house Huber four-circle diffractometer, and the *a*, *b* and *c* axes identified.

4.2.2 Powder Diffraction

Powder diffraction was carried out on a sample of the powder, using a Cu K_α x-ray source. Data was collected between detector angle 2θ, of 10° to 120°. A Rietveld refinement of the diffraction intensity was performed using the Fullprof software suite. FeCrAs was

found to be the majority phase with a refinement r-factor R_{Bragg} = 10.66. Figure 4.4 shows the observed and refined calculated diffraction intensity. The green ticks mark the positions of the Bragg peaks from FeCrAs crystal structure. There are a few weak peaks in the data, unaccounted for by the FeCrAs crystal structure. A minority phase of FeO was added to the refinement, which accounts for the peak at 36.6°. There is still an unaccounted reflection at 54.8°, and it has not been possible with any confidence to identity the impurity phase from a single weak reflection.

Parameter	**Value** (Error)	**Literature Values** [132]
a	6.109(1)	6.0954
c	3.646(1)	3.6663
Fe x	0.247(1)	0.2485(1)
Cr x	0.589(1)	0.5854(1)

Table 4.1: Best fit parameters from the Rietveld refinement of the x-ray powder diffraction measurement, shown in figure 4.4. Comparison is made to those report in reference [132]

The lattice parameters and atomic positions, given in table 4.1 agree with those measured by W. Wu [132].

4.2.3 EDX Spectroscopy

Energy dispersive X-ray (EDX) spectroscopy was performed on the powder sample of FeCrAs. EDX spectroscopy reveals information about which constituent elements are present, but does not contain information about the bonding environment and structure of that element. An electron microscopy image of the powder sample is shown at the top of figure 4.5, and in the rest of the figure are the fluorescence maps from each element present plus oxygen for the area shown in the electron microscopy image. The iron and chromium fluorescence maps show these elements to be fairly equally distributed, the arsenic fluorescence indicates a slight arsenic deficiency. The oxygen fluorescence is in agreement with the observed FeO impurity in the powder diffraction refinement. The oxygen fluorescence also suggests a small amount of chromium oxide impurities. The fluorescence maps also rule out the presence of any single element grains.

The EDX spectroscopy results rule out contamination from any other elements. The fluorescence spectra was measured at eight different sites, and are shown in figure 4.6.

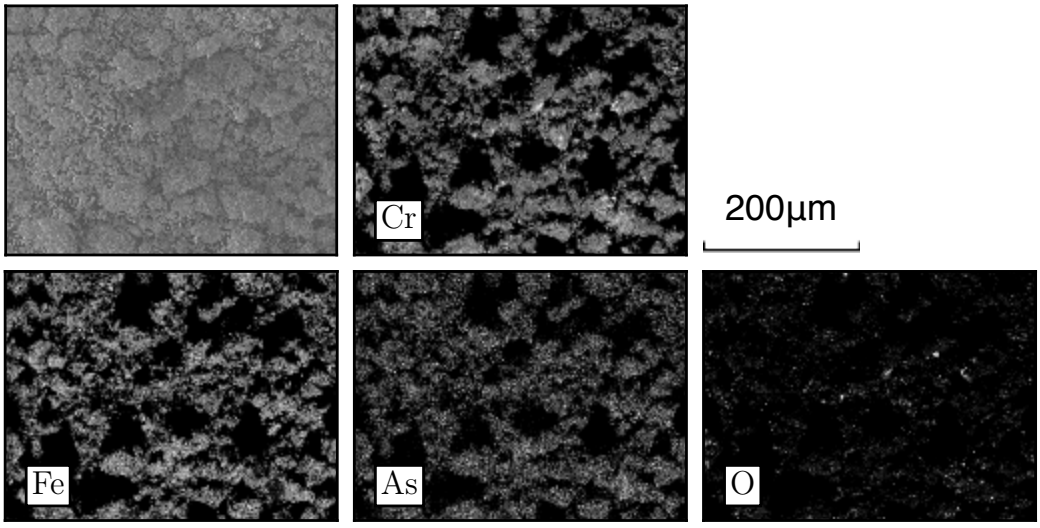

Figure 4.5: (Top) Electron microscopy image of the powder sample of FeCrAs. (Below) EDX maps of the same area tuned into fluorescence from a specific element, Iron, chromium, arsenic and oxygen.

The elements responsible for the fluorescence peaks have been labelled and the relative abundance of the elements at each site have been calculated and are presented in table 4.2. The oxygen content was difficult to determine due to the presence of a secondary arsenic fluorescence peak near the oxygen peak. The largest ratio of oxygen found in the sample was 4.97 %, but was typically around 1 %. Half of the sites investigated had roughly equal proportions of the chromium, iron and arsenic, the other half appear chromium rich, with up to 82 % chromium. Although only eight sites have been examined using the EDX technique, the results suggest the powder is inhomogeneous. Although some areas agree with expected results for FeCrAs, other areas are dominated by chromium. The powder diffraction and EDX spectroscopy techniques appear to give contradictory results.

In EDX spectroscopy a beam of electrons is used to stimulate the emission of characteristic x-rays from the constituents of the sample. The penetration depth of this technique is 1000-2000 nm [133], and the x-rays are emitted from the excited atom in all directions. The likelihood of an x-ray escaping the sample is absorption dependent, and therefore dependent on the wavelength. When the sample is inhomogeneous, such as a rough surface or a powder, the technique is much more sensitive to the surface composition than

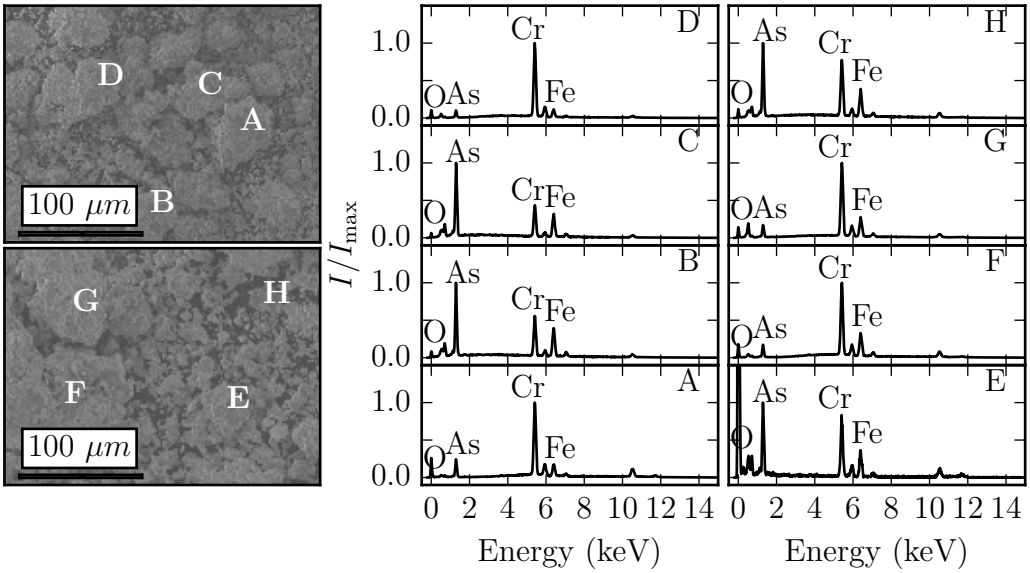

Figure 4.6: Fluorescence spectra from eight different sites labelled in the electron microscopy images at the top. Main contributions from elements are labelled, all unlabelled peaks are secondary peaks from the elements already labelled. The intensities have been normalised for each spectra.

the bulk. Interpreting the EDX and powder diffraction data together, the sample bulk is majority FeCrAs, with iron and chromium oxide impurities on the surface of the powder grains.

Site	Fe (%)	Cr (%)	As (%)	O (%)
A	14.54	74.5	10.61	0.35
B	36.79	30.81	31.41	0.99
C	37.15	26.8	34.79	1.26
D	10.81	82.32	5.35	1.52
E	30.93	39.01	29.32	0.74
F	12.82	74.72	7.5	4.97
G	12.78	78.21	8.22	0.79
H	43.57	30.21	23.01	3.22

Table 4.2: Relative elemental abundance from fluorescence data shown in figure 4.6

4.3 Results

4.3.1 Heat Capacity

The heat capacity, C of a single crystal of FeCrAs was measured using a Quantum Designs Physical Properties Measurement System (PPMS). The sample was mounted in a small amount of thermal grease on a puck. Measurements were also made on the puck without the sample to infer the effects of the sample. The heat capacity was measured over a temperature range of 3 to 300 K. Figure 4.7 shows the results of the heat capacity measurement. The heat capacity increases smoothly with temperature, levelling out towards a value of 80 J mol^{-1} K^{-1}. The lattice and electronic contributions to the heat capacity can be modelled using a sum of the Sommerfeld, Debye and Einstein models for heat capacity, shown in equation 4.2, with coefficients A_E and A_D.

$$C(T) = \gamma T + A_E C_E(T, \theta_E) + A_D C_D(T, \theta_D) \tag{4.2}$$

The Sommerfeld term is simply proportional to temperature and can be derived from the free electron model, where γ is proportional to the density of states at the Fermi energy. The Einstein and Debye terms account for contributions to the heat capacity from lattice vibrations. The principal difference between the Einstein term and the Debye term, is how they treat the lattice vibrations. The Einstein model considers a solid as a collection of non-interacting quantum oscillators, whilst the Debye model treats the vibrations as phonons in a box. Equation 4.3 and 4.4 show the form of the einstein and Debye equations, respectively, where N is the number of atoms in the crystal, and θ_E and

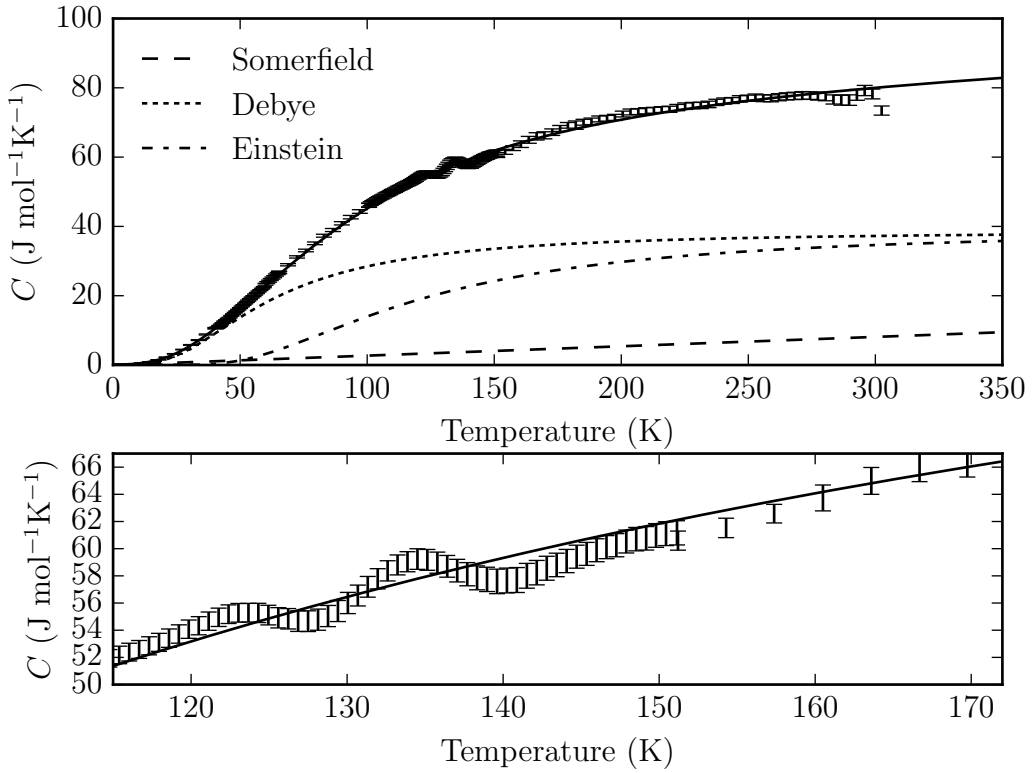

Figure 4.7: (Top) Heat capacity per mole (C) as a function of temperature (T) for a single crystal. The fit from model shown in equation 4.2, shown by the solid line, Debye contribution shown in small dashes, Einstein contribution shown in dash-dot, and Sommerfeld contribution shown in large dashes. (Bottom) Close up of the discontinuity around 125 K.

θ_D are the einstein and Debye temperatures, which are specific to the materials.

$$C_V = 3Nk\left(\frac{\theta_E}{T}\right)^2 \frac{e^{\theta_E/T}}{(e^{\theta_E/T}-1)^2} \tag{4.3}$$

$$C_V = 9Nk\left(\frac{T}{\theta_D}\right)^3 \int_0^{\theta_D/T} \frac{x^4 e^x}{(e^x-1)^2} dx \tag{4.4}$$

Both models predict the levelling out in the high temperature region, whilst the Debye model correctly predicts the low temperature behaviour. Due to assumptions made to simplify the problem, the Debye model struggles to predict the intermediate temperature range correctly. The Einstein and Debye models, are only dependent on the temperature,

and a characteristic temperature, θ_E and θ_D, respectively. It is often reported in the literature, to fit the heat capacity as a sum of all three terms. This has been shown to be successful in the related superconducting iron pnictides [134].

Parameter	Value (Error)
γ	27.0(1) mJ mol^{-1}K^{-2}
A_E	1.57(5)
θ_E	369(7) K
A_D	1.55(5)
θ_D	255(4) K

Table 4.3: Best fit parameters of the Heat capacity model for FeCrAs, defined in equation 4.2. Sommerfeld constant (γ), Einstein temperature (θ_E), Debye Temperature (θ_D). A_E and A_D are simply scale factors for the Einstein and Debye terms.

The heat capacity per mole measured against temperature is shown in figure 4.7. The solid black line shows the model for the total heat capacity, the large dashes, small dashes and dash-dot lines show the contributions from the Sommerfeld, Debye, and Einstein terms, respectively. The defining parameters of theses terms are shown in table 4.3. At low temperatures the Debye heat capacity can be approximated to a T^3 dependence, shown in Equation 4.5, alternatively this can be expressed as a linear relationship between C/T and T^2.

$$\begin{aligned} C &= \gamma T + AT^3 \\ \frac{C}{T} &= \gamma + AT^2 \end{aligned} \tag{4.5}$$

Heat capacity over temperature (C/T) has been plot against temperature-squared (T^2) in figure 4.8. The bottom figure shows that at low temperatures, below 35 K, C/T behaves linearly with T^2, with the y-intercept being the Sommerfeld parameter, at 27.0(1) mJ mol^{-1}K^{-2}. This agrees with previous studies that found the Sommerfeld coefficient to be 31.6 mJ mol^{-1}K^{-2}, but with up to 20% variation between samples [108]. A value of 27.0 mJ mol^{-1}K^{-2} for the Sommerfeld constant is quite high for d-electron system, but is in agreement with measurements carried out on other iron pnictides. Certain dopings of $SmFeAsO_{1-x}F_x$ were found to have Sommerfeld coefficient as high as 137 mJ mol^{-1}K^{-2},

whilst LiFeAs has a Sommerfeld coefficient of 23.3 mJ $mol^{-1}K^{-2}$. [134]. Extracting the Debye temperature from the gradient A of low temperature approximation, gives a value of 109.5±0.1 K. This value is significantly different from that obtained in table 4.3, and is due to the effects of including ther einstein model.

A discontinuity is evident in the heat capacity, between 125 K and 150 K. Figure 4.7 (bottom) shows the heat capacity over this range. This discontinuity occurs over the range where the magnetic transition is reported to occur. Monte-Carlo simulations of the magnetic contribution to the heat capacity reported by Redpath *et al.* [110], predicts a peak in the heat capacity around the transition temperature, but the discontinuity measured in the data, does not take the form of the single distinct peak as expected.

4.3.2 Bulk Magnetisation Measurements

Magnetic susceptibility and magnetisation were measured as a function of temperature and applied magnetic field, H. These measurements were carried out using a Quantum Design Magnetic Properties Measurement System (MPMS), using the Superconducting QUantum Interference Device (SQUID) magnetometer to measure very small changes in magnetisation. Both a powdered sample, 167.17 mg and the single crystal, 1.94 mg (aligned with the field applied along the a- and c-directions) were measured. The temperature dependence of the magnetisation was measured over a range from 1.8 K to 300 K. A magnetic-field of 1000 Oe was applied across the sample at each temperature to measure the susceptibility. This measurement was repeated for both zero field cooled (ZFC), and field cooled (FC) in an applied field of 5000 Oe. Magnetisation against magnetic field curves (M-H) were measured for all three samples at temperatures of 2 K, 125 K and 300 K. The magnetisation isotherms were measured using a field up to ±5 T.

Figure 4.9 shows the magnetic susceptibility (χ) per mole for the powdered sample of FeCrAs. The inverse susceptibility is plotted on the same x-axis, but with a different y-axis (right). A transition is apparent in the magnetisation data, around 125 K, where upon cooling the susceptibility increases rapidly. This transistion is easier to see in the 1^{st} derivative of susceptibility, shown in figure 4.10, where a clear transistion is seen starting at 125 K. The susceptibility continues to increase until the sample is cooled to a temperature of $T \sim 45$ K where the susceptibility begins to level off, and decreases below 20 K. The inverse susceptibility is an indicator of paramagnetic behaviour as the Curie-Weiss law describes a linear relationship between inverse susceptibility and temperature.

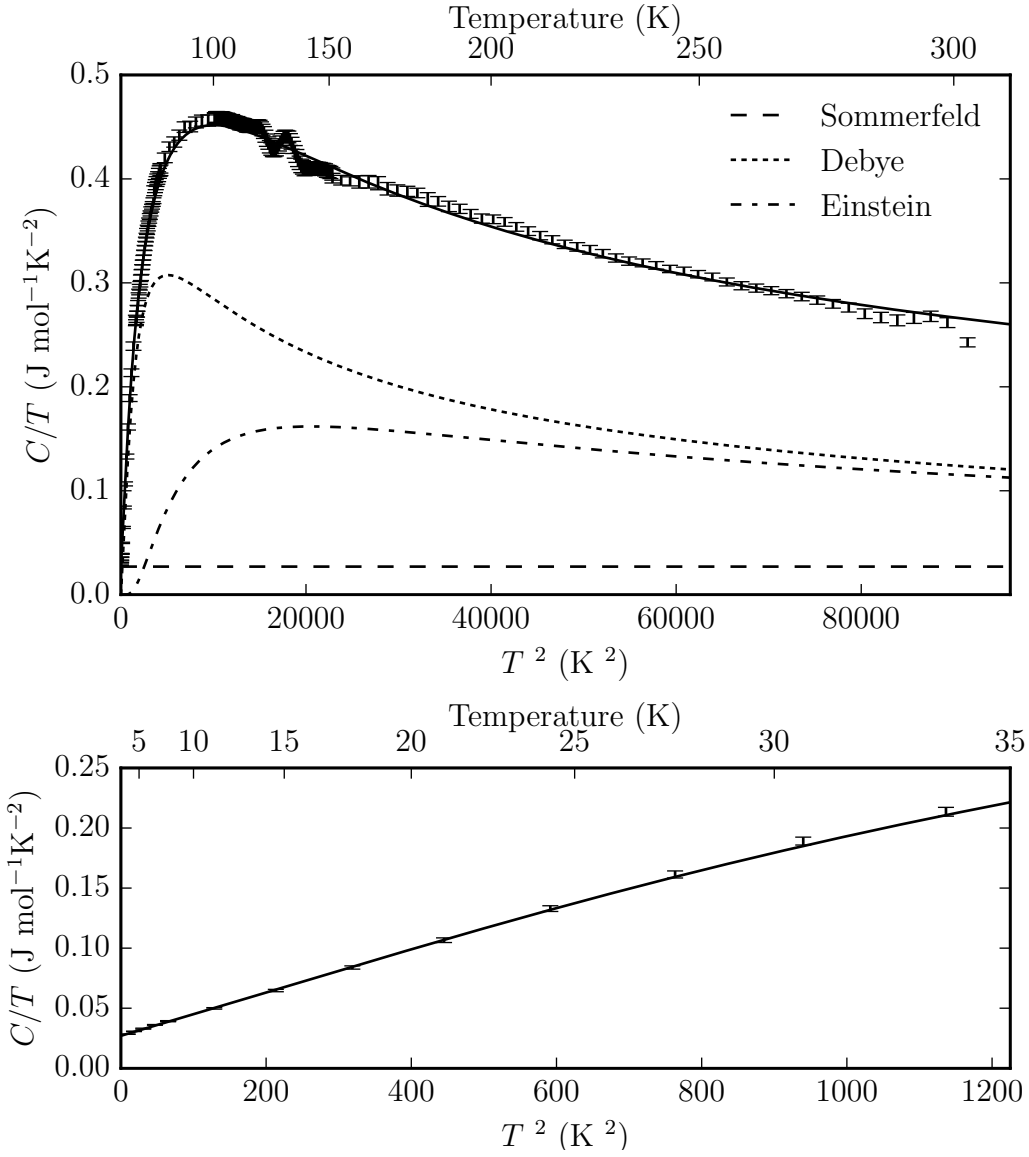

Figure 4.8: (Top) Heat capacity per mole over temperature (C/T) as a function of temperature squared (T^2) for a single crystal, showing the expected T^3 dependence of the heat capacity. The fit from model shown in equation 4.2, shown by the solid line, Debye contribution shown in small dashes, Einstein contribution shown in dash-dot, Sommerfeld contribution shown in large dashes. (Bottom) Close up of the low temperature T^3 response of the heat capacity, the y-intercept shows the linear Sommerfeld response.

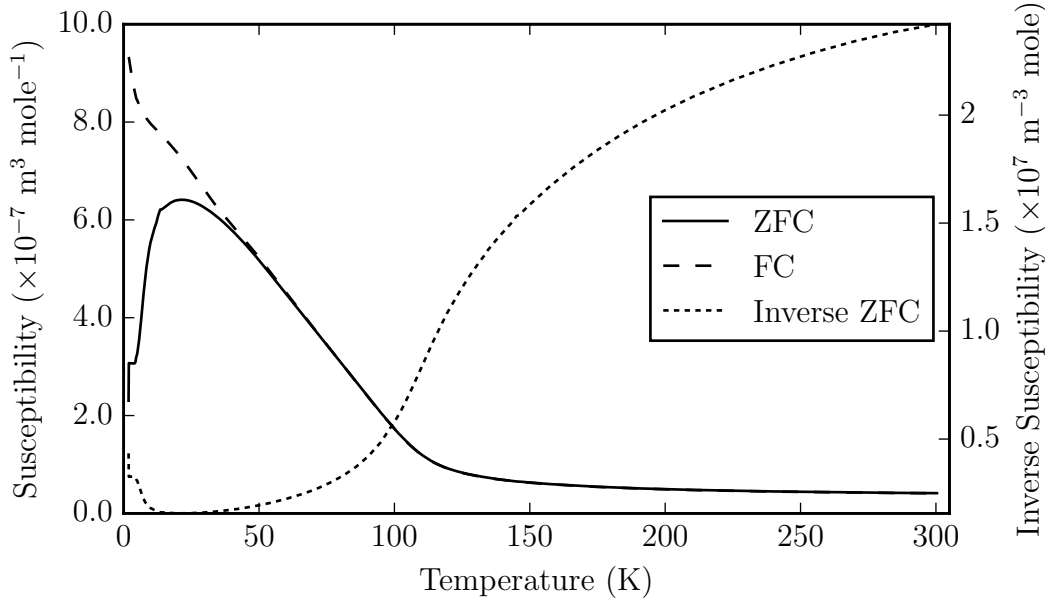

Figure 4.9: Magnetic susceptibility per mole of powdered FeCrAs, measured on an Quantum Designs MPMS system, with applied field of 1000 Oe. The zero field cooled measurement is shown in black, and the field cooled in 0.5 T is shown in dashed. Inverse susceptibility is shown on the right hand *y*-axis in the fine dashed line.

It is quite clear that no part of the inverse susceptibility below 300 K behaves linearly with temperature, ruling out any Curie-Weiss paramagnetic behaviour.

Figure 4.11 shows the temperature dependence of the susceptibility for the single crystal sample. The single crystal is only about 1% the mass of the powder sample, but the magnetic moment measured was 1000 times smaller than the powder sample. This apparent difference between the powder and single crystal magnetisation data can be attributed to difference in mass between the single crystal and the powder, and the effect this has on the error. The susceptibility along both the *a*- and *c*- crystallographic axes shows qualitatively the same behaviour as the powder sample, with a transition around 125 K, below which the susceptibility increases and a lower transition around 20-48 K where the susceptibility decreases. The susceptibility along the *a*-axis is consistently higher for the entire temperature range than along *c*-axis. The susceptibility was measured under an applied field of 0.5 T. In both cases, the single crystal and powder, there is dramatic splitting between the FC and ZFC behaviour, at a temperature $\approx$ 48 K. As stated

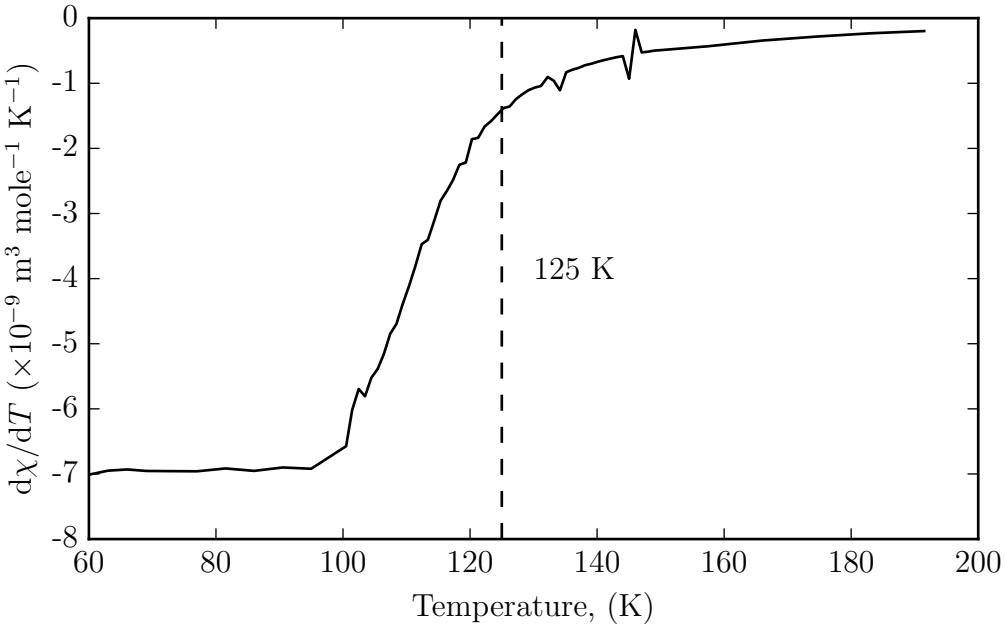

Figure 4.10: The first derivative of the magnetic susceptibility per mole with respect to temperature for powdered FeCrAs. The 1st derivative was calculated from the ZFC data shown in figure 4.9

earlier for the ZFC measurement the susceptibility decreases at low temperatures, whilst the FC measurement continues to increase. This FC splitting is symptomatic of a spin freezing phenomena.

The magnetisation against applied field measurements are shown in figure 4.12. No hysteresis was observed at any temperature on either the powder or the single crystal. The powder and the single crystals both show a strong magnetisation response to the applied field. For both the crystal and powder samples, the magnetisation response increases for decreasing temperature. The powder appears to show a stronger magnetisation response, than either the *a* or *c* direction, this again is a consequence of sample size. In the powder sample, a curve in the M-H behaviour is seen at the lowest temperature of 2 K.

4.3.3 Muon Spin Relaxation

To investigate the complex magnetic behaviour present in FeCrAs, a muon spin relaxation (μSR) study was performed using the ARGUS μSR beam line at ISIS, Didcot, UK. The ISIS muon source operates using a double pulse muon beam, with typically 10,000 muons

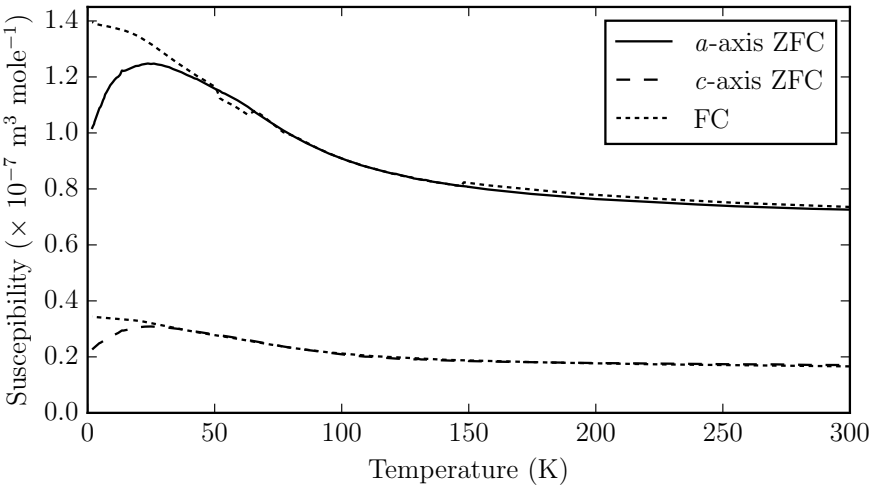

Figure 4.11: Magnetic susceptibility per mole of single crystal sample of FeCrAs, measured on an Quantum Designs MPMS system, with applied field of 1000 Oe. Zero field-cooled with measurement field applied along the c-axis (dashed), and the field along the a-axis (solid), and 0.5 T field cooled shown in fine dashed for both directions.

in each pulse. The gap between pulses is sufficiently large, to monitor decays up to 15 muon lifetimes. The pulsed structure reduces the number of background positron detections, compared to the continuous beam alternatives, providing more sensitivity to weaker fields. Approximately 230 mg of FeCrAs was ground up to a fine powder, and mounted in thermal grease in a silver foil packet on the cold finger of a cryostat. Further foil was added to the cryostat to act as shielding.

The cryostat was placed in the spectrometer and cooled to 5 K. To calibrate the spectrometer forward-back asymmetry, a weak transverse field is applied to the sample. Under a transverse field, the muon's spin will precess with time, this oscillation should be approximately centred on the zero asymmetry point. Due to the differing efficiency between the forward and back detectors, this is seldom the case, and a correction is applied to the raw data.

$$A(t) = \frac{N_F - \alpha N_B}{N_F + \alpha N_B} \tag{4.6}$$

In equation 4.6 the value α can be fitted from the data, is related to the efficiencies of the forward- and back-detector groups and should be close to 1. A weak transverse

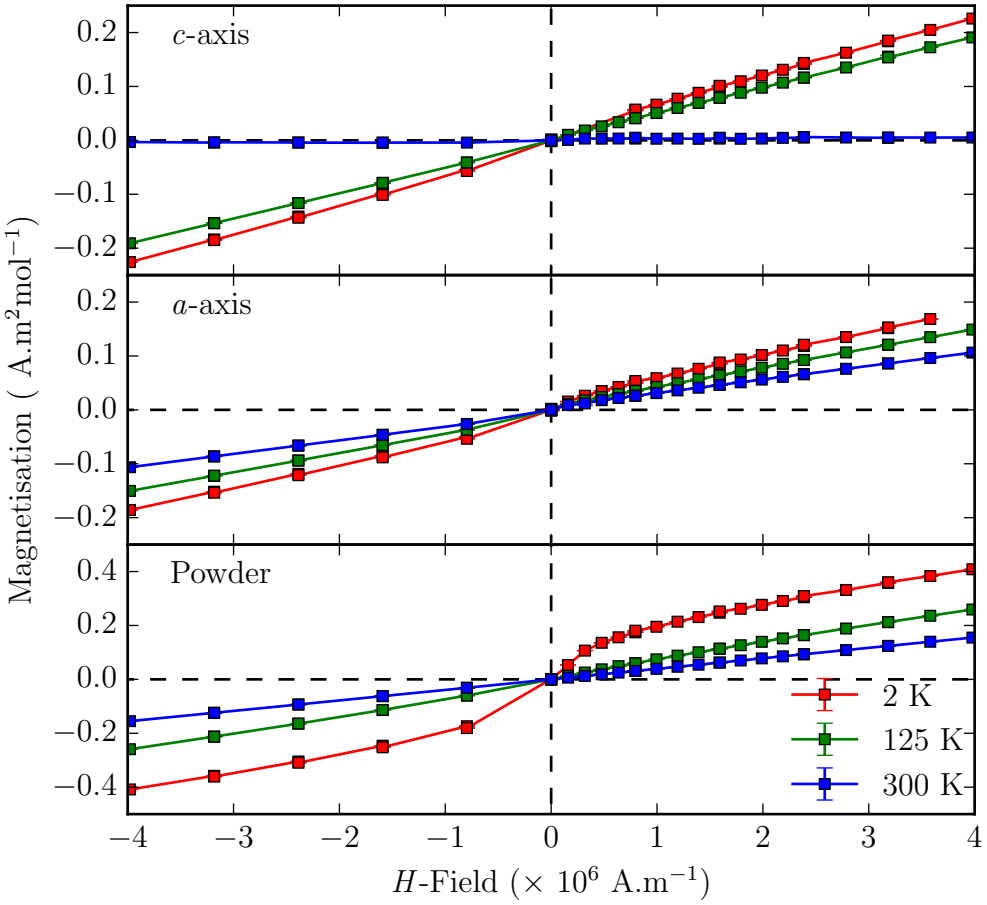

Figure 4.12: Magnetisation per mole of FeCrAs, (Top) Single crystal aligned with c-axis parallel to field. (Middle) Single crystal with a-axis in direction of field. (Bottom) Powder sample. Measurements taken at 300 K (blue), 125 K (green) and 2 K (red).

magnetic field of 985 ±1 μT was applied across the sample at 20 K, and a spectrum was measured until 25 million positron emission events had been collected. Figure 4.13 shows the spectrum for the transverse field. The top figure shows the raw data for the forward and backwards detectors, solid and dashed line respectively. The decay events in both forward and back channels, show an exponential decay, which has been highlighted by the logarithmic y-scale. There is also an oscillatory component to the decay with the front and back channels appearing to be out of phase. The bottom figure shows the forward/back (F/B) asymmetry between the two detector groups, calculated using equation 4.6. The

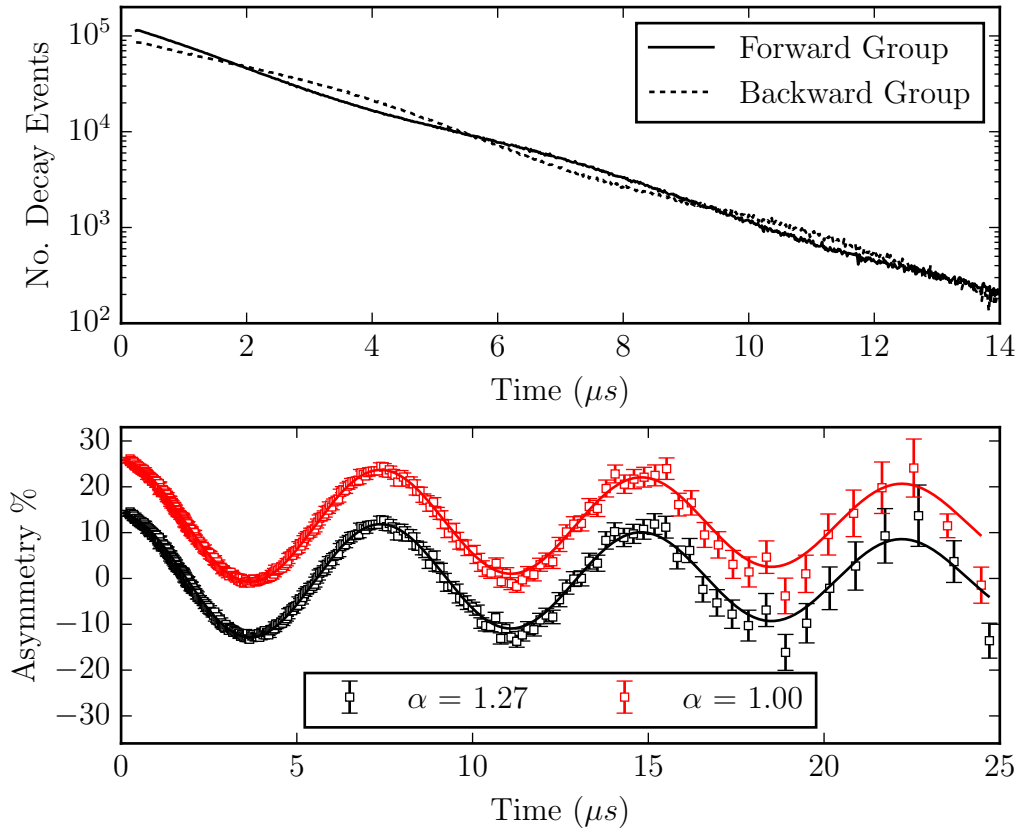

Figure 4.13: (Top) Raw data for positron emission time spectra for the forward and backward detector groups at 20 K and a transverse magnetic field of 985±1 μT, 25 millions positron emission events were collected. (Bottom) Forward/back asymmetry for the same data set with different instrument forward/back asymmetry values, calculated using equation 4.6

red data shows the asymmetry with $\alpha = 1$, while the black data shows the asymmetry with $\alpha = 1.27$. The asymmetry spectra was fitted using a decaying cosine function and a constant background, and a least squares fitting algorithm was used to find the value for α where the asymmetry oscillates around zero (background went to zero). This fit resulted in a value of $\alpha = 1.27 \pm 0.01$, this value of α was used to calculate the asymmetry on all subsequent data.

The fit to the transverse field spectra was found to have a frequency of 0.135±0.001 MHz. Given the gyromagnetic ratio for a muon is 135.5 MHz T^{-1}, for an applied field of

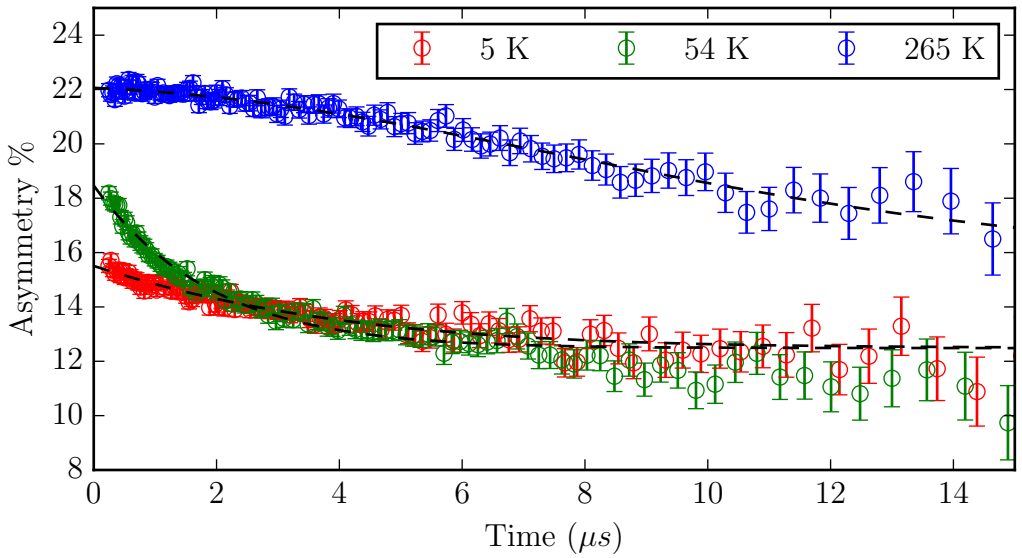

Figure 4.14: Selected forward-backward detector asymmetry spectra of the muon decay. Spectra measured at 265 K (blue), 54 K (green) and 5 K (red). The fits, shown in black dashed line, from the decay function $A_0 e^{-\lambda t} e^{-\frac{1}{2\sigma^2}t^2} + C_{B.G.}$, with σ fixed at 8.59 μs.

985 μT, the muon should precess with a frequency of 0.133 MHz, in agreement with the experimental data.

The magnetic field was removed, and muon decay spectra were collected as a function of temperature. A minimum of 25 million positron detection events were recorded at each temperature. Initially spectra were collected every 10 K between 5 K and 105 K, and every 20 K between 105 K and 265 K. Once regions of interest were identified, additional spectra were collected every 3 - 5 K. Three qualitatively different spectra were found at different temperatures, figure 4.14, shows three selected temperatures to highlight the difference. In the high temperature region the muon depolarisation spectra shows Gaussian-like behaviour, whilst at lower temperatures the muon depolarisation spectra shows exponential-decay-like behaviour.

The high temperature Gaussian behaviour is typical for relaxation due to static nuclear dipolar fields. In order to get a more quantitative understanding of the muon relaxation spectra, a single function describing the asymmetry, to fit the entire temperature range is desirable. After trialling several functions, the best results were attained using a combi-

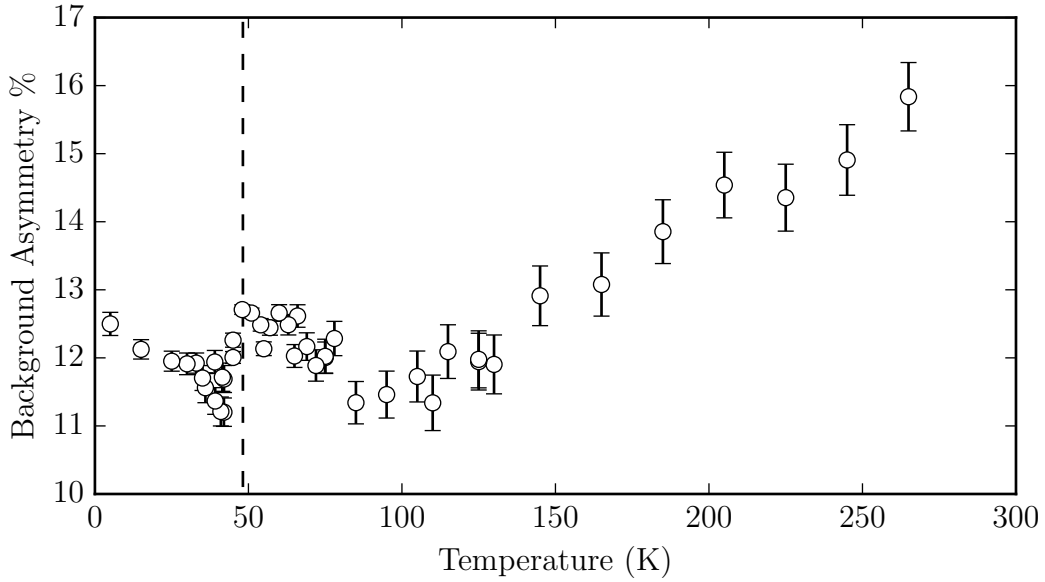

Figure 4.15: Background constant from the fit to forward-backward asymmetry decay as a function of temperature.

nation of a Gaussian and an exponential with a constant background.

$$A(t) = A_0 e^{-\lambda t} e^{-\frac{1}{2\sigma^2}t^2} + C_{B.G.} \tag{4.7}$$

The initial asymmetry is given by $A_0 + C_{B.G.}$, the Gaussian width is given by σ and the rate of the exponential decay is given by λ. The value of the Gaussian width was found to be independent of temperature, and was fixed across the entire temperature range. Using a Levenberg-Marquardt non-linear least squares algorithm [135, 136], a value for the Gaussian width was found to be 8.59±0.01 μs. It was necessary to allow the A_0, λ and $C_{B.G.}$ to vary with each temperature.

The background was found to decrease linearly as temperature decreased, until around 100 K, where the background levels out at approximately 12%, shown in figure 4.15. The initial asymmetry and decay rate, λ are shown in figure 4.16. Three different regions can be seen in the initial asymmetry and decay rate, the high temperature regime, 100 - 265 K, where the decay rate is close to zero, and the initial asymmetry is at it's highest. In the temperature regime, 48 K to 100 K, there is a rapid increase in decay rate, with a peak of λ = 0.75 MHz, at 48 K. In the same temperature regime the initial asymmetry experiences

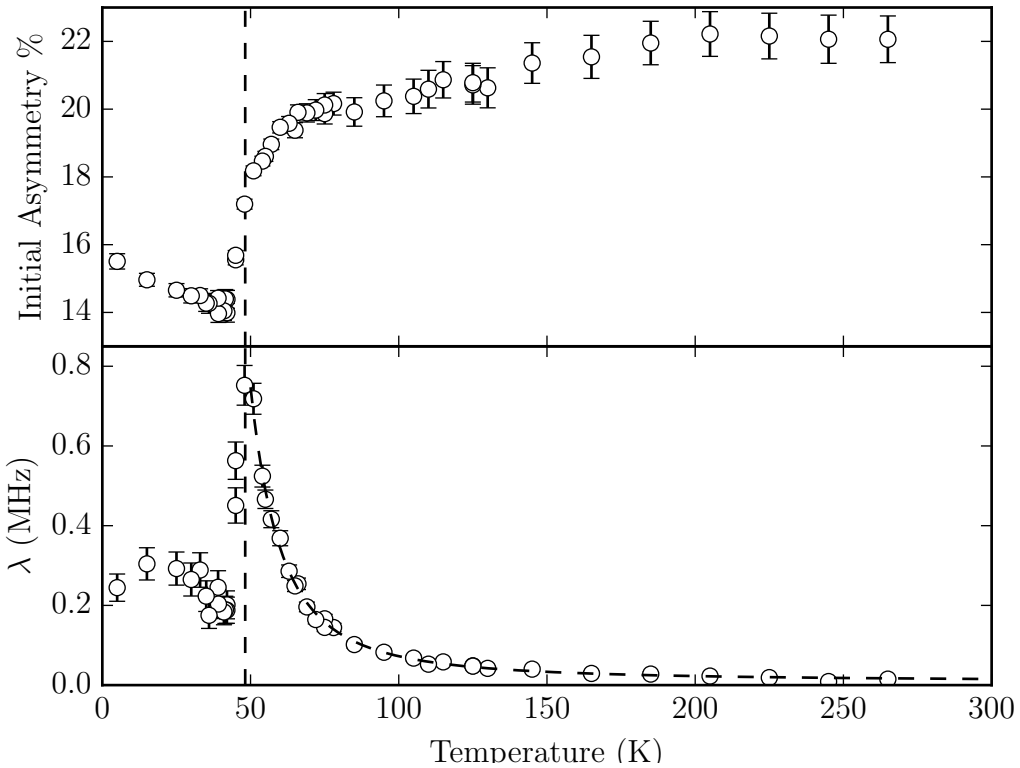

Figure 4.16: Temperature dependence of parameters from the relaxation function $A_0 e^{-\lambda t} e^{-\frac{1}{2\sigma^2}t^2} + C_{B.G.}$, with σ fixed at 8.59 μs. (Top) Initial asymmetry (%), sum of amplitude of decay function and background. (Bottom) Relaxation decay constant, λ. Black dashed line shows $\lambda \propto e^{\frac{\Delta}{T}}$

a drop from 20% down to 14%. Finally below this transition in the region of 5 K to 48 K the decay rate has drop to approximately $\lambda \approx 0.25$ MHz, where it remains stable, whilst the initial asymmetry stabilises at around 15%.

The decay rate λ at temperatures between 48 K and 100 K, appears to increase almost exponentially upon cooling. Upon further cooling below the transition point at 48 K, there is a discontinuity where the decay rate rapidly drops. The decay rate above this discontinuity appears to be related to the temperature with a Boltzmann-like exponential.

$$\lambda \propto e^{\left(\frac{\Delta}{k_b T}\right)} \tag{4.8}$$

This relationship can be seen in figure 4.17, where 1/T has been plotted against the

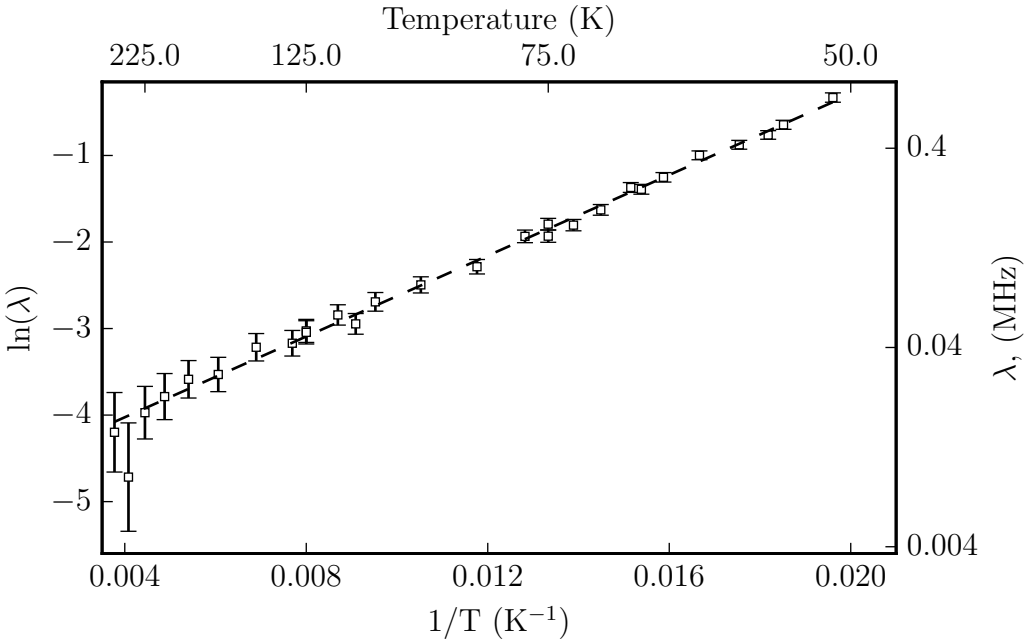

Figure 4.17: Logarithm of the decay exponent, ln(λ), as a function of 1/T. The dashed line shows a linear fit with gradient 233±5 K

ln(λ). A linear relationship exists between 1/T and ln(λ), between 48 K and 225 K, and a straight line has been fit to the data giving a gradient of 233±5 K, this gradient gives a Δ = 20.1±0.4 meV. This relationship from equation 4.8, between decay rate and temperature has been plotted on the figure 4.16, shown by the black dashed line, highlighting the discontinuity at 48 K. The Δ value can be interpreted as the energy difference between the high- and low- energy states that the muon can flip between, when interacting with the polarisation of the host lattice. A quantum of energy of $\hbar\omega_\mu$ can be supplied to the muon from the host lattice to transition the muon between a spin-up and spin-down states. A spin-flip transition in the host lattice can provide this energy.

Longitudinal magnetic field dependences were collected either side of the magnetic transition at 20 K and 120 K. The sample was cooled to 120 K allowed to stabilise, and muon relaxation spectra were collected for a minimum of 25 million positron emission events, for a range of applied longitudinal magnetic fields. The magnetic field was changed on a logarithmic scale collecting spectra at 0, 1.00, 1.77, 3.14, 5.56, 9.85, 17.45,

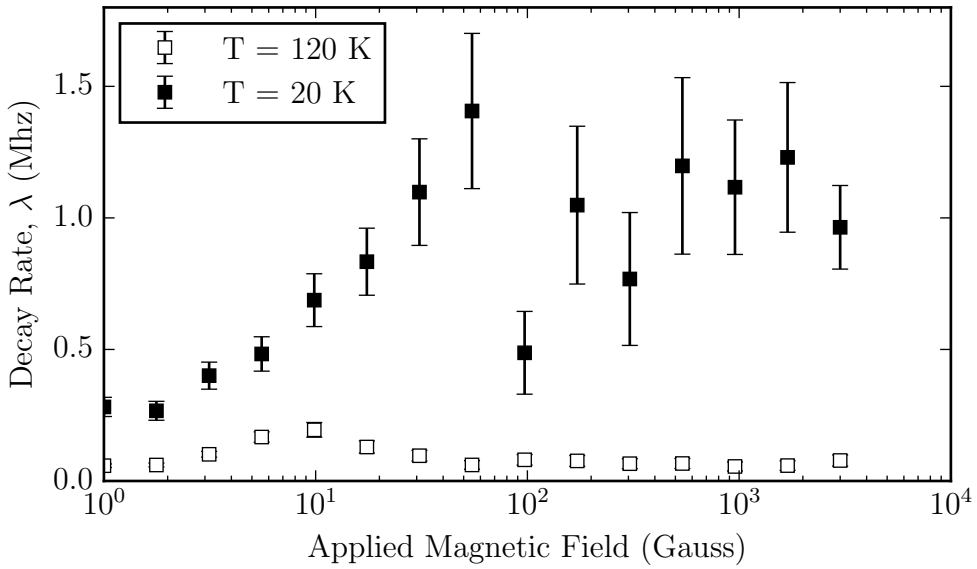

Figure 4.18: The effects on the decay rate, λ, from the relaxation function defined in equation 4.7 as a function of longitudinal magnetic field

30.92, 54.77, 97.03, 171.91, 304.55, 539.54, 955.85, 1693.38 and 3000 Gauss. The same function from equation 4.7 was used to fit the asymmetry for the field dependences, figure 4.18 shows the results of the fits to the high and low temperature field dependences.

The background term was found to increase as a function of magnetic field for both magnetic regimes at 20 K and 120 K. The effects of longitudinal applied magnetic field on the decay rate, λ is shown in figure 4.18. Applying a longitudinal field has very little effect on the high temperature regime (T = 120 K), with a slight peak at 10 Gauss. Below the transition at 20 K, applying a longitudinal magnetic field causes the value of λ to increase from around 0.2 MHz to 1.4 MHz at around 50 Gauss, where it appears to reach a noisy plateau with further applied field.

4.4 Discussion

It has been suggested in the literature, [108] that the electronic behaviour of FeCrAs warrants a new class of non-Fermi liquid. Although unable to measure resistivity ourselves, due to small sample size, FeCrAs has been established to be "non-metallic", due to its increasing resistivity with a decrease in temperature. A study of resistivity as a function of applied pressure, was carried out by Tafti *et al.* [137]. FeCrAs was found to keep its non-

metallic behaviour with pressures up to 17 GPa, beyond the suppression of the magnetic order, suggesting long-range order of the moments does not play a significant role in determining the non-metallic behaviour. Our own heat capacity results show similar results to those reported by Wu *et al.* [108] with the same high temperature plateau value of 80 J $mol^{-1}K^{-1}$ and a similar Sommerfeld coefficient 27 mJ $mol^{-1}K^{-2}$. The primitive unit cell has 3 Fe, 3 Cr, and 3 As, if the heat capacity per mole of unit cell is used instead, the high temperature heat capacity levels out at 26.6 J mol^{-1} K^{-1}, which is close to the prediction of the Dulong-Petit Law of $3R \approx 25$ J $mol^{-1}K^{-1}$. The measured Sommerfeld coefficient is unusually high for a *d*-electron metal, but is a common feature in the parent compounds of the iron pnictide superconductors. At low temperatures the heat capacity shows metallic-like behaviour with its T^3 dependence. The fits to the Debye and Einstein models show similar results to superconductors LiFeAs and $LaFeAsO_{0.9}F_0.1$ but with a slightly higher Debye temperature. Our sample of FeCrAs, shows a more pronounced feature at 125 K in the temperature dependence of the heat capacity than that previously reported by Wu *et al* [108, 132]. Magnetic susceptibility results are qualitatively different to those reported previously [108, 132]. Of the eleven growths reported by Wu [132], markedly different susceptibilities were measured, whilst the "non-metallic" resistivity and "metallic" heat capacity remained consistent across the samples. In frustrated lattice systems, such as the kagomé lattice, it is not surprising that the magnetism is highly sensitive to the crystalline quality.

The sample, presented by Wu as the highest quality, shows an antiferromagnetic transition at at 125 K, with a clear peak in the magnetisation. Our sample shows a rapid increase in the susceptibility below 125 K, with an antiferromagnetic-like transition around 25-48 K. Below this transition at 48 K FC splitting is observed. This splitting is indicative of a spin-freezing phenomena, where below the transition at 48 K the spins become fixed in a energetically stable disordered state (spin glass). Thermal irreversibility between FC and ZFC susceptibility below the spin-freeze transition are characteristic properties of a spin glass. If the system is cooled through the spin-freeze transition in an applied field the system is more susceptible to further applied field. The field cooled splitting was seen in all of the growths by Wu *et al.*, but the effect was small in their highest quality growth sample, around 5% increase occurring below 20 K, whereas the FC splitting in our sample was more drastic, with a 300% increase for the powder sample and 40% increase for the single crystal.

Over the entire temperature range measured, no Curie-Weiss paramagnetic behaviour has been observed, in agreement with the measurements by Wu *et al.* [108]. The inverse susceptibility suggests that the system may enter a paramagnetic phase above 300 K.

Results from the muon relaxation study, shed some light on the magnetism. Three different regimes are identified between 5 K and 300 K. Firstly, a high temperature regime, were the muon relaxation asymmetry is Gaussian-like. This is indicative of muon polarisation precessing in a dipolar field from the nuclear moments. This is the expected behaviour above any magnetic transition, where nuclear moments dominate the asymmetry.

As the sample is cooled down the shape of the asymmetry spectra becomes more exponential-decay-like, as the muons depolarise faster. In this regime, the muon is more sensitive to electronic magnetic fields. Below 100 K the decay rate, λ begins to increase rapidly. The temperature dependence of the decay rate, λ is described by an $\exp\left(\frac{\Delta}{k_B T}\right)$, where Δ is measured to be 20.1±0.4 meV. The plot of 1/T against $ln(\lambda)$ clearly shows a linear relation between 225 K and 48 K. The value Δ is indicative of the energy required to cause a muon to flip between a high and low energy state. At 48 K there is a discontinuity in the temperature dependence of the decay rate, where the decay rate rapidly drops. This third regime below 48 K, coincides with the field splitting in the susceptibility data. In this regime the asymmetry spectra is almost constant at around 12% with a slow decay rate. This regime is clearest to see in the plot of initial asymmetry, where over the spin freeze transition, the initial asymmetry drops rapidly from around 20% to 14%. The increase in muon depolarisation decay rate, λ as the spin-freeze transition is approached and then consequent drop in decay rate in the spin glass phase has been observed by μsr in spin glass materials before. In the kagomé lattice system, hydronium jarosite $(H_3O)Fe_3(OH)_6(SO_4)_2$, the muon depolarisation can be described by an stretched exponential decay [138]. The decay rate λ shows qualitatively similar behaviour in $(H_3O)Fe_3(OH)_6(SO_4)_2$, increasing rapidly on cooling towards spin-freezing before dropping off in the spin-glass phase. In similar kagomé system , Cr-jarosite ($KCr_3(OH)_6(SO_4)_2$), and kagomé like $(Cu_xZn_{1-x})_3V_2O_7(OH_2)(H_2O)_2$, the muon depolarisation also has a exponential-decay-like behaviour, but without any sign of spin-freezing down to 25 mK and 50 mK, respectively [139, 140]. In the regime above the spin-freeze transition, between 225 K and 48 K, the muons experience dynamic magnetic fields, brought about by spin fluctuations. Below the spin-freeze transition, the muon

experiences static magnetic fields associated with the spin glass state.

The kagomé lattice allows a coplanar X-Y 120° ground state, as shown in figure 4.3. The kagomé geometry also permits continuous spin folding zero energy modes, that preserve the 120° structure through "spin facets" [141]. Spins which lie on the edge of the facets can rotate around the common axis of a facet with no energy cost. The magnetic susceptibility measurement, showed that the magnetic moments do not behave paramagnetically, above the spin freezing temperature. Below 225 K patches of short-range metastable spin-glass begin to appear. The geometry of the kagomé lattice allow low-energy excitations of these extended blocks of spin [138]. These blocks of magnetic order are not ordered with neighbouring blocks. As the sample is cooled towards the spin-freezing transition of 48 K, more of these spin blocks form, and these blocks become larger until the spin freezing temperature is reached. As more of these blocks of metastable spin glass appear the muon depolarisation decay rate increases until the spin freezing transition.

Monte-Carlo simulations of FeCrAs by Redpath *et al.* [110] modelled FeCrAs as a stack of a chromium on a distorted Kagomé lattice and iron molecules on a triangular lattice. In their simulations they have two exchange terms, J_1 between nearest neighbours in the kagomé net, and J_2 between the chromiums in the kagomé net and the iron trimers on the triangular lattice. The kagomé lattice will only display short-range ordering, until absolute zero, the addition of the coupling between the layers of kagomé and triangular lattices allows the system to order at a non-zero temperature.

From the susceptibility, heat capacity and muon relaxation spectra results, two magnetic transitions appear to occur. Above 48 K short-range ordering exists between chromiums on the kagomé net, but thermal background stops the interactions between layers playing a role. Below 48 K, spins freezing sets in. At 225 K where the short range order first appears, $k_BT \approx 20$ meV, which is in agreement with the interaction energy extracted from the μsr. At 48 K, $k_BT \approx 4$ meV, if this is compared to the value of Δ extracted from the μsr data of 20.1 meV, we can get a rough idea of the strength of the coupling interactions, J_1 and J_2. Mainly the interaction within the chromium kagomé net is 5 times stronger than the coupling between the kagomé net and the triangular lattice of iron trimers. Redpath *et al.* compared their simulation to magnetic susceptibility data collected by Wu *et al.*, to find a relative interaction strength of $J_2/J_1 \approx 1/9$.

The longitudinal field dependence of the μSR asymmetry spectra at 120 K show little

variation, with an increase in background the only noticeable effect up to 3000 Gauss. The low temperature longitudinal field dependence at 20 K, also shows this increase in background, but in addition shows a large increase in decay rate with field. This agrees with the *M-H* curves, which showed a far bigger susceptibility in the spin-glass phase at 2 K than at 125 K. The decay rate λ increases with field until the measurement taken at 54.77 Gauss, after which it reaches a noisy plateau. This noisy plateau may be due to the frequency response limitations of the ARGUS instrument. The magnetic field dependence, further confirms the different nature of the magnetic phases above and below the spin-freezing transition.

The magnetism in our sample of FeCrAs is very different to that reported in the literature. Although x-ray powder diffraction, confirms our sample to be majority phase FeCrAs, the x-ray probe is not sufficient to distinguish doping of chromium atoms on the iron site, due to their similar x-ray scattering lengths. The EDAX spectroscopy suggests the sample might be slightly chromium rich, but can not accurately quantify the chromium content. A neutron powder diffraction measurement would be the ideal probe to measure any chromium doping on the iron site as the neutron scattering lengths for chromium and iron are 3.635 fm and 9.45 fm respectively [142]. A spin glass is also seen in the CrFe alloy system. Chromium has an unusual spin-density-wave antiferromagnetic ground state, by doping with iron, the $Cr_{1-x}Fe_x$ system can show an spin glass transition. If $x < 0.16$ the system exhibits the spin density wave, $x > 0.19$ the system exhibits ferromagnetism, between $0.16 < x < 0.19$ the system exhibits a spin-glass magnetic phase [143]. It has also been shown that the spin density wave and spin glass phase can coexist for $Cr_{1-x}Fe_x$ [144]. A μsr study on the spin-glass phase of the $x = 0.175$ compound shows similar exponential behaviour to that observed in our sample of FeCrAs, with a rapid increase of depolarisation rate, λ as the system is cooled down towards the spin-freezing transition [145]. Further work may be to consider the system $Fe_{1-x}Cr_{1+x}As$, which our own sample may fall into. As Mössbauer meausrements suggest little to no magnetic moment on the iron [122], doping of chromium onto the iron site should drastically change the magnetic coupling between the kagomé lattice and the triangular lattice layers. There may even be phase coexistence between the spin-glass phase observed in this study and the $(1/3, 1/3, 0)$ antiferromagnetism observed by Swainson *et al.* [121]. Further muon beamtime will be used to study, in collaboration, the sample used in the neutron measurement by Swainson *et al.*. In addition, beamtime has also been obtained to perform

a resonant scattering experiment, on the ($^1/_3$, $^1/_3$, 0) antiferromagnetism, to make use of the element specificity, to understand the role of the iron trimers in the magnetic ground state.

4.5 Conclusions

Samples of FeCrAs were grown by the flux method, and show the same metallic heat capacity as presented in the literature. The magnetic ground state, however was very different from ($^1/_3$, $^1/_3$, 0) antiferromagnetism found by Swainson *et al.* Magnetic susceptibility results show a spin-freezing phenomena below 48 K. Muon spin relaxation provided evidence of three distinct magnetic phases. A high temperature regime where the nuclear magnetic moments dominate the muon spectra, a mid-temperature region, between 48 K and 225 K, where the muon spectra is dominated by depolarisation effects from dynamic magnetic field from spin fluctuations, and a low temperature phase, where the spins freeze and the decay rate of muon depolarisation drops. Comparing these results to the literature, this behaviour is characteristic of a spin-glass transition on a kagomé lattice. Although the spin freezing transition does not occur till 48 K, there is evidence of the short-range spin blocks freezing from 225 K. The muon depolarisation decay rate in the 45-225 K regime, fits a Boltzmann-like exponential, with respect to temperature, with an exchange energy of $\Delta = 20.1 \pm 0.4$ meV. Comparing this to the thermal energy of the spin freeze transition of 48 K, $k_BT \approx 4$ meV, an estimate can be made of the exchange interactions within the plane, and between the planes. A Monte-Carlo study by Redpath *et al.* suggests the magnetism in the kagomé lattice remains short-range, unless interactions between the chromium and iron layers are considered. The short-range ordering first appears at 225 K, where $k_BT \approx 20$ meV and agrees with the interaction energy from the muon measurement,$\Delta = 20.1 \pm 0.4$ meV, suggesting the interaction between chromiums in the kagomé lattice, although short-range is around 20 meV. The spin-glass transition is at 48 K, $k_BT \approx 4$ meV and from the Monte-Carlo simulations by Redpath *et al.* can be thought of as the energy at which the interaction between the chromium and iron layers drive the spin freeze transition. The differing results of the spin-glass observed compared to the antiferromagnetism measured by Swainson *et al.*, may be due to doping of chromium on the iron site, strengthening the coupling between layers.

Chapter 5

Helical Spin Structures in FeAs

5.1 Introduction

In this chapter, the magnetic structure of FeAs will be investigated using resonant x-ray scattering. Until recently very little had been published on the binary system FeAs, the crystal and magnetic structure was studied by powder neutron diffraction in 1969-1972 [146–148]. With the discovery of high-temperature superconductivity in the $La[O_{1-x}F_x]FeAs$ system in 2008 [93], the field of iron pnictide based superconductors rapidly emerged, with other superconducting systems being discovered, $(Ba,K)Fe_2As_2$ [94], LiFeAs [95] and, $FeSe_{1-\delta}$ [96]. Since then, interest has picked up on FeAs, especially its magnetic properties. Magnetism and superconductivity are traditionally considered antagonistic phenomena. For conventional s-wave superconductors magnetic moments break up the spin singlet Cooper pairs, destroying the superconductivity [98]. For many of the iron pnictide endmembers, the undoped non-superconducting materials have a spin density wave ground state [149]. Many of these antiferromagnetic systems, such as $BaFe_2As_2$ and LaFeAsO also show high electrical conductivity. Upon chemical doping, high pressure or oxygen deficiency, these systems lose their antiferromagnetic ordering and become superconducting [150–153]. Phonon coupling has been ruled out as the sole mechanism of the superconductivity, as calculations of the $La[O_{1-x}F_x]FeAs$ system show it to be a poor electron phonon superconductor [154]. The existence of adjacent magnetism and superconducting regions in the phase diagrams of these systems suggest magnetic fluctuations may play a role in the origin of the superconductivity in the iron pnictides.

	x	y	z
Fe_1	0.004	0.25	0.199
Fe_2	0.496	0.75	0.699
Fe_3	0.996	0.75	0.801
Fe_4	0.504	0.25	0.301

Table 5.1: Four equivalent iron sites in the orthorhombic unit cell. Coordinates are given as fractions of the lattice parameters

Iron pnictide superconductors, like their cuprate cousins, have a layered crystal structure. All superconducting iron pnictides have active planar layers of tetrahedrally coordinated FeAs. FeAs like the other end members of the iron pnictides is an itinerant magnet, where the conductivity increases in the long-range ordered antiferromagnetic ground state. Recent papers published on FeAs, since the discovery of superconductivity in the iron pnictides, show that the magnetic ground state may be more complicated than previously thought [155, 156].

5.1.1 The MnP Structure

The binary compund FeAs is known to adopt the MnP type structure [146]. This is an orthorhombic structure consisting of distorted $FeAs_6$ octahedra. These octahedra are face sharing along the a-axis and edge sharing along the b- and c-axis. The unit cell has the space group *Pnma* and lattice parameters $a = 5.456$, $b = 3.328$ and $c = 6.031$ Å [146, 156]. There is some confusion in the literature as b and c are often reported interchangeably. The iron atoms sit at the *4c* Wyckoff site, giving rise to four equivalent positions in the unit cell, (1) x, $\frac{1}{4}$, z, (2) $\bar{x}+\frac{1}{2}$, $\frac{3}{4}$,$z+\frac{1}{2}$, (3) $\bar{x}$, $\frac{3}{4}$, $\bar{z}$, and (4) $x+\frac{1}{2}$, $\frac{1}{4}$, $\bar{z}+\frac{1}{2}$. Table 5.1 shows the positions of atoms found by neutron powder diffraction from Rodriguez *et al.* [156], where x and z were found to be 0.004 and 0.199 respectively.

The FeAs crystal structure is shown in figure 5.1, the view along the b-axis, shows the face sharing octahedra along the a-axis. The distorted octahedra are tilted in the ac-plane and not in the bc-plane. The iron layers in the superconducting structures are tetrahedrally coordinated by arsenic, rather than octahedrally coordinated, as in FeAs. Unlike in superconducting structures where iron atoms form a square lattice, there is no lower dimensionality in the binary FeAs structure. The MnP structure is a common

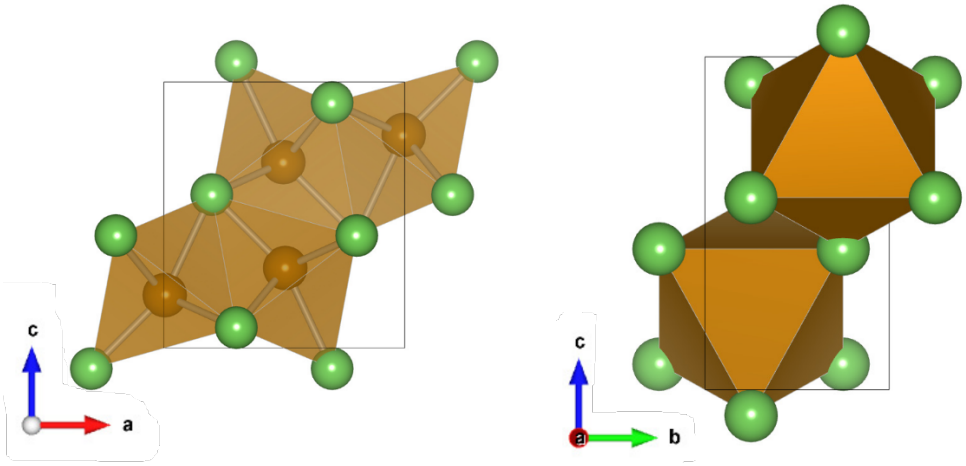

(a) **(b)**

Figure 5.1: Crystal Structure of FeAs. Iron atoms are shown in brown, and Arsenic atoms are shown in green. (a) *a*-*c* plane, (b) *b*-*c* plane.

structure for a number of different binary metal (Cr, Fe, Co, Ru and V) arsenides and phosphides [157, 158], and can be thought of as a distortion of the more common [159] hexagonal NiAs-type structure [157, 160]. Bonding interactions between the metal ions can lead to a phase transition between the two structures [161, 162].

5.1.2 Magnetism in FeAs

Results from a neutron powder diffraction study in 1972 [147] show a transition to a long-range ordered antiferromagnetic state at 77 K. Refinement of the neutron powder diffraction found a helical magnetic structure with a wavevector of $q = (0, 0, 0.375)$ best described the data. They also found a moment of 0.5 μ_B. Isostructural MnP has a rich magnetic phase diagram with competing collinear and non-collinear ground states [163, 164], but the zero-field ground state of MnP is the a magnetic helix [165]. A more general relation between the MnP type crystal structure and the helical magnetic structure may exist [166].

In 2008, a magnetic susceptibility and transport study by Segawa *et al.* [155], gave results that disagree with a simple helical magnetic structure. The susceptibility, shown in figure 5.2 shows a kink at 70 K in the *a*- and *b*-direction but not in the *c*-direction (Segawa *et al.* use a convention where *b* and *c* are swapped). Although this agrees with the helical

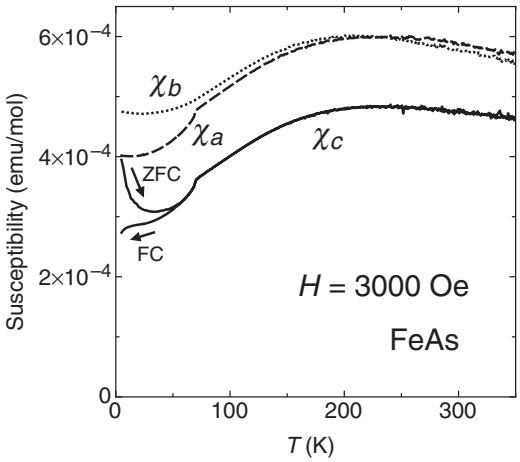

Figure 5.2: Magnetic susceptibility data measured along the *a*-, *b*- and *c*-directions, taken from Segawa *et al.* [155]. The *b* and *c*-axis labelling are the reverse of the convention used in this study.

structure, the susceptibility along the *b*-axis is lower than along *a*, and only the *b*-axis displays a magnetic field splitting. The anisotropy in the susceptibility between the *a*- and *b*-axes raises doubt as to the simple spin helix, suggesting the magnetic ground state is more complicated, although the lack of features in the *c*-axis measurement suggests the magnetic moment is fixed to the *a*-*b* plane. The resistivity measurement by Segawa *et al.*, confirmed the itinerant behaviour of FeAs, with the resistivity decreasing below 150 K. A kink was also observed in the resistivity at 70 K. Segawa *et al.* drew parallels to another itinerant magnet CrB_2, which was also reported to have a helical ground state [167, 168], where NMR studies have recently questioned the helical structure [169].

In 2011 a neutron diffraction study was carried out by Rodriguez *et al.* [156] on FeAs, using a combination of powder and polarised single-crystal neutron diffraction. This study reported a slightly different incommensurate wavevector of (0,0,0.395). Powder diffraction studies cannot differentiate between a spin helix and a collinear spin-density-wave. The polarised neutron diffraction results confirmed a spin helix, but the spin flip ratios suggest a 15% larger moment along the *b*-axis than the *a*-axis, suggesting a slightly elliptical spin helix.

Shubnikov groups are not sufficient to solve the helical incommensurate magnetic

structure [170, 171], and representational analysis has to be employed. For representational analysis the program Baslreps was used. There are 8 symmetry elements of the crystallographic space group *Pnma*, these are E, C_{2x}, C_{2y}, C_{2z}, I, σ_x, σ_y, and σ_z. The little group G_q is formed by those symmetry elements of *Pnma* which leave the incommensurate wavevector $q = (0, 0, 0.395)$ unchanged. The little group G_q is composed of the four symmetry elements E, C_{2Z}, σ_x, σ_y. The matrix form of these symmetry elements, in the basis of the unit cell, are given below in 5.1

$$E = \begin{pmatrix} 1 & 0 & 0 \\ 0 & 1 & 0 \\ 0 & 0 & 1 \end{pmatrix}, \quad C_{2z} = \begin{pmatrix} -1 & 0 & 0 \\ 0 & -1 & 0 \\ 0 & 0 & 1 \end{pmatrix}$$
$$\sigma_x = \begin{pmatrix} -1 & 0 & 0 \\ 0 & 1 & 0 \\ 0 & 0 & 1 \end{pmatrix}, \quad \sigma_y = \begin{pmatrix} 1 & 0 & 0 \\ 0 & -1 & 0 \\ 0 & 0 & 1 \end{pmatrix} \tag{5.1}$$

Upon application of the symmetry elements in subgroup G_q on the atom postions given in table 5.1, Fe_1 and Fe_2 transform into each other by way of a return vector, $e^{-iq\pi}$, similarly Fe_3 and Fe_4 transform into each other. $Fe_{1,2}$ is no longer equivalent to $Fe_{3,4}$, creating two orbits in the magnetic structure with a phase difference between them. This type of magnetic structure is often termed a double-helical structure [172–175].

5.2 Experimental

The sample was grown by an iodine vapour transport method by our collaborator K. A. Ziq from the King Fahd University of Petroleum & Minerals [131]. The growth method resulted in a selection of single crystals of typical dimensions of hundred of microns. Several samples were studied using the in-house four-circle diffractometer, and a single crystal selected, with a natural c-axis facet and a sharp $(0, 0, 2)$ reflection with a rocking width of 0.0025°. This single crystal was used for all subsequent experiments.

Resonant x-ray diffraction experiments were carried out at both the soft Fe $L_{\mathrm{II/III}}$ and the hard Fe K absorption edges. For the Fe L edges experiments the beamlines ID08, ESRF and I10, Diamond were used. For the K edge experiments the beamline P09, Petra III was used [176]. All three beamlines are situated on an undulator insertion device.

ID08 does not provide post-scatter polarisation analysis. I10 does provide post-scatter polarisation analysis, as well as full control of incident linear polarisation, allowing for full polarisation analysis measurements. ID08 and I10 are equipped with a Janis liquid helium cryostat, enabling base temperatures of 12 K to reached. P09 has a six-circle diffractometer with post-scatter polarisation analysis, and a Joule-Thompson cryostat, enabling a base temperature of 1.4 K.

For all diffraction experiments the sample was mounted with the c-axis surface normal. For the ID08 and I10 experiments the sample was mounted with the b-axis in the scattering plane. For the P09 experiment the [-1,0,0] reciprocal direction was used as the azimuthal reference vector. In all cases vertical scattering geometry was used.

5.3 Results

In this section the results from the resonant scattering experiments will be described. All experiments were performed on the same sample of FeAs. Two experiments were performed at the Fe $L_{\mathrm{II/III}}$ absorption edge using the beamlines ID08, ESRF and I10, Diamond. The Fe K edge experiment was performed at P09, Petra III.

5.3.1 ID08 REXS experiment

At the Fe L_{III} energy ($\approx$ 707 eV) the radius of the Ewald sphere limits access along the l reciprocal direction to $l = 0.68$. Within this limit two resonant reflections were found along the l direction, at positions $l = 0.389$ and $l = 0.611$. A scan along the [00L] direction is shown in figure 5.3. The shape of the peaks are asymmetric, with the peak at $l = 0.611$ having the reverse asymmetry to the $l = 0.389$ reflection. A likely explanation of the asymmetric peak shape, is the shape of the energy profile coming from the undulator. The (0,0,0.611) reflection having the reverse shape of the [0,0,0.389] reflection reveals the (0,0,0.611) to be a satellite of the (0,0,1) forbidden Bragg peak. The two reflections can be indexed up as (0,0,0)+(0,0,τ) ($\boldsymbol{\tau}$), and (0,0,1)-(0, 0, τ) (1 $-$ $\boldsymbol{\tau}$), where $\tau = 0.389$.

Energy resonances of the two reflections, without post-scatter polarisation analysis are shown in figure 5.4. These scans were performed by decreasing the energy of the incident x-ray whilst maintaining the diffraction condition for the magnetic peak. The resonances were measured with both σ- and π-polarised incident light. Assuming a dipole-dipole transition (E1E1) is responsible for the resonant feature, the transition is from the Fe 2p orbital to the Fe 3d band. Exciting into the Fe 3d causes the large sensitivity to the

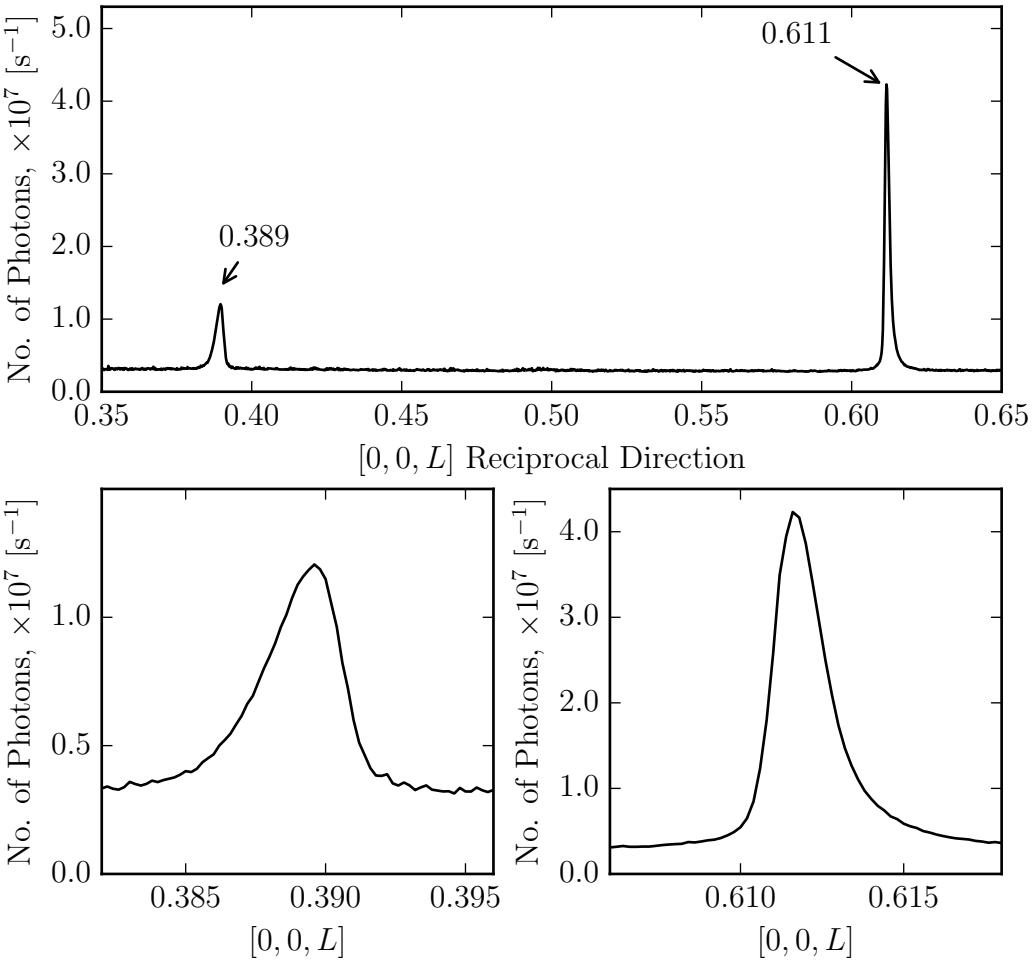

Figure 5.3: Scan along the L reciprocal lattice direction, at the Fe L_{III} edge. Due to the large wavelength of the Fe L_{III} edge the Ewald sphere is limited to $0.68c^*$.

magnetism, as it is the *3d* orbitals that are the magnetically active spin-polarised band for iron. The $\boldsymbol{\tau}$ reflection shows a marked difference between the two channels, this is sufficient to rule out charge scattering and simple collinear structures along the *a*-, *b*-, or *c*-directions assuming a $E1E1$ origin to the scattering. Without post-scatter polarisation analysis it is not possible to draw more specific conclusions. The $1-\boldsymbol{\tau}$ reflection shows very different behaviour, showing equal intensity with incident σ- and π-polarised light. This indicates a different origin for the $1-\boldsymbol{\tau}$ peak to the $\boldsymbol{\tau}$ peak. The $\boldsymbol{\tau}$ and $1-\boldsymbol{\tau}$ reflections occur at θ angles of 34.4° and 63.7°, respectively. These angles are not close to 45° or 90°,

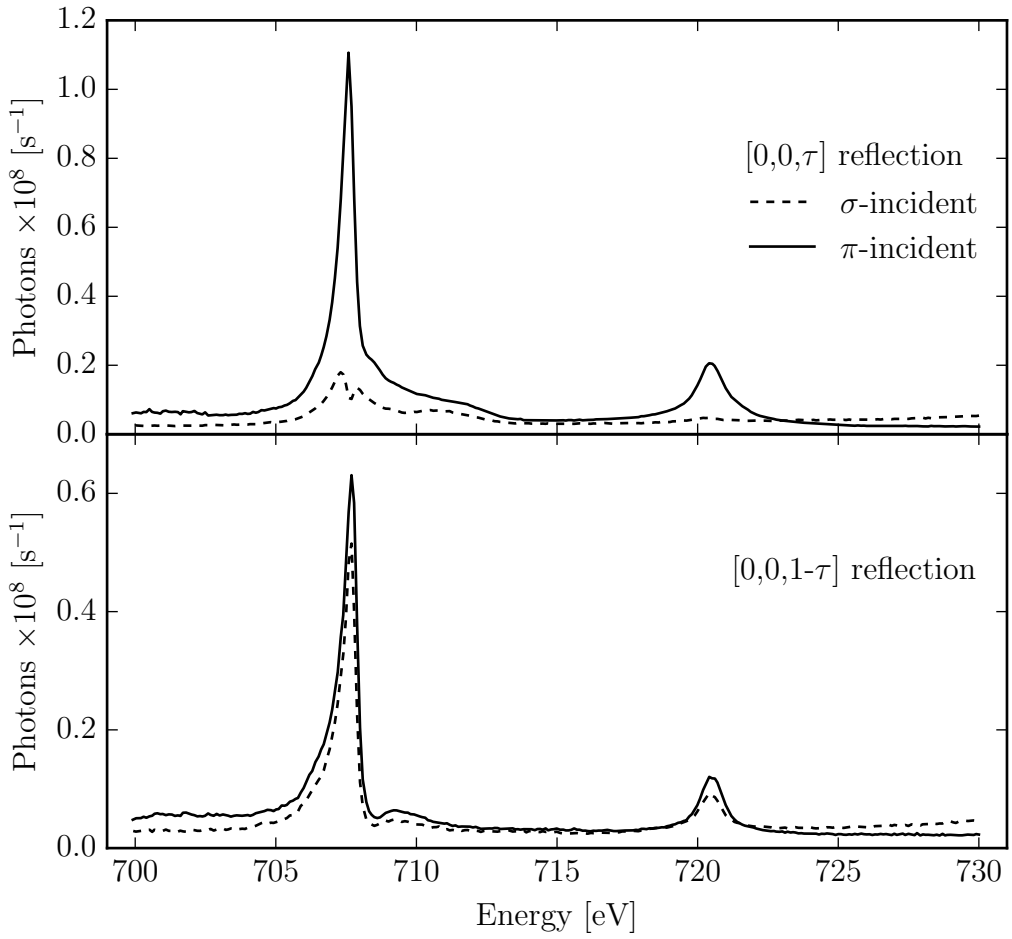

Figure 5.4: Energy resonance of the magnetic satellite peaks, $(0, 0, \tau)$ (top) and $(0, 0, 1-\tau)$ (bottom), with σ- and π- polarised incident light. No post-scatter polarisation analysis was used.

which may cause a suppression of scattering due to the θ dependences of the scattering amplitude.

The energy scans were repeated with circular-positive and circular-negative light, shown in figure 5.5. For the $\boldsymbol{\tau}$ reflection the intensity in the circular-positive channel is roughly twice that of the circular-negative channel. This is a good indication of a non-collinear spin structure. The $1 - \boldsymbol{\tau}$ reflection has equal intensity in the circular-positive and circular-negative channels. This again shows very different behaviour to the $\boldsymbol{\tau}$ peak.

A temperature dependence of the $(0, 0, \tau)$ peak was performed by measuring the diffrac-

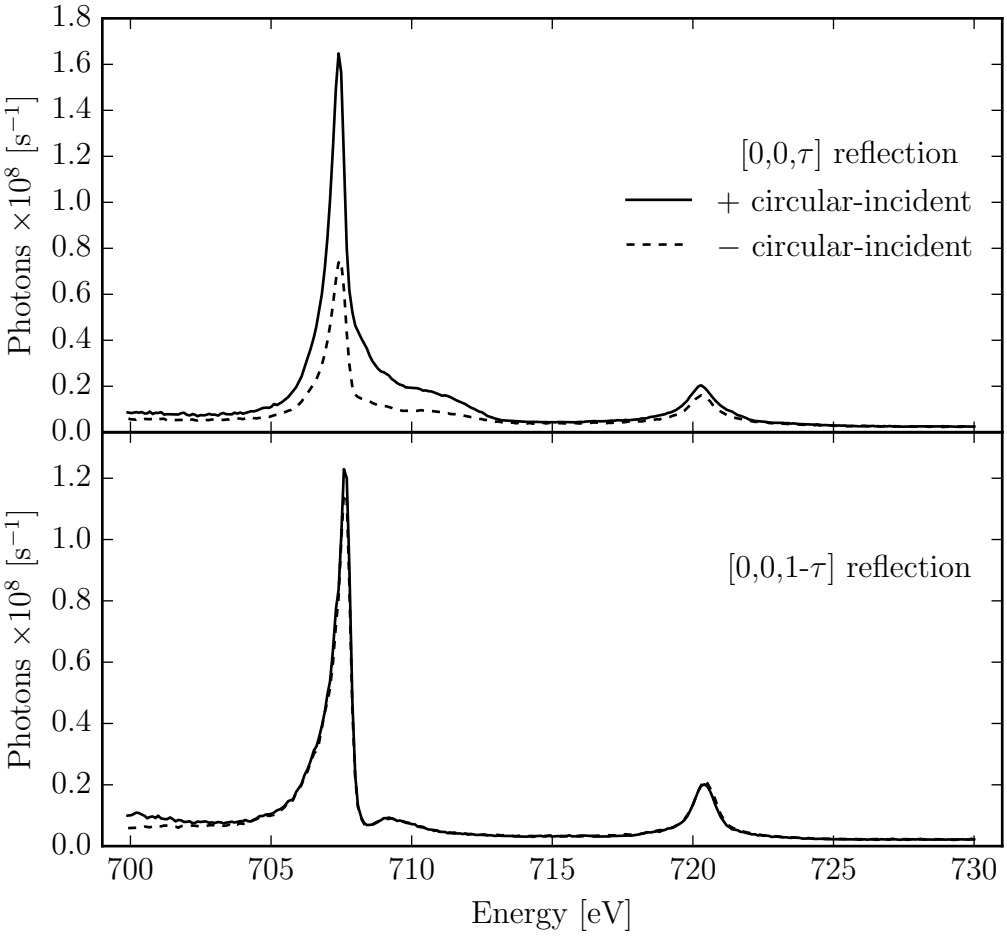

Figure 5.5: Energy resonance of the magnetic satellite peaks, $(0, 0, \tau)$ (top) and $(0, 0, 1-\tau)$ (bottom), with circular-positive and negative-polarised incident light.

tion in the $[0, 0, L]$ direction on warming. The results are shown in figure 5.6. The magnetic $(0, 0, \tau)$ peak disappears at 70.5 K. The temperature dependence was analysed by fitting the $[0, 0, L]$ scans using a Lorentzian-squared peakshape. The wavevector is temperature dependent appearing at $q = 0.402$ at 70.5 K, and moving gradually to $q = 0.389$ at 12 K. The neutron study be Rodriguez *et al.* [156] found that the wavevector shift followed a quadratic path with a 0 K intercept at 0.389. The temperature dependence in figure 5.6 shows similar quadratic behaviour for the wavevector as that reported by Rodriguez *et al.* [156], but with a small difference at higher temperatures, as the magnetic

peak disappears at $q = 0.402$, compared to the neutron studied which found the peak moved all the way to $q = 0.404$. The neutron diffraction measurement was of lower resolution with a peak width of 0.03 r.l.u. which is six times larger than the total movement of the incommensurate q-vector, compared to our x-ray study, with a width of 0.002 r.l.u. The quadratic shape of the wavevector temperature dependence suggests the incommensurate wavevector locks into a constant, potentially commensurate value of 0.389, or $^{7}/_{18}$ at low temperatures. The temperature dependence of the width of the magnetic peak was extracted from the measurement and used to calculate the correlation length of the magnetism. As a Lorentzian-squared peakshape was the best fit to the reflection profile in the L-direction, the correlation length can be calculated simply using the relation shown in equation 5.2.

$$\Delta x = \frac{1.38127}{\Delta q} \tag{5.2}$$

The correlation length is shown in figure 5.6 in black circles. At the base temperature of 12 K, the magnetism is most correlated with a correlation length of 5000 Å, roughly 830 unit cells. Upon warming the magnetism becomes less correlated as expected, till around 40 K, where the correlation length flattens off around 4200 Å, about 700 unit cells. Above 64 K, the correlation length increases, unusually the magnetism becomes more correlated until the magnetic reflection disappears at T_N. The integrated intensity is shown in the same figure, but in open circles. The integrated intensity was fitted using a critical exponent function, shown in equation 5.3 below.

$$I(T) = I_0 \left(\frac{T_N - T}{T_N} \right)^{2\beta} \tag{5.3}$$

The exponent $\beta = 0.124 \pm 0.009$ was found by fitting the data in the region close to the transition (65-70.5 K), this fit also refined the transition temperature to $T_N = 70.59 \pm 0.06$ K. The exponent is close to the value reported by Rodriguez *et al.* [156]. In their study they used the intensity of 12 points in a temperature range from 55-70 K to fit the critical exponent, whilst this study used 35 data points within 5 K of the transition.

Figure 5.7 shows a log-log plot of the reduced temperature which is defined as $^{(T_N - T)}/_{T_N}$ against the scattering intensity. If the magnetisation of the system follows the function given in equation 5.3, then a log-log plot would show a straight line with an intercept of zero and a gradient of 2β. The dashed line shows the result of a least-square fit of $y = mx$,

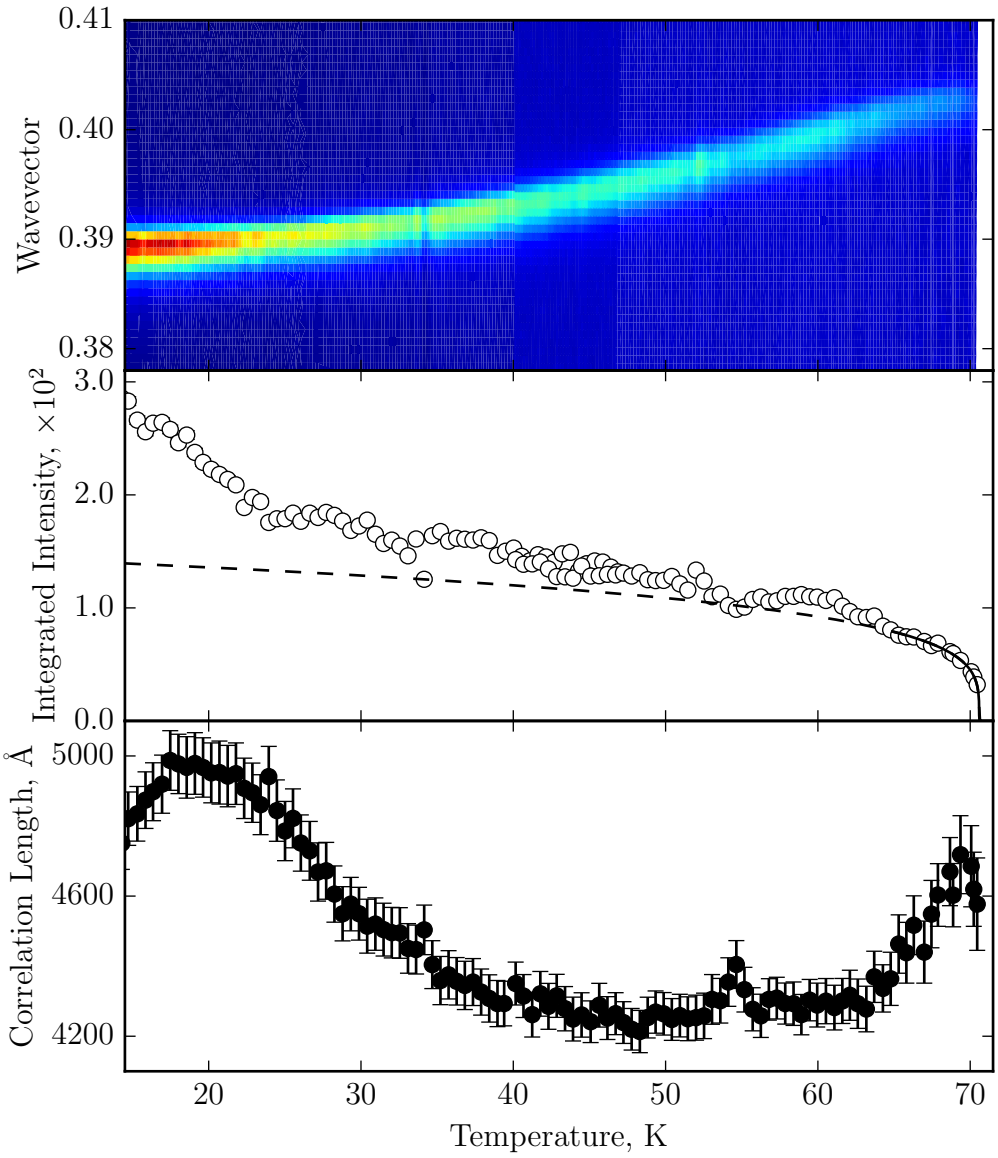

Figure 5.6: Temperature dependence of the (0,0,τ) magnetic diffraction peak, (top) shows the change in incommensurate wavevector as a function of temperature. (middle) The integrated intensity is shown in open circles. (bottom) The correlation length calculated from the peak, shown in black circles.

with the intercept fixed at zero. The gradient is $m = 0.244 \pm 0.002$, which yields a β value of $\beta = 0.122 \pm 0.001$.

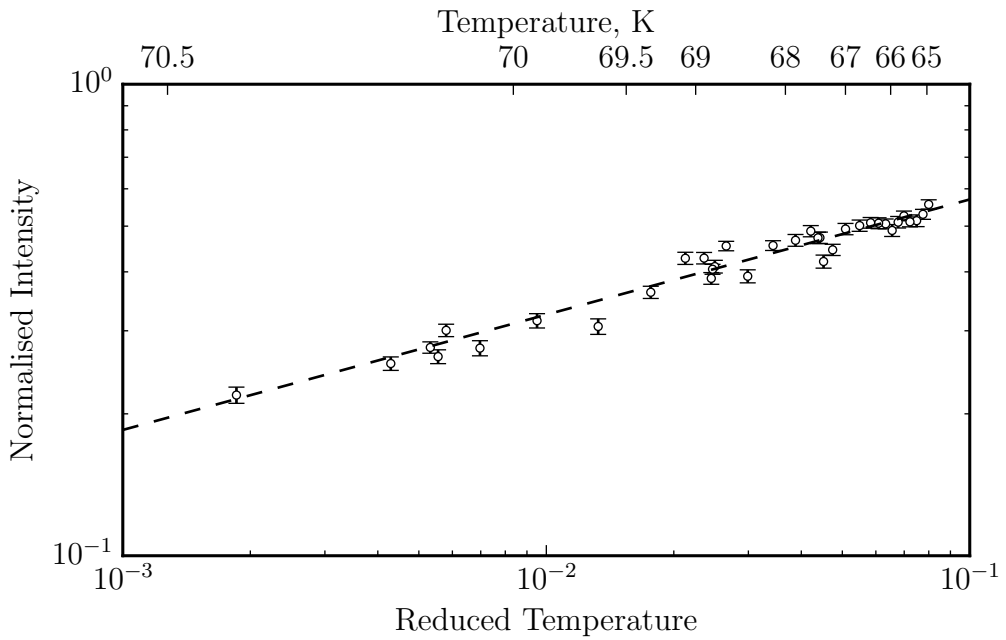

Figure 5.7: A log-log plot of the magnetic x-ray scattering intensity from the $(0, 0, \tau)$ reflection as a function of reduced temperature. A gradient of a line $y = mx$ which passes through zero has been fit to the data. The gradient was found to be $m = 0.244 \pm 0.002$.

5.3.2 I10 REXS experiment

The same sample was mounted in the ultra-high vacuum diffractometer, RASOR at I10. The incident x-ray source was tuned to the Fe L_{III} absorption edge and the τ and $1 - \tau$ diffraction peaks were found. A full linear polarisation analysis was carried out on both peaks and the results are shown in figure 5.8. In this measurement the incident linear light is rotated through a full 180°, and at each incident polarisation angle, the polarisation state of the scattered beam is measured. Figure 5.8 plots the incident polarisation angle against the outgoing polarisation using Poincaré-Stokes parameters, P_1 and P_2 (these are defined in section 2.1.1). The results show a very different polarisation analysis for the τ and $1 - \tau$ reflections, confirming they have very different origins. The solid and dashed lines in figure 5.8 show the results of simulations based on structure factor calculations which are explained in the next section.

For the τ reflection the incident x-ray beam was polarised to both circular positive

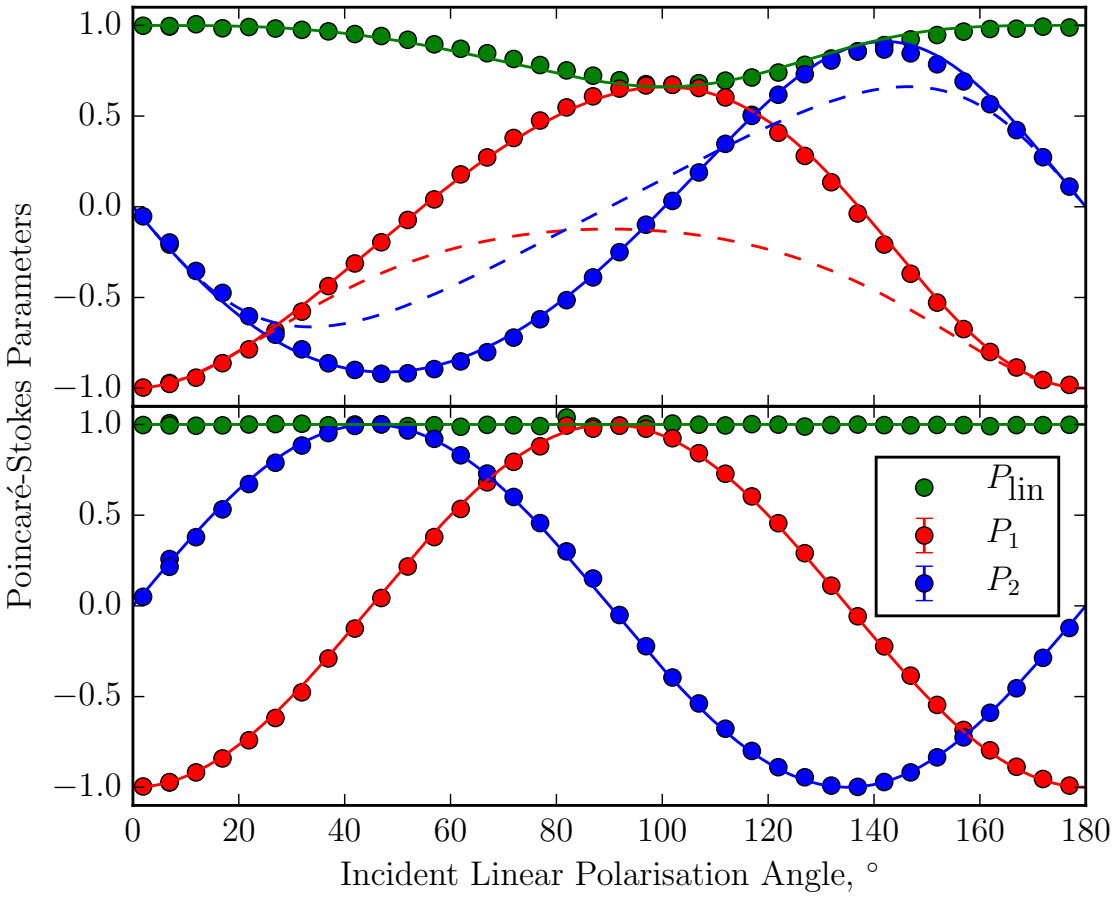

Figure 5.8: Full linear polarisation analysis (FLPA). The linear polarisation state of the incident beam, was rotated through a full 180°, at each incident polarisation angle, the polarisation state of the scattered beam was measured, and described using the Poincaré-Stokes parameters. (Top) FLPA measured on the $(0, 0, \tau)$ reflection. (bottom) FLPA measured on the $(0, 0, 1 - \tau)$ reflection. The lines are a model based on the derived structure factor in section 5.4.2.

and circular negative and the polarisation state of the outgoing beam was measured by a rotation of the polarisation analyser crystal. The results of this are shown in figure 5.16, and should yield information about the chirality of the magnetic helix.

5.3.3 P09 REXS experiment

A resonant x-ray experiment was carried out at the hard x-ray energy of the Fe K absorption edge. This type of experiment allows for a far wider field of access to reciprocal space than the technically difficult experiments at the soft energies of ID08 and I10 experiments, but at a cost of sensitivity to the magnetism. A typical $E1E1$ transition at the Fe K absorption edge, excites a Fe $1s$ electron into the empty Fe $4p$ band. The sensitivity to magnetism arises from any overlap, or hybridisation, between the Fe $3d$ and Fe $4p$ bands.

A survey of resonant reflections was conducted and satellite reflections were found at $(0, 0, 2-\tau)$, $(0, 0, 2+\tau)$, $(0, 0, 4-\tau)$, $(0, 0, 4+\tau)$, as well as at $(0, 0, 2\tau)$, and $(0, 0, 3\tau)$. An off-axis reflection was also observed at the $(1, 0, 3-\tau)$ position. No reflections were found at positions away from the odd forbidden Bragg peaks ($(0, 0, 1\pm\tau)$ & $(0, 0, 3\pm\tau)$). Figures 5.9, 5.10 and 5.11 show the resonances and reciprocal space scans of the $(0, 0, 2-\tau)$, $(0, 0, 2\tau)$, and $(0, 0, 3\tau)$. All three types of satellite reflection show a sharp resonant feature at 7110 eV. The reciprocal space scans show the $(0, 0, 2-\tau)$ peak to be the sharpest with a width of 0.0006 ± 0.0001 r.l.u., whist the 2τ and 3τ reflections are wider with widths of 0.0019 ± 0.0001 and 0.0014 ± 0.0001 r.l.u. respectively. The $\boldsymbol{\tau}$ and 2τ reflections were found only in the $\sigma-\pi$ channnel and not in the $\sigma-\sigma$ channel, whilst the 3τ reflection was found in both channels but was stronger in the $\sigma-\sigma$ channel. An $E1E1$ type transition can produce $\boldsymbol{\tau}$ and $2\boldsymbol{\tau}$ reflections, but a quadrupole-quadrupole type transition (E2E2) is required to explain the presence of a 3τ reflection. An $E2E2$ transition would be an excitation from the $1s$ orbital into the magnetically active $3d$ spin-polarised band.

An azimuthal measurement was performed on the $(0, 0, 2-\tau)$ reflection, shown in figure 5.12. The azimuth direction is a rotation of the sample around the scattering vector, maintaining the diffraction condition (A rotataion around U_3 in figure 2.2). In this measurement reciprocal space $[0, 0, L]$ scans are collected as a function of azimuthal angle around the scattering vector. The zero point on the azimuthal axis is defined when the $[-1, 0, 0]$ reciprocal vector is in the scattering plane away from the incident beam. The lines in figure 5.12 show the simulations of azimuths based on the structure factor explained in the next section. Qualitatively, this azimuth data rules out a simple non-elliptical helix. For the $(0, 0, 2-\tau)$ reflection, the scattering vector is parallel to the magnetic propagation direction, an azimuthal measurement rotates around the magnetic propagation vector. If the magnetic helix was circular, then there would be no change in

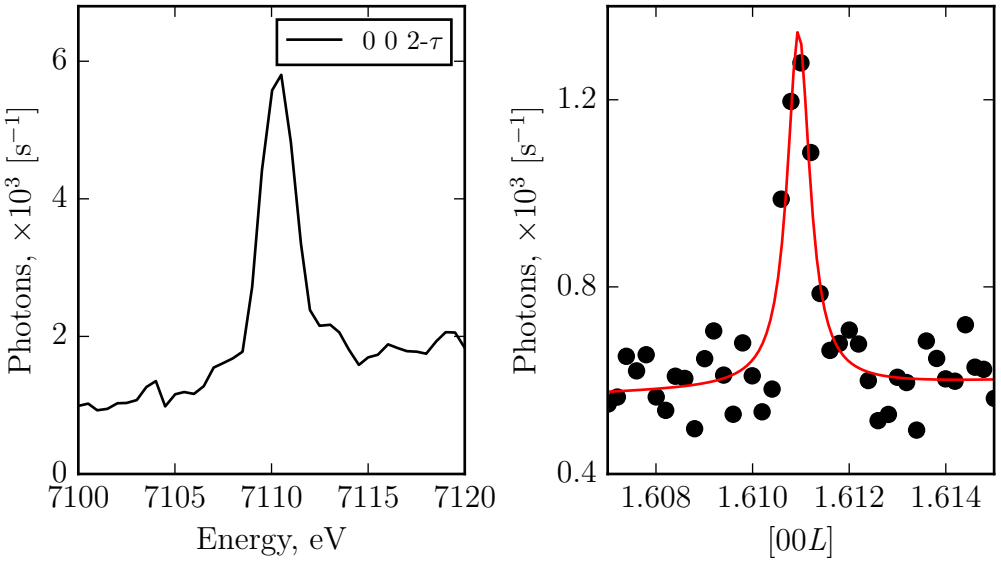

Figure 5.9: Energy scan of resonance of the $(0, 0, 2 - \tau)$ magnetic reflection (left). $[00L]$ Reciprocal space scan of $(0, 0, 2 - \tau)$ (right). Scans were performed in the $\sigma - \pi$ channel.

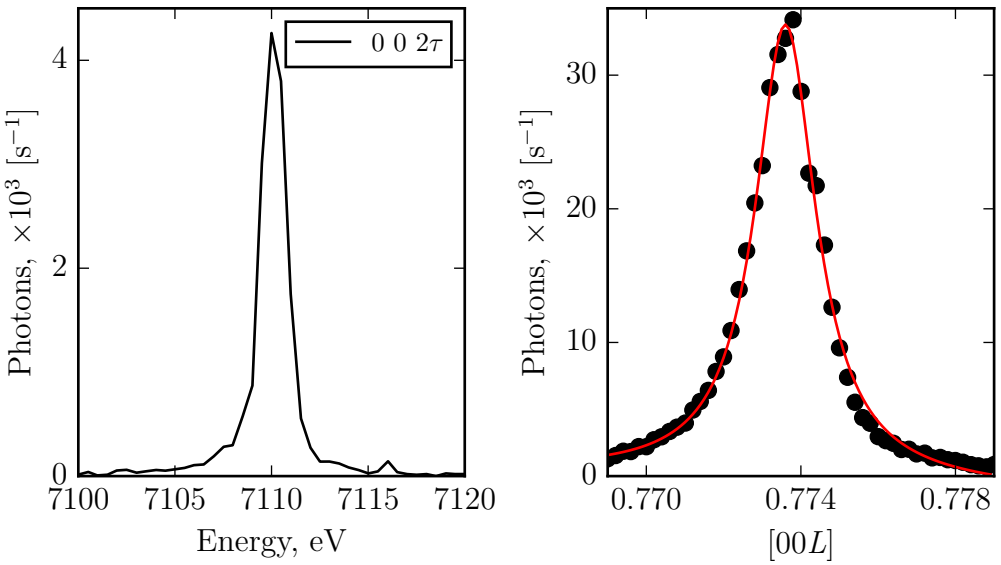

Figure 5.10: Energy scan of resonance of the $(0, 0, 2\tau)$ magnetic reflection (left). $[00L]$ Reciprocal space scan of $(0, 0, 2\tau)$ (right). Scans were performed in the $\sigma - \pi$ channel.

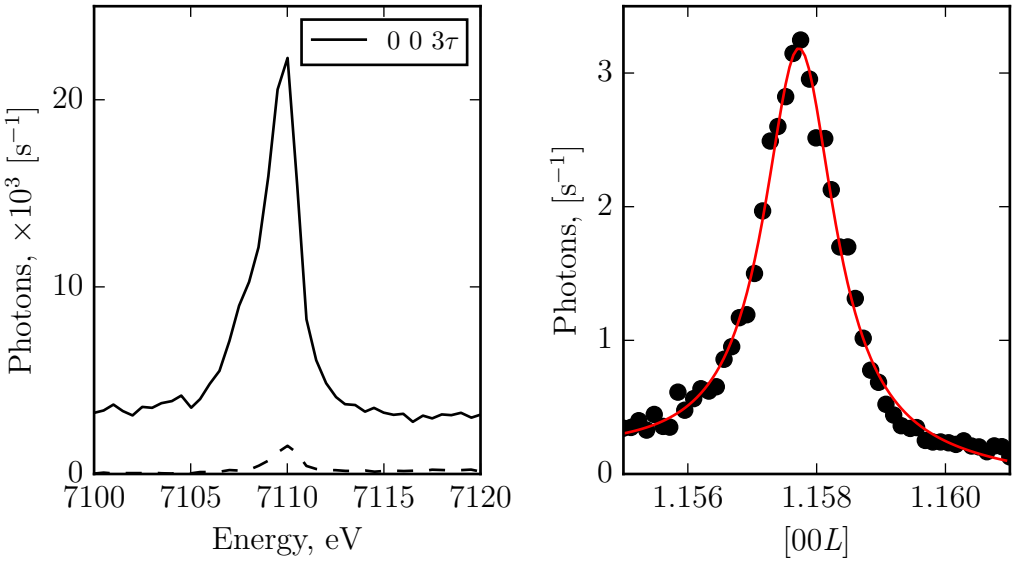

Figure 5.11: Energy scan of resonance of the $(0, 0, 3\tau)$ magnetic reflection (left). $[00L]$ Reciprocal space scan of $(0, 0, 3\tau)$ (right). Scans were performed in the $\sigma - \sigma$(solid) and $\sigma - \pi$ (dashed) channel.

moment direction upon an azimuthal rotation, and constant intensity would be expected.

An azimuthal measurement was performed on the off-axis magnetic reflection $(1, 0, 3-\tau)$. This reflection is approximately 23° away from the surface normal. A consequence of the off-axis nature of the reflection is the volume absorption by the sample will not be constant as the sample is rotated through the azimuth. This a large source of error on an azimuthal measurement.

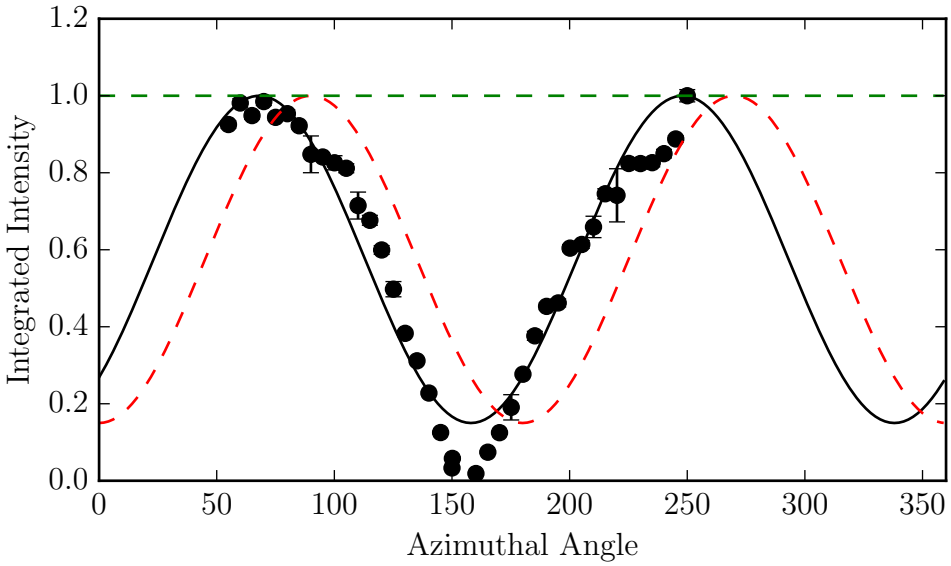

Figure 5.12: Azimuthal measurement of the $(0, 0, 2-\tau)$ magnetic Bragg peak. The dashed and solid lines show predictions made using the structure factor formulated in section 5.4.2. The green dashed line shows the expected azimuth for circular helical magnetic structure. The red dashed line shows the expected azimuth for a elliptical helical magnetic structure ($m_a : m_b = 1 : 2.58$). The solid black line shows the prediction for the elliptical helix rotated by -22° around the *c*-axis.

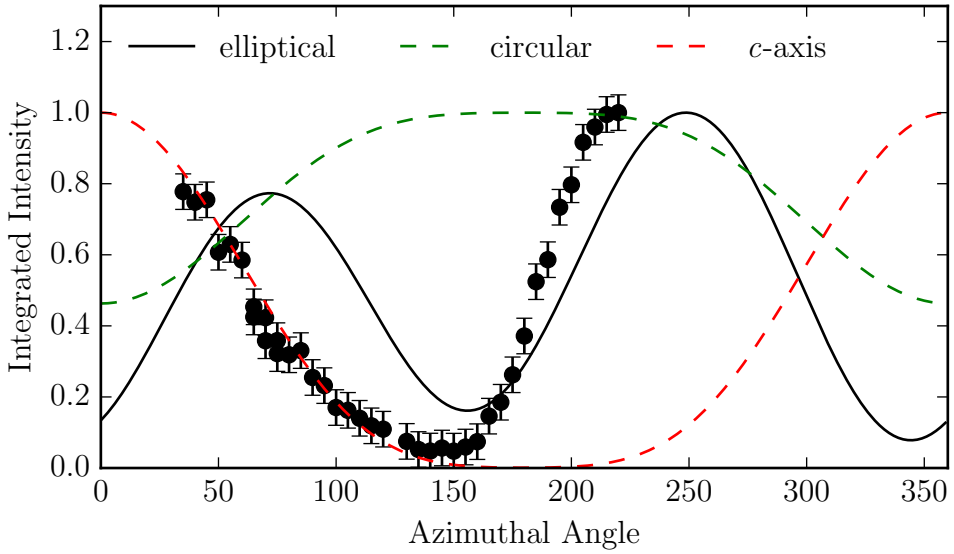

Figure 5.13: Azimuthal measurement of the $(1, 0, 3-\tau)$ magnetic Bragg peak. The green dashed line shows the predicted azimuth for a circular helical magnetic structure. The black solid lines shows the prediction for an elliptical rotated magnetic structure. The red dashed line shows predicted c-axis structure. These predictions were calculated using the structure factor formulated in section 5.4.2.

5.4 Discussion

5.4.1 Scattering at the Critical point of Phase Transition

The temperature dependence of the correlation length of the magnetism shows unusual behaviour. There appears to be two mechanisms acting on the magnetism, one which causes the usual behaviour of the system becoming more correlated as it cools. There is a second mechanism at high temperatures which is acting to make the magnetism less correlated upon cooling. This type of behaviour is similar to the inverse melting phenomena that has been observed for charge ordering in the nickelate, $La_{5/3}Sr_{1/3}NiO_4$ [177]. The flat region of low correlation between 40-65 K is a consequence of these two competing mechanisms.

The scaling theory of critical phase transitions states that the critical exponent β of the phase transition should only be dependent on the universality class of the system [13]. This means for a continuous phase transition the critical exponent should depend on the dimensionality of the system, *i.e.* 1D, 2D, 3D, the dimensionality of the order parameter, *i.e.* for magnetism, Ising, XY, Heisenberg, and finally whether the forces are short or long range [13]. The critical exponent from the x-ray magnetic data was found to be $\beta = 0.122 \pm 0.002$. For a 3D XY model, the typical class for a helical structure, the critical exponent has been predicted to be 0.345, this is quite different from the observed value. The observed value of β is closer to that of the 2D Ising model of 0.125, which is inconsistent with a helical magnetic structure. The measured value of β is similar to that found in K_2NiF_4 and K_2MnF_4 with values of 0.138 ± 0.004 and 0.15 ± 0.01respectively [178,179], both these systems are best described by a 2D Heisenberg moment. Kawamura has shown that chirality makes a difference to the universality class [180–182]. A helical magnetic structure has a chiral degeneracy, as a left-handed helix and a right-handed helix are equally favoured. Kawamura predicted a value of $\beta = 0.253$ for a chiral helical magnet [180–182], which was later shown to consistent with the critical scattering in archetypal helical magnet $\beta-MnO_2$ [183]. Although this is closer to the measured value of β than the 2D XY case, it is still significantly different. This unexpected critical exponent combined with the unusual correlation length behaviour, suggests the magnetism in FeAs is more complicated than a simple helical magnet.

5.4.2 Structure Factor Calculation

To explain the appearance of both $(0, 0, \tau)$ and $(0, 0, 1-\tau)$ reflections, the structure factor needs to be considered.

There are four iron sites in the unit cell of FeAs, given in table 5.1, taking positions (1) x, $\frac{1}{4}$, z, (2) $\bar{x}$+$\frac{1}{2}$, $\frac{3}{4}$,z+$\frac{1}{2}$, (3) $\bar{x}$, $\frac{3}{4}$, $\bar{z}$, (4) x+$\frac{1}{2}$, $\frac{1}{4}$, $\bar{z}$+$\frac{1}{2}$ where $x = 0.004$ and $z = 0.199$. The general conditons for reciprocal space positions of the Bragg peaks from the crystal structure are given by if $h = 0$, then k+$l = 2n$ and if $l = 0$, then $h = 2n$. This means along the $[0, 0, L]$ direction, only *even* Bragg peaks exist.

For a $E1E1$ resonance the magnetic structure factor for a reflection k can be written as a polarisation factor $\boldsymbol{\varepsilon}' \times \boldsymbol{\varepsilon}$, and a sum of atomic phase factors multiplied by the magnetic axis for each atom, $e^{i\mathbf{k}\cdot\mathbf{R}_h}\mathbf{m}(\mathbf{R}_h)$, over the whole crystal, where $\mathbf{k}$ is the reciprocal lattice vector, and $\mathbf{R}_h$ is the position vector to the atom h, as shown in equation 5.4.

$$f = -i\frac{1}{N_0}\frac{3}{4\pi|\mathbf{q}|}\left(F^1_{-1} - F^1_{+1}\right)(\boldsymbol{\varepsilon}' \times \boldsymbol{\varepsilon}) \cdot \sum_h^V e^{i\mathbf{k}\cdot\mathbf{R}_h}\mathbf{m}(\mathbf{R}_h) \tag{5.4}$$

where N_0 is the number of unit cells, and F^L_M are dimensionless resonance strength terms dependent on atomic properties defined in section 2.1.8, and $\mathbf{q}$ is the wavevector of the incident x-ray.

For the magnetic helix, the magnetic axis is fixed in a plane perpendicular to the propagation vector. In the case of FeAs the magnetic axis is fixed in the a-b plane, and rotates as you move along the c axis. We can describe this magnetisation vector using equation 5.5, where $\boldsymbol{\tau}$ is the propagation vector, $\mathbf{r}$ is a position vector in the crystal, χ can be ± 1 and describes the chirality of the helix and is ψ_n is a phase shift for the orbit on atom n. For completeness the factors S_a and S_b are included as these describe the size of the moment along the respected direction, for a circular helix these are equal.

$$\mathbf{m}_{n,j}\left(\mathbf{r}_{\mathbf{n,j}}\right) = S_a \cos\left(\boldsymbol{\tau}\cdot\mathbf{r}_{n,j} - \psi_n\right)\hat{\mathbf{a}} + S_b \cos\left(\boldsymbol{\tau}\cdot\mathbf{r}_{n,j} - \psi_n + \chi\frac{\pi}{2}\right)\hat{\mathbf{b}} \tag{5.5}$$

These can be simplified using Euler's formula, $e^{i\theta} = \cos(\theta) + i\sin(\theta)$, to give the result in terms of exponentials given in equation 5.6. Here the magnetic helix is expressed as a complex vector, where the direction of the magnetic moment vector is independent of $\boldsymbol{\tau}$

and position $\mathbf{r}$.

$$\begin{aligned}\mathbf{m}_{n,j}\left(\mathbf{r}_{n,j}\right) &= \frac{S_a}{2}\left[e^{i\boldsymbol{\tau}\cdot\mathbf{r}_{n,j}}e^{-i\psi_n} + e^{-i\boldsymbol{\tau}\cdot\mathbf{r}_{n,j}}e^{i\psi_n}\right]\hat{a} + \frac{S_b}{2}\left[e^{i\boldsymbol{\tau}\cdot\mathbf{r}_{n,j}}e^{-i\psi_n}e^{i\chi\frac{\pi}{2}} + e^{-i\boldsymbol{\tau}\cdot\mathbf{r}_{n,j}}e^{i\psi_n}e^{-i\chi\frac{\pi}{2}}\right]\hat{b} \\ &= \frac{e^{i\boldsymbol{\tau}\cdot\mathbf{r}_{n,j}}e^{-i\psi_n}}{2}\left[S_a\hat{a} + i\chi S_b\hat{b}\right] + \frac{e^{-i\boldsymbol{\tau}\cdot\mathbf{r}_{n,j}}e^{i\psi_n}}{2}\left[S_a\hat{a} - i\chi S_b\hat{b}\right] \\ &= \frac{e^{i\boldsymbol{\tau}\cdot\mathbf{r}_{n,j}}e^{-i\psi_n}}{2}\mathbf{M} + \frac{e^{-i\boldsymbol{\tau}\cdot\mathbf{r}_{n,j}}e^{i\psi_n}}{2}\mathbf{M}^* \qquad (5.6)\end{aligned}$$

Where $\mathbf{M} = \left[S_a\hat{\mathbf{a}} + i\chi S_b\hat{\mathbf{b}}\right]$

We can simplify the structure factor further by using the lattice relation that any point in the crystal can be defined by a position vector $\mathbf{r}_{n,j}$, from some arbitrary origin. Due to the periodic nature of a lattice this vector can be split into two parts $\mathbf{r}_{n,j} = \mathbf{l}_j + \mathbf{d}_n$, a set of vector $\mathbf{l}_j$, defining the origin of j^{th} unit cell, and a vector $\mathbf{d}_n$ describing the position of n^{th} atom in the unit cell. When using the basis vectors of the unit cell, a, b, c, the vector $\mathbf{l}_j$ takes integer values, and $\mathbf{d}_n$ takes fractional coordinates. The general structure factor shown in equation 5.4 can be simplified for a magnetic helix, using the magnetisation vector shown in equation 5.6.

$$\begin{aligned}f &\propto (\boldsymbol{\varepsilon}'\times\boldsymbol{\varepsilon})\cdot\sum_{n=1}^{4}\sum_{j}^{\infty}e^{i\mathbf{k}\cdot\mathbf{r}_{n,j}}\left(\frac{e^{i\boldsymbol{\tau}\cdot\mathbf{r}_{n,j}}e^{-i\psi_n}}{2}\mathbf{M} + \frac{e^{-i\boldsymbol{\tau}\cdot\mathbf{r}_{n,j}}e^{i\psi_n}}{2}\mathbf{M}^*\right) \\ &\propto (\boldsymbol{\varepsilon}'\times\boldsymbol{\varepsilon})\cdot\sum_{n=1}^{4}\sum_{j}^{\infty}\frac{1}{2}e^{i\left(\mathbf{k}\cdot\mathbf{r}_{n,j}+\boldsymbol{\tau}\cdot\mathbf{r}_{n,j}\right)}e^{-i\psi_n}\mathbf{M} + \frac{1}{2}e^{i\left(\mathbf{k}\cdot\mathbf{r}_{n,j}-\boldsymbol{\tau}\cdot\mathbf{r}_{n,j}\right)}e^{i\psi_n}\mathbf{M}^* \\ &\propto (\boldsymbol{\varepsilon}'\times\boldsymbol{\varepsilon})\cdot\sum_{n=1}^{4}\sum_{j}^{\infty}\frac{1}{2}e^{i(\mathbf{k}+\boldsymbol{\tau})\cdot\mathbf{r}_{n,j}}e^{-i\psi_n}\mathbf{M} + \frac{1}{2}e^{i(\mathbf{k}-\boldsymbol{\tau})\cdot\mathbf{r}_{n,j}}e^{i\psi_n}\mathbf{M}^* \\ &\propto (\boldsymbol{\varepsilon}'\times\boldsymbol{\varepsilon})\cdot\sum_{n=1}^{4}\sum_{j}^{\infty}\frac{1}{2}e^{i(\mathbf{k}+\boldsymbol{\tau})\cdot\left(\mathbf{l}_j+\mathbf{d}_n\right)}e^{-i\psi_n}\mathbf{M} + \frac{1}{2}e^{i(\mathbf{k}-\boldsymbol{\tau})\cdot\left(\mathbf{l}_j+\mathbf{d}_n\right)}e^{i\psi_n}\mathbf{M}^* \\ f &\propto (\boldsymbol{\varepsilon}'\times\boldsymbol{\varepsilon})\cdot\sum_{j}^{\infty}e^{i(\mathbf{k}\pm\boldsymbol{\tau})\cdot\mathbf{l}_j}\sum_{n=1}^{4}\frac{1}{2}e^{i(\mathbf{k}\pm\boldsymbol{\tau})\cdot\mathbf{d}_n}e^{\mp i\psi_n}\begin{pmatrix}S_a\\ \pm i\chi S_b\\ 0\end{pmatrix} \qquad (5.7)\end{aligned}$$

Similar to the case for Thompson diffraction from a charge unit cell, the sum of the phase factors $e^{i(\mathbf{k}\pm\boldsymbol{\tau})\cdot\mathbf{l}_j}$ over a very large lattice vanishes unless the phase factors are identi-

cal.

$$\sum_{j}^{\infty} e^{i(\mathbf{k}\pm\boldsymbol{\tau})\cdot\mathbf{l}_j} \rightarrow N_0\delta_{\mathbf{k}\pm\boldsymbol{\tau},\mathbf{g}} \tag{5.8}$$

Where N_0 is the number of unit cells and $\delta_{\mathbf{k}\pm\boldsymbol{\tau},\mathbf{g}}$ is the Kronecker delta function, which has the value 1, when $\mathbf{k} \pm \boldsymbol{\tau} = \mathbf{g}$, zero otherwise. This states that scattering only occurs when the scattering vector $\mathbf{k}$, matches the reciprocal lattice vector $\mathbf{g}$ plus or minus the propagation vector of the spin helix $\boldsymbol{\tau}$. This means that for a spin helix, with a propagation vector $\boldsymbol{\tau}$, additional satellite peaks appear around the charge Bragg peaks, $\mathbf{g} = h\mathbf{a}^* + k\mathbf{b}^* + l\mathbf{c}^*$, at positions $\mathbf{hkl} \pm \boldsymbol{\tau}$.

Using equation 5.8, we can simplify the structure factor for a spin helix in equation 5.7.

$$\begin{aligned} f &\propto N_0\delta_{\mathbf{k}\pm\boldsymbol{\tau},\mathbf{g}}\,(\boldsymbol{\varepsilon}'\times\boldsymbol{\varepsilon})\cdot\sum_{n=1}^{4}\frac{1}{2}e^{i(\mathbf{k}\pm\boldsymbol{\tau})\cdot\mathbf{d}_n}e^{\mp i\psi_n}\begin{pmatrix} S_a \\ \pm i\chi S_b \\ 0 \end{pmatrix} \\ &\propto \frac{N_0}{2}\,(\boldsymbol{\varepsilon}'\times\boldsymbol{\varepsilon})\cdot\mathbf{M}\sum_{n=1}^{4}e^{i2\pi\begin{pmatrix}h\\k\\l\end{pmatrix}\cdot\begin{pmatrix}x_n\\y_n\\z_n\end{pmatrix}}e^{-i\psi_n}\Bigg|_{\mathbf{k}=\mathbf{hkl}-\boldsymbol{\tau}} \\ &\qquad + \frac{N_0}{2}\,(\boldsymbol{\varepsilon}'\times\boldsymbol{\varepsilon})\cdot\mathbf{M}^*\sum_{n=1}^{4}e^{i2\pi\begin{pmatrix}h\\k\\l\end{pmatrix}\cdot\begin{pmatrix}x_n\\y_n\\z_n\end{pmatrix}}e^{i\psi_n}\Bigg|_{\mathbf{k}=\mathbf{hkl}+\boldsymbol{\tau}} \end{aligned} \tag{5.9}$$

Equation 5.9 can trivially be split up into two separate sums, for the satellite peaks either side of the reciprocal lattice point at **hkl**. As the vector describing the moment's direction of anisotropy is independent of n, this can be taken out of the sum, which leaves the sum over the 4 atoms in a single unit cell where x_n, y_n, z_n are the fractional coordinates of the n^{th} atom and ψ_n is the phase shift associated with the orbit on that atom. The factor of 2π arises from the choice of basis vectors for the real- and reciprocal-space vectors, when using fractional coordinates and Miller indices.

The structure factor shown in equation 5.9 holds for any particular reciprocal lattice point. If we look at the satellites along the l-direction only, by setting h and k to zero, we can simplify the structure factor further.

$$f_{00l} \propto \frac{N_0}{2}(\boldsymbol{\varepsilon}' \times \boldsymbol{\varepsilon}) \cdot \mathbf{M} \sum_{n=1}^{4} e^{i2\pi l z_n} e^{-i\psi_n}\Big|_{\mathbf{k}=00\mathbf{l}-\boldsymbol{\tau}} + \frac{N_0}{2}(\boldsymbol{\varepsilon}' \times \boldsymbol{\varepsilon}) \cdot \mathbf{M}^* \sum_{n=1}^{4} e^{i2\pi l z_n} e^{i\psi_n}\Big|_{\mathbf{k}=00\mathbf{l}+\boldsymbol{\tau}} \tag{5.10}$$

The fractional position along the c -axis of the four iron atoms in the unit cell can be can be expressed in terms of first iron atom labelled Fe_1 in table 5.1. $z_1 = 0.199$, $z_2 = z_1 + 1/2$, $z_3 = 1 - z_1$, and $z_4 = 1/2 - z_1$. Expanding the sum in equation 5.10 over the four iron atoms yields the following results.

$$\begin{aligned} f_{00l} &\propto \frac{N_0}{2}(\boldsymbol{\varepsilon}' \times \boldsymbol{\varepsilon}) \cdot \mathbf{M}\left(e^{i2\pi z_1 l} e^{-i\psi_1} + e^{i2\pi z_1 l} e^{i\pi l} e^{-i\psi_2} + e^{-i2\pi z_1 l} e^{i2\pi l} e^{-i\psi_3} + e^{-i2\pi z_1 l} e^{i\pi l} e^{-i\psi_4}\right)\Big|_{\mathbf{k}=00\mathbf{l}-\boldsymbol{\tau}} \\ &+ \frac{N_0}{2}(\boldsymbol{\varepsilon}' \times \boldsymbol{\varepsilon}) \cdot \mathbf{M}^*\left(e^{i2\pi z_1 l} e^{i\psi_1} + e^{i2\pi z_1 l} e^{i\pi l} e^{i\psi_2} + e^{-i2\pi z_1 l} e^{i2\pi l} e^{i\psi_3} + e^{-i2\pi z_1 l} e^{i\pi l} e^{i\psi_4}\right)\Big|_{\mathbf{k}=00\mathbf{l}+\boldsymbol{\tau}} \\ &\propto \frac{N_0}{2}(\boldsymbol{\varepsilon}' \times \boldsymbol{\varepsilon}) \cdot \mathbf{M}\left(e^{i2\pi z_1 l}\left(e^{-i\psi_1} + (-1)^l e^{-i\psi_2}\right) + e^{-i2\pi z_1 l}\left(e^{-i\psi_3} + (-1)^l e^{-i\psi_4}\right)\right)\Big|_{\mathbf{k}=00\mathbf{l}-\boldsymbol{\tau}} \\ &+ \frac{N_0}{2}(\boldsymbol{\varepsilon}' \times \boldsymbol{\varepsilon}) \cdot \mathbf{M}^*\left(e^{i2\pi z_1 l}\left(e^{i\psi_1} + (-1)^l e^{i\psi_2}\right) + e^{-i2\pi z_1 l}\left(e^{i\psi_3} + (-1)^l e^{i\psi_4}\right)\right)\Big|_{\mathbf{k}=00\mathbf{l}+\boldsymbol{\tau}} \end{aligned} \tag{5.11}$$

It is clear from equation 5.11 that there is a difference between satellite peaks originating from an odd and even (0,0,l) reflections. For even l values, the structure factor is related to the sum of the phases of the Fe_1 and Fe_2, and Fe_3 and Fe_4, whilst for odd l values the structure factor is related to the difference between the phases of the Fe_1 and Fe_2, and Fe_3 and Fe_4. Using the symmetry arguments that split the iron sites into two orbits, Fe_1 and Fe_2 are still related by symmetry and will have the same phase, $\psi_1 = \psi_2$, and similarly for Fe_3 and Fe_4, $\psi_3 = \psi_4$.

$$\begin{aligned} f_{00l} &\propto \frac{N_0}{2}(\boldsymbol{\varepsilon}' \times \boldsymbol{\varepsilon}) \cdot \mathbf{M}\left(e^{i2\pi z_1 l} e^{-i\psi_1}\left(1 + (-1)^l\right) + e^{-i2\pi z_1 l} e^{-i\psi_3}\left(1 + (-1)^l\right)\right)\Big|_{\mathbf{k}=00\mathbf{l}-\boldsymbol{\tau}} \\ &+ \frac{N_0}{2}(\boldsymbol{\varepsilon}' \times \boldsymbol{\varepsilon}) \cdot \mathbf{M}^*\left(e^{i2\pi z_1 l} e^{i\psi_1}\left(1 + (-1)^l\right) + e^{-i2\pi z_1 l} e^{i\psi_3}\left(1 + (-1)^l\right)\right)\Big|_{\mathbf{k}=00\mathbf{l}+\boldsymbol{\tau}} \end{aligned} \tag{5.12}$$

The structure factor for satellite reflections around forbidden odd Bragg peaks along the $[00L]$ direction is zero, whilst nonzero for allowed even Bragg peaks. For an elliptical helix, along the $[0,0,L]$ direction, satellites peaks only appear around even Bragg reflections.

$$f_{00l} \propto N_0 \left(\boldsymbol{\varepsilon}' \times \boldsymbol{\varepsilon}\right) \cdot \mathbf{M} \left(e^{i2\pi z_1 l} e^{-i\psi_1} + e^{-i2\pi z_1 l} e^{-i\psi_3}\right)\Big|_{\mathbf{k=00l-\tau}} + N_0 \left(\boldsymbol{\varepsilon}' \times \boldsymbol{\varepsilon}\right) \cdot \mathbf{M}^* \left(e^{i2\pi z_1 l} e^{i\psi_1} + e^{-i2\pi z_1 l} e^{i\psi_3}\right)\Big|_{\mathbf{k=00l+\tau}} \tag{5.13}$$

From equations 5.12 and 5.13, a simple helix magnetic moment modulation does not account for the reflection that occurred at the (0,0,1-τ) positions in figure 5.3. The polarisation and azimuthal dependence of the structure factor for the (0,0,τ) reflection is also independent of the phase difference between the $Fe_{1,2}$ and $Fe_{3,4}$ orbits. The phase difference acts as a scale factor, changing the predicted intensity of the reflection. The approach employed in using complex numbers in calculating the structure factor, allows for the separation of the magnetisation vector from the sum over atom positions in the unit cell. The long-range magnetic order is expressed as Fourier components of the crystallographic unit cell, negating the need to sum over an extended magnetic cell. This divides the structure factor into two parts, a sum of atom dependent phase factors which just contribute to the strength of the satellite reflection, and a term independent of atom positions, $\boldsymbol{\varepsilon}' \times \boldsymbol{\varepsilon} \cdot \mathbf{M}$ which describes the polarisation and azimuthal dependences. Using the Jones matrix approach, explained in section 2.1.2, the polarisation and azimuthal dependences can be easily calculated from this structure factor. A non-linear least-squares regression based on the Levenberg-Marquardt algorithm or damped least-squares method [135, 136], was used to fit the ellipticity to the full polarisation analysis of the $(0,0,\tau)$ reflection in figure 5.8 (top) and the azimuthal measurement of the $(0,0,2-\tau)$ reflection shown in figure 5.12. Figure 5.12 shows the predicted azimuthal dependences for perfectly circular helical structure, and elliptical structures. The circular structure predicts a constant intensity as a function of azimuthal angle, as expected. As the structure is made more elliptical the azimuth changes from a constant to a sinusoidally changing intensity between a higher and lower value, with a frequency of 180°. If the magnetic structure has the long axis of the ellipse pointing down the b-axis, then the azimuth goes to a minimum at 180°. The azimuth of the $(0,0,2-\tau)$ reflection goes to a minimum at around 157°.

In the current magnetisation model, the azimuth intensity can only go to zero at 0°and 180° or 90° and 270° depending on whether the long axis of the ellipse is along the *a*- or *b*-axis. To account for this, the ellipse is allowed to rotate such that long- and short-axes no longer point along the *a*- and b-axes. This can simply be achieved by transforming the magnetisation vector **M** by a rotation matrix which rotates the magnetisation vector by an angle ζ around the propagation axis, *i.e.* the *c*-axis. Equation 5.14 shows the form of this rotation matrix, in the basis of the unit cell.

$$R = \begin{pmatrix} \cos\zeta & -\sin\zeta & 0 \\ \sin\zeta & \cos\zeta & 0 \\ 0 & 0 & 1 \end{pmatrix} \tag{5.14}$$

In order to fit the azimuth of the $(0, 0, 2-\tau)$, the long axis of the ellipse has to be placed along the *b*-axis and rotated by -21° around the *c*-axis. As the magnetic structure is elliptical rather than circular, the form of the full linear polarisation analysis of the $(0, 0, \tau)$ should be highly dependent on the azimuth at which the measurement is taken. A minor disadvantage of carrying out resonant scattering at the soft x-ray energies, is the small size of the Ewald sphere, which frequently restricts access to Bragg peaks. The lack of accessible Bragg peaks, combined with the experimental limitation in moving the sample out of the scattering plane, makes establishing an alignment UB matrix an impossibility. A limitation to align the sample, provides the largest source of error for the azimuth position. For all the resonant experiments carried out in this study, the sample was aligned in-house using Cu K_α emission x-ray source (8047.78 eV [184]). The sample's orientation was found, but due to its small size, there will be a source of error on azimuth when mounting the sample on the RASOR diffractometer's mount.

For the model of the full linear polarisation analysis of the $(0, 0, \tau)$ reflection the rotation of the ellipse has a similar effect to changing the azimuth position the calculation is performed at. The effect of ellipticity on the full polarisation measurement is quite dramatic, and is shown in figure 5.8. The circular model is shown with a dashed line, whilst the elliptical model is shown with the solid line. For a circular magnetic structure, the predicted P_1 remains negative for all incident angles. The full linear polarisation analysis does not require a rotation of the magnetic ellipse to fit the data, but the rotation can be accommodated by correcting for a potential offset in the azimuth position.

A final fit was performed, combining both the azimuth of the $(0, 0, 2 - \tau)$ reflection and the full linear polarisation analysis of the $(0, 0, \tau)$ reflection. This fit uses only three parameters, the ellipticity, ${}^{S_b}/_{S_a}$, the rotation, ζ and the azimuth offset of the polarisation analysis measurement ψ_{flpa}.

The final fit results in an ellipticity of ${}^{S_b}/_{S_a} = 2.58 \pm 0.03$, which is far more substantial than the ellipticity of 1.15 proposed by the neutron experiment of Rodriguez *et al.* [156]. Due to the covariance of the rotation angle ζ and the azimuthal offset ψ_{flpa} in the polarisation analysis model, fitting both these two variables from the flpa measurement results in large errors. The azimuthal measurement suggests a rotation of the ellipse of $-21.9 \pm 0.2^{\circ}$. As a consequence the azimuthal position of full linear polarisation measurement needs to be $11.0 \pm 0.2^{\circ}$. This value of the azimuthal offset from the *b*-axis is within the experimental uncertainty of mounting the sample.

Although the $(0, 0, 1 - \tau)$ reflection is predicted to have zero intensity from the above structure factor, the polarisation term can still be calculated neglecting the phase sum and the resulting polarisation dependence does not resemble the experimentally collected data, even qualitatively. This provides evidence that a different origin is needed to explain the appearance of the $(0, 0, 1 - \tau)$ reflection.

5.4.3 Canted Structure Factor

In order to explain the origin of the (0,0,1-$\boldsymbol{\tau}$) reflections, a spin helix restricted within the *a*-*b* plane is not sufficient. It should also be apparent that the phase difference brought about by the two-orbit structure is the origin for the predicted extinction of the $(0, 0, 1 - \tau)$ reflection, and not the direction of the magnetisation vector. This means that changing the magnetic structure **M** to a cycloid or collinear spin density wave will not change the extinction of the $(0, 0, 1 - \tau)$, whilst the two-orbit structure remains. It is also the case that adding a canting in the *c* direction will not contribute to a satellite peak, as it will have no periodicity, and any effects will be hidden under the charge Bragg peak at **hkl**.

Adding a *c*-axis component to the magnetic moment that oscillates with a periodicity of $\boldsymbol{\tau}$ will contribute to the satellite of allowed Bragg peaks, (*i.e.* the $(0, 0, \tau)$) but will not break the predicted extinction of the $(0, 0, 1 - \tau)$ from that of equation 5.12, it will just add a *c*-axis component to the vector **M**.

If we re-examine the crystal structure of FeAs shown in figure 5.1, the unit cell is made up of 4 iron atoms, octahedrally coordinated by arsenic in a three-dimensional network.

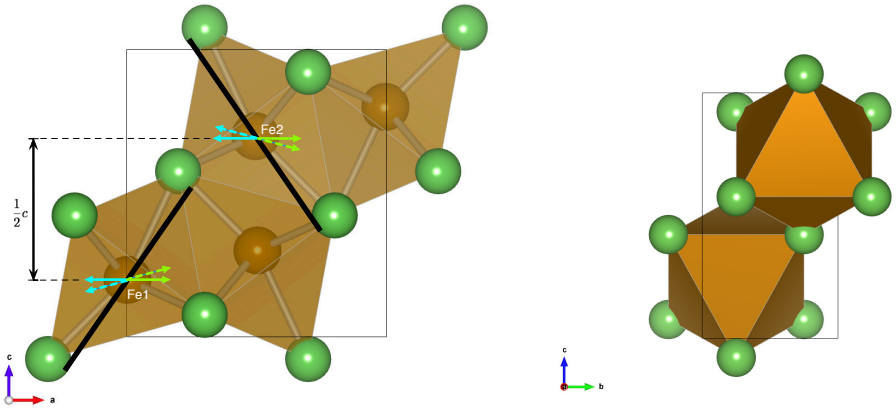

(a) **(b)**

Figure 5.14: Crystal structure of FeAs. (a) *a*-*c* plane, (b) *b*-*c* plane. The local crystal geometry of the Fe sites suggests that the magnetic easy-axis lies in the *a*-*c* plane as the distorted octahedra are tilted in the *a*-*c* plane not the *b*-*c* plane. The black lines shows a suggested direction of magnetic easy-axis. The blue and green arrows show the canting effect towards the easy-axis of the *a*-axis component of the moment. This holds true for any direction the easy-axis may take in the *a*-*c* plane.

These octahedra are tilted in the *a*-*c* plane, figure 5.14a, remaining untilted in the *b*-*c* plane, figure 5.14b. If we assume the existence of an easy-axis for the magnetic moment tied to the crystal geometry, it is reasonable to assume that this easy -axis lies in the *a*-*c* plane. The black line in figure 5.14a shows a example direction for the easy-axis, and the green and blue arrows show the canting effect on the *a* component of the moment towards the easy-axis. For the moments on the Fe_1 and Fe_2 sites that make up one orbit of the helix, the magnetic easy-axis on the Fe_2 site will be a reflection by the σ_x mirror plane of the easy-axis on site Fe_1, resulting in a canting in the opposite direction along the *c*-axis. The same relationship holds for the canting effects between the Fe_3, Fe_4 sites. As Fe_1 and Fe_2 are half a unit cell apart the oscillation in the *c*-axis canting can be described by a cosine with a periodicity of the unit cell, with a phase shift between the two orbits, proportional to the difference in *z* component of the positions of Fe_1 and Fe_3. The resulting *c*-axis component to the magnetic moment, is dependent on both its position along the *c*-direction in the unit cell and the position around the magnetic helix, as only the *a*-axis component of the moment experiences a canting effect.

$$m_{n,j}\left(\mathbf{r}_{n,j}\right)\cdot\hat{\mathbf{c}} = \alpha_{a,c}\beta_n S_a \cos\left(\boldsymbol{\tau}\cdot\mathbf{r}_{n,j} - \psi_n\right) \tag{5.15}$$

Equation 5.15 shows the c-axis component to the magnetic moment, where $S_a \cos\left(\boldsymbol{\tau}\cdot\mathbf{r}_{n,j} - \psi_n\right)$ is the magnitude of the a component, and $\alpha_{a,c}$ is a constant that is determined by the strength of the canting effect, and β_n takes the value ± 1 depending on the atoms site, *i.e.* Fe_1 and Fe_3 take the value +1 and Fe_2 and Fe_4 the value -1. The specific direction of magnetic easy-axis is included in the value β_n, if the easy-axis is perpendicular to the example shown in figure 5.14a, then $\alpha_{a,c}$ simply takes a negative value. If the easy-axis is entirely along the a- or c-axis we expect $\alpha_{a,c}$ to be zero.

$$\begin{aligned} m_{n,j}\left(\mathbf{r}_{n,j}\right) &= m^H_{n,j}\left(\mathbf{r}_{n,j}\right) + \alpha_{a,c}\beta_n S_a \cos\left(\boldsymbol{\tau}\cdot\mathbf{r}_{n,j} - \psi_n\right)\hat{\mathbf{c}} \\ &= m^H_{n,j}\left(\mathbf{r}_{n,j}\right) + \alpha_{a,c}\beta_n S_a \left(e^{i\boldsymbol{\tau}\cdot\mathbf{r}_{n,j}}e^{-i\psi_n} + e^{-i\boldsymbol{\tau}\cdot\mathbf{r}_{n,j}}e^{i\psi_n}\right)\hat{\mathbf{c}} \end{aligned} \tag{5.16}$$

The added complexity of having a term with a periodicity of $\boldsymbol{\tau}$ and β with periodicity of c^*, means that taking out a factor of $e^{\pm i\boldsymbol{\tau}\cdot\mathbf{r}_{n,j}}$ does not leave a term independent of atom position n. The magnetic moment can be written as a sum of the magnetic moment for the a-b confined helical case $m^H_{n,j}\left(\mathbf{r}_{n,j}\right)$, defined in equation 5.6 with a periodicity of $2.57\mathbf{c}$ ($1/0.389$) and the magnetic moment in the c direction which oscillates with a periodicity of roughly of $18.0\mathbf{c}$. If we substitute this into the structure factor equation given in 5.4 the first term remains the same as the structure factor for a a-b helical spin structure given in equation 5.9, but we get two addition terms shown in equation 5.17.

$$\begin{aligned} f \propto (\boldsymbol{\varepsilon}'\times\boldsymbol{\varepsilon})\cdot\Bigg(&\sum_j^{\infty} e^{i(\mathbf{k}\pm\boldsymbol{\tau})\cdot\mathbf{l}_j}\sum_{n=1}^{4}\frac{1}{2}e^{i(\mathbf{k}\pm\boldsymbol{\tau})\cdot\mathbf{d}_n}e^{\mp i\psi_n}\begin{pmatrix} S_a \\ \pm i\chi S_b \\ 0\end{pmatrix} \\ &+\sum_j^{\infty} e^{i(\mathbf{k}+\pm\boldsymbol{\tau})\cdot\mathbf{l}_j}\sum_{n=1}^{4}\frac{\beta_n}{2}e^{i(\mathbf{k}\pm\boldsymbol{\tau})\cdot\mathbf{d}_n}e^{\mp i\psi_n}\begin{pmatrix} 0 \\ 0 \\ \alpha_{a,c}S_a\end{pmatrix}\Bigg) \end{aligned} \tag{5.17}$$

Given that the sum $\sum_{j}^{\infty} e^{i\mathbf{Q}\cdot\mathbf{l}_j}$ is only non-zero when $\mathbf{Q} = [h, k, l]$, where h, k and l are integers.

$$
\begin{aligned}
f_{hkl} \propto \frac{N_0}{2}(\boldsymbol{\varepsilon}' \times \boldsymbol{\varepsilon}) \cdot \begin{pmatrix} S_a \\ +i\chi S_b \\ 0 \end{pmatrix} \sum_{n=1}^{4} e^{i2\pi \begin{pmatrix} h \\ k \\ l \end{pmatrix} \cdot \begin{pmatrix} x_n \\ y_n \\ z_n \end{pmatrix}} e^{-i\psi_n} \Bigg|_{\mathbf{k}=\mathbf{hkl}-\boldsymbol{\tau}} \\
+ \frac{N_0}{2}(\boldsymbol{\varepsilon}' \times \boldsymbol{\varepsilon}) \cdot \begin{pmatrix} S_a \\ -i\chi S_b \\ 0 \end{pmatrix} \sum_{n=1}^{4} e^{i2\pi \begin{pmatrix} h \\ k \\ l \end{pmatrix} \cdot \begin{pmatrix} x_n \\ y_n \\ z_n \end{pmatrix}} e^{i\psi_n} \Bigg|_{\mathbf{k}=\mathbf{hkl}+\boldsymbol{\tau}} \\
+ \frac{N_0}{2}(\boldsymbol{\varepsilon}' \times \boldsymbol{\varepsilon}) \cdot \begin{pmatrix} 0 \\ 0 \\ \alpha_{a,c} S_a \end{pmatrix} \sum_{n=1}^{4} \beta_n e^{i2\pi \begin{pmatrix} h \\ k \\ l \end{pmatrix} \cdot \begin{pmatrix} x_n \\ y_n \\ z_n \end{pmatrix}} e^{-i\psi_n} \Bigg|_{\mathbf{k}=\mathbf{hkl}-\boldsymbol{\tau}} \\
+ \frac{N_0}{2}(\boldsymbol{\varepsilon}' \times \boldsymbol{\varepsilon}) \cdot \begin{pmatrix} 0 \\ 0 \\ \alpha_{a,c} S_a \end{pmatrix} \sum_{n=1}^{4} \beta_n e^{i2\pi \begin{pmatrix} h \\ k \\ l \end{pmatrix} \cdot \begin{pmatrix} x_n \\ y_n \\ z_n \end{pmatrix}} e^{i\psi_n} \Bigg|_{\mathbf{k}=\mathbf{hkl}+\boldsymbol{\tau}}
\end{aligned} \tag{5.18}
$$

For the case of $(0, 0, L)$ type reflections, as before the first two terms only appear for even values of l, shown in equation 5.12. The addition of the β_n term, for the second two terms, changes this condition, shown in equation 5.19 below. If l is even the structure factor becomes zero, the second set of $\boldsymbol{\tau}$ satellite peaks are only allowed around the odd $(0, 0, l)$ reflections. This magnetic structure results in the satellite peaks at $\pm\boldsymbol{\tau}$ positions around both even and odd Bragg peaks. The polarisation dependence of even and odd satellites is expected to have hugely different behaviour, as even satellite peaks are only sensitive to the components of the moment present in the *a*-*b* plane, whilst odd satellite peaks are sensitive only to the moment in the *c* direction.

$$
\begin{aligned}
f_{00l} \propto & \frac{N_0}{2}(\boldsymbol{\varepsilon}' \times \boldsymbol{\varepsilon}) \cdot \begin{pmatrix} 0 \\ 0 \\ \alpha_{a,c} S_a \end{pmatrix} \Big(e^{i2\pi z_1 l}\left(e^{-i\psi_1}\beta_1 + (-1)^l e^{-i\psi_2}\beta_2\right) \\
& + e^{-i2\pi z_1 l}\left(e^{-i\psi_3}\beta_3 + (-1)^l e^{-i\psi_4}\beta_4\right)\Big)\Big|_{\mathbf{k=00l-\tau}} \\
& + \frac{N_0}{2}(\boldsymbol{\varepsilon}' \times \boldsymbol{\varepsilon}) \cdot \begin{pmatrix} 0 \\ 0 \\ \alpha_{a,c} S_a \end{pmatrix} \Big(e^{i2\pi z_1 l}\left(e^{i\psi_1}\beta_1 + (-1)^l e^{i\psi_2}\beta_2\right) \\
& + e^{-i2\pi z_1 l}\left(e^{i\psi_3}\beta_3 + (-1)^l e^{i\psi_4}\beta_4\right)\Big)\Big|_{\mathbf{k=00l+\tau}} \\
\propto & \frac{N_0}{2}(\boldsymbol{\varepsilon}' \times \boldsymbol{\varepsilon}) \cdot \begin{pmatrix} 0 \\ 0 \\ \alpha_{a,c} S_a \end{pmatrix} \Big(e^{i2\pi z_1 l}\left(e^{-i\psi_1} - (-1)^l e^{-i\psi_1}\right) \\
& + e^{-i2\pi z_1 l}\left(e^{-i\psi_3} - (-1)^l e^{-i\psi_3}\right)\Big)\Big|_{\mathbf{k=00l-\tau}} \\
& + \frac{N_0}{2}(\boldsymbol{\varepsilon}' \times \boldsymbol{\varepsilon}) \cdot \begin{pmatrix} 0 \\ 0 \\ \alpha_{a,c} S_a \end{pmatrix} \Big(e^{i2\pi z_1 l}\left(e^{i\psi_1} - (-1)^l e^{i\psi_1}\right) \\
& + e^{-i2\pi z_1 l}\left(e^{i\psi_3} - (-1)^l e^{i\psi_3}\right)\Big)\Big|_{\mathbf{k=00l+\tau}}
\end{aligned}
\tag{5.19}
$$

The simulation of the full polarisation analysis of the $(0, 0, 1-\tau)$ is shown by the solid line in figure 5.8 (bottom). The predicted structure factor for the $(0, 0, 1-\tau)$ is only dependent on the c-axis component of the magnetisation vector. There are no parameters to fit in simulating the full linear polarisation analysis, as the only parameter $\alpha_{a,c}$, controls the strength of the tilting, *i.e.* the magnitude of the c-axis component with respect to the helical component, and consequently has no impact on the polarisation dependence of the $(0, 0, 1-\tau)$ which is only sensitive to the c-axis component. The simulation of the polarisation dependence of the $(0, 0, 1-\tau)$ reflection agrees perfectly with a collinear c-axis moment. This confirms the canted model, where only the component of the moment in the b-direction experiences a canting effect, and the $Fe_{1,3}$ and $Fe_{2,4}$ sites have opposite canting effects. Unfortunately, the full polarisation analysis of the $(0, 0, 1-\tau)$ reflection does not contain the information for the magnitude of the canting. The $(0, 0, \tau)$ reflection only contains information about the a-b helical component and the $(0, 0, 1-\tau)$ only contains information about the c-axis component. It is not possible to extract the size of the canting from polarisation analysis of reflections along the $[0, 0, L]$ direction. The structure factor for satellite peaks along other directions does not separate the helical and

canting components so completely. Equation 5.20 shows the general structure factor for a satellite reflection from a position (h,k,l), where h,k,l are integers

$$f_{hkl} \propto \frac{N_0}{2}(\boldsymbol{\varepsilon}' \times \boldsymbol{\varepsilon}) \cdot \begin{bmatrix} (i)^k e^{i\psi_{1,2}} e^{i2\pi l z_1}\left[\mathbf{M}^*_H\left(e^{i2\pi h x_1} + (-1)^{h+k+l} e^{-i2\pi h x_1}\right)\right. \\ \left. +\mathbf{M}_C\left(e^{i2\pi h x_1} - (-1)^{h+k+l} e^{-i2\pi h x_1}\right)\right] \\ +(-i)^k e^{i\psi_{3,4}} e^{-i2\pi l z_1}\left[\mathbf{M}^*_H\left(e^{-i2\pi h x_1} + (-1)^{h-k+l} e^{i2\pi h x_1}\right)\right. \\ \left. +\mathbf{M}_C\left(e^{-i2\pi h x_1} - (-1)^{h-k+l} e^{i2\pi h x_1}\right)\right] \end{bmatrix} \tag{5.20}$$

The vectors $\mathbf{M}^*_H$ and $\mathbf{M}_C$ are the helical component and canted component to the magnetic structure. The above equation holds for the plus satellite terms, whilst for the minus satellites, the terms in red need to be replaced with their complex conjugates. It should be apparent from the general formula, that whilst $h = 0$, and $k+l$ is even then only the helical term contributes to the satellite reflections, if $h = 0$ and $k + l$ is odd then only the canted term contributes. The situation becomes more complicated if $h \neq 0$, as the helical and canted terms both contribute to the same reflections. Either the helical term or the canting term dominates, dependent on the **hkl** and the phase difference between the two orbits. The relative contribution of the canting term is dependent on both the phase difference between the two orbits and the strength of the canting.

The $(1,0,3-\tau)$ reflection was measured and an azimuthal dependence of the scattering collected. The structure factor for this reflection is dominated by the helical magnetic term, unless the phase difference between the orbits falls within the range 1.8 and 2.0 radians, canting strength dependent, in which case the canting component becomes the more dominant. Figure 5.13 shows the results of the azimuthal dependence of the $(1,0,3-\tau)$ satellite reflection. This was measured on the same experiment as the $(0,0,2-\tau)$ reflection, resulting in the $(1,0,3-\tau)$ reflection being around 23° away from the surface normal. An attempt was made to correct for non-constant absorption on the azimuth by measuring the $(1,0,3)$ Bragg peak as a function of azimuth to counter the effects of the odd geometry. Three different models are shown in figure 5.13, the predicted azimuth for a circular helical structure, a rotated elliptical structure, and the c-component only. The data quantitatively does not agree with any of the three models, while qualitatively it most resembles the elliptical model. The c-component and circular models are significantly different from the measured result. This result is sufficient to further rule out the non-elliptical case, but the measurement is not sufficient to gain any information about the

phase difference between the two orbits or the magnitude of the canting.

To explain the presence of $(0, 0, 1 - \tau)$ reflection, canting of the a-axis component along the c-axis with the periodicity of the unit cell is required. The full linear polarisation analysis confirms that the $(0, 0, 1 - \tau)$ reflection is due to magnetic moment pointing along the c-axis.

5.4.4 Chirality

The magnetic helix structure has a choice of handedness (chirality). This is the choice of direction of rotation of the helix along the propagation vector and is either right-handed or left-handed. The chirality is given by the term χ in equation 5.5, which describes the magnetisation axis. This term takes the value ± 1 dependent on whether the magnetism is being described as a right-handed or left-handed helix. FeAs has two inequivalent helical orbits. Both orbits could be either left-handed or right-handed, or one could be left-handed and the other right-handed, as is the case for the material $CeAl_2$, which is known as a non-chiral spiral (helix) [185]. The chirality has no effect on the simulations for a full linear polarisation analysis, but is important when circular incident light is used [186]. For a chiral magnetic structure incident circular positive and incident circular negative light can be used to establish the chirality [186]. Energy scans of the $(0, 0, \tau)$ and $(0, 0, 1 - \tau)$ reflections were performed at the Fe $L_{\mathrm{II/III}}$ edges and were shown in figure 5.5. The predicted intensities of the $(0, 0, \tau)$ and $(0, 0, 1 - \tau)$ peaks were made using the structure factor calculations from sections 5.4.2 and 5.4.3 for both chiralities, these are shown figure 5.15. The intensity of the $(0, 0, 1 - \tau)$ reflection does not change between circular positive and circular negative incident light, as this peak is sensitive only to the c-axis component, which does not have a chiral nature. The $(0, 0, \tau)$ peak does show a variation with incident circular light, and predictions show that one circular channel is expected to be over twice as intense as the other. This is observed to be the case. The predictions also show that for a right-handed chiral helix the positive circular channel is expected to be the most intense, and for a left-handed chiral helix the negative circular channel is expected to be more intense. The non chiral case, where the two orbits have opposite chirality, is predicted to show equal intensity in the circular positive and negative channels. The energy scans show the positive circular channel was the most intense channel, ruling out the non-chiral case and strongly suggesting the magnetic helix is right-handed.

The linear polarisation analyser was used to examine the scattered beam from the

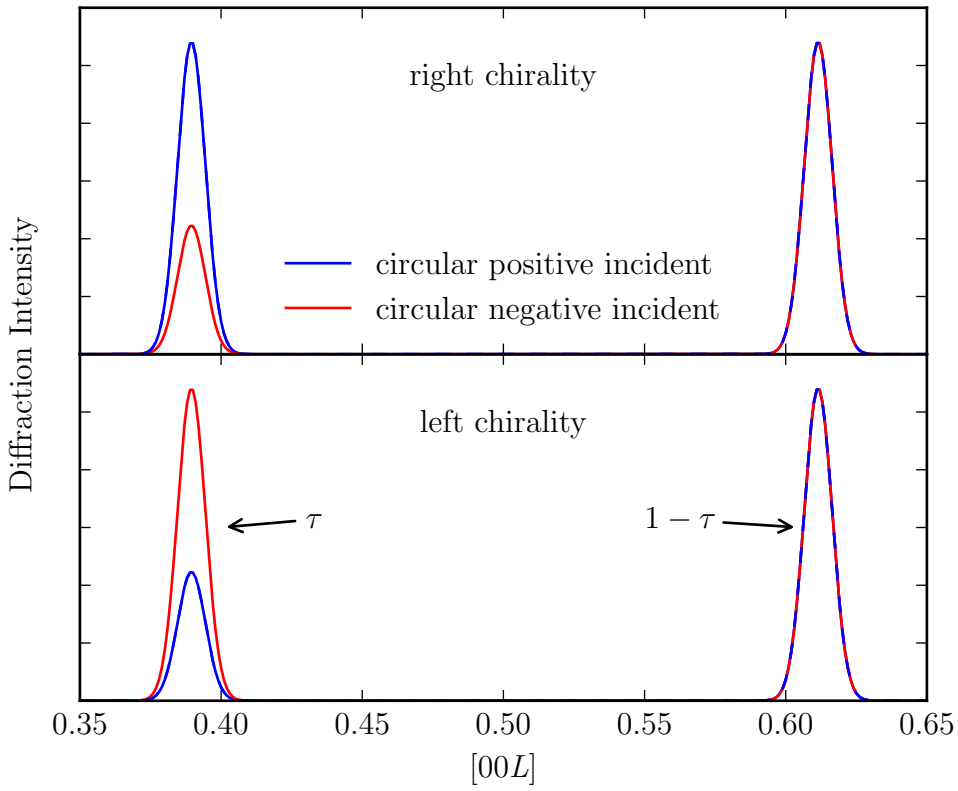

Figure 5.15: Predicted intensities for circular incident polarisation for the $(0,0,\tau)$ and $(0,0,1-\tau)$ for both right chiral (top) and left chiral (bottom) helical magnetic structure.

$(0,0,\tau)$ satellite reflection, with both circular positive and circular negative incident light. The analyser Stokes scan are shown in the top of figure 5.16, for circular positive, blue, and circular negative, red, incident light. Using the helical structure factor, with the parameters from the fit of the linear polarisation and azimuth measurements, the analyser scans were simulated for both chiral cases. For the left and right-handed chiral cases the positive and negative incident lights are predicted to show opposite behaviour. The data resembles the right-handed chiral structure, proving again that the magnetic helix has right-handed chirality

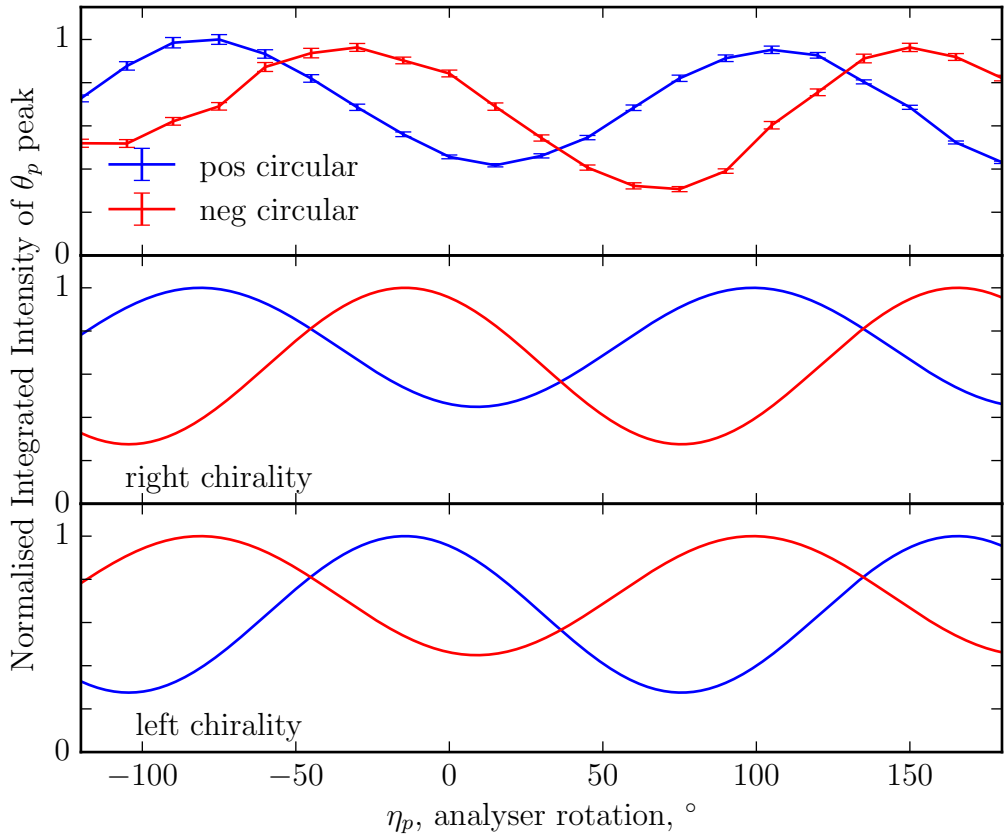

Figure 5.16: (top) Rotation of polarisation analyser around the scattered beam for circular incident polarisation for the $(0, 0, \tau)$ magnetic Bragg peak. (middle) & (bottom) Predicted Stokes scans for a right-handed and left-handed helical magnetic structure.

5.4.5 Satellite Peaks at the K edge

Unlike the resonances at the Fe $L_{\text{II/III}}$ absorption edge, at the Fe K absorption edge along the $(0, 0, L)$ satellite peaks were only observed around even l positions and not l odd positions. Given that the $(0, 0, \tau)$ and $(0, 0, 1 - \tau)$ satellite peaks are roughly the same magnitude at the Fe $L_{\text{II/III}}$ edges, it is surprising that odd satellite peaks are not observed. The difference between a resonance transition at the Fe K edge than the $L_{\text{II/III}}$ edge is the intermediate state in which the electron is excited into. For the simple $E1E1$ case, the K edge excites an electron into the empty Fe $4p$ band, whilst a resonance at the $L_{\text{II/III}}$ excites an electron into the Fe $3d$ band. The K edge transition gets its sensitivity to magnetism

from any overlap of the Fe $4p$ band with the Fe $3d$ band.

The magnetic moment is composed of a spin component and a orbital component. Under the formulation of resonant scattering length the total moment is observed, and spin and orbital components behave the same with polarisation and azimuth. Although resonant scattering cannot distinguish between the orbital and spin components of the moment, orbital and spin components can contribute different amounts at the resonances at the K and $L_{\mathrm{II/III}}$. For a resonance from the $1s$ orbital (K edge) resonant scattering is only sensitive to the orbital component of the magnetic moment. For systems where the spin and orbital components have the same structure this has no effect on the scattering. If the c-axis canting only effects the spin component of the moment, and the resonance at the $L_{\mathrm{II/III}}$ is more sensitive to the spin component, then the odd satellites may only be visible at Fe $L_{\mathrm{II/III}}$. In order to confirm or reject this hypothesis, a non-resonant x-ray magnetic scattering experiment is needed. Although the non-resonant x-ray scattering has the disadvantage of being a weak effect, it has the major advantage over neutron and resonant magnetic scattering, that the spin and orbital components to the total moment have different polarisation and azimuthal dependences. Carrying out a full linear polarisation analysis on the $(0, 0, \tau)$ and $(0, 0, 1 - \tau)$ off-resonance would be needed to determine the spin and orbit nature of the magnetic structure.

The appearance of the $(0, 0, 2\tau)$ and $(0, 0, 3\tau)$ higher harmonic satellite peaks at the Fe K edge is expected and has been observed before in the helimagnet phase in holmium [187]. The presence of the $\boldsymbol{\tau}$ and $2\boldsymbol{\tau}$ reflections can be explained simply by the $E1E1$ scattering process [187, 188]. While the 3τ reflection can not be recreated by $E1E1$ scattering process and requires an $E2E2$ scattering process.

5.4.6 Conclusion

This chapter has described how detailed polarised resonant x-ray magnetic scattering can be used to provide quantitative information on the complex magnetic ordering of the helices in FeAs. The critical scattering analysis performed on the temperature dependence shows unusual behaviour, displaying an almost 2D Ising-like transition. The correlation length shows a peculiar behaviour with temperature, becoming less correlated with reducing temperature below the transition. The resonant scattering results have shown that a double circular helical magnetic structure is insufficient, and that the helix maps out an ellipse. This ellipse has been shown to have an major axis 2.58 times longer than the

minor axis. The azimuthal measurement, showed that major axis of the ellipses is rotated -21° around the *c*-axis. The full polarisation analysis of the unexpected $(0, 0, 1 - \tau)$ peak, requires a canting of the *a*-axis component of the moment along the *c*-direction with a periodicity of the unit cell. The absolute magnitude of the canting cannot be found from the measurements taken, just its presence. The phase difference between the two magnetic orbits has not been found. Figure 5.17 shows the *a*-, *b*-, and *c*-axis components of the magnetic moment for the canted spin helix, for one orbit.

The effect of canting the *a*-axis component of the helix with the periodicity of the unit cell *c* parameter, results in a total magnetic structure with a periodicity longer than given by $\boldsymbol{\tau}$. If we assign $\boldsymbol{\tau}$, 0.389 the commensurate position of $^{7}/_{18}$, the effect of the canting is to make the system repeat every 18 unit cells along the *c*-axis. This can be seen in figure 5.17 where the moment rotates around the helix seven times before returning to its starting position. It should be noted that although the canting effect is assumed to be restricted to the *a*-*c* plane due to crystal symmetry arguments, the structure factor calculation just requires it to be fixed to single direction in the helical plane and not necessarily the *a*-axis. This unusual canting effect which only occurs along one direction of the helix combined with the ellipticity explains the unusual magnetic susceptibility measured by Segawa *et al.* [155]. The zero-field splitting only occurs in the *b*-direction, shows a definite anisotropy between the *a*- and *b*-axis. Whilst an elliptical helical structure goes some way to explain why the susceptibility along the *b*-direction is lower than along the *a*-direction, it does not explain the presence of the field splitting in only one direction. The presence of *c*-axis canting, with the periodicity of the unit cell only along one of the directions of the helix plane explains the difference in field-cool splitting.

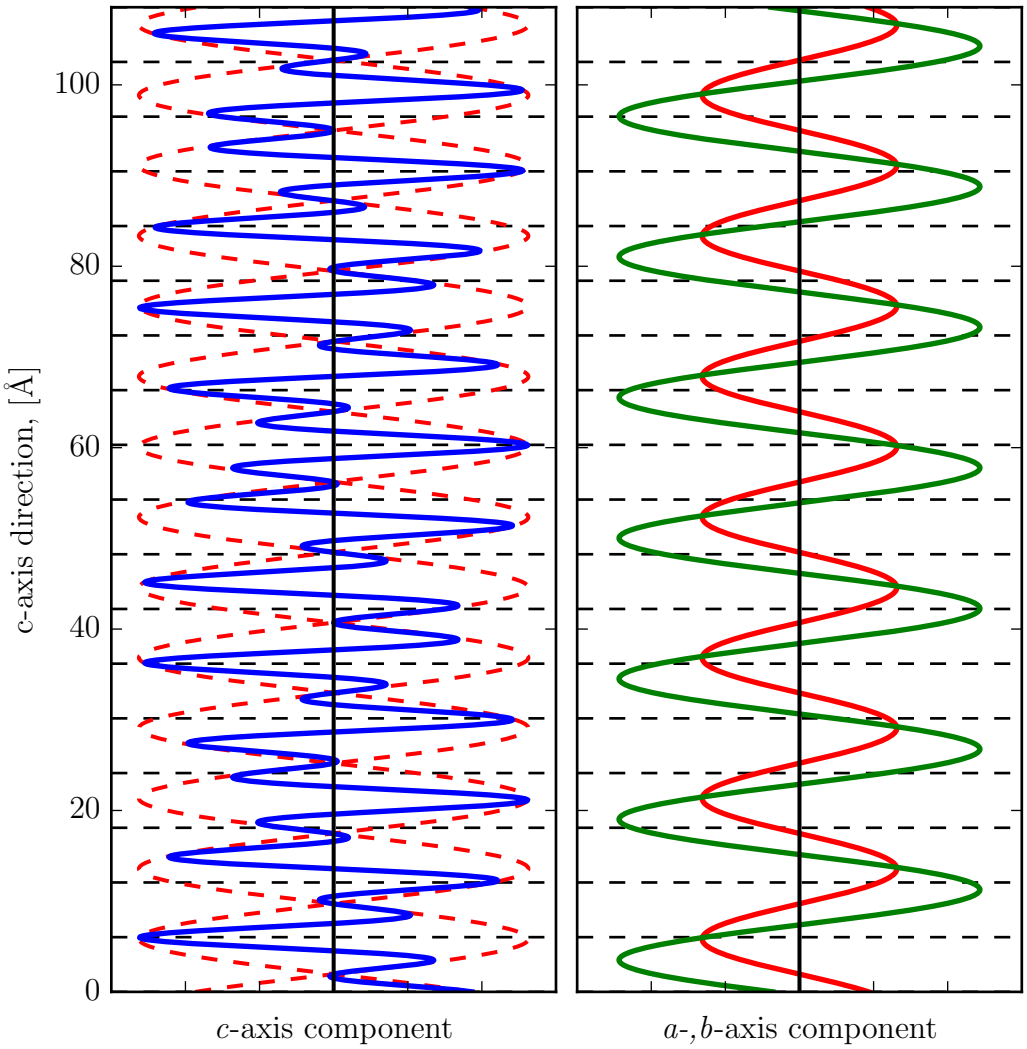

Figure 5.17: *a*-, *b*-, and *c*-axis components of the magnetic helix, shown in red, green and blue respectively. Dashed red line shows *a*-axis component envelope around the *c*-axis component.

Chapter 6

Magnetism of Frustrated system, $CuFeO_2$

6.1 Introduction

Triangular lattice systems exhibit a wealth of electronic phenomena and unusual magnetic ground states. These phenomena are due to geometric spin frustrations, where primary magnetic interactions are unable to be satisfied, and secondary interactions play a vital role in determining the ground state. The delafossite crystal structure is a common frustrated structure adopted by a number of ABO_2 materials. Many triangular lattice antiferromagnets belong to this structure. $CuFeO_2$ belongs to this structure and should be considered a classic triangular lattice antiferromagnet, except its behaviour is unlike most, with a strong anisotropic Ising-like nature below 14 K, and a ferroelectric polarisation with applied magnetic field. The chapter reports findings from neutron and x-ray diffraction experiments exploring the zero- and high-field behaviour of $CuFeO_2$.

6.2 Delafossite Crystal Structure

Delafossite is the mineral name for the compound $CuFeO_2$, first identified by Charles Friedel in 1873. The delafossite structure was first determined in 1935 with a synthetic sample [189], and 1946 with a mineral sample [190].

Materials that adopt the delafossite structure belong to a family of ternary oxides with the general formula ABO_2. Materials with the formula ABO_2, adopt a range of different structures, with four different coordination classes identified, $A^{\mathrm{VI}}B^{\mathrm{VI}}O_2^{\mathrm{VI}}$, $A^{\mathrm{IV}}B^{\mathrm{IV}}O_2^{\mathrm{IV}}$, $A^{\mathrm{VIII}}B^{\mathrm{IV}}O_2^{\mathrm{VI}}$, and $A^{\mathrm{II}}B^{\mathrm{VI}}O_2^{\mathrm{IV}}$.

ABO_2 materials adopt structures, from the hexagonal delafossite structure of $CuFeO_2$,

to the orthorhombic β-$NaFeO_2$, tetragonal α-$LiFeO_2$, and orthorhombic $KFeO_2$. The ionic radius of the A and B cation appears to be the defining variable in determining which structure to adopt. Marquardt *et al.* [191] compiled a structure map using the ionic radius of around 80 known ABO_2 oxide materials. A material only adopts the delafossite structure when composed of the smaller ionic radius A cations. The delafossite structure only exists for four small radius A site cations, Cu^+, Pd^+, Pt^+ and Ag^+, typically 2.8 to 3.0 Å , whilst several B site cation are possible, including p-block metals, transition metals, and rare-earth ions. The A site has a valency of +1, and is linearly coordinated to two oxygen. The B site cation has a valency of +3, and is coordinated by oxygen in a distorted edge-shared octahedra.

The delafossite structure is built of alternating layers of A site cations in a triangular pattern, and layers of edge sharing BO_6 octahedra, along the c-axis. The distorted BO_6, are tilted with respect to the c-axis, such that the B-site cation, and the oxygen also sit on a triangular lattice in the a-$b$plane. Two polytypes exist for the delafossite structure, depending on the stacking. The $2H$ type, where alternate double layers of A & BO_6 are oriented 180° relative to each other. The $3R$ polytype is formed from stacking three double layers, oriented in the same direction, but with an offset between each layer. These polytypes are shown in figure 6.1.

The $2H$ polytype belongs to the hexagonal $P6_3/mmc$ space group, whilst the $3R$ polytype belongs to the rhomberhedral $R\bar{3}m$ space group. Figure 6.1c shows the $2H$ polytype, this has a hexagonal primitive unit cell with a six-fold rotation axis along the c-direction. The $3R$ polytype shown in figure 6.1b has a non-primitive hexagonal unit cell with three lattice points and only has a three-fold improper rotation axis along the c-direction. The three-fold improper rotation can be seen more clearly by taking the primitive unit cell, which is the rhombehedra shown in figure 6.1a.

$CuFeO_2$ adopts the $3R$ polytype, with the Fe^{3+} ions sitting in the octahedral sites in close packed oxygen double layers, and the Cu^+ ions linearly coordinated to oxygen atoms. The trivalent and monovalent oxidation states of the iron and copper respectively, has been confirmed by lattice energy calculations and Mössbauer spectroscopy [192–194]. The room temperature crystal structure has lattice parameters $a_H = b_H = 3.0351$ Å and $c_H = 17.166$ Å in the hexagonal basis [195], equivalent to $a_{rh} = b_{rh} = c_{rh} = 5.9843$Å and $\alpha = 29.380°$ in the rhombohedral basis. In the hexagonal basis the angle between the reciprocal lattice vectors $\mathbf{b}_1$ and $\mathbf{b}_2$ is 60° and $\mathbf{b}_3$ normal to the $\mathbf{b}_1 - \mathbf{b}_2$ plane. The

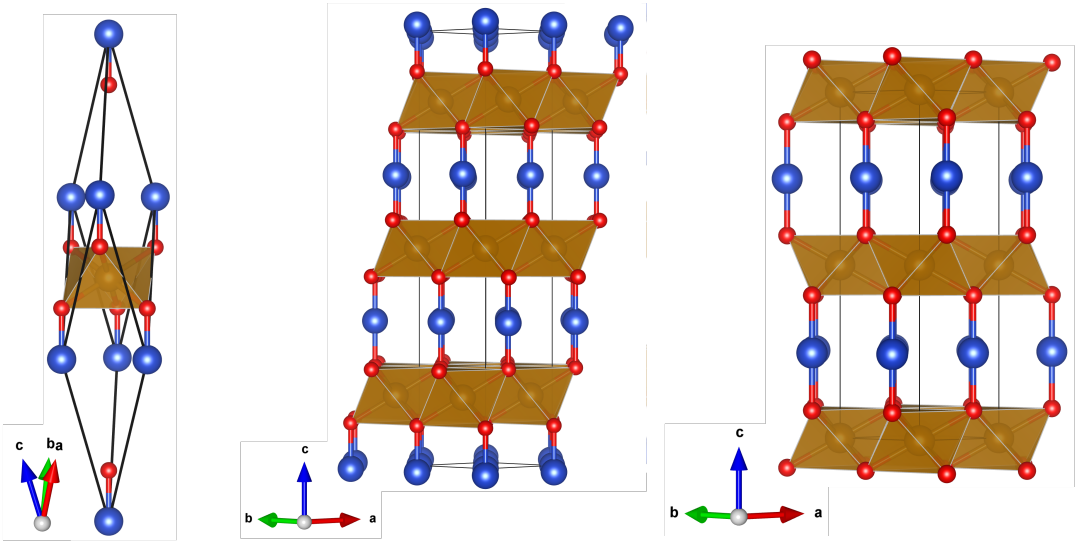

(a) **(b)** **(c)**

Figure 6.1: Two polytypes that the delafossite structure can take. The constituents of ABO_2 are shown in blue (A), brown (B) and red (O). The lattice directions are a, b and c are shown by the red, green, and blue arrows respectively. (a) & (b) show the rhombohedral and hexagonal unit cells for the 3R polytype. Stacking of ABO_6 double layer with an offset between layers in a three layer sequence. (c) 2H polytype. Stacking of the ABO_6 double layer with alternate layers orientated 180° to each other.

reciprocal lattice has three-fold improper rotation symmetry, causing Bragg diffraction from the crystal lattice to occurs at reciprocal-lattice positions where $-h + k + l = 3n$ where h, k, l and n are integers. This gives rise to families of reflections with two, six and twelve multiplicities. hk planes with $l = 3n$ have six-fold symmetry, whilst hk planes with $l = 3n \pm 1$ have three-fold symmetry, with planes of $\pm l$ being inverted.

6.3 Magnetism in $CuFeO_2$

As stated earlier all three constituent atoms form triangular lattices in the ab plane, with nearest neighbours being 3.03 Å apart, with Fe neighbours between planes being 5.98 Å apart. As established in section 4.1.2 and figure 4.2, placing spins on a triangular lattice creates an issue of geometrical frustration. By placing spins on the vertices of an equilateral triangle, the interactions between all three spins are equal. For the antiferromagnetic Ising spin case it is not possible to satisfy all the magnetic exchange interactions, inducing a large magnetic ground state degeneracy. In triangular lattice systems where a magnetic

ground state forms, magnetic moments tend to adopt a noncollinear 120° spin configuration to alleviate this frustration, as shown in figure 4.2c and 4.2d. Related magnetic materials, $LiCrO_2$, $AgCrO_2$ and $CuCrO_2$ all share the delafossite structure, and at low temperatures adopt a form of the standard 120° spin structure [196–198].

The Fe^{3+} is the only magnetic ion in $CuFeO_2$, the Cu^+ and O^{2-} have filled electronic shells. The trivalent Fe^{3+} ion has a half filled $3d^5$ *d*-orbital, which using Hund's rules gives a $S = 5/2$ spin state. In addition the magnetic moments interact antiferromagnetically, making $CuFeO_2$ a model triangular lattice antiferromagnet (TLA). The antiferromagnetic exchange interaction is expected to be isotropic, resulting in a purely Heisenberg moment. Unusually for a TLA, $CuFeO_2$ adopts a collinear Ising-like ground state below 11 K [199]. Two transitions were observed to occur in $CuFeO_2$, at 14 K and 11 K. Above 14 K the system exhibits paramagnetic behaviour. Between 14 K and 11 K the phase is described as a partial disordered incommensurate structure, with wavevector $(q,q,3/2)$, with q close to $1/5$ [199, 200]. In this phase $1/5$ of the moments remain paramagnetic. Below the 11 K transition, the system adopts a four sublattice (4SL) collinear structure with magnetic wavevector $(1/4,1/4,3/2)$. Spins align parallel to the *c*-axis, with two up and two down in the *a*-*b* plane [201, 202].

Monte Carlo simulations up to third nearest neighbours of a two-dimensional Ising TLA describe successive magnetic phases in $CuFeO_2$, although does not provide justification for assuming Ising-like spins [201–205]. Relative strengths of exchange interactions up to third nearest neighbours $J_1 : J_2 : J_3$ were found to be $1 : 1/2 : 3/4$, with J_1 approximately 1.2 meV [203, 206, 207].

The magnetisation was observed to be highly isotropic above 14 K, but undoubtedly anisotropic below the transition. The 2D Ising model can not account for this isotropic behaviour, and this is where this model breaks down [203, 207–209]. Structural distortion has been observed in $CuFeO_2$, concurrent with the magnetic transitions. At 14 K, the hexagonal $R\bar{3}m$ symmetry reduces to monoclinic $C2/m$. At 11 K the symmetry reduces to a lower monoclinic group [210–213]. This structural distortion can be explained classically by the "spin Jahn-Teller" effect, with notable spin-lattice coupling inducing a structural distortion, reducing the spin-state degeneracy in the system [214–216]. Alternatively the low temperature structural distortion, results in a lattice of scalene triangles, splitting the nearest neighbour interactions into three unequal interactions [210–213]. It has been suggested this structural distortion introduces a magnetic easy-axis along the *c*-axis [217].

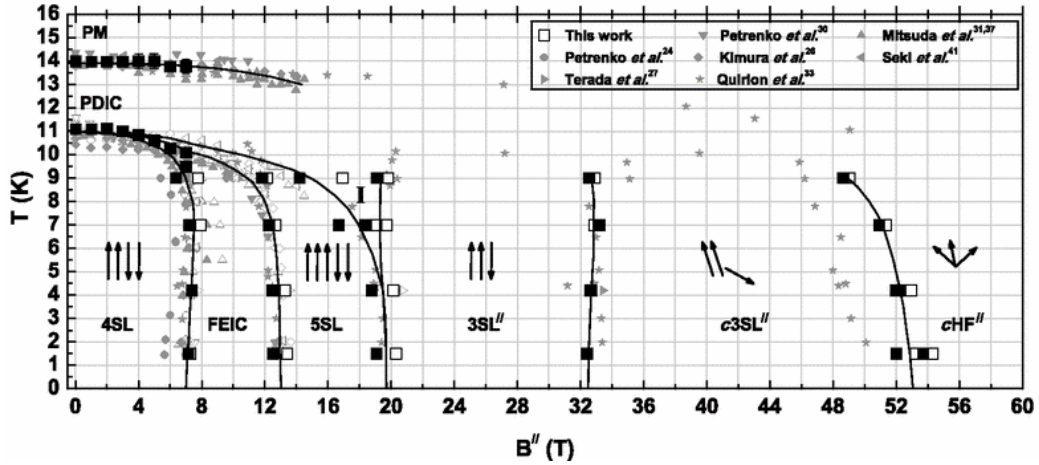

Figure 6.2: Magnetic field (*c*-axis oriented) temperature phase diagram of $CuFeO_2$ taken from [2]. The diagram summarises bulk magnetisation, susceptibility, specific heat and dielectric measurements measurements taken from a range of different studies [2, 207, 209, 217, 220, 221, 223–225].

A Heisenberg Hamiltonian with a single-ion anisotropy term and strong spin-phonon coupling can explain the Ising-type behaviour [2, 216, 218]. An inelastic neutron scattering experiment has shown the spin-driven lattice distortions significantly affect the exchange interactions in $CuFeO_2$ [219]. Upon application of an external magnetic field along the *c*-axis, $CuFeO_2$ undergoes several magnetic transitions. The exact position, in field, of these transitions is temperature dependent, at 1.5 K they occur at 7 T, 13 T, 20 T, 34 T and 53 T, finally saturating at approximately 70 T [203, 207, 209, 217, 218, 220–223]. The magnetic-field temperature phase diagram shown in figure 6.2, has been taken from [2] and summarises bulk magnetisation, susceptibility, specific heat, and dielectric measurements from a range of studies [2, 207, 209, 217, 220, 221, 223–225].

The ground state four-sublattice structure persists until a magnetic field of around 7 T is applied. Measurements of the magnetoelectric current show that between 7 and 13 T the system develops an electric polarisation, revealing this phase to be ferroelectric [209]. Single crystal neutron diffraction studies by Mitsuda *et al.* [224] and Petrenko *et al.* [220] confirms the four-sublattice structure of the zero-field phase, with the appearance of magnetic satellite peaks at positions ($^1/_4$, $^1/_4$, $^3/_2$) away from Bragg peaks. Due to experimental limitations when carrying out diffraction with an applied magnetic field along the *c*-axis, the accessible diffraction was confined to the *hk0* plane. In the four-sublattice phase, no

magnetic peaks are visible in the *hk0* plane. Above 7 T weak incommensurate magnetic peaks appear at $2q$ positions away from Bragg peaks, with q taking an incommensurate value close to $1/5$. The peaks were labelled up as $2q$ as a pulsed neutron experiment performed earlier identified a wavevector close to $1/5$ [226]. This has led to the labelling the state between 7 and 13 T as ferroelectric incommensurate (FEIC) phase. Additionally a peak was observed at $(1/2 + 2q, 1/2 + 2q, 0)$ position in the FEIC phase. Above 13 T, strong magnetic reflections were seen at commensurate *hh*0 positions with $h = 1/5, 2/5, 3/5, 4/5$, identifying the 13-20 T phase as having a five-sublattice structure with moment pattern ↑↑↑↓↓.

Doping a small amount (2-4%) of non-magnetic impurity, such as aluminium or gallium, can drastically alter the ground state of the system, and in some cases bring the FEIC phase down to zero applied magnetic field. To date the only way to get an insight into the magnetic structure of the FEIC phase is to examine it in a doped sample, removing the experimental limitation brought on by a high-field magnet. For the doped system, the FEIC phase was found to have an incommensurate wavevector $(q, q, 3/2)$ with q close to a $1/5$. The spin structure was determined by neutron diffraction to be an incommensurate helix [227]. Further work by Arima [228] and Nakajima *et al.* [229], has gone on to show the ferroelectricity is induced by a proper-screw type magnetic order. In the case of $CuFe_{1-x}Al_xO_2$ the proper helical magnetic ordering induces a spontaneous electric polarisation parallel to the vector spin chirality. The spin current model of Katsura, Nagaosa, and Balatsky has been successful in explaining the origin of ferroelectricity in a number of helimagnet multiferroics [230], but is unable to explain the ferroelectricity in $CuFe_{1-x}Al_xO_2$ as the electric polarisation is parallel to the vector spin chirality. Arima [228] successfully explained the origin of ferroelectricity in $CuFe_{1-x}Al_xO_2$. Arima found that in systems with with triclinic, monoclinic or rhombohedral symmetries, ferroelectricity can be induced by a proper screw type magnetic ordering through the variation in the metal-ligand hybridisation with spin-orbit coupling.

The magnetic structures at higher fields have not been experimentally verified, by a diffraction technique. Lummen *et al.* [2, 218] have characterised the high-field structures from the bulk susceptibilty measurement using a phenomenological classical spin model.

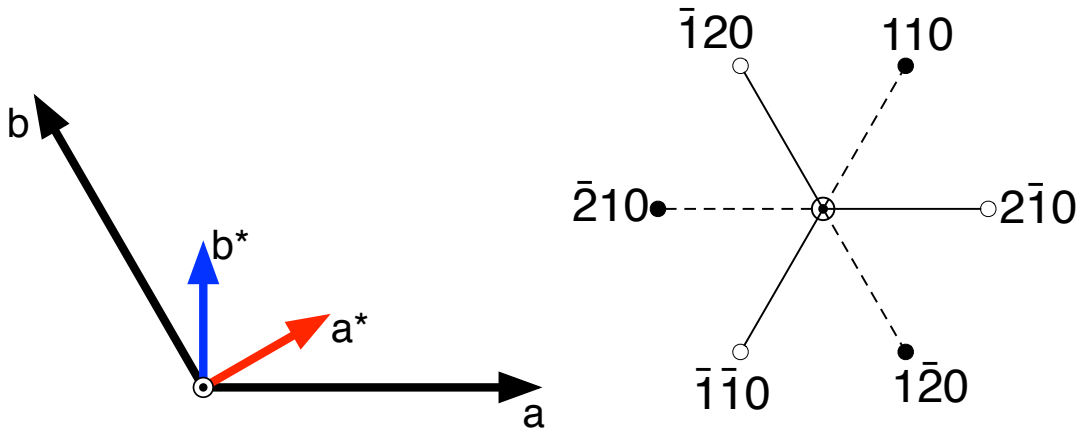

(a) **(b)**

Figure 6.3: (a) Relation between crystallographic axes and the reciprocal lattice for the hexagonal system. The c and c^* vectors point out of the page. (b) Six directions in the hexagonal basis which are equivalent. In the rhombahedral symmetry with $\bar{3}$ improper rotation, the direction indicated by a dashed and solid lines are inequivalent.

6.4 Experimental

A single crystal sample of $CuFeO_2$ was grown by the floating zone method [84] by C. H. Du at Tamkang University, Taiwan. The hexagonal structure was confirmed using the in-house four-circle Eulerian-cradle diffractometer. Reciprocal lattice vector will be given in the hexagonal basis for the rest of this chapter, unless explicitly stated otherwise. Reciprocal lattice indexing in a hexagonal case, is less intuitive than in an orthorhombic case. As in the case of orthorhombic lattice the hexagonal c-axis and the reciprocal c^* point along the same direction. The a-b plane is slightly more complicated, due to the 120° angle between the a- and b-axis. The a^* reciprocal vector is perpendicular to the b-c planes and similarly the b^* vector is perpendicular to the c-a plane. This results in the a^* and b^* reciprocal vectors not pointing along the same direction as there corresponding crystallographic vector. Additionally the a^* and b^* reciprocal vectors point 60° apart, as shown in figure 6.3a. This leads to some counter intuitive situations where reflections (110) and ($\bar{2}$,1,0) have the same d-spacing.

The sample's alignment was determined and two faces were ground and polished along the [116] direction, as well as the [001] direction. The same sample was used for all the neutron and synchrotron experiments. A single crystal neutron experiment was per-

formed on the time-of-flight (tof) powder diffractometer, WISH at the ISIS pulsed neutron spallation source [58]. The WISH beamline sits on a solid methane moderator, providing neutrons with a wavelength range 1.5-15 Å enabling a *d*-spacing range of 0.7-17 Å to be examined. The instrument has 10 banks of pixelated He^3 detectors symmetrically arranged covering a range of scattering angles from 10-170°, without any gaps. The He^3 detectors have an active height of 1 m, providing ±12° access to out-of-plane diffraction. When using the powder instrument in single crystal mode the wide in-plane and out-of-plane access allows comprehensive Laue images to be taken with the tof spectra providing $d-$spacing sensitivity. The WISH instrument has a dedicated 13.4 T superconducting vertical magnet, which reduces the out of plane access to -5°/+10°.

The sample was mounted in the magnet with the *c*-axis along the field direction. The sample was cooled to a base temperature of 1.5 K, and the magnetic field phase diagram was studied with access to the out of plane [q,q,½] reflections for the first time. Laue images were collected at 1.5 K in steps of 1 T up to a maximum field of 13.4 T, then at a constant field of 13 T from 3 K to 15 K.

In order to probe the magnetic structure in the zero-field phase, two iron *K* edge magnetic resonant x-ray scattering experiments were carried at I16, Diamond and P09, Petra III [176]. At both beamlines, a focussed monochromatic x-ray beam was optimised with a incident energy of 7112 eV. Harmonic rejection mirrors were utilised to remove higher harmonics from the x-ray beam. Both beamlines provide post-scatter polarisation analysis using a copper polarisation analyser crystal scattering from the [220] surface.

I16 has a six-circle kappa-geometry diffractometer, with both an APD point detector (on the polarisation stage) and Pilatus 100K area detector. The kappa geometry gives a wider access to the crystal than the Euler-geometry. The sample was cooled to a base temperature of 7.8 K, using a closed cycle cryostat. A survey of magnetic peaks was performed and an azimuthal rotation measurement was taken on the strongest peak. The intensity of the magnetic peak was measured in the $\sigma - \sigma$ and $\sigma - \pi$ polarisation channels as a function of the rotation of the crystal around the scattering vector.

The P09 beamline has a six-circle Eulerian-cradle diffractometer, with a Displex cryostat with a Joule-Thompson cooling stage which has a base temperature of 1.7 K. The P09 beamline comes equipped with a set of diamond phase plates [231], which allow the polarisation of the incident x-ray beam to be any incident linear angle, and circular polarised left and right. A full linear polarisation analysis of the resonant magnetic peak

was performed. In this measurement the crystal is placed in the diffraction condition for a magnetic Bragg peak and the angle of the linear polarisation of the incident beam, η is rotated through a full 180°. At each incident linear polarisation angle, η, the polarisation analyser stage is rotated around the scattered beam through at least 180°, enabling the polarisation state of the scattered beam to be extracted.

A second experiment was performed at the P09 beamline using the heavy-load diffractometer with a 14 T magnet. In this setup, the magnetic field is perpendicular to the scattering plane and there is only a very small motion out of plane. The sample was mounted with the *c*-axis along the magnetic field direction, requiring the $[HK0]$ plane to be in the scattering plane. A scattering experiments was performed at 1.8 K at the iron *K* absorption edge, examining the higher magnetic field phases. The heavy-load diffractometer operates in a horizontal scattering mode, consequently the incident polarisation is π polarised without the use of the phase plates.

6.5 Results

6.5.1 Neutron Diffraction

The single crystal neutron experiment was able to access the PD, 4SL, FEIC and the 5SL phases. At each point measured in the phase diagram, two Laue images were collected with the sample orientated 60° apart in the *a*-*b* plane. Each Laue image was collected for a total integrated current of 20 μAhr, averaging around 30 minute collection time on target station 2 which has a current of 40 μA. Each pixel on the Laue images taken on WISH corresponds to a time-of-flight spectra. Using instrument specific parameters $d-$spacing spectra can be calculated from time-of-flight for each pixel. The Mantid software suite was used to extract the data from Laue images, this software provides the necessary routines to convert the units and mask areas of pixels.

Figure 6.4 shows the $d-$spacing spectra totalling over all the areas of intensity on the Laue images. The four figures shows the $d-$spacing spectras in different phases in the phase diagram, with 6.4(a) and (d) being in the paramagnetic phase, with a magnetic field of 0 T and 13 T respectively. Figures 6.4 (b) and (c) show the material in the 4SL and FEIC phases respectively. These phases are clearly distinguished by the appearance of additional diffraction peaks, which are highlighted in green. Across the three phases between 0 T and 13.4 T, 23 magnetic peaks where identified with 12 existing in all three

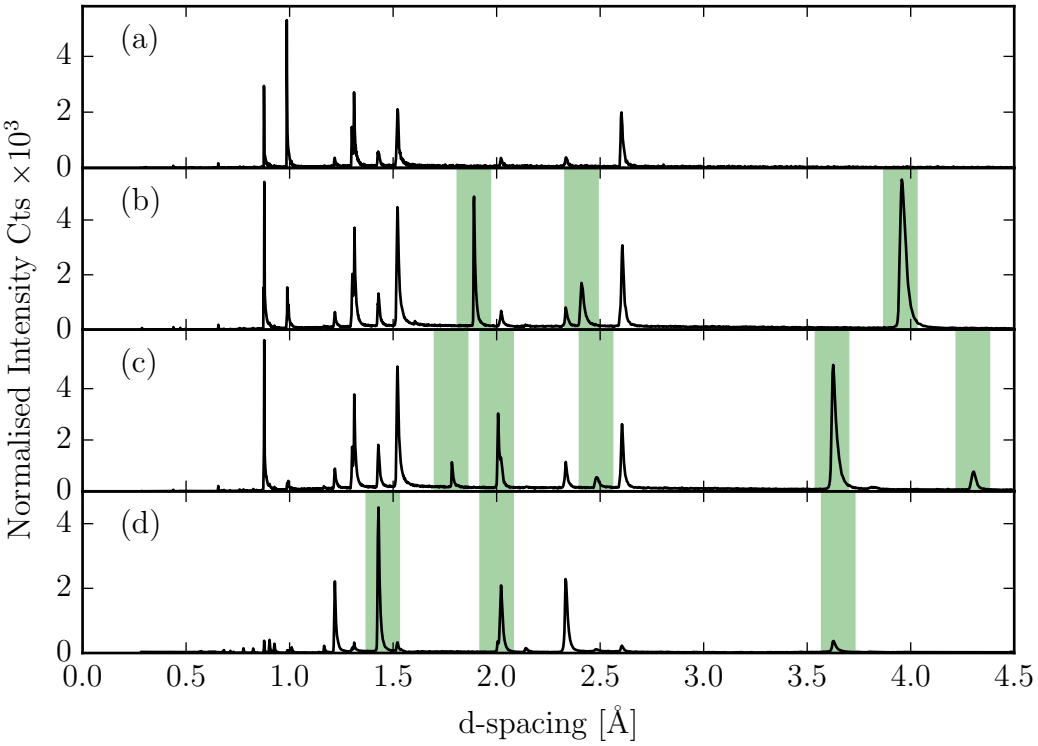

Figure 6.4: *d*-spacing plot from time-of-flight single-crystal neutron diffraction . (a) Paramagnetic phase. (b) Four sub-lattice phase. (c) Ferroelectric incommensurate phase. (d) Five sub-lattice phase.

phases (4SL, FEIC, 5SL) with changing wavevector, and eight additional peaks only existing in the FEIC phase and three additional peaks only existing in the 5SL phase.

The 12 peaks that belong to all the low temperature phases have three different $d-$spacings, and can be indexed up as $(HKL) + \boldsymbol{\tau}$ where (HKL) are nuclear Bragg peaks and $\boldsymbol{\tau}$ is the magnetic wavevector. Due to the threefold improper rotation symmetry, the magnetic wavevector, $\boldsymbol{\tau}$, $(q,q,3/2)$ is equivalent to $(q,-2q,3/2)$, $(-2q,q,3/2)$, $(-q,-q,-3/2)$, $(-q,2q,-3/2)$ and $(2q,-q,-3/2)$.

Figure 6.5 shows contour plots of selected magnetic and nuclear Bragg peaks with applied magnetic field. $d-$spacing is presented on the x-axis and and the applied magnetic field on the y-axis. The intensity of the diffraction is represented by a spectral colour map. The colour is calibrated on each map, and it is not possible to compare intensities between peaks using figure 6.5. The top row shows the $d-$spacing of magnetic peaks at

positions with a wavevector (q,q,$^3/_2$), or equivalent, away from nuclear Bragg peaks. The peak positions all show qualitative similar behaviour with applied magnetic field. The $d-$spacing stays constant with field until around 7 T, where the peak jumps to a different $d-$spacing, both higher and lower position, reflection dependent. The $d-$spacing then linearly shift with higher applied field until 13 T where the $d-$spacing appears to stay constant.

The bottom left frame shows the $d-$spacing of the (1,1,0) nuclear peak with applied magnetic field. The (1,1,0) does not change with applied field position to within the resolution of the instrument, suggesting the a lattice parameter does not change significantly with applied magnetic field. The remaining figures in 6.5 show the appearance of (q,q,0), (2q,2q,0), and (3q,3q,0) reflections at 13.4 T, in the 5SL phase. All three of these reflections appear at the same position on the Laue image as the (1,1,0) Bragg peak, but are separable in time-of-flight. Both the nuclear and magnetic Bragg diffraction peaks in the time-of-flight spectra have a distinctive asymmetric shape. A convolution of a back-to-back exponential and a Gaussian function provides a close approximation to the time-of-flight diffraction peaks. There are five fitting parameters to the function, the integrated intensity, I, the peak position, x_0, the standard deviation of the Gaussian part, σ, and exponential constant of the rising and decaying part of the peak, A and B. Equation 6.1 shows the form of this function, where erfc is the error function.

$$I(x) = I\frac{AB}{2\left(A+B\right)}\left[\exp\left(\frac{A\left[A\sigma^2+2\left(x-x_0\right)\right]}{2}\right)\mathrm{erfc}\left(\frac{A\sigma^2+\left(x-x_0\right)}{\sigma\sqrt{2}}\right)\right.$$
$$\left.+\exp\left(\frac{B\left[B\sigma^2+2\left(x-x_0\right)\right]}{2}\right)\mathrm{erfc}\left(\frac{B\sigma^2+\left(x-x_0\right)}{\sigma\sqrt{2}}\right)\right] \quad (6.1)$$

For each magnetic peak the exponential rise and decay terms A and B were held constant with field and temperature, and only the integrated intensity, position and Gaussian standard deviation were allowed to vary. Figure 6.6 shows the variation of wavevector with applied magnetic field for the $(1-2q, q, -\frac{1}{2})$, $(1-q, 2q, -\frac{1}{2})$, $(2q, 1-q, \frac{1}{2})$, and $(q, 1-2q, \frac{1}{2})$ reflections. The time-of-flight position was extracted by fitting with the back-to-back exponential function, converted to $d-$spacing, and used to calculate the q from the wavevector (q,q,$\frac{3}{2}$). The four-sublattice phase exists up to and including 7 T at 1.5 K, with the wavevector commensurate at $q = {}^1/_4$. At 8 T $CuFeO_2$ enters the ferroelec-

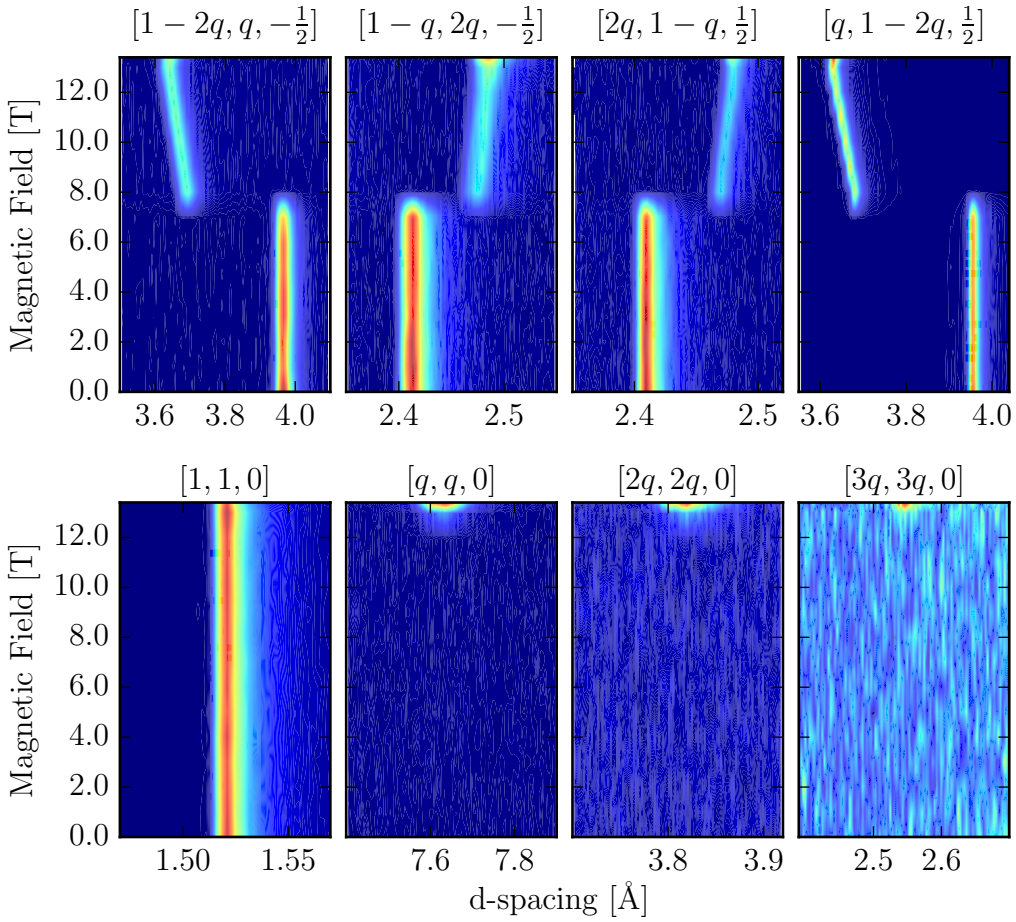

Figure 6.5: Neutron diffraction contour maps showing $d-$spacing of seven satellite reflections and the (110) Bragg peak as a function of applied magnetic field along the c-axis at a temperature of 1.5 K.

tric incommensurate phase where the wavevector jumps to an incommensurate position $q \sim 0.21$. The wavevector then decreases linearly with magnetic field till 13 T where $q = \frac{1}{5}$. Between 13 and 13.4 T the system enters the five-sublattice phase, where $q = \frac{1}{5}$.

The transition between all the phases, particularly the FEIC and 5SL phase, are more easily seen in the variation of intensity shown in figure 6.7. For the 4SL and FEIC phase a constant intensity has been fit and plotted using a dashed line. These dashed lines act as a guide to the eye to highlight the different phases. The magnetic peaks appear to get weaker in the FEIC phase.

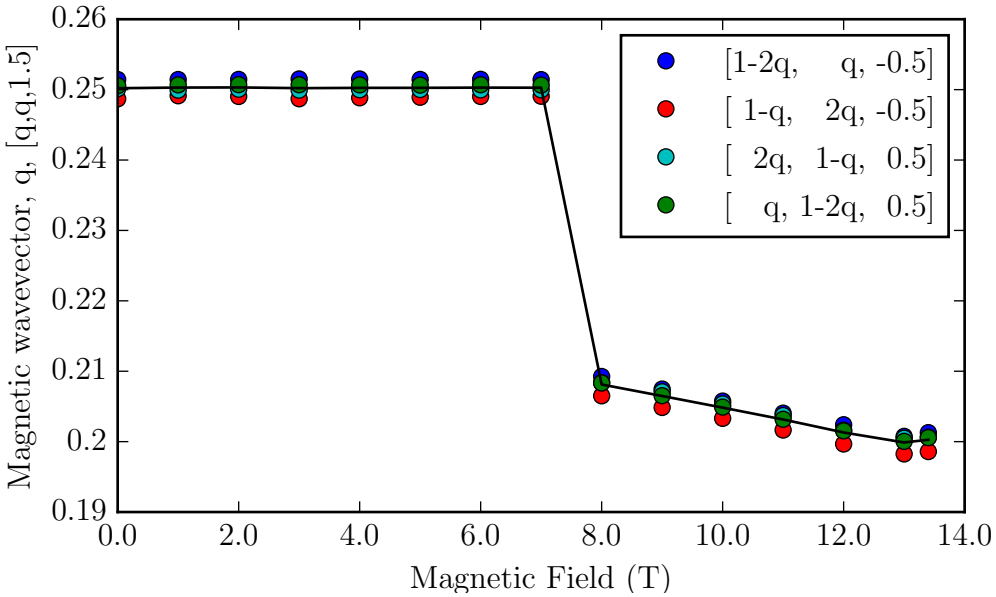

Figure 6.6: Wavevector q of the magnetic satellite peaks as a function of magnetic field at 1.5 K, extracted from fitting the time-of-flight neutron data of the four satellite reflections shown in the top of figure 6.5 using a back-to-back exponential function. The q-wavevector has been calculated using the a lattice parameter measured from the (1,1,0) Bragg peak at each field.

In the FEIC phase, seven additional peaks appeared at reciprocal space positions (q,q,3/2) away from 1/2 positions, e.g. (1/2 + q,q − 1/2,1/2). It is not possible to comment on whether these peaks exist in the 4SL phase, because with q = 1/4 the additional 1/2 − $\boldsymbol{\tau}$ peaks overlap with the $(HKL) - \boldsymbol{\tau}$ peaks. Figure 6.8 shows a colour-map of the intensity and variation of wavevector of the (1/2 − q, 2q, 1/2) peak with applied magnetic field. The 1/2 − $\boldsymbol{\tau}$ reflection's incommensurate position has identical behaviour as the $(HKL) - \boldsymbol{\tau}$ type reflections. The intensity of the peak is strongest when it first appears at 8 T and gradually gets weaker with applied field. At 13.4 T, the peak appears to vanish completely, however a peak remains with an intensity of 1 % of it's maximum value.

A temperature scan was performed, by collecting Laue images in an applied field of 13 T, from 3 K until it disappeared around a temperature of 14 K. This scan starts in the five-sublattice phase and passing through the partially disordered phase, before the peaks disappear in the paramagnetic phase. Figure 6.9 shows contour maps of a selected number of magnetic and nuclear Bragg peaks, plotting the $d-$spacing on the $x-$axis and

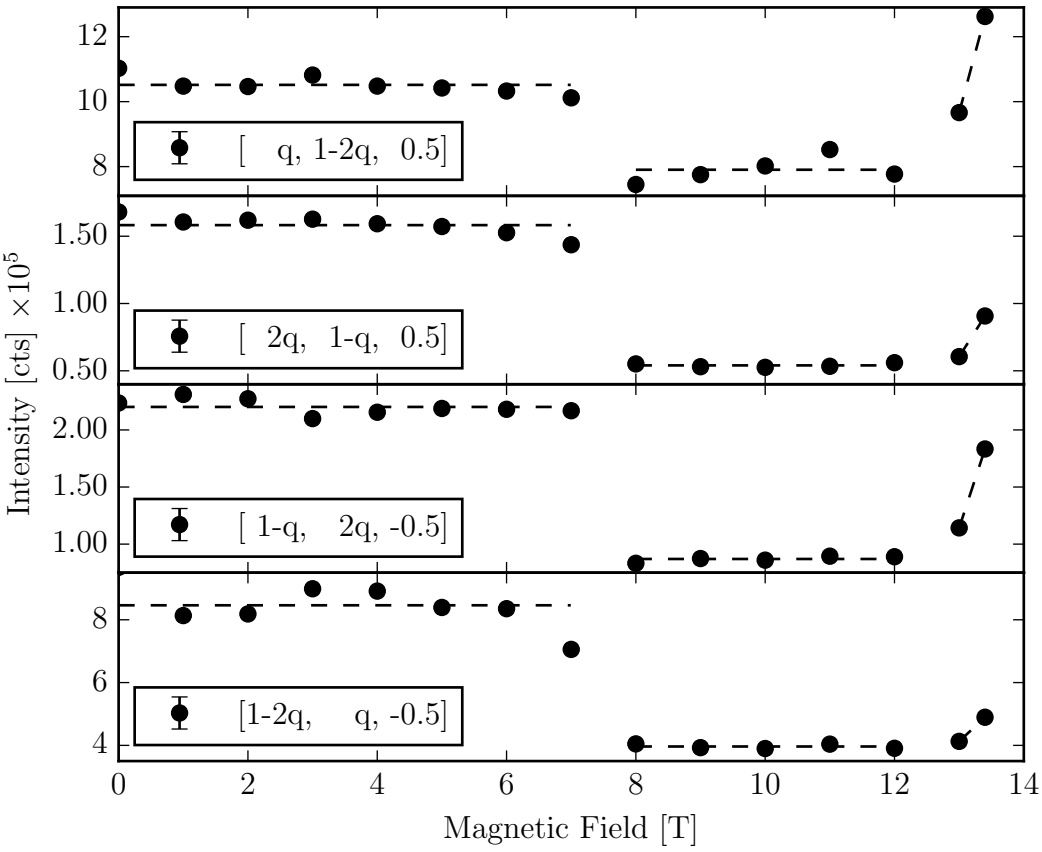

Figure 6.7: The integrated intensity of the magnetic satellite peaks as a function of magnetic field. Integrated intensity was measured from fitting the time-of-flight neutron data of the four satellite reflections shown at the top of figure 6.5 using a back-to-back exponential function. Three distinct phases can be seen in the intensity, with the linear fits acting as guides to the eye.

the temperature on the $y-$axis. The top row shows the $(HKL)-\boldsymbol{\tau}$ type reflection, where a commensurate to incommensurate transition occurs between 9 and 10 K. The $d-$spacing remains fixed on warming from 3 K to 9 K and begins to vary above 9 K. Above 10 K the intensity of the peak slowly decreases before disappearing completely above 13 K. The lower right frame in figure 6.9 shows the behaviour of the (110) nuclear Bragg peak. This does not, as expected, appear to vary significantly with temperature compared to the magnetic peaks.

The remaining three contour maps on the bottom right of figure 6.9 show the $(q,q,0)$, $(2q,2q,0)$, $(3q,3q,0)$ type reflections. The $(q,q,0)$ and $(3q,3q,0)$ type reflections disap-

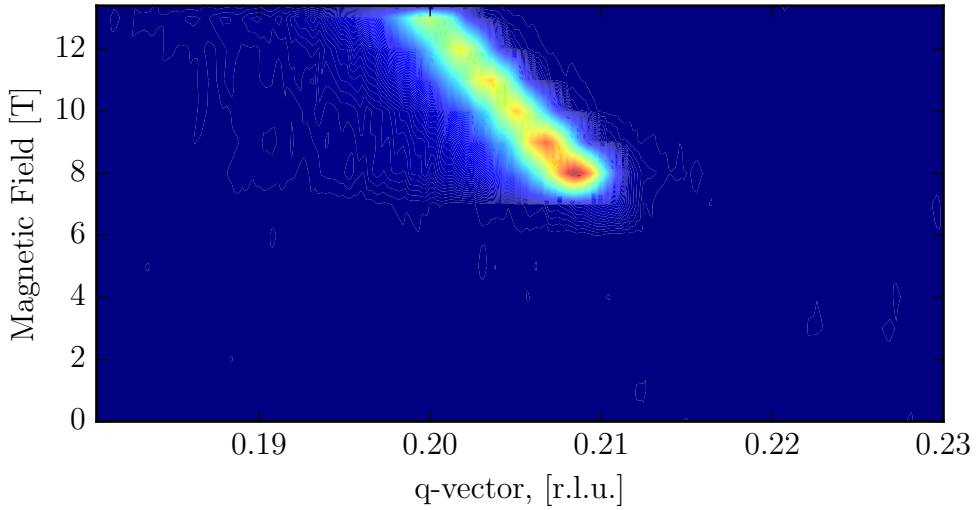

Figure 6.8: Contour colour plot showing the q wavevector of the $(1/2 - q, 2q, 1/2)$ as a function of magnetic field. The $q = 1/4$ 4SL phase the peak would overlap with the $(q, 1 - 2q, 1/2)$ type reflection. A very weak peak remains at 13.4 T, approximately 1% of the maximum intensity.

pear at 9 K where the $(HKL) - \boldsymbol{\tau}$ type reflections become incommensurate. The $(2q, 2q, 0)$ reflection shows similar behaviour to the odd reflections up until 9 K, but shows incommensurate behaviour above 9 K, before disappearing above 13 K. Once again a convolution of a back-to-back exponential and a Gaussian (equation 6.1), was used to fit the diffraction peaks in the time-of-flight spectra.

Figure 6.10 shows the temperature dependence of the wavevector for a selection of reflections. The top frame shows the wavevector q for reflections of type $(HKL) - (q, q, 3/2)$. For the calculation from $d-$spacing to wavevector, q, the a lattice parameter was extracted from the $(1, 1, 0)$ Bragg peak, whilst the literature value of the c-lattice parameter was used (a = 17.17 Å [211]). There is a systematic offset on the calculated wavevector between different magnetic Bragg peaks. This maybe due to the hexagonal lattice not being the correct basis to expresss the wavevector in, as a lower monoclinic structure has been shown to be necessary to describe $CuFeO_2$ at low temperatures [210–213]. The results show the wavevector, starts with $q = 1/5$ in the five-sublattice phase at 3 K. With increasing temperature the wavevector remains constants at $1/5$ until 9 K, above which the wavevector becomes incommensurate, gradually moving with temperature until disappearing at $q = 0.193$ around 13 - 14 K.

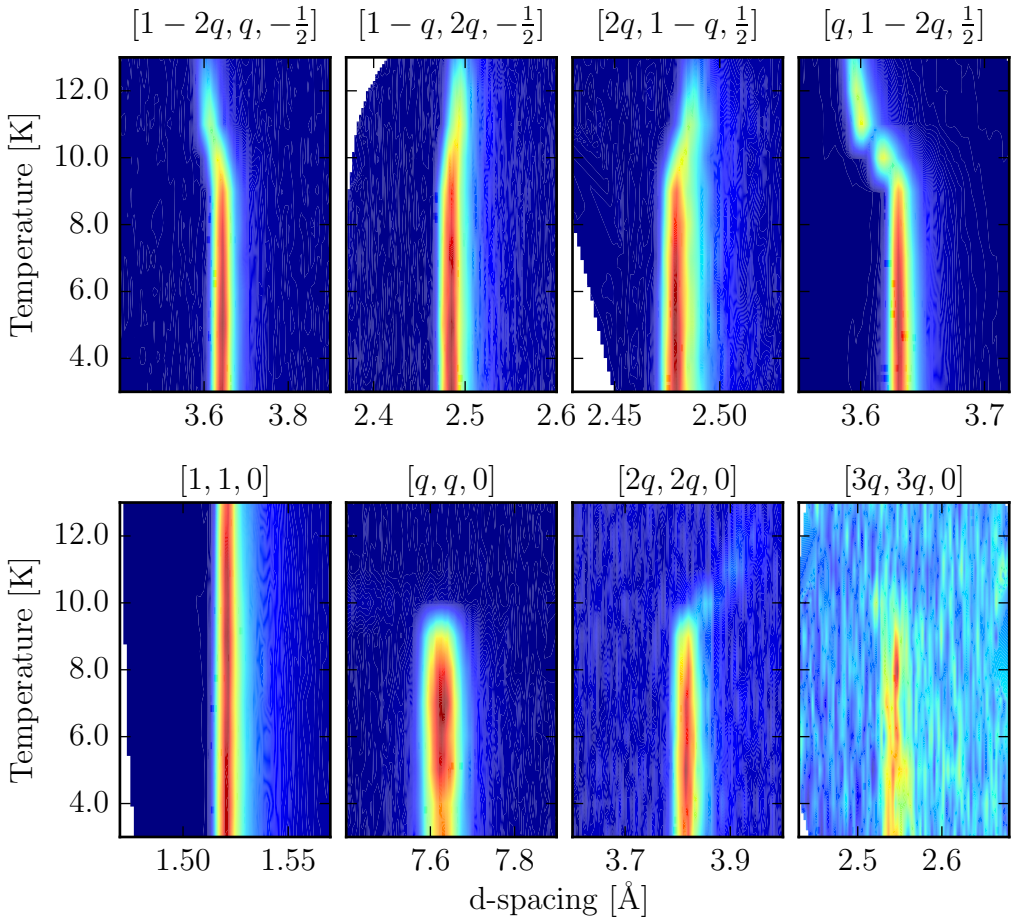

Figure 6.9: Neutron diffraction heat maps showing $d-$spacing of seven satellite reflections and the (1,1,0) Bragg peak as a function of increasing temperature in an applied magnetic field along the c-axis of 13 T.

The lower frame in figure 6.10 shows the temperature dependence of the wavevector q for the $(q, q, 0)$ type reflections. The odd multipules, i.e. $(q, q, 0)$ and $(3q, 3q, 0)$ stay constant at $q = 1/5$, then disappear above 9 K. The $(2q, 2q, 0)$ reflection remains constant at $q = 1/5$ until 9 K, at which point it becomes incommensurate shifting with temperature to a lower value around $q = 0.194$ before vanishing at 14 K. Figures 6.11 and 6.12 show the temperature dependence of integrated intensity of the $(HKL) - \boldsymbol{\tau}$ and $(q, q, 0)$ type magnetic reflections. The pink area indicates the temperature range where the wavevector transitions from commensurate to incommensurate. In the case of the $(HKL) - \boldsymbol{\tau}$

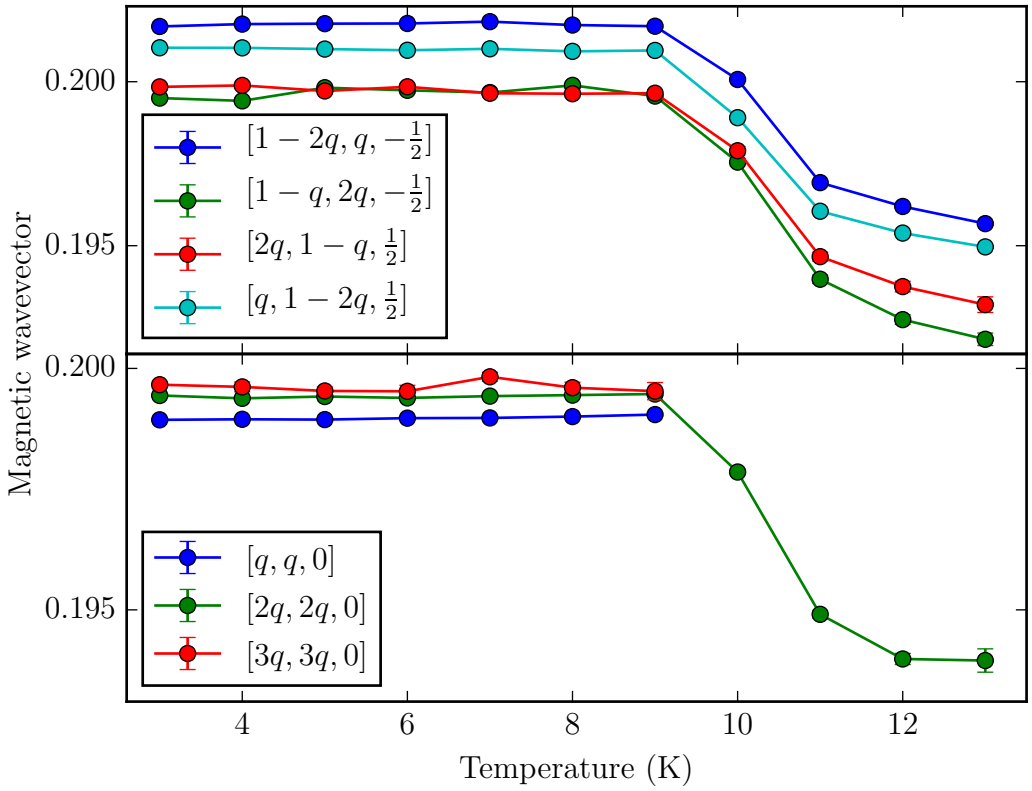

Figure 6.10: Wavevector q of the magnetic satellite peaks as a function of temperature, extracted from fitting the time-of-flight neutron data of the seven satellite reflections shown in top of figure 6.9 using a back-to-back exponential function. The q-wavevector has been calculated using the a lattice parameter measured from the (1,1,0) Bragg peak at each temperature.

reflections the intensity was fitted with a critical exponent of the form shown in equation 6.2.

$$I(T) = I_0 \left(\frac{T_c - T}{T_c} \right)^{2\beta} \tag{6.2}$$

In figure 6.11, the critical exponent fits are plotted in a dashed red line. The results of fitting the critical exponent found a transition temperature of 13.6 K and β values in the range 0.17 - 0.27. From the integrated intensity data alone, shown in figure 6.11 it is not possible to identify the commensurate to incommensurate transition.

Reflection	Type	$d-$spacing, Å	Phase
$(-q, 1-q, 1/2)$, $(q, 1-2q, 1/2)$, $(1-q, -1+2q, 1/2)$, $(1-2q, -1+q, 1/2)$, $(-1+2q, -q, 1/2)$, $(1-2q, q, -1/2)$, $(1-q, -q, -1/2)$	$(HKL)-\tau$	3.57-3.94	4SL, FEIC, 5SL, PD
$(2q, 1-q, 1/2)$, $(1-q, 2q, -1/2)$, $(1-q, -2q, -1/2)$	$(HKL)-\tau$	2.48-2.40	4SL, FEIC, 5SL, PD
$(-q, 1+2q, 1/2)$, $(q, 1+q, 1/2)$	$(HKL)-\tau$	2.01-1.88	4SL, FEIC, 5SL, PD
$(-1/2+q, 1/2+q, 1/2)$, $(1/2-q, 2q, 1/2)$, $(1/2+q, -2q, 1/2)$	$1/2-\tau$	4.21-4.28	FEIC
$(1-2q, 1/2+q, 1/2)$, $(1/2+q, 1-2q, -1/2)$, $(3/2-q, -1+2q, -1/2)$	$1/2-\tau$	2.34-2.32	FEIC
$(1/2+q, -2q, 1/2)$	$1/2-\tau$	4.21-4.28	FEIC
$(q, q, 0)$	$(q, q, 0)$	7.57	5SL
$(2q, 2q, 0)$	$(q, q, 0)$	3.79-3.92	5SL, PD
$(3q, 3q, 0)$	$(q, q, 0)$	2.53	5SL

Table 6.1: Table of magnetic reflections detected in the Laue images across all accessible phases. Reflections are divided up by type and $d-$spacing as well as which phases they were detected in. In the case where $d-$spacing is given as a range, is due to the variation of q across the phase diagram, all the reflections have the same spacing for a particular field and temperature.

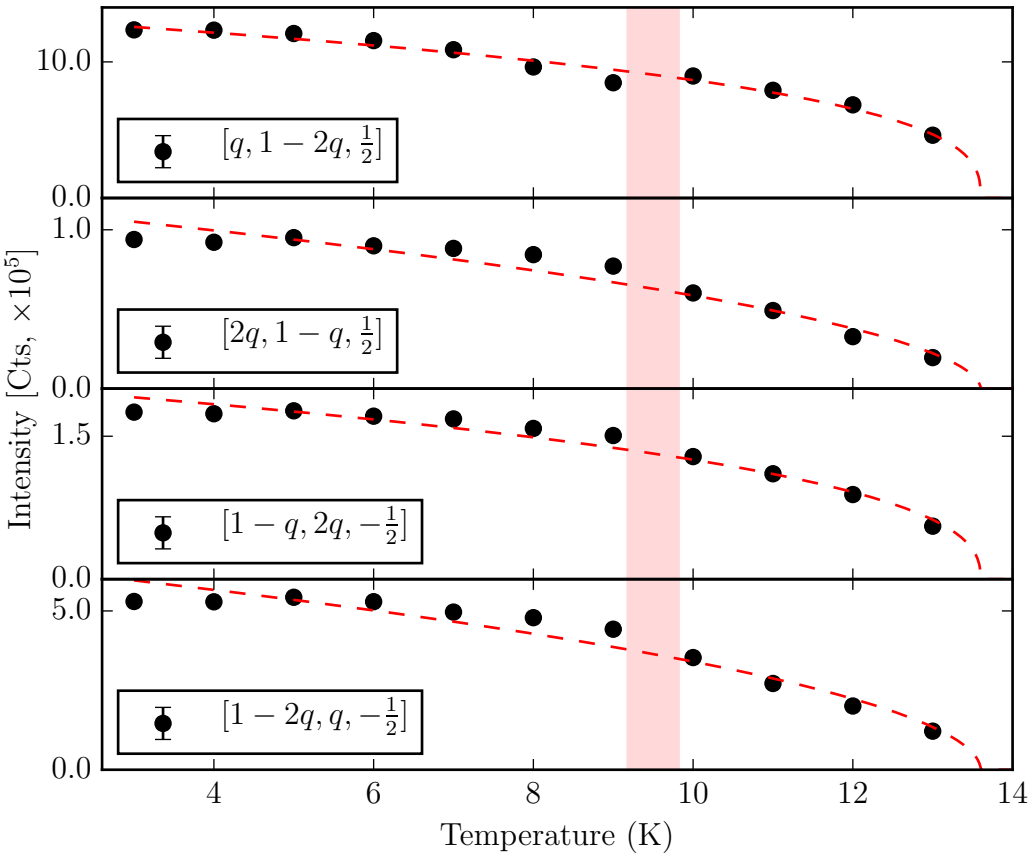

Figure 6.11: Integrated intensity of the $(q, q, 3/2)$-type magnetic satellite peaks as a function of temperature. The integrated intensity was measured from fitting the time-of-flight neutron data of the reflection shown at the top of figure 6.9 using a back-to-back exponential function. A critical exponent curve has been fitted to the data. The transparent red line indicates the transition from commensurate to incommensurate wavevector.

6.5.2 High-field x-ray diffraction

Figures 6.13, 6.14 and 6.15 show the results of the high-field x-ray diffraction experiment performed at P09. The experiment was performed at the iron *K* edge, in the hopes of detecting a magnetic reflection on resonance. The experiment was confined to the *a*-*b* plane, and no resonantly enhanced satellite reflections were detected. A non-resonant reflection was found at a position of [0.6, 0.6, 0) in the five-sublattice phase, this could be indexed up as either a $(3q, 3q, 0)$ reflection or a $(1, 1, 0) - (2q, 2q, 0)$ type reflection. Figure 6.13 shows the contour plots of the $(0.6, 0.6, 0)$ reflection for field and tempera-

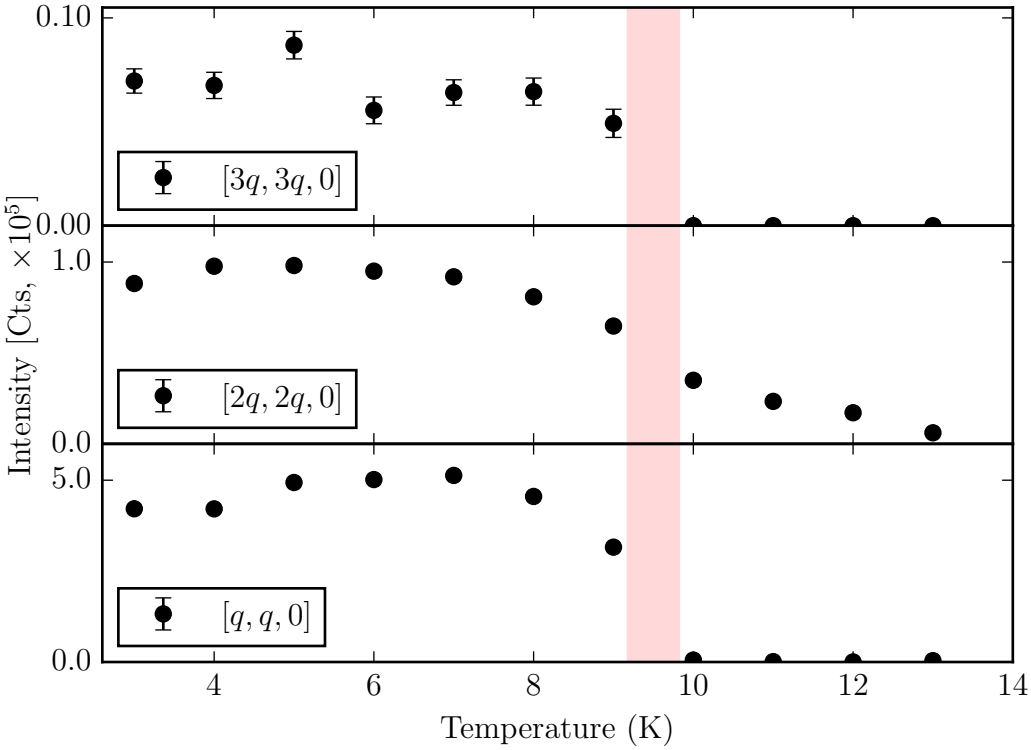

Figure 6.12: Integrated intensity of the $(q, q, 0)$-type magnetic satellite peaks as a function of temperature. The integrated intensity was measured from fitting the time-of-flight neutron data of the reflections shown at the bottom of figure 6.9 using a back-to-back exponential function. The transparent red line indicates the transition from commensurate to incommensurate wavevector.

ture dependences across the phase diagram. The contour plots were measured by taking reciprocal space scans along the $[HH0]$ direction at different temperatures and magnetic fields. Figure 6.13(a) shows a schematic of the magnetic field phase diagram of $CuFeO_2$, with the two temperature scans (A&B) and magnetic field scan (C) shown. Figure 6.13(d) shows an applied magnetic field scan at 2 K. This scan clearly indicates the $(0.6, 0.6, 0)$ only exists above 12.5 T in the five-sublattice phase.

Figure 6.13(b) and (c) show the temperature dependences of the $(0.6, 0.6, 0)$ reflection at different applied magnetic fields, 13 T and 11 T respectively. In the 11 T scan the $(0.6, 0.6, 0)$ reflection does not appear until the system is warmed up above 8.5 K, whilst in the 13 T scan, the reflection is there from 2 K but gets stronger on warming. This shows a curved boundary between the FEIC phase and the 5SL phase. Both scans at 11 T

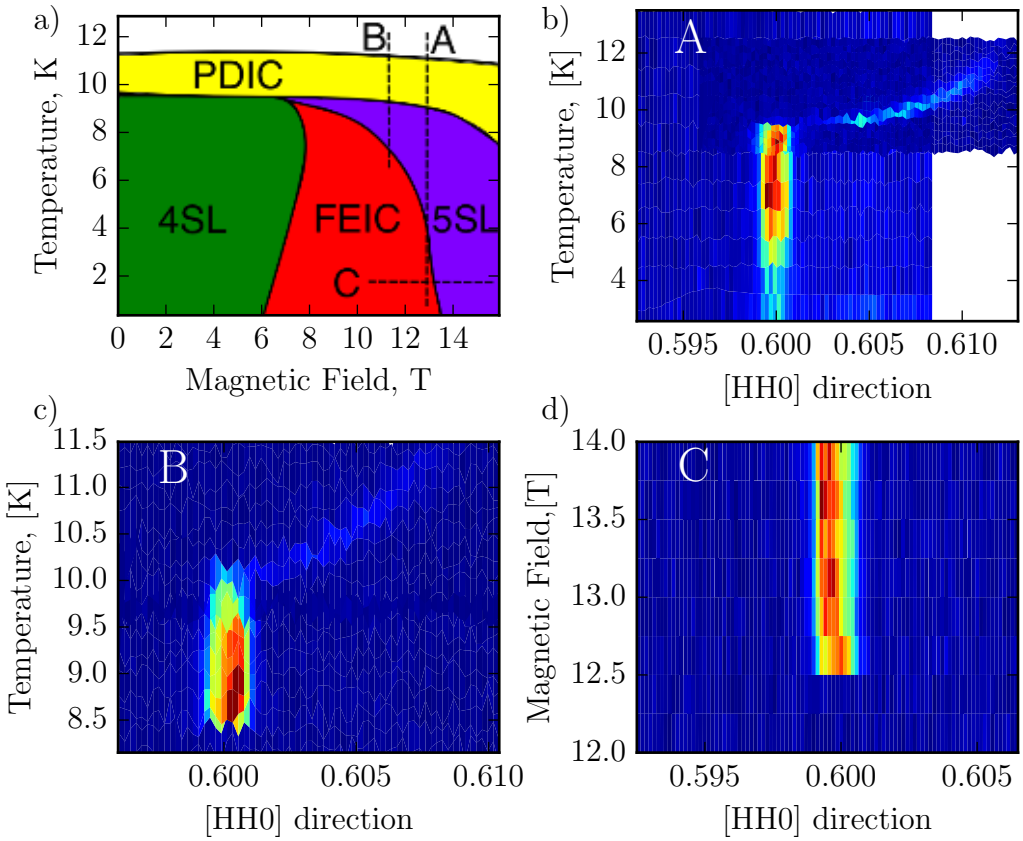

Figure 6.13: X-ray diffraction performed in high magnetic field. (a) Magnetic phase diagram highlighting scan directions. (b) Temperature dependence of the (0.6,0.6,0) reflection at magnetic field of 13 T, labelled A in fig a). (c) Temperature dependence of the (0.6,0.6,0) reflection at magnetic field of 11 T, labelled B in fig a). (d) Magnetic field dependence of of (0.6,0.6,0) reflection at a temperature of 2 K, labelled C in fig a)

and 13 T show the reflection to transition to a incommensurate wavevector above 10 K. The wavevector gradually increases with temperature until $q = 0.613$ at which point the reflection disappears at 12 K. This indicates that the reflection should be indexed up as the $(1, 1, 0) - (2q, 2q, 0)$ as the wavevector is shown to decrease in the partial disordered phase from the neutron results. Figure 6.14 shows a high-resolution $[HH0]$ reciprocal space scan using a post-scatter polarisation analyser. The polarisation analysis shows the diffraction is only present in the $\pi - \pi$ channel and is completely absent from the $\pi - \sigma$

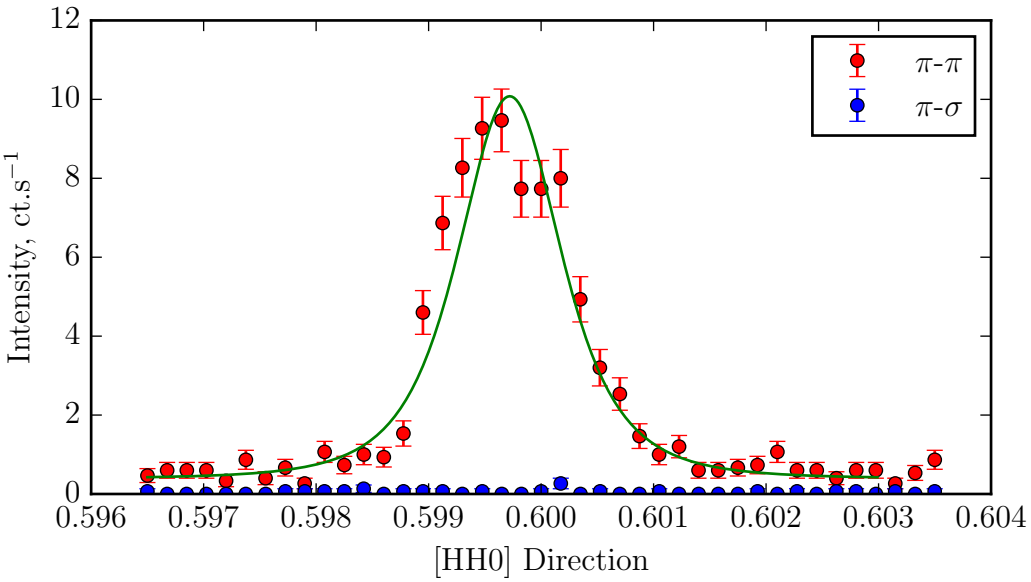

Figure 6.14: Reciprocal space scan in the $[HH0]$ direction, using a polarisation analyser crystal with π incident light. $\pi-\pi$ channel shown in red and $\pi-\sigma$ channel shown in blue.

channel. The polarisation analysis combined with the non-resonant nature of the satellite peak indicates this reflection is structural in origin. The temperature dependence at 13 T, was analysed by fitting a Lorentzian-squared peakshape to the reciprocal space scans. Figure 6.15 shows the temperature dependence of the centre of the diffraction peak and the width of the diffraction peak. The transition from commensurate to incommensurate wavevector is at 9.3 K. The satellite peak disappears at 11.8 K. Beam heating from the x-ray beam, will cause a systematic offset in transition temperatures between x-ray and neutron measurements. The commensurate-incommensurate transition shows the same wavevector behaviour as the neutron diffraction. The width of the peak increases as the system cools down through the partially disordered phase between 11.8 K and 9.3 K. Below 9.3 K the width of the peak jumps to a narrower value, similar to the value at 11.8 K, where it remains constant on further cooling. The peak width is inversely proportional to the correlation length of the phase. An increase in peak width of the structural satellite upon cooling is a peculiar trait as electronic phases tend to become more correlated upon cooling. This behaviour indicates a clear difference between the five-sublattice phase and the partially disordered phase.

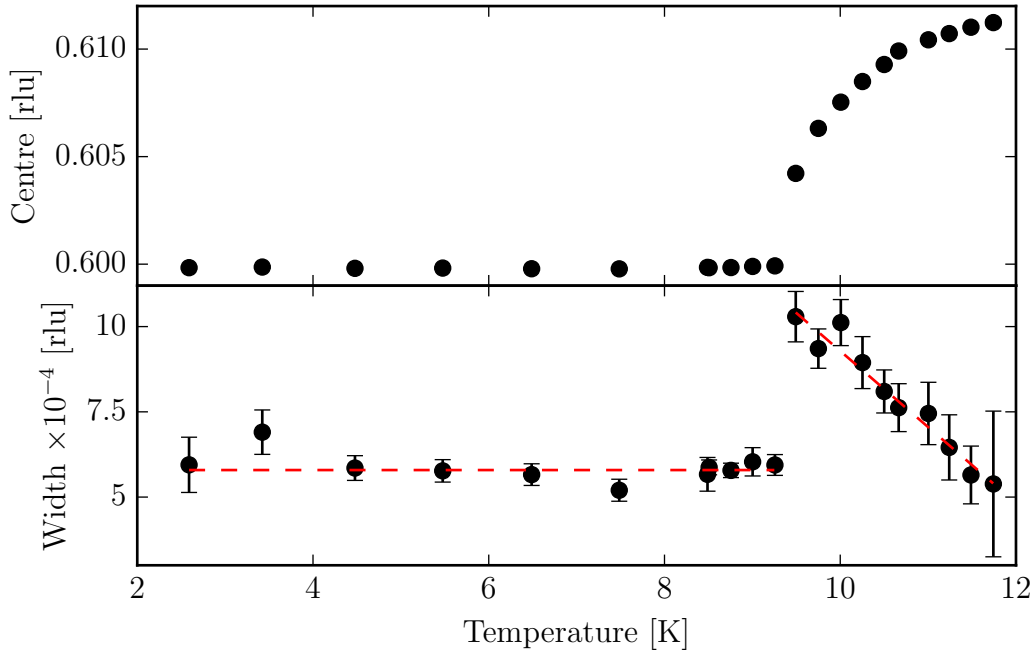

Figure 6.15: Temperature dependences of the (0.6,0.6,0) satellite peak. The [HH0] reciprocal space scan was fitted with a Lorentzian-squared and the centre (top) and width (bottom) were extracted.

6.5.3 Zero-field x-ray experiments

Figures 6.16, 6.17, 6.19 and 6.20 show the results of a resonant x-ray scattering study of the zero field four-sublattice phase, and fig 6.18 of the zero-field partial disordered incommensurate phase. The experiments were performed at the iron K absorption edge. The experiment was performed at I16, the ($^{-}3/4, 2\,1/4, 3/2$) satellite reflection was detected and found to resonate. This reflection can be indexed up as a satellite of the $(2,-1,0)$, being ($1/4, 1/4, 3/2$) away. Figure 6.16 shows the energy resonance spectra of the ($^{-}3/4, 2\,1/4, 3/2$) reflection in the $\sigma-\sigma$ (top) and $\sigma-\pi$ (bottom) polarisation channels measured at a number of different azimuthal positions. Resonant contributions appear in both polarisation channels. The measured spectra show multiple contributions to the resonance structure with different azimuthal dependences. An azimuthal measurement was undertaken at 7115 eV in the $\sigma-\pi$ channel and 7118 eV in the $\sigma-\sigma$ channel. The $[0,0,1]$ direction was used as the azimuthal reference vector. This means the zero point on the azimuth corresponds to when the $[0,0,1]$ lies in the scattering plane closest to $\mathbf{k}'$. Figure 6.17 shows the results

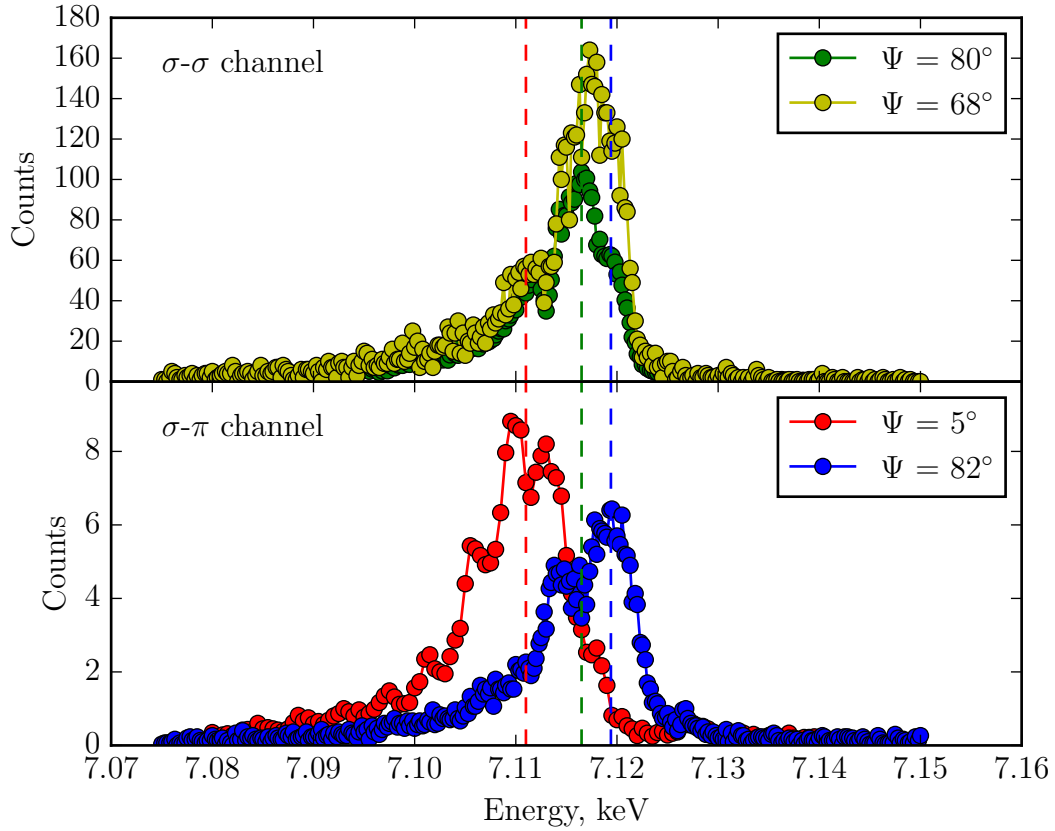

Figure 6.16: Energy scans across the resonance of the $(-3/4, 21/4, 3/2)$ magnetic satellite peak at the Fe K absorption edge at different azimuths in the $\sigma-\sigma$ and $\sigma-\pi$ polarisation channels.

of the azimuthal measurement. The dashed blue and green lines show simulations for a collinear magnetic structure with magnetic moments pointed along the c-axis. $E2E2$ scattering is required to simulate the scattering in the $\sigma-\sigma$ channel, as $E1E1$ scattering process does not have a contribution in the $\sigma-\sigma$ channel. The simulations for $E1E1$ and $E2E2$ scattering have the same azimuthal dependence in the $\sigma-\pi$ channel. For $E2E2$ scattering the intensity is calculated to be 100 times stronger in the $\sigma-\sigma$ channel than the $\sigma-\pi$ channel. Both $E1E1$ and $E2E2$ scattering processes are needed to fully explain the azimuthal data.

At high azimuth angles the simulation differs significantly from the data, although qualitatively shows similar behaviour. The sample was not mounted with the $(-3/4, 21/4, 3/2)$

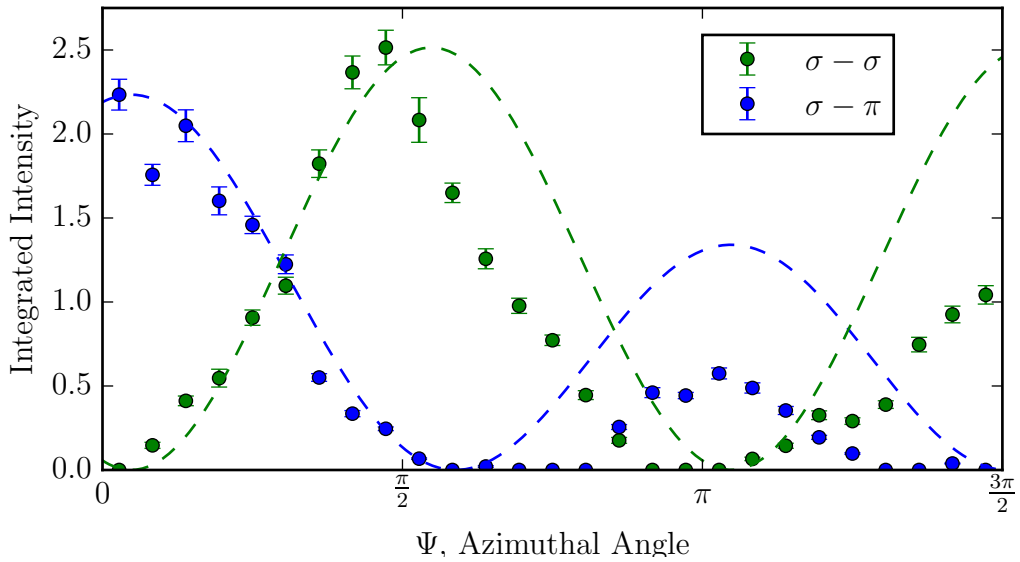

Figure 6.17: Intensity of the ($^{-3}/_4, 2^1/_4, ^3/_2$) magnetic satellite peaks as a function of azimuthal angle, measured from the [001] in the both $\sigma - \sigma$ and $\sigma - \pi$ polarisation channels. The $\sigma - \sigma$ channel was measured at 7118 eV and $\sigma - \pi$ channel at 7115 eV. The simulations require both $E1E1$ and $E2E2$ type resonant transitions.

reflection as the surface-normal direction. A change in the amount of x-rays absorbed as the sample is rotated around the azimuth, is likely to be the cause of the low intensity at high azimuth. Additionally an incommensurate peak was found in the partially disordered phase at 11 K in zero magnetic field. Figure 6.18 shows reciprocal space scan across the incommensurate peak. The wavevector was found to be $q = 0.211(1)$, closer to $^1/_5$ than $^1/_4$.

In the experiment performed at P09, resonantly enhanced reflections were found at the ($^1/_4, ^1/_4, ^3/_2$) and ($^3/_4, ^3/_4, ^9/_2$) ($(1, 1, 6) - (^1/_4, ^1/_4, ^3/_2)$) positions. Both these reflections are along the same crystallographic direction. Figure 6.19 shows the resonance spectra of the ($^1/_4, ^1/_4, ^3/_2$) and ($^3/_4, ^3/_4, ^9/_2$) reflections, in the top and bottom frames respectively. The dashed line shows the fluorescent spectra, whilst the red lines shows the resonance spectra of the ($2^1/_4, ^{-3}/_4, ^3/_2$) reflection measured at I16. The point of inflexion in the fluorescent absorption measurement is at 7123.5 eV. The main resonance feature appears at 7129.5 eV, with extra resonance peaks at 7114.5, 7140, 7175 eV. This is a highly unusual structure for a K edge resonance, especially the resonance feature 50 eV above the absorption edge.

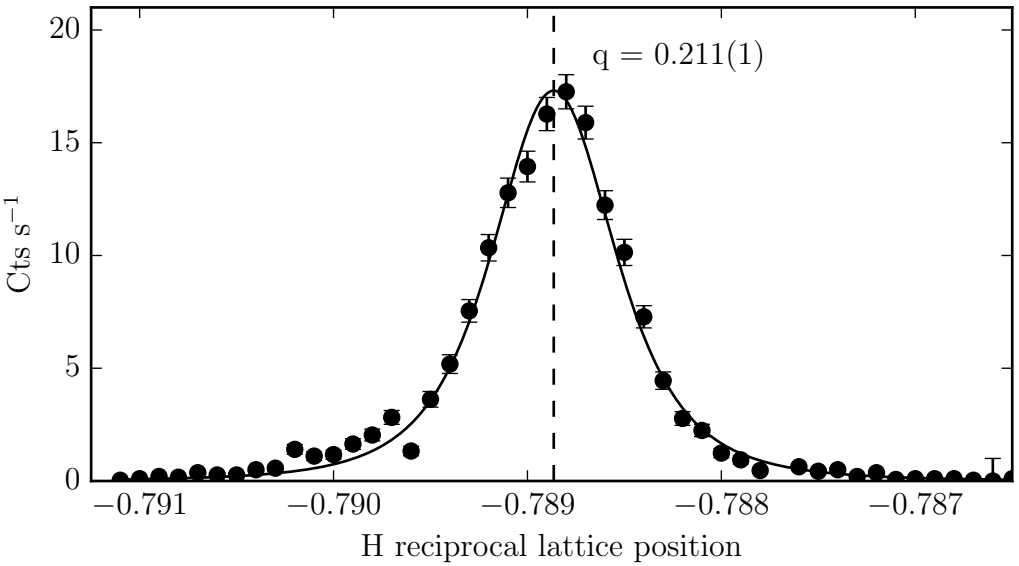

Figure 6.18: Scan measured along the $[-1, 2, 0]$ direction of the incommensurate peak $(-0.789, 1.422, 1.5)$ in the partially disordered phase at 0 T and 11 K.

A full linear polarisation analysis was performed on the main resonance feature at 7129.5 eV of the $(1/4, 1/4, 3/2)$ reflection. The polarisation analysis was performed at an azimuth of 24.5° with the azimuthal reference vector defined as the $[-1, 0, 0]$. Figure 6.20 shows the result of the polarisation analysis, with the outgoing polarisation expressed using the Poincaré-Stokes parameters. Experimentally only P_1 and P_2 can be found, as it is not possible to distinguish the circular polarised contribution from the unpolarised signal. The solid lines are simulations of the diffraction from a collinear magnetic structure, with the magnetic moment pointed along the c-axis. $E2E2$ resonance is necessary to simulate the data, as $E1E1$ requires P_1 and P_2 to be -1 and 0 for an incident polarisation of 0°. In order to fully simulate the data, the fact that the incident polarisation is not 100% polarised has to be taken into account. For the phase plates at P09 the linear Poincaré-Stokes component can be expressed approximately using equation 6.3 [231].

$$P_{\mathrm{Lin}} = \sqrt{P_1^2 + P_2^2} \approx 0.95 + 0.05 \sin(2\eta + \pi/2) \tag{6.3}$$

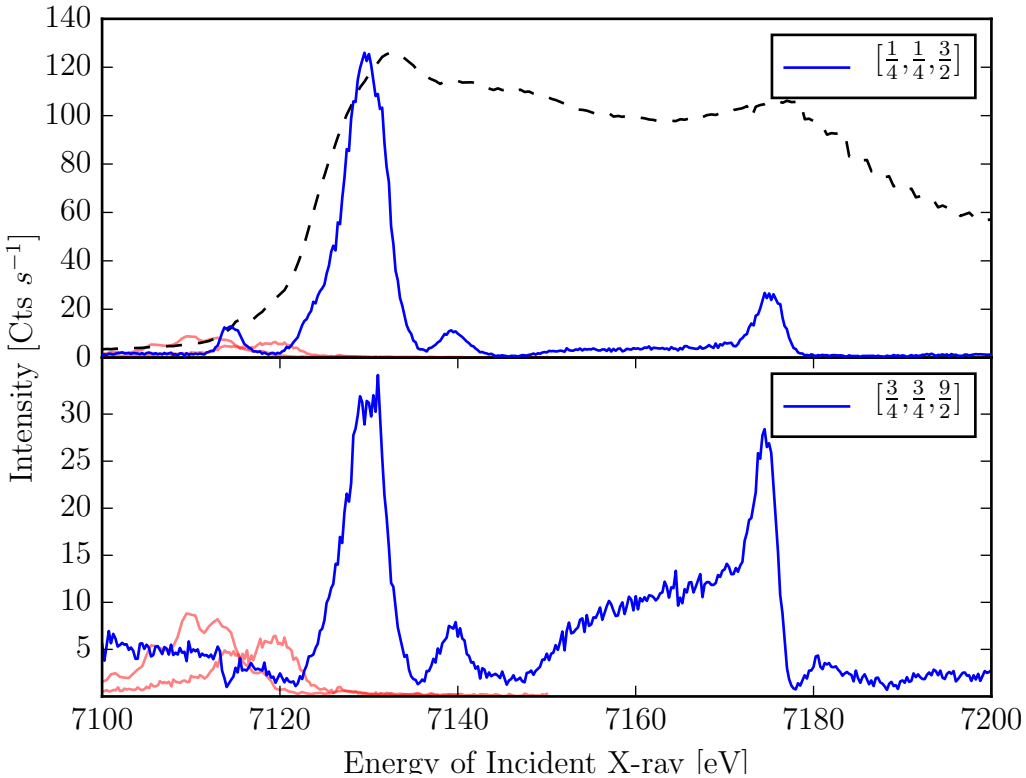

Figure 6.19: Energy scans across the resonance of the (¼, ¼, ³/₂) (top) and (¾, ¾, ⁹/₂) (bottom) magnetic satellite peak at Fe K absorption edge in the σ-π polarisation channels. The resonance shown in red is the I16 data measured at the ($^{-}$¾, 2¼, ½) satellite peak. The fluorescence scan is shown in black.

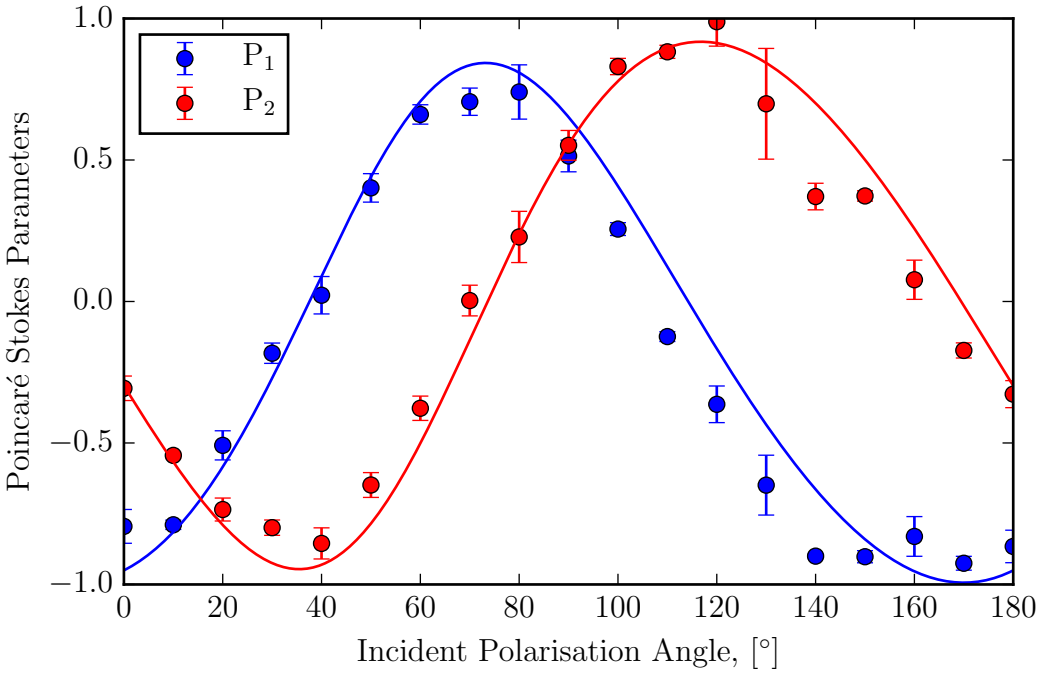

Figure 6.20: Full linear polarisation measurement of the (¼, ¼, ³⁄₂) magnetic satellite peak on top of the resonance at 7129.5 eV. The Poincaré-Stokes parameters P_1 and P_2 of the scattered x-ray are shown in blue and red circles respectively. The solid lines are calculated from a simulation of $E2E2$ electric transition with the magnetic moment aligned along the c-axis.

6.6 Discussion

The neutron experiment on WISH marks the first diffraction measurements out of the $[HH0]$ plane for the FEIC and 5SL phase for undoped $CuFeO_2$. The neutron results clearly reveal four distinct phases in the magnetic field phase diagram. The diffraction from the 4SL is simply composed of a star of satellites of wavevector $(1/4, 1/4, 3/2)$ away from the allowed nuclear Bragg peak. The five-sublattice is composed of two types of reflections, with wavevectors $(1/5, 1/5, 3/2)$ and $(1/5, 1/5, 0)$. The FEIC phase is composed of reflections with wavevector $(q, q, 3/2)$ away from nuclear Bragg peaks as well as away from half-positions in reciprocal space. Finally the PDIC phase was found to have incommensurate reflections at positions $(q, q, 3/2)$ away from nuclear Bragg peaks as well as at $(2q, 2q, 0)$ reflection. It is not possible to distinguish between a multi-**q** structure where the magnetic phase is described by six **k**-vectors, or simply contributions from three magnetic domains contributing $\pm\mathbf{k}$ wavevectors. Figure 6.21 shows a HK reciprocal space map with $l = 1/2$ (left) and $l = -1/2$ (right). The magnetic Bragg peaks measured in the neutron experiment are shown by circles, with $(HKL) - \boldsymbol{\tau}$ reflections shown in black and $1/2 - \boldsymbol{\tau}$ shown in red. The symmetrically related reflections are shown slightly transparent. The arrows indicate the direction the magnetic diffraction peaks would move with an increasing magnetic wavevector q. The maps are drawn with $q = 1/5$, with the $q = 1/4$ positions indicated at the end of the arrow. The anomalous reflection circled in the $l = 1/2$ map indexes up as $(1/2, -1/2, -1] + [q, q, 3/2)$ reflection.

Neutron and resonant x-ray diffraction in the 4SL phase, measured magnetic Bragg reflections which could be indexed up as being $(1/4, 1/4, 3/2)$ away from crystallographic Bragg peaks. The measured positions of the magnetic reflections is in agreement with Mitsuda *et al.* [201] and Mekata *et al.* [199], who both performed neutron diffraction on powder samples of $CuFeO_2$. Mekata *et al.* found eight reflections, two of which were indexed up with $l = 1/2$. For our neutron diffraction measurement out-of-plane access was restricted, and only reflections with $l \pm 1/2$ were measured. Single crystal studies by Petrenko *et al.* and Mitsuda *et al.* [200, 220] restricted themselves to the $[HHL]$ diffraction plane, and consequently only observed reflection at positions $(\frac{2n+1}{4}, \frac{2n+1}{4}, \frac{6m+3}{2})$, where n and m are integers. There are no $l = \pm 1/2$ reflections in the $[HHL]$ diffraction plane. Both the azimuthal and FLPA measurement from resonant x-ray diffraction confirm the magnetic moment is collinear and lies along the c-axis. From the wavevector of $(1/4, 1/4, 3/2)$,

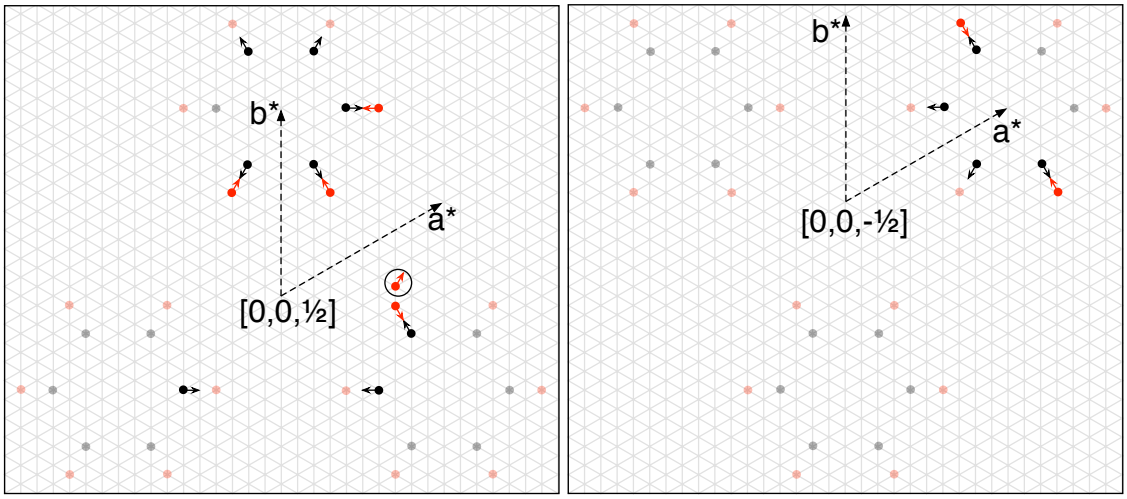

(a) **(b)**

Figure 6.21: Reciprocal space maps of the $l = {}^{1}/_{2}$ and $l = {}^{-1}/_{2}$ planes. The black marks indicates the $(HKL) - \boldsymbol{\tau}$ type reflections and the red marks indicate the ${}^{1}/_{2} - \boldsymbol{\tau}$ type reflections. The arrows indicate the directions the magnetic Bragg peaks would move with increasing q.

the magnetic cell requires a super cell of $4a_H \times 4b_H \times 2c_H$ of the hexagonal crystal cell. The l component of the magnetic wavevector is $l = {}^{3}/_{2}$. This arises from the antiferromagnetic stacking between layers in the c-direction. There are three offset triangular lattice layers in one crystallographic unit cell. The layers are stacked antiferromagnetically, $| \rightarrow\leftarrow\rightarrow | \leftarrow\rightarrow\leftarrow |$, resulting in three repeats of the magnetic stacking in two unit cells in the c-direction [199, 201], shown in figure 6.22a. The resonant x-ray diffraction showed both $E1E1$ and $E2E2$ resonant transitions. The observation of resonance at the iron K edge, rules out a purely spin moment, challenging the position of $CuFeO_2$ as an archetypal triangular lattice antiferromagnet with $S = {}^{5}/_{2}$. An unusually strong $E2E2$ contribution to the resonance has been measured. $E2E2$ is normally a weak effect in comparison to $E1E1$ scattering. Additionally there is a resonance 50 eV above the K edge, which is unusual for a K edge transition. The K edge, corresponds to a transitions from the $1s$ orbital, which has $l = 0$ and cannot be split. The unusual resonance spectra is purely a result of spin splitting of the $3d$ and $4p$ bands, and the role spin-orbit coupling plays in this material. In order to recreate Ising-like spin structure present in $CuFeO_2$, strong spin-phonon coupling has to be included in Monte Carlo simulations [207]. It may

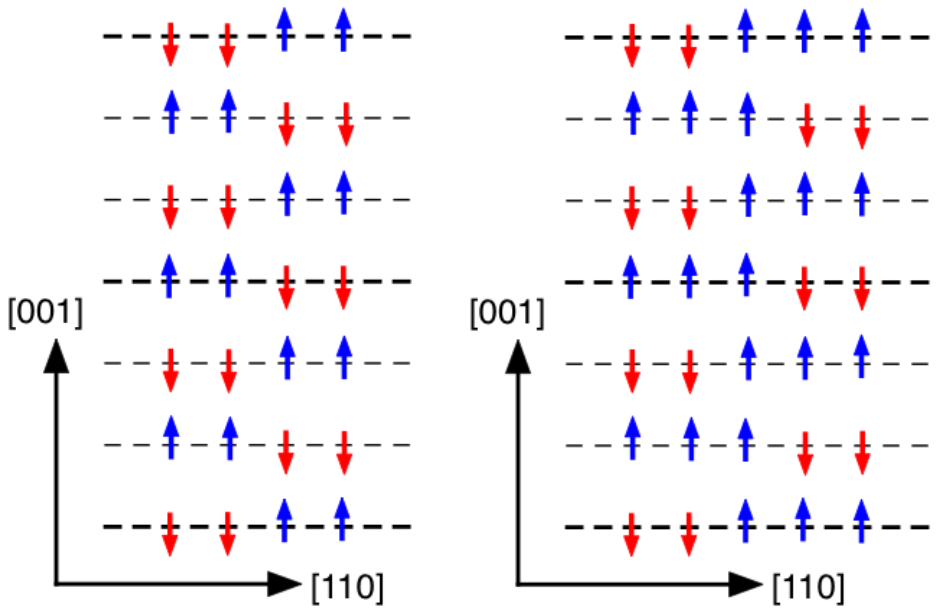

(a) **(b)**

Figure 6.22: Possible magnetic structures of the 4SL (left) and 5SL (right) phases. The large dashed line indicate the unit cells, whilst the thin dashed line indicates an Fe layer inside the unit cell. The origin of the $l = 3/2$ component of the magnetic wavevector can be seen as there are three repeats of the antiferromagnetic motiff in two crystallographic unit cells in the c-direction. The 5SL phase is composed of a antiferromagnetic cell and ferromagnetic cell giving rise to the two wavevectors, $(q, q, 3/2)$ and $(q, q, 0)$.

be the coupling of the lattice and spin degrees of freedom, that give $CuFeO_2$ its unusual resonance spectra.

Neutron measurements of the 5SL phase, resulted in two types of reflections, corresponding to $(1/5, 1/5, 3/2)$ and $(1/5, 1/5, 0)$ wavevectors. These two wavevectors correspond to a 5SL structure with a ferromagnetic component [220, 224]. Figure 6.22b shows the 5SL structure. Four of the moments stack antiferromagnetically, as in the 4SL case, with one moment stacking ferromagnetically between layers. The four antiferromagnetically stacked moments contribute to the $(1/5, 1/5, 3/2)$ type reflections, whilst the ferromagnetically aligned moment contributes to the $(1/5, 1/5, 0)$ type reflections.

When warming out of the 5SL phase into the PDIC phase, the $(q, q, 3/2)$ reflections

remain with q becoming incommensurate, becoming less the $^1/_5$. Of the $(q, q, 0)$ type reflections only the $(2q, 2q, 0)$ remains. The PDIC phase has been identified as a collinear incommensurate phase [199, 200]. This phase has been identified to be truly incommensurate, a study by Ye *et al.* [211] has shown that in zero field the wavevector, q, in the incommensurate phase moves from 0.19 to 0.22 on cooling, without locking in at $q = {}^1/_5$.

The $(2q, 2q, 0)$ reflection has been observed before in the PDIC phase under field by Mitsuda *et al.* [224]. Their interpretation of the $2q$ reflection, is that of a slight ferromagnetic component to the collinear incommensurate spin density wave, whose projection on to the [110] axis oscillates with a periodicity of $2q$. X-ray diffraction performed on the 5SL phase, identified a $(1 - 2q, 1 - 2q, 0)$ reflection. This reflection was not found to resonate, evidence of its structural origin. The temperature dependence of the wavevector of the structural distortion measured by x-rays is exactly twice the magnetic wavevector measured by neutrons. The identical wavevectors confirm the structural distortion from the hexagonal unit cell is driven by the magnetism; providing evidence that spin-lattice coupling plays a major role in determining the ground state of the system [207]. The temperature dependence of the width of the structural peak shows an unusual behaviour. The width of the structural satellite can be interpreted as how well the structural phase is correlated. On warming through the 5SL phase the widths remains constant. When warming into the PDIC phase the width discontinuously increases, and then proceeds to decrease upon further warming. This is odd behaviour as electronic phases tend to become better correlated on cooling not on warming, as was the case for the structural satellite measured in $SrFeO_3$ in figure 3.9. This is clear evidence of a second structural transition between the PDIC phase and the 5SL phase, at 11 K, distinct from the structural transition at 14 K.

The zero-field resonant x-ray diffraction experiment, recorded a magnetic satellite reflection in the PDIC phase at a single temperature, with a wavevector of $q \sim 0.211$, greater than $^1/_5$. This result confirms the result by Mitsuda *et al.* and Ye *et al.* [200, 211], that at zero field the PDIC wavevector on warming starts above $^1/_5$. The temperature dependence of the $(^2/_5, ^2/_5, 0)$ structural satellite measured at different magnetic fields shows the 5SL phase exists between the FEIC and PDIC phases, as shown in phase diagram in figure 6.13(a). Only two different fields were examined, so the FEIC phase and PDIC phase sharing a phase transition at a field lower than 11 K cannot be ruled out. At some point in the phase diagram for the PDIC phase, the incommensurate structure changes from being purely incommensurate, to tending towards $^1/_5$, when it shares a phase transition with the

5SL phase.

These results mark the first measurements of out-of-plane $(q, q, 3/2)$ type reflection in the FEIC phase in the undoped $CuFeO_2$ system. Extremely weak $(2q, 2q, 0)$ reflections have been measured by Mitsuda *et al.* [224]. The FEIC phase has been studied to great length in zero field, in the aluminium and gallium doped systems, $CuFe_{1-x}Al_xO_2$ and $CuFe_{1-x}Ga_xO_2$ [227, 232, 233]. In the FEIC phase, magnetic reflections appeared at $(q, q, 3/2)$ positions as well as $1/2 - (q, q, 3/2)$ positions. Upon application of magnetic field, the $(q, q, 3/2)$ type reflections have a discontinuous change in q, from $q = 0.25$ in the 4SL phase to $q = 0.21$ in the FEIC phase. Upon application of further magnetic field the wavevector $(q, q, 3/2)$ gradual shifts towards $q = 1/5$ at the 5SL phase transition.

Both the PDIC phase and FEIC phases have incommensurate wavevectors close to a $1/5$, suggesting a close connection to the 5SL phase. In the aluminium-doped samples the FEIC phase is thought to adopt a spin helical structure [227, 232]. The appearance of the $1/2 - (q, q, 3/2)$ type reflections is associated to the structural transition creating to inequivalent iron sites in the *a-b* plane. The two inequivalent iron sites cause two orbits of the helical structure to form with a phase difference between them. If this phase difference in not zero or π then magnetic satellites are predicted away from $1/2$ positions in reciprocal space. It is not possible to determine if the $1/2 - (q, q, 3/2)$ reflections exist in the 4SL phase, as they overlap exactly with reflection away from crystallographic Bragg peaks, shown in figure 6.21. The $1/2 - (q, q, 3/2)$ peaks were not observed in the 5SL phase, suggesting no phase shift between the two inequivalent sites. A phase shift between the two orbits in the FEIC phase, confirm the FEIC phase has a similar spin density wave magnetic ordering to the doped systems. The noncollinear spin density wave was shown to be a helix in the aluminium doped sample, by comparing intensities of reflections in different l layers [227]. Unfortunately this approach cannot be used in this study as only reflection in $l = \pm 1/2$ planes were measured. It has not been possible to distinguish cycloidal or helical ordering in the FEIC phase from this study. Different origins for the formation of the ferroelectric moment exist depending on whether the FEIC phase is described by a cycloidal or helical spin structure [228, 230]. In order to confirm whether the FEIC phase in $CuFeO_2$ adopts the same helical structure as the doped material, polarised neutrons will need to be employed [234]. The instrument WISH at ISIS is predominantly a powder instrument, and does not have the capabilities for polarised neutrons. In order to further characterise the FEIC phase, a different instrument with different capabilities is needed.

6.7 Conclusion

Neutron and x-ray scattering experiments have been performed on a single crystal sample of $CuFeO_2$. The Ising-like nature of the spin structure has been reconfirmed. Structural satellites have been found with twice the magnetic wavevector in the $[1, 1, 0]$ direction, confirming the strong spin-lattice coupling that occurs in this material. Evidence of two distinct structural transitions at 14 K and 11 K from the unusual temperature dependence of the $2q$ structural satellites. The behaviour of the width of the structural reflection between 11 and 14 K, identifies these two transitions not be be continuous. The 5SL phase was found to have a multi-**q** spin structure, with an antiferromagnetic ($^1/_5, ^1/_5, ^3/_2$) and a ferromagnetic ($^1/_5, ^1/_5, 0$) contributions. Diffraction from the FEIC phase was measured and shown to have similar behaviour to the aluminium doped counterparts. Although the measurement was not sufficient to distinguish between the cycloidal and helical spin structures, the appearance of $^1/_2 - (q, q, ^3/_2)$ type reflections show that the noncollinear structure is split into two inequivalent orbits. The phase shift between the two orbits is not known. Mapping out of the $2q$ structural satellites suggest the 5SL phase may separate the FEIC phase from the PDIC phase. The resonant scattering spectra rebut the idea that $CuFeO_2$ is a pure spin triangular lattice antiferromagnet, showing both the $3d$ and $4p$ bands are spin-polarised.

Chapter 7

Conclusions

In this thesis four different crystalline materials were studied using x-ray, neutron, and muon experimental techniques. These materials all contain iron but display a variety of different and interesting electronic phenomena. Understanding the microscopic mechanisms that leads to these electronic phenomena will aid in the design of new materials with technological applications.

The third chapter studied the an oxygen-vacancy-ordered perovskite $SrFeO_{3-\delta}$. This system has five structures separated by miscibility gaps. The $\delta = 1/8$ structure displays both negative and positive colossal magnetoresistance. The $\delta = 1/8$ structure has three different iron sites with different valencies. Bulk transport measurements of the magnetic susceptibility and resistivity characterised the magnetoresistance transition, and x-ray diffraction identified a structural transition as well as incommensurate structural satellites. Resonant x-ray scattering at the iron L_{III} edge showed that charge-ordering occurs at the same incommensurate wavevector. The temperature dependence of the incommensurate satellite peaks show a incommensurate-commensurate transition, locking into $q = (0, 0, 5/8)$ concomitant with the appearance of negative magnetoresistance. An additional reflection was found at the iron L_{III} edge at the $q = (0, 0, 0.5)$ position whose origin was determined to be magnetic. The temperature dependence of the magnetic and charge reflections suggest that the magnetism is the driving order-parameter which causes both the structural and incommensurate-commensurate charge-order transitions. This provides a mechanism between the magnetism and the resistivity of the sample providing an explanation for the magnetoresistance. The magnetic reflection was also shown to resonate at the oxygen K-edge, providing direct evidence of spin-polarised oxygen with a small

orbital moment present at the oxygen site. This confirms an indirect exchange-interaction via the oxygen anion is crucial in determining the magnetic ground state. The long-range charge-, and magnetic-, order are both mediated via shared oxygen ligands, providing a likely origin for the microscopic mechanism responsible for the magnetoresistance.

The fourth chapter looked at the distorted kagomé lattice material FeCrAs. This material has two magnetic ions, the chromium atoms sit on the kagomé lattice and the iron atoms sit on a triangular lattice of iron trimers. Previous studies have suggested the iron magnetic moment is quenched and the chromium site orders in a $\sqrt{3} \times \sqrt{3}$ supercell at a relatively high temperature of 125 K. A combination of susceptibility, heat capacity and muon relaxation spectroscopy measurements were used to study this system. No evidence of a simple antiferromagnetic transition was seen. A spin-freezing phenomena was measured at low temperatures in the magnetic susceptibility measurement. Muon spectroscopy shed light on the complex magnetism in this system, and three different magnetic phases were identified by taking muon spectra at different temperatures. At room temperature the muon spectroscopy is dominated by the nuclear moments. Upon cooling below 225 K the muons depolarise more rapidly. The frequency of depolarisation increases upon cooling down to 48 K where the frequency drops sharply when the system enters a spin-frozen phase. The depolarisation rate of the middle phase can be described by a Boltzmann-like exponential with a characteristic energy of 20 meV. This characteristic energy matches to the thermal energy of the transition temperature of 225 K. The spin-freezing transition temperature, where this magnetic behaviour disappears at 48 K has a thermal energy of 4 meV. Monte Carlo simulations predict that the chromium on the kagomé lattice will only remain short-ranged ordered. The 20 meV energy can be interpreted as the strength of the short-range interactions between the chromium atoms. Monte Carlo simulations suggest the system may undergo long-range order if interactions between the iron and chromium layers are taken into consideration. The 4 meV energy at 48 K may refer to the strength of the interaction between chromium and iron layers, and only below 48 K, when interlayer interactions take effect, can the system enter a spin-glass phase.

The fifth chapter looked at the iron pnictide end member FeAs. Since the discovery of superconductivity in the iron pnictides in 2008, there has been much interest in this family of compounds. FeAs is a simply binary system with the iron and arsenic forming a $3d$ network of face sharing octahedra. FeAs is an itinerant magnet. Previous neutron diffrac-

tion studies identified FeAs to have a magnetic helix ground state. More recent magnetic susceptibility and polarised neutron studies have suggested the magnetic structure is more complex, with asymmetry seen within the plane of the helix. We completed a resonant x-ray scattering study of a single crystal of FeAs at both the soft x-ray iron $L_{\mathrm{II/III}}$ edges and the hard x-ray iron K edge. Detailed full polarisation analysis of the resonant scattering was able to reveal quantitative information about the magnetic structure. The results of full polarisation and azimuthal analysis of the resonant x-ray scattering, showed the helical structure was quite elliptical, with the moment along the b-axis being 2.58±0.03 times longer than the moment along the a-axis. The scattered linear polarisation of the resonant scattering was measured for incident circularly polarised x-rays, revealing the chirality of the magnetic helix to be right-handed. The appearance of a magnetic satellite around the forbidden $(0, 0, 1)$ Bragg peak at the iron L_{III} edge could only be explained by out-of-plane c-axis canting of the moment. Due to the crystal symmetry this canting would flip between equivalent iron sites in the unit cell, creating a secondary spatial frequency to the periodicity of the magnetic helix, creating a longer repeat unit than given by the magnetic wavevector $\tau = 0.389$. Full polarisation analysis of this second satellite peak showed it's origin to be from a c-axis component.

The sixth chapter looked at the frustrated triangular lattice antiferromagnet, $CuFeO_2$. This system should be considered an archetypal triangular lattice antiferromagnet, except it shows an unusual Ising-like transition at 14 K. The magnetic field phase diagram for $CuFeO_2$ shows a wealth of different phases. In zero magnetic field the system changes from paramagnetic to a incommensurate partially-disordered phase at 14 K, and then to a four-sublattice phase below 11 K. Upon application of a magnetic field this four-sublattice phase changes to a ferroelectric incommensurate phase at 7 T, then a five-sublattice phase around 13 T. We performed neutron and x-ray scattering experiments exploring this phase diagram. Resonant x-ray scattering of the four-sublattice phase showed that the system does have a collinear Ising-type structure. The resonant spectra showed unusually large contributions from E2E2 scattering and rebut the idea the $CuFeO_2$ is a pure spin triangular lattice antiferromagnet, showing that both the $3d$ and $4p$ bands are spin-polarised. Structural satellites were identified at twice the magnetic wavevector with x-ray diffraction, confirming the strong spin-lattice coupling which creates the Ising-like behaviour. Studying the structural peaks over the transition between the partially disordered incommensurate phase and the five-sublattice phase showed this transition to be discontinuous.

The five-sublattice phase was found to have a multi-**q** magnetic structure with both an antiferromagnetic ($^1/_5, ^1/_5, ^3/_2$) and ferromagnetic ($^1/_5, ^1/_5, 0$) contributions. Neutron scattering in the ferroelectric incommensurate phase was not sufficient to distinguish between a cycloidal and helical spin structure. The appearance of additional ($q, q, ^3/_2$) satellite reflections around ($^1/_2, ^1/_2, 0$) type positions, in the ferroelectric phase showed the non-collinear structure splits into two inequivalent orbits of the non-collinear structure with a phase difference between them.

These four magnetic materials all contain iron, but show a broad range of magnetic phases. The interplay between the crystal symmetry of the iron site, ligand co-ordination and valency cause this variety of possible electronic phases to exist for iron-based compounds from spin-glass, ferroelectricity, elliptical spin helices, charge-order and magnetoresistance.

There are always more questions that can be answered and the future work to build upon that completed in this thesis splits into two parts; the continuation of research around the materials studied and the development of experimental techniques in accessing quantitative information. Performing diffraction experiments on $SrFeO_{3-\delta}$ under magnetic field would give insight into the origin of the magnetoresistance. FeCrAs is is very sensitive to the occupancy of the iron and chromium site. Exploring the phase diagram of the system $Fe_{1+x}Cr_{1-x}As$ would reveal information on the interaction between the trimer and kagomé layers. Full polarisation analysis of the FeAs provided new quantitative information on the structure of magnetic helix. Future work would include performing the diffraction technique on other noncollinear systems, such as the non-chiral spiral present in $CeAl_2$. This technique should be sensitive to pick up any deviations from a perfect circular helix in systems like the archetypal helical magnet holmium. Further research on $CuFeO_2$ requires the development of new diffractometers which can apply magnetic fields at angles other than perpendicular to the scattering plane. This constraint is a limiting factor in the application of a whole host of existing diffraction techniques to the problem, as the engineering constraints of supporting a large magnet on a diffractometer make them currently impossible to carry out. Single crystal time of flight Laue images on WISH provided an alternative but further work would require much larger access to reciprocal space, and the development of refinement procedures to analyse the patterns.

Bibliography

[1] A. Lebon, P. Adler, C. Bernhard *et al.*, *Phys. Rev. Lett.*, **92** 037202 (2004).

[2] T. T. A. Lummen, C. Strohm, H. Rakoto *et al.*, *Phys. Rev. B*, **81** 224420 (2010).

[3] A.-M. Haghiri-Gosnet and J.-P. Renard, *J. Phys. D Appl. Phys.*, **36** 127 (2003).

[4] F. Zheng, Z. Wang, Z.-G. Fu *et al.*, *Europhys. Lett.*, **103** 27001 (2013).

[5] F. L. Pratt, P. J. Baker, S. J. Blundell *et al.*, *Nature*, **471** 612 (2011).

[6] A. Kholkin, N. Pertsev, and A. Goltsev, In A. Safari and E. Akdoan (Eds.), *Piezoelectric and Acoustic Materials for Transducer Applications*, pp. 17–38. Springer US (2008).

[7] D. I. Khomskii, *J. Magn. Magn. Mater.*, **306** 1 (2006).

[8] S. D. Matteo, *J. Phys. D: Appl. Phys.*, **45** 163001 (2012).

[9] J. B. Clark, J. W. Hastie, L. H. E. Kihlborg *et al.*, *Pure Appl. Chem.*, **66** 577 (1994).

[10] S. Blundell, *Magnetism in Condensed Matter (Oxford Master Series in Physics)*. Oxford University Press (2001).

[11] R. Peierls, T. A. Kaplan, and P. W. Anderson, *Phys. Today*, **44** 13 (1991).

[12] P. W. Anderson, P. Langacker, and A. K. Mann, *Phys. Today*, **43** 117 (1990).

[13] M. F. Collins, *Magnetic critical scattering*. Oxford University Press (1989).

[14] V. M. Dubovik and V. V. Tugushev, *Phys. Rep.*, **187** 145 (1990).

[15] J. D. Jackson, *Classical Electrodynamics Third Edition*. Wiley (1998).

[16] G. Subías, J. Herrero-Martín, J. García *et al.*, *Phys. Rev. B*, **75** 235101 (2007).

[17] S. Di Matteo, Y. Joly, A. Bombardi *et al.*, *Phys. Rev.*, **91** 257402 (2003).

[18] V. Scagnoli, U. Staub, Y. Bodenthin *et al.*, *Science*, **332** 696 (2011).

[19] N. A. Spaldin, M. Fiebig, and M. Mostovoy, *J. Phys. Condens. Mat.*, **20** 434203 (2008).

[20] T. V. Ramakrishnan, H. R. Krishnamurthy, and S. R. Hassan, *Phys. Rev.*, **92** 157203 (2004).

[21] K. Liu, X. W. Wu, K. H. Ahn *et al.*, *Phys. Rev. B*, **54** 3007 (1996).

[22] M. Angst, R. P. Hermann, W. Schweika *et al.*, *Phys. Rev. Lett.*, **99** 256402 (2007).

[23] M. A. Ruderman and C. Kittel, *Phys. Rev.*, **96** 99 (1954).

[24] T. Kasuya, *Prog. Theor. Phys.*, **16** 45 (1956).

[25] K. Yosida, *Phys. Rev.*, **106** 893 (1957).

[26] I. Dzyaloshinsky, *J. Phys. Chem. Solids*, **4** 241 (1958).

[27] T. Moriya, *Phys. Rev.*, **120** 91 (1960).

[28] S.-W. Cheong and M. Mostovoy, *Nat. Mater.*, **6** 13 (2007).

[29] H. A. Jahn and E. Teller, *P. Roy. Soc. Lond. A Mat.*, **161** 220 (1937).

[30] J. B. Goodenough, *Phys. Rev.*, **100** 564 (1955).

[31] J. Rodríguez-Carvajal and F. Bourée, *EPJ Web of Conferences*, **22** 00010 (2012).

[32] C. G. Barkla, *P. Roy. Soc. Lond. A Mat.*, **77** 247 (1906).

[33] M. Born and E. Wolf, *Principles of Optics*. Cambridge University Press, 7th ed. (1999).

[34] M. Blume and D. Gibbs, *Phys. Rev. B*, **37** 1779 (1988).

[35] F. de Bergevin and M. Brunel, *Acta Crystallogr. Sec. A*, **37** 314 (1981).

[36] F. W. Lipps and H. A. Tolhoek, *Physica*, **20** 85 (1954).

[37] U. Fano, *Rev. Mod. Phys.*, **29** 74 (1957).

[38] F. W. Lipps and H. A. Tolhoek, *Physica*, **20** 385 (1954).

[39] R. C. Jones, *J. Opt. Soc. Am.*, **31** 488 (1941).

[40] H. Hurwitz, Jr and R. C. Jones, *J. Opt. Soc. Am*, **31** 493 (1941).

[41] R. C. Jones, *J. Opt. Soc. Am.*, **31** 500 (1941).

[42] R. C. Jones, *J. Opt. Soc. Am*, **38** 671 (1948).

[43] V. B. Berestetskii, E. M. Lifshitz, and L. P. Pitaevskii, *Quantum Electrodynamics*. Reed, 2nd ed. (1982).

[44] A. Akhiezer and V. Berestetskii, *Quantum Electrodynamics*. Wiley (1965).

[45] M. Blume, *J. Appl. Phys.*, **57** 3615 (1985).

[46] M. Altarelli, In E. Beaurepaire, H. Bulou, F. Scheurer *et al.* (Eds.), *Magnetism: A Synchrotron Radiation Approach*, vol. 697 of *Lect. Notes Phys.*, pp. 201–242. Springer Berlin Heidelberg (2006).

[47] G. Taylor, *Acta Crystallogr. Sec. D*, **59** 1881 (2003).

[48] P. J. Brown, A. G. Fox, E. N. Maslen *et al.*, *Intensity of diffracted intensities*. John Wiley & Sons, Ltd (2006).

[49] J. P. Hill and D. F. McMorrow, *Acta Crystallogr. Sec. A*, **52** 236 (1996).

[50] S. D. Matteo, *J. Phys. D: Appl. Phys.*, **45** 163001 (2012).

[51] J. P. Hannon, G. T. Trammell, M. Blume *et al.*, *Phys. Rev. Lett.*, **61** 1245 (1988).

[52] L. Koester, In *Neutron Physics*, vol. 80 of *Springer Tracts in Modern Physics*, pp. 1–55. Springer Berlin Heidelberg (1977).

[53] A. Foderaro, *The Neutron Interaction Theory*. The MIT Press, Cambridge, Massachusetts and London, England (1971).

[54] S. W. Lovesey, *The Theory of Neutron Scattering from Condensed Matter: Volume I (The International Series of Monographs on Physics) (v. 1)*. Oxford University Press (1985).

[55] S. Mughabghab, M. Divadeenam, and N. Holden, *Academic, New York* (1981).

[56] L. D. Landau and L. M. Lifshitz, *Quantum Mechanics, Third Edition: Non-Relativistic Theory (Volume 3)*. Butterworth-Heinemann (1981).

[57] S. W. Lovesey, *The Theory of Neutron Scattering from Condensed Matter: Volume II (The International Series of Monographs on Physics)*. Clarendon Press (1986).

[58] L. C. Chapon, P. Manuel, P. G. Radaelli *et al.*, *Neutron News*, **22** 22 (2011).

[59] A. D. McNaught and A. Wilkinson, *IUPAC. Compendium of Chemical Terminology*. Blackwell Scientific Publications, 2nd ed. (1997).

[60] J. G. Bednorz and K. A. Müller, *Eur. Phys. J. B*, **64** 189 (1986).

[61] L. F. Schneemeyer, J. V. Waszczak, T. Siegrist *et al.*, *Nature*, **328** 601 (1987).

[62] H. Maeda, Y. Tanaka, M. Fukutomi *et al.*, *Jpn. J. Appl. Phys.*, **27** L209 (1988).

[63] Y. Moritomo, A. Asamitsu, H. Kuwahara *et al.*, *Nature*, **380** 141 (1996).

[64] N. B. Aetukuri, A. X. Gray, M. Drouard *et al.*, *Nat. Phys.*, **9** 661 (2013).

[65] F. Kubel and H. Schmid, *Acta Crystallogr. Sec. B*, **46** 698 (1990).

[66] T. Kimura, T. Goto, H. Shintani *et al.*, *Nature*, **426** 55 (2003).

[67] S.-W. Cheong, *Nat. Mater.*, **6** 927 (2007).

[68] H. Bethe, *Ann. Phys.*, **395** 133 (1929).

[69] J. Van Vleck, *Phys. Rev.*, **41** 208 (1932).

[70] S. Jin, T. H. Tiefel, M. McCormack *et al.*, *Science*, **264** 413 (1994).

[71] G.-Q. Gong, C. Canedy, G. Xiao *et al.*, *Appl. Phys. Lett.*, **67** 1783 (1995).

[72] J. Hodges, *J. Solid State Chem.*, **151** 190 (2000).

[73] P. K. Gallagher, *J. Chem. Phys.*, **45** 2466 (1966).

[74] T. Takeda, Y. Yamaguchi, and H. Watanabe, *J. Phys. Soc. Jpn.*, **33** 967 (1972).

[75] A. Bocquet, A. Fujimori, T. Mizokawa *et al.*, *Phys. Rev. B*, **45** 1561 (1992).

[76] J. Rodríguez-Carvajal, M. Hennion, F. Moussa *et al.*, *Phys. Rev. B*, **57** R3189 (1998).

[77] J. MacChesney, R. C. Sherwood, and J. F. Potter, *J. Chem. Phys.*, **43** 1907 (1965).

[78] P. K. Gallagher, J. MacChesney, and D. Buchanan, *J. Chem. Phys.*, **41** 2429 (1964).

[79] Y. Tsujimoto, C. Tassel, N. Hayashi *et al.*, *Nature*, **450** 1062 (2007).

[80] L. Seinberg, T. Yamamoto, C. Tassel *et al.*, *Inorg. Chem.*, **50** 3988 (2011).

[81] P. Adler, A. Lebon, V. Damljanovič *et al.*, *Phys. Rev. B*, **73** 094451 (2006).

[82] M. Takano, T. Okita, N. Nakayama *et al.*, *J. Solid State Chem.*, **73** 140 (1988).

[83] M. Reehuis, C. Ulrich, A. Maljuk *et al.*, *Phys. Rev. B*, **85** 184109 (2012).

[84] W. Pfann and J. K. Kennedy, *J. Electrochem. Soc.*, **114** 26C (1967).

[85] J. Loudon, S. Cox, A. Williams *et al.*, *Phys. Rev. Lett.*, **94** 097202 (2005).

[86] C. H. Chen and S.-W. Cheong, *Phys. Rev. Lett.*, **76** 4042 (1996).

[87] G. C. Milward, M. J. Calderon, and P. B. Littlewood, *Nature*, **433** 607 (2005).

[88] M. Abbate, F. M. F. de Groot, J. C. Fuggle *et al.*, *Phys. Rev. B*, **46** 4511 (1992).

[89] O. Bunău and Y. Joly, *J. Phys. Condens. Mat.*, **21** 345501 (2009).

[90] T. A. W. Beale, S. B. Wilkins, R. D. Johnson *et al.*, *Phys. Rev. Lett.*, **105** 087203 (2010).

[91] V. Scagnoli, S. W. Huang, M. Garganourakis *et al.*, *Phys. Rev. B*, **88** 104417 (2013).

[92] S. Srinath, M. M. Kumar, M. L. Post *et al.*, *Phys. Rev. B*, **72** 054425 (2005).

[93] Y. Kamihara, T. Watanabe, M. Hirano *et al.*, *J. Am. Chem. Soc.*, **130** 3296 (2008).

[94] M. Rotter, M. Tegel, D. Johrendt *et al.*, *Phys. Rev. B*, **78** 020503 (2008).

[95] X. C. Wang, Q. Q. Liu, Y. X. Lv *et al.*, *Solid State Commun.*, **148** 538 (2008).

[96] F.-C. Hsu, J.-Y. Luo, K.-W. Yeh *et al.*, *Proc. Natl. Acad. Sci. U.S.A.*, **105** 14262 (2008).

[97] K. Ishida, Y. Nakai, and H. Hosono, *J. Phys. Soc. Jpn*, **78** 062001 (2009).

[98] I. Felner, U. Asaf, Y. Levi *et al.*, *Phys. Rev. B*, **55** R3374 (1997).

[99] D. A. Dikin, M. Mehta, C. W. Bark *et al.*, *Phys. Rev. Lett.*, **107** 056802 (2011).

[100] H. Eisaki, H. Takagi, R. J. Cava *et al.*, *Phys. Rev. B*, **50** 647 (1994).

[101] S. S. Saxena, P. Agarwal, K. Ahilan *et al.*, *Nature*, **406** 587 (2000).

[102] D. Aoki, A. Huxley, E. Ressouche *et al.*, *Nature*, **413** 613 (2001).

[103] C. Pfleiderer, M. Uhlarz, S. M. Hayden *et al.*, *Nature*, **412** 58 (2001).

[104] A. A. Aczel, E. Baggio-Saitovitch, S. L. Budko *et al.*, *Phys. Rev. B*, **78** 214503 (2008).

[105] H. Luetkens, H. H. Klauss, M. Kraken *et al.*, *Nat. Mat.*, **8** 305 (2009).

[106] S. Takeshita, R. Kadono, M. Hiraishi *et al.*, *J. Phys. Soc. Jpn.*, **77** (2008).

[107] S. Takeshita, R. Kadono, M. Hiraishi *et al.*, *Phys. Rev. Lett.*, **103** 027002 (2009).

[108] W. Wu, A. McCollam, I. Swainson *et al.*, *Europhys. Lett.*, **85** 17009 (2009).

[109] M. L. Fornasini and F. Merlo, *J. Alloy. Compd.*, **219** 63 (1995).

[110] T. E. Redpath, J. M. Hopkinson, A. A. Leibel *et al.*, *arXiv.org* (2011).

[111] S. Blundell, *Magnetism in Condensed Matter (Oxford Master Series in Physics)*. Oxford University Press (2001).

[112] S. Gondek, S. Baran, A. Szytuła *et al.*, *J. Magn. Magn. Mater.*, **285** 272 (2005).

[113] A. Szytuła, B. Penc, and J. Hernandez-Velasco, *Acta Phys. Pol. A*, **106** 583 (2004).

[114] N. D. Mermin and H. Wagner, *Phys. Rev. Lett.*, **17** 1133 (1966).

[115] J. T. Chalker, P. Holdsworth, and E. F. Shender, *Phys. Rev. Lett.*, **68** 855 (1992).

[116] D. A. Huse and A. D. Rutenberg, *Phys. Rev. B*, **45** 7536 (1992).

[117] J. N. Reimers and A. J. Berlinsky, *Phys. Rev. B*, **48** 9539 (1993).

[118] A. Chubukov, *Phys. Rev. Lett.*, **69** 832 (1992).

[119] Harris, AB, C. Kallin, and A. J. Berlinsky, *Phys. Rev. B*, **45** 2899 (1992).

[120] A. Danielian, *Phys. Rev.*, **133** A1344 (1964).

[121] I. P. Swainson, W. Wu, A. McCollam *et al.*, *Can. J. Phys.*, **88** 701 (2010).

[122] D. G. Rancourt, *Hyperfine field fluctuations in the Mössbauer spectrum of magnetic materials: Applications to Small Particles and to the bulk Antiferromagnet* $Fe_{2-x}Cr_xAs$. Phd thesis, Graduate Department of Physics, University of Toronto (1984).

[123] S. Ishida, T. Takiguchi, S. Fujii *et al.*, *Phys. B*, **217** 87 (1996).

[124] D. Schmalfuß and J. Richter, *Phys. Rev. B*, **70** 184412 (2004).

[125] M. Zelli, K. Boese, and B. Southern, *Phys. Rev. B*, **76** 224407 (2007).

[126] T. Moriya, *Phys. Rev.*, **120** 91 (1960).

[127] F. Torres, D. Altbir, and M. Kiwi, *Europhys. Lett.*, **106** 47004 (2014).

[128] M. Elhajal, B. Canals, and C. Lacroix, *Phys. B*, **312-313** 716 (2002).

[129] u. Gondek and A. Szytuła, *J. Alloy Compd.*, **442** 111 (2007).

[130] J. G. Rau and H.-Y. Kee, *Phys. Rev. B*, **84** 104448 (2011).

[131] K. A. Ziq and A. F. Salem, *J. Supercond. Nov. Magn.*, **26** 1185 (2012).

[132] W. Wu, *Novel metallic states at low temperatures in strongly correlated systems*. Phd thesis, Graduate Department of Physics, University of Toronto (2010).

[133] J. Goldstein, D. E. Newbury, D. C. Joy *et al.*, *Scanning Electron Microscopy and X-ray Microanalysis: Third Edition*. Springer (2007).

[134] P. J. Baker, S. R. Giblin, F. L. Pratt *et al.*, *New J. Phys.*, **11** 025010 (2009).

[135] K. Levenberg, *Q. J. Appl. Math.*, **2** 164 (1944).

[136] D. W. Marquardt, *J. Soc. Ind. Appl. Math.*, **11** 431 (1963).

[137] F. F. Tafti, *Non-metallic, non-Fermi-liquid resistivity of FeCrAs from 0 to 17 GPa*. Phd thesis, Graduate Department of Physics, University of Toronto (2013).

[138] A. Harrison, K. M. Kojima, A. S. Wills *et al.*, *Phys. B*, **289** 217 (2000).

[139] A. Keren, K. Kojima, L. P. Le *et al.*, *Phys. Rev. B*, **53** 6451 (1996).

[140] A. Fukaya, Y. Fudamoto, I. M. Gat *et al.*, *Phys. Rev. Lett.*, **91** 207603 (2003).

[141] I. Ritchey, P. Chandra, and P. Coleman, *Phys. Rev. B* (1993).

[142] V. F. Sears, *Neutron News*, **3** 26 (1992).

[143] R. D. Shull and P. A. Beck, In *AIP Conference Proceedings Vol. 24*, pp. 95–96. AIP (1974).

[144] J. O. Strom-Olsen, D. F. Wilford, and S. K. Burke, *J. Phys. F Met. Phys.* (1979).

[145] M. Telling and R. Cywinski, *J. Magn. Magn. Mater.*, **140** 45 (1995).

[146] K. Selte and A. Kjekshus, *Acta Chem. Scand.*, **23** 2047 (1969).

[147] K. Selte, A. Kjekshus, and A. Andresen, *Acta Chem. Scand.*, **26** 3101 (1972).

[148] K. Selte and A. Kjekshus, *Acta Chem. Scand.*, **27** 1448 (1973).

[149] J. Paglione and R. L. Greene, *Nat. Phys.*, **6** 645 (2010).

[150] Z.-A. Ren, G.-C. Che, X.-L. Dong *et al.*, *Europhys. Lett.*, **83** 17002 (2008).

[151] C. de la Cruz, Q. Huang, J. W. Lynn *et al.*, *Nature*, **453** 899 (2008).

[152] M. Rotter, M. Tegel, D. Johrendt *et al.*, *Phys. Rev. B*, **78** 020503(R) (2008).

[153] H. Kito, H. Eisaki, and A. Iyo, *J. Phys. Soc. Jpn.*, **77** 063707 (2008).

[154] L. Boeri, M. Calandra, I. I. Mazin *et al.*, *Phys. Rev. B*, **82** 020506 (2010).

[155] K. Segawa and Y. Ando, *J. Phys. Soc. Jpn*, **78** 104720 (2009).

[156] E. E. Rodriguez, C. Stock, K. L. Krycka *et al.*, *Phys. Rev. B*, **83** 134438 (2011).

[157] S. Rundqvist, *Acta Chem. Scand.*, **16** 287 (2007).

[158] B. Saparov, J. E. Mitchell, and A. S. Sefat, *Supercond. Sci. Tech.*, **25** 084016 (2012).

[159] S. Lidin, *Acta Cryst.*, **54** 97 (1998).

[160] P. S. Lyman and C. T. Prewitt, *Acta Crystallogr. Sec. B*, **40** 14 (2015).

[161] H. F. Franzen, C. Haas, and F. Jellinek, *Phys. Rev. B*, **10** 1248 (1974).

[162] W. Tremel, R. Hoffmann, and J. Silvestre, *J. Am. Chem. Soc.*, **108** 5174 (1986).

[163] C. C. Becerra, Y. Shapira, N. F. Oliveira, Jr *et al.*, *Phys. Rev. Lett.*, **44** 1692 (1980).

[164] Y. Shapira, C. C. Becerra, N. F. OLIVEIRA *et al.*, *Phys. Rev. B*, **24** 2780 (1981).

[165] J. B. Forsyth, S. J. Pickart, and P. J. Brown, *P. Phys. Soc.*, **88** 333 (1966).

[166] M. Morifuji and K. Motizuki, *J. Magn. Magn. Mater.*, **70** 70 (1987).

[167] T. Tanaka, H. Nozaki, E. Bannai *et al.*, *J. Less-Common Met.*, **50** 15 (1976).

[168] S. Funahashi, Y. Hamaguchi, T. Tanaka *et al.*, *Solid State Commun.*, **23** 859 (1977).

[169] C. Michioka, Y. Itoh, K. Yoshimura *et al.*, *J. Magn. Magn. Mater.*, **310** e620 (2007).

[170] E. Bertaut, *J. Appl. Phys.*, **33** 1138 (1962).

[171] E. Bertaut, *Acta Crystallogr. Sec. A*, **24** 217 (1968).

[172] E. Bertaut, *J. Appl. Phys.*, **40** 1592 (1969).

[173] G. P. Felcher, F. A. Smith, D. Bellavance *et al.*, *Phys. Rev. B*, **3** 3046 (1971).

[174] A. Kallel, H. Boller, and E. Bertaut, *J. Phys. Chem. Solids*, **35** 1139 (1974).

[175] K. Selte, H. Fjellvag, A. Kjekshus *et al.*, *Acta Chem. Scand.*, pp. 727–731 (1979).

[176] J. Strempfer, S. Francoual, D. Reuther *et al.*, *J. Synchrotron Rad.*, **20** 541 (2013).

[177] S.-H. Lee, Y.-C. Lai, C.-H. Du *et al.*, *arXiv.org* (2014).

[178] R. J. Birgeneau, J. Skalyo, Jr, and G. Shirane, *Phys. Rev. B*, **3** 1736 (1971).

[179] R. J. Birgeneau, H. J. Guggenheim, and G. Shirane, *Phys. Rev. B*, **8** 304 (1973).

[180] H. Kawamura, *J. Appl. Phys.*, **63** 3086 (1988).

[181] H. Kawamura, *J. Phys. Soc. Jpn.*, **61** 1299 (1992).

[182] H. Kawamura, *J. Phys. Condens. Matter*, **10** 4707 (1998).

[183] H. Sato, *Physica B*, **329-333** 757 (2003).

[184] A. Thompson, D. Attwood, E. Gullikson *et al.*, *URL http://xdb. lbl. gov* (2009).

[185] E. M. Forgan, B. D. Rainford, S. L. Lee *et al.*, *J. Phys. Condens. Matter*, **2** 10211 (1999).

[186] A. M. Mulders, S. M. Lawrence, A. J. Princep *et al.*, *Phys. Rev. B*, **81** 092405 (2010).

[187] D. Gibbs, D. R. Harshman, E. D. Isaacs *et al.*, *Phys. Rev. Lett.*, **61** 1241 (1988).

[188] J. P. Hill and D. F. McMorrow, *Acta Crystallogr. Sec. A*, **52** 236 (1996).

[189] W. Soller, *Bull. Am. Phys. Soc.*, **10** 17 (1935).

[190] A. Pabst, *Am. Mineral.*, **31** 539 (1946).

[191] M. A. Marquardt, N. A. Ashmore, and D. P. Cann, *Thin Solid Films*, **496** 146 (2006).

[192] R. D. Shannon, C. T. Prewitt, and D. B. Rogers, *Inorg. Chem.*, **10** 719 (1971).

[193] J.-P. Doumerc, A. Ammar, A. Wichainchai *et al.*, *J. Phys. Chem. Solids*, **48** 37 (1987).

[194] J.-P. Doumerc, A. Wichainchai, A. Ammar *et al.*, *Mater. Res. Bull.*, **21** 745 (1986).

[195] R. D. Shannon, D. B. Rogers, and C. T. Prewitt, *Inorg. Chem.*, **10** 713 (1971).

[196] H. Kadowaki, H. Takei, and K. Motoya, *J. Phys. Condens. Matter*, **7** 6869 (1995).

[197] Y. Oohara, S. Mitsuda, H. Yoshizawa *et al.*, *J. Phys. Soc. Jpn.*, **63** 847 (1994).

[198] M. Frontzek, G. Ehlers, A. Podlesnyak *et al.*, *J. Phys. Condens. Matter*, **24** 016004 (2011).

[199] M. Mekata, N. Yaguchi, T. Takagi *et al.*, *J. Phys. Soc. Jpn.*, **62** 4474 (1993).

[200] S. Mitsuda, N. Kasahara, T. Uno *et al.*, *J. Phys. Soc. Jpn.*, **67** 4026 (1998).

[201] S. Mitsuda, H. Yoshizawa, N. Yaguchi *et al.*, *J. Phys. Soc. Jpn.*, **60** 1885 (1991).

[202] M. Mekata, N. Yaguchi, T. Takagi *et al.*, *J. Magn. Magn. Mater.*, **104-107** 823 (1992). Proceedings of the International Conference on Magnetism, Part {II}.

[203] Y. Ajiro, T. Asano, T. Takagi *et al.*, *Physica B*, **201** 71 (1994).

[204] T. Takagi and M. Mekata, *J. Phys. Soc. Jpn.*, **64** 4609 (1995).

[205] S. Mitsuda, T. Uno, M. Mase *et al.*, *J. Phys. Chem. Solids*, **60** 1249 (1999).

[206] F. Ye, J. A. Fernandez-Baca, R. S. Fishman *et al.*, *Phys. Rev. Lett.*, **99** 157201 (2007).

[207] O. A. Petrenko, M. R. Lees, G. Balakrishnan *et al.*, *J. Phys. Condens. Matter*, **17** 2741 (2005).

[208] T.-R. Zhao, M. Hasegawa, and H. Takei, *J. Cryst. Growth*, **166** 408 (1996).

[209] T. Kimura, J. C. Lashley, and A. P. Ramirez, *Phys. Rev. B*, **73** 220401 (2006).

[210] N. Terada, S. Mitsuda, H. Ohsumi *et al.*, *J. Phys. Soc. Jpn.*, **75** 023602 (2006).

[211] F. Ye, Y. Ren, Q. Huang *et al.*, *Phys. Rev. B*, **73** 220404 (2006).

[212] N. Terada, Y. Tanaka, Y. Tabata *et al.*, *J. Phys. Soc. Jpn.*, **75** 113702 (2006).

[213] N. Terada, Y. Tanaka, Y. Tabata *et al.*, *J. Phys. Soc. Jpn.*, **76** 068001 (2007).

[214] Y. Yamashita, *Phys. Rev. Lett.*, **85** 4960 (2000).

[215] O. Tchernyshyov, R. Moessner, and S. L. Sondhi, *Phys. Rev. B*, **66** 064403 (2002).

[216] F. Wang and A. Vishwanath, *Phys. Rev. Lett.*, **100** 077201 (2008).

[217] N. Terada, Y. Narumi, Y. Sawai *et al.*, *Phys. Rev. B*, **75** 224411 (2007).

[218] T. Lummen, C. Strohm, H. Rakoto *et al.*, *Phys. Rev. B*, **80** 012406 (2009).

[219] T. Nakajima, A. Suno, S. Mitsuda *et al.*, *Phys. Rev. B*, **84** 184401 (2011).

[220] O. A. Petrenko, G. Balakrishnan, M. R. Lees *et al.*, *Phys. Rev. B*, **62** 8983 (2000).

[221] S. Mitsuda, M. Mase, T. Uno *et al.*, *J. Phys. Soc. Jpn.*, **69** 33 (2000).

[222] N. Terada, Y. Narumi, K. Katsumata *et al.*, *Phys. Rev. B*, **74** 180404(R) (2006).

[223] G. Quirion, M. Plumer, O. Petrenko *et al.*, *Phys. Rev. B*, **80** 064420 (2009).

[224] S. Mitsuda, M. Mase, K. Prokes *et al.*, *J. Phys. Soc. Jpn.*, **69** 3513 (2000).

[225] S. Seki, Y. Yamasaki, Y. Shiomi *et al.*, *Phys. Rev. B*, **75** 100403 (2007).

[226] S. Mitsuda, T. Uno, M. Mase *et al.*, *J. Phys. Chem. Solids*, **60** 1249 (1999).

[227] T. Nakajima, S. Mitsuda, S. Kanetsuki *et al.*, *J. Phys. Soc. Jpn.*, **76** 043709 (2007).

[228] T.-H. Arima, *J. Phys. Soc. Jpn.*, **76** 073702 (2007).

[229] T. Nakajima, S. Mitsuda, S. Kanetsuki *et al.*, *Phys. Rev. B*, **77** 052401 (2008).

[230] H. Katsura, N. Nagaosa, and A. V. Balatsky, *Phys. Rev. Lett.*, **95** 057205 (2005).

[231] S. Francoual, J. Strempfer, D. Reuther *et al.*, *J. Phys. Conf. Ser.*, **425** 132010 (2013).

[232] N. Terada, S. Mitsuda, T. Fujii *et al.*, *J. Phys. Soc. Jpn.*, **74** 2604 (2005).

[233] N. Terada, S. Mitsuda, and A. Gukasov, *Phys. Rev. B*, **73** 014419 (2006).

[234] M. Soda, K. Kimura, T. Kimura *et al.*, *J. Phys. Soc. Jpn.*, **78** 124703 (2009).